The Role of Accurate Earthquake Locations in the Mapping of the Volcanic Plumbing System at Soufrière Hills Volcano, Montserrat

Doctor of Philosophy

Jade Hannah Webb Eyles

University of East Anglia
School of Environmental Sciences

November 2021

Abstract

Volcanic seismicity is used to monitor volcanic activity worldwide, with seismic monitoring the main method used to monitor Soufrière Hills Volcano, Montserrat. Soufrière Hills began erupting on the 18^{th} July 1995 and has undergone five phases of activity, which were preceded by an increase in seismicity. Earthquake location is a complex problem, with several unknowns; computed hypocenters represent the optimal solution given the information available. Synthetic earthquakes allow the testing of velocity models and location methods to be compared with known earthquake locations. The current location method used at Montserrat Volcano Observatory produced large hypocenter errors, with poor constraints on hypocenters at particular depths. Comparison with other velocity models and location methods shows the *Rowe et al.* (2004) velocity model with *NonLinLoc* produces locations that more accurately represent synthetic earthquake locations. This new location method was used to relocate the seismic catalogue at Montserrat from 1995 to 2018, to understand how changes in hypocenters influence interpretations. Relocations show a migration of hypocenters towards St Georges Hill on the 12^{th}–14^{th} August 1995; this alongside computed focal mechanisms, suggests dyke propagation and inflation, differing from previous interpretations. Prior to a Vulcanian Explosion on the 29^{th} July 2008, relocated hypocenters are located in SE Montserrat. The majority were located using four P phases; this has been shown to produce large hypocenter errors with synthetic testing. Therefore, earthquakes were repicked for additional P and S phases to improve locations during this period. This resulted in reduced hypocenter errors, with the majority of earthquakes relocated beneath Soufrière Hills with minimal SE locations. This project highlights the importance of using a robust location method suitable for the region to ensure that outputted hypocenters are trustworthy and accurate. Use of unsuitable methods can influence earthquake patterns and thus interpretations. This impacts understanding of volcanic systems, and ultimately hazard assessment.

Contents

List of Figures

Preface

This PhD was supported by the Natural Environmental Research Council and the EnvEast Doctoral Training Partnership [grant number NE/L002582/1]. Seismic Data was provided by the Montserrat Volcano Observatory under a data licence agreement with them. Any requests for the data used in this thesis should be directed to MVO. Paddy Smith and Victoria Miller provided support with seismicity analysis, and understanding of seismic processing and operations at Montserrat Volcano Observatory.

Figures throughout this thesis were created using Generic Mapping Tools: Wessel, P., W. H. F. Smith, R. Scharroo, J. Luis, and F. Wobbe, Generic Mapping Tools: Improved Version Released, EOS Trans. AGU, 94(45), p. 409–410, 2013. The topography that is used in the images throughout is from *Stinton* (2015). Bathymetry is reproduced from the BODC-GEBCO 30 arc-second global grid.

Acknowledgments

I developed an interest in natural hazards at a young age after my grandma gave me a book on volcanoes, but it was only when I was 14 that I decided I wanted to pursue a career as a seismologist. I have been fortunate to pursue that dream so far, and am grateful for all the opportunities that I have had throughout my PhD that have helped me achieve this. There are several people that I would like to thank who have supported me throughout my journey. A big thanks to Mike Lewis who put on Geology classes after school, and to the rest of the teachers at Pitsford School who have supported me throughout. Thank you to Derek Keir, Finnigan Illsley-Kemp, Matthew Head, Joseph Asplet and the rest of my undergraduate geophysics class that not only supported me throughout my masters project, but also gave me the confidence to pursue a PhD, and provided support when the PhD was not always going to plan. Without these people, I would not have reached this point, so a massive thank you. A big thanks to my PhD office: Bridie, James, Richmal, Miles, Emma and Nicola, who provided many baked goods and cheer during cold winter days. Of course, I could have not completed the PhD without the support from my supervisors Jenni Barclay, Jessica Johnson, Paddy Smith and Vicky Miller, alongside the Volcano Crew at UEA who kept my mind busy with outreach, field trips and all things earth science!

I could not have done this PhD without the support from my friends and family. I am so grateful for all the friends I have met throughout the university experience, and who have kept my head above water on days when I questioned why I was doing a PhD. Ruth Matthews and Becca Allen played an integral part in my wellbeing, especially through a year of lockdown; they have ignited my love for plants and all things crafting, which was always a welcome release after a hard day. Thanks to the SSR crew who provided me a community at UEA for the past two years; this gave me a wealth of support in ways I never expected. A huge thank you to Benjamin Bone for acknowledging my issues, dealing with many tears and convincing me that I could finish my PhD. To Paula, Harry and Ava - thank you for being supportive and offering many cups of tea. And finally, but most importantly, thank you to my parents who have supported me throughout the past four years; I definitely could not have completed this without their support and opportunities

they have given me throughout the past 26 years.

”Failure is not an option” - Gene Kranz

NASA Flight Director Gemini and Apollo Missions

Chapter 1

Introduction

1.1 Summary

This thesis aims to improve the accuracy of locating earthquakes at Montserrat Volcano Observatory (MVO) by comparing the current methodology with other location methods and seismic velocity models available. This will help constrain future seismic events used in monitoring Soufrière Hills Volcano, and will also be used to relocate the past seismic catalogue from 1995 to 2018. The relocated catalogue is then used to build on current interpretations that will aid our understanding of the volcanic plumbing system beneath Soufrière Hills. This methodology will give a greater understanding of which parameters affect earthquake location in general, and therefore can be applied to locating seismicity in other volcanic regions.

The thesis first compares different location methods, seismic velocity models and station configurations to understand how accurately the current methodology locates earthquakes, and if locations can be improved by using different location methods and seismic velocity models. The most suitable method from the comparison will be used to relocate the seismic catalogue from 1995 to 2018 to improve the accuracy of earthquake hypocenters. Producing higher accuracy locations allows more earthquakes to be included for analysis, which can result in more detailed geophysical interpretations, and understandings of the volcanic plumbing system. In the last chapter, synthetic earthquakes are used to understand how a small number of seismic stations can effect locations and calculated hypocenter errors, and how in turn this can effect interpretations of seismic activity. A case study of precursory activity prior to a large vulcanian explosion in July 2008 is studied in more detail due to

a large number of earthquakes recorded, but only a small number of seismic stations being used to pick arrival times.

Soufrière Hills Volcano began erupting in July 1995 after three years of increased seismicity; it has undergone five main phases of eruptions, and is still thought to be active. The Montserrat Volcano Observatory has used the same seismic velocity model and location method since the broadband network was installed in October 1996. Since then, several 1D (*Rowe et al.*, 2004) and 3D (*Paulatto et al.*, 2012; *Shalev et al.*, 2010) seismic velocity models have been produced for Montserrat. Additionally, new location methods have been developed which have been shown to work well in complex environments, such as *NonLinLoc* (*Lomax*, 2001), *QuakeMigrate* (*Winder et al.*, 2021) and *Bayesloc* (*Myers et al.*, 2011).

It is important to use a reliable location method, so that there is strong confidence in the calculated locations. This is particularly important when being used in real time for hazard assessment, as an accurate depth and epicentre location can contribute to a better understanding of the location of magma, which is used to anticipate when an eruption may be more likely. An example of this was the 2014–2015 Bardharbunga–Holuhraun event, where over 30,000 earthquakes were recorded during dyke propagation; this allowed further understanding of dynamic processes occurring between dyke propagation and recorded seismicity, and the implications this has for hazard monitoring (*Woods et al.*, 2019).

Throughout this thesis, accuracy, precision and confidence are referred to when discussing different earthquake location methods, and the relocated seismic catalogue. In terms of earthquake location, high accuracy is when the earthquake is relocated close to the true hypocenter of the earthquake. This is shown in Figure 1.1 where earthquakes would be located close to the bullseye - the true earthquake origin. High precision is when a group of earthquakes are relocated to within a close distance to each other; these can be accurate (close to the true location) or not accurate (located poorly in absolute location but located well in respect to each other). This thesis is comparing absolute location methods instead of relative methods, and hence aims to improve the accuracy of locations. Each earthquake is thought to be independent of each other, and hence we can not determine precision unless further analysis is done to determine that a set of earthquakes have originated from the same location or process. This then allows relative location methods to be used to further constrain earthquake locations relative to one another. In this thesis, confidence refers to

whether we can trust the outputted earthquake location with the calculated error. This is explored further in Section 4.2.3 where a term 'trusted earthquake' is defined. If we have a method that produces a high percentage of trusted earthquakes, then we have a high confidence in the outputted locations, as we can trust the results that method produces.

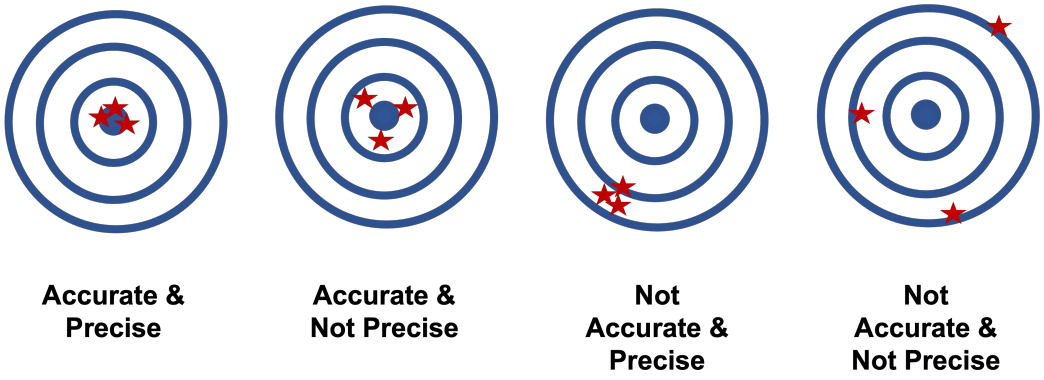

Figure 1.1: Schematic showing the difference between accuracy and precision. In this thesis, the stars represent earthquakes located hypocenter, with the bullseye representing the true earthquake location.

It is also important to have trustworthy locations when interpreting past seismicity, so that patterns in hypocenters can be deduced and understood. For example, seismicity beneath St George's Hill was recorded in August 1995; if we can not trust the locations related to this it can be difficult to say if this is a true change in hypocenters, or if it is a result of poorly-constrained locations. This thesis aims to improve the accuracy of computed locations, and tests to see if the new methodology can be trusted, so that we can have confidence in earthquake hypocenters from the seismic catalogue.

1.2 Motivation

Volcanic seismicity is a useful indicator of activity at volcanoes worldwide, and seismic monitoring is one of the main short term monitoring methods used by volcanic observatories (*Luckett et al.*, 2007). In active fault zones, the location of an earthquake provides information on the locality of damage, the potential for tsunami warnings and can be used for future hazard planning (*Lomax et al.*, 2009). For volcanic systems, seismic analysis can give a wealth of information; the number of events over a given time period highlights increasing activity; different seismic signals can give an indication of the internal dynamics of the volcanic system, such as magma movement or magma pressurisation; and the earth-

quake location itself can determine the source location of the magmatic system/conduit. Rock fracture earthquakes, otherwise known as Volcano-Tectonic earthquakes, can be used to track the movement of magma, such as a propagating dyke, which gives an indication of the eruptive site (*Bakker et al.*, 2016; *Eyles et al.*, 2018; *Marchetti et al.*, 2009; *Woods et al.*, 2018). Accurate earthquake locations can greatly improve the understanding of subsurface processes at volcanoes globally.

There are several challenges faced with earthquake location; one of the main issues arises from the lack of a complete seismic velocity model of the region. Normally location algorithms use a simplified 1D velocity model, or can use more complex 2D and 3D models. Additional errors are introduced with more complex models, as these themselves have had to be calculated through several iterative processes. In essence, we can never truly know the complete velocity model, especially beneath volcanic regions where the magmatic system can be constantly changing in the lead-up to an eruption. The volcanic edifice is likely heterogeneous, with steep topography, which makes portraying the velocity model difficult. At volcanic observatories, resources can be limited, and therefore full seismic networks are not always deployed until activity increases. This can result in a loss of information of internal dynamics during the initial processes, and can delay interpretations of the volcanic system. Another challenge is that the earthquake location itself is not always well constrained, with calculated hypocenters representing the most optimal solution with the given input data. It is therefore hard to test different location methods and velocity models, as a change in location with each method does not clearly define which method produces the most accurate result. Use of synthetic earthquakes (where we control the location of the earthquake, and calculate exact travel times to the stations) helps eliminate the unknown of the original earthquake location, allowing the velocity model and location method to be tested for suitability.

Different location methods have not been compared for their applicability in locating earthquakes on Montserrat before; a crucial step that can be used to understand how much confidence we have in MVO's locations. *Miller* (2011) compared three 1D seismic velocity models by relocating one VT earthquake that was recorded during a time period with a large number of active seismic stations (an additional 26 temporary SEA-CALIPSO stations, alongside MVO's nine permanent stations). Time residuals were compared at each

seismic station, alongside the location of the relocated earthquake. *Miller* (2011) found that the Rowe seismic velocity model (*Rowe et al.*, 2004) was better at predicting arrival times at the North of the island, but RMS values over the island were smaller with the SEA-CALIPSO velocity model. However, *Miller* (2011) tested these velocity models with a high density seismic network, not representative of MVO's current configuration. This was tested on only one VT earthquake, and so does not give a good representation of the velocity model for the whole island, such as earthquakes occurring in the North, or at varying depths. Using a grid of synthetic earthquakes across Montserrat at several depths will allow a full understanding of how each seismic velocity model performs, and where weaknesses may occur.

This thesis is using absolute location methods for relocation (where earthquakes are located individually and not relative to one another), which has a limit on what structures can be resolved. Absolute location methods are more useful for volcanic observatories as they allow an initial location for the earthquake to be computed relatively quickly and per earthquake, instead of having to use a cluster of earthquakes. Relative location methods are best for constraining faults and layers in the subsurface, although these can still be located with absolute location methods (used in this thesis), but with lower certainty. These locations can then be combined with other geophysical methods and models of the subsurface to help interpret the recorded seismicity.

Improving earthquake locations gives an improved understanding of processes leading up to and during the eruption at Soufrière Hills Volcano, by helping to refine what location and depths the seismicity was at during different stages of the eruption. Trends in seismicity with time can highlight dyke propagation, distal clusters and magma movement — all of which are useful in understanding the magmatic system, and for future understanding for hazard assessment. For example, there are several proposed orientations for a dyke during the early stages of the Soufrière Hills eruption; if location errors can be reduced, and locations refined, this can be used alongside other geophysical data to constrain the orientation and location of the dyke, confirming or providing alternative interpretations to previous research.

Accurate locations also aid placing rough boundaries of the magmatic chamber - a region where we see less volcano-tectonic earthquakes. This has been estimated to be around 5 km

depth using earthquake locations from (*Aspinall et al.*, 1998) alongside other geophysical and geological models. Reducing location errors on relocated earthquakes will aid constraining the depth to the top of the magmatic system, providing additional evidence on where this resides.

There are limits to the work used in this study: 1D seismic velocity models are rough estimates of Montserrat and do not represent the whole island perfectly - with differences in seismic velocity expected beneath Soufrière Hills Volcano compared to the North of the island. However, they provide a good starting estimate for the velocity in this region and are still useful in producing meaningful locations. This thesis also looks at including a 3D seismic velocity model for location, although this also provides its own errors due to the way the model is created. There is also a limit to what structures can be defined using this method. It is unlikely to resolve hydrothermal systems or previous volcanic deposits; these are better imaged using relative location methods or seismic tomography. Overall, relocations provided in this thesis will improve the locations in the seismic catalogue during the five phases of eruption, which can then be used in conjunction with other research to solidify our interpretations of volcanic processes during this timeframe.

1.3 Geology

Montserrat is a 16 km by 10 km volcanic island situated in the Lesser Antilles in the Caribbean, North-West of Guadeloupe (Figure 1.2). Soufrière Hills Volcano is situated in the south of the island and began erupting in July 1995 after three years of increased seismicity (*Young et al.*, 1998). Soufrière Hills Volcano is still thought to be active, with MVO using seismic analysis as one of its primary monitoring tools.

The Lesser Antilles arc has formed due to the subduction of the North American plate under the Caribbean plate at 2 cm/year (*Wadge et al.*, 2014). North of St Lucia, the Lesser Antilles arc subdivides into two branches: an external eastern arc that was active 55–30 Ma and that is now overlain by carbonate sediments, and an inner arc where volcanism begun 22 Ma, and now consists of the current volcanic islands (*Bouysse and Westercamp*, 1990; *Paulatto et al.*, 2010a). *López et al.* (2006) proposes that the Northern Lesser Antilles forearc block is separated from the Caribbean plate by a strike-slip fault system; this change

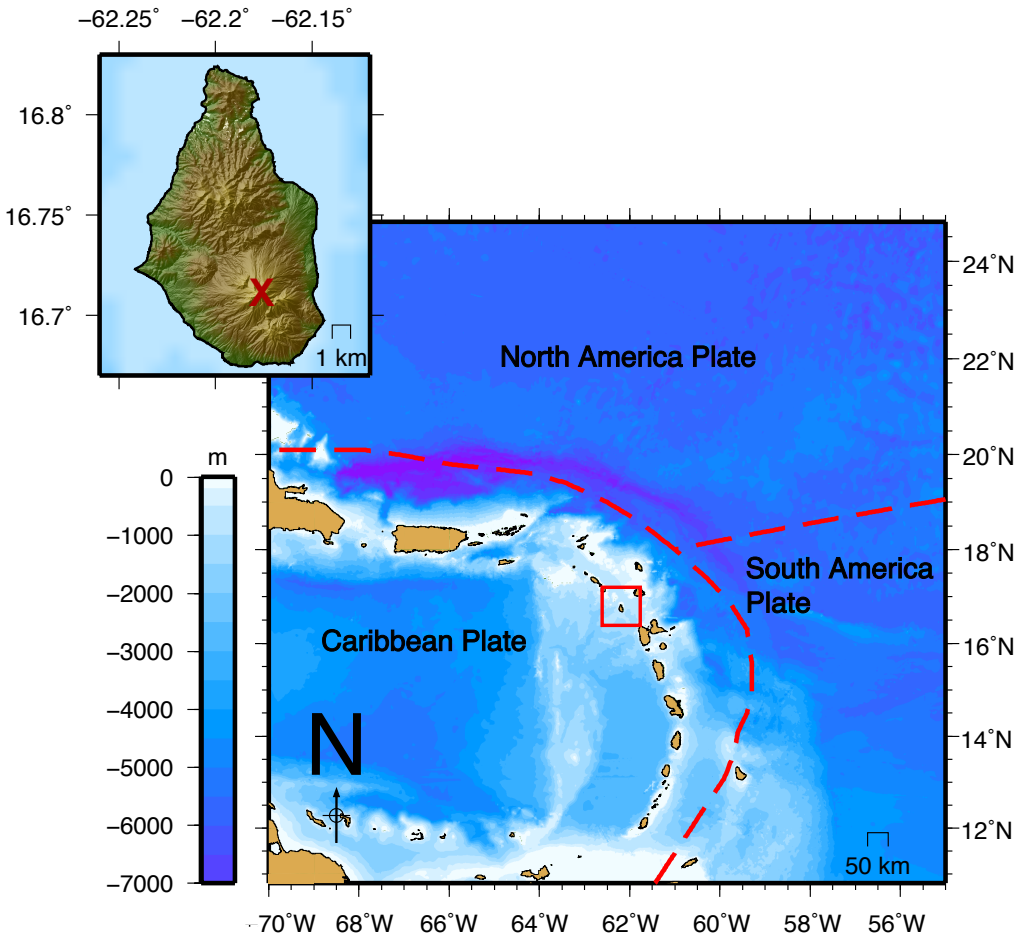

Figure 1.2: Map showing the location of Montserrat in the Lesser Antilles. Red line denotes plate boundaries between the North America, South American and Caribbean plate. Plate boundaries taken from *Bird* (2003). Inset image shows Montserrat, with red cross marking Soufrière Hills Volcano. Bathymetry data is from BODC-GEBCO 30 arc-second global grid.

in arc type is interpreted to represent the westward shift of the volcanic front which is seen today (*Macdonald et al.*, 2000).

Montserrat consists of a number of volcanic centres up to 2.6 Ma years old (*Harford et al.*, 2002) including: Silver Hills in the north of the island (2600–1200 ka), Centre Hills situated in the centre (950–550 ka), and Soufrière Hills and South Soufrière Hills situated in the south (170 ka–present), shown in Figure 1.3 (*Harford et al.*, 2002; *Sparks and Young*, 2002). Radiocarbon dating of pyroclastic deposits suggest that Soufrière Hills Volcano was active 24 and 16 Ka years ago (*Wadge and Isaacs*, 1988). Prior to the 1995 eruption, Soufrière Hills Volcano consisted of five central andesitic lava domes formed during past eruptions: Gages Mt, Chances Peak, Galway's Mt, Perches Mt and Castle Peak (*Wadge and Isaacs*, 1988). Castle Peak was buried during the recent eruption.

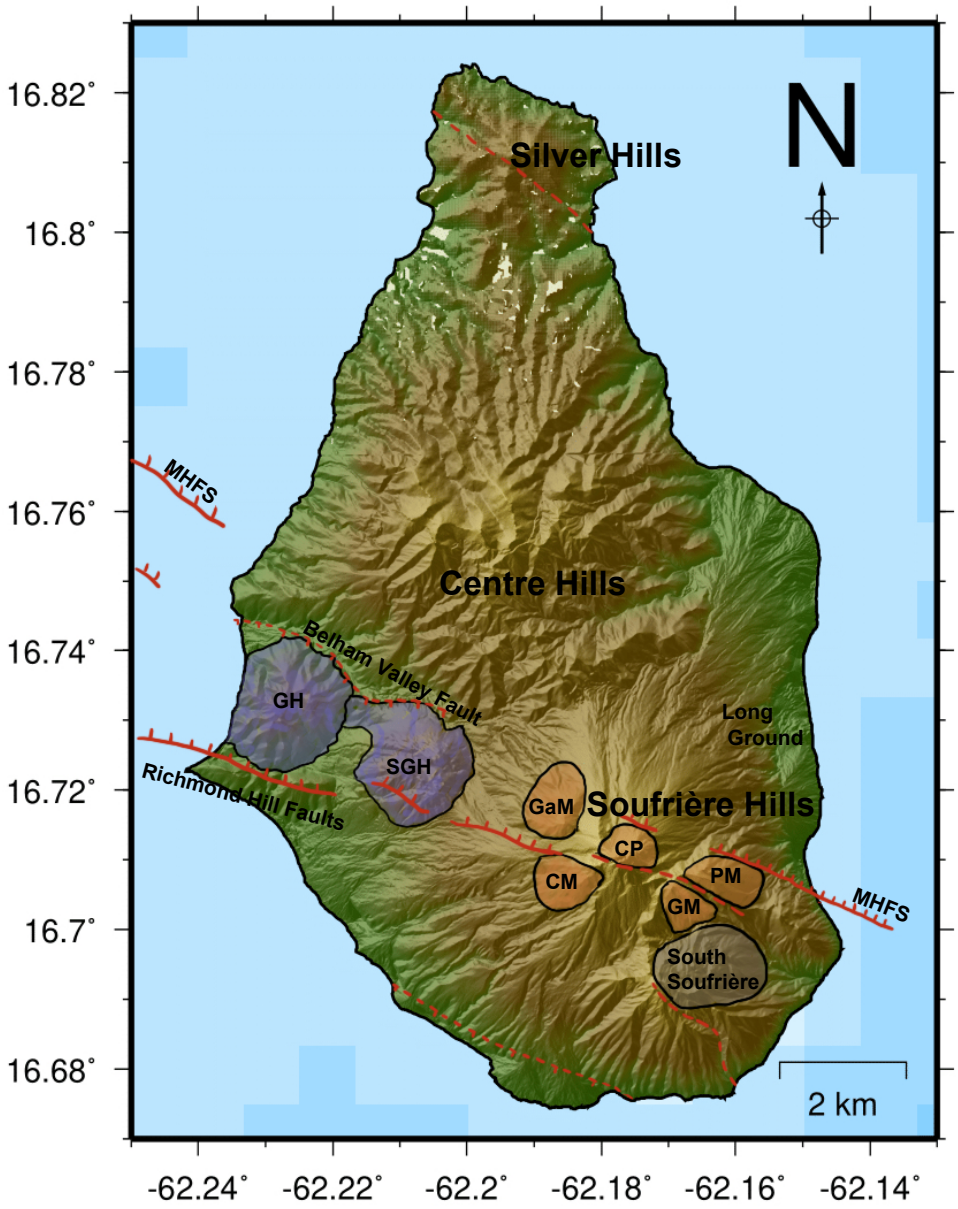

Figure 1.3: Figure showing the faults and geological complexes on Montserrat. Locations of faults and geological features are taken and adapted from *Baird et al.* (2015). Coloured regions represent volcanic complexes grouped by age; orange areas represent complexes relating to Soufrière Hills. Annotations: GH = Garibaldi Hill, SGH = St George's Hill, MHFS = Montserrat-Havers Fault System, CP = Castle Peak, GM = Galways Mt, CM = Chances Peak, PM = Perches Mt and GaM = Gages Mt. Topography used from *Stinton* (2015); this source for topography is used from here on. Darker blue regions represent increase in bathymetry.

A number of faults cross through Montserrat, making the tectonic structure complex (Figure 1.3). The Belham Valley Fault cuts across the centre of Montserrat through the Soufrière Hills complex and has an ESE trend (*Harford et al.*, 2002). The five volcanic domes align

along the ESE trending fault; this is interpreted as a zone of crustal weakness which formed during periods of past dome growth at Soufrière Hills resulting in crustal extension (*Baird et al.*, 2015; *Wadge and Isaacs*, 1988). The Bouilante-Montserrat half graben extends SE towards Guadeloupe and is thought to interact with Montserrat in the south of the island (*Feuillet et al.*, 2001, 2002). Related faults to the Belham Valley fault strike WNW and bound St George's Hill in the west and across the Soufrière Hills complex including Richmond Hill; these are thought to extend offshore to the SE forming the Montserrat Havers Fault System (*Baird et al.*, 2015; *Miller et al.*, 2010).

Soufrière Hills Volcano has one of the most active hydrothermal systems in the Lesser Antilles, with hot springs and fumaroles spread across the island (*Chiodini et al.*, 1996). Prior to the eruption in 1995, hydrothermal activity was mainly seen along the western and southern flanks of the volcano, and on the northern rim of English's crater (*Boudon et al.*, 1998). *Kenedi and Ryan* (2010) suggests that a network of faults beneath St George's Hill complex is responsible for a hydrothermal circulation system, which has previously altered the rocks in the local vicinity. St George's Hill has faults on both sides, and is an uplifted block of volcaniclastic deposits (*Harford et al.*, 2002). This area has undergone several seismic crises, first recorded in 1933 (*Aspinall et al.*, 1998); this yields further evidence to the complex nature of a fault system beneath St George's Hill. P wave tomography data also shows a low velocity zone beneath this region (*Shalev et al.*, 2010); this is looked at in more detail in Section 1.6.

Soufrière Hills Volcano is a Pelean style volcano comprised of predominantly andesitic prodcuts containing 40% phenocrysts (*Barclay et al.*, 1998), with the volcano flanks dominated by previous dome collapse material (*Sparks and Young*, 2002; *Wadge and Isaacs*, 1988). Volcanic rocks on Montserrat date back to 2.6 Ma (*Harford et al.*, 2002). Eruptions consisted of mostly dome growth with frequent dome collapses, pyroclastic density currents (PDC's), and block and ash flows (*Sparks and Young*, 2002). A large collapse 4000 years ago resulted in English Crater being formed (*Roobol and Smith*, 1998).

Prior to the 1995 eruption there had been no volcanic eruption since European habitation on the island in 1632 AD; however, there is evidence that Soufrière Hills Volcano was active in the 1500s and 1600s due to partial dome regrowth inside English Crater (*Young et al.*, 1998). Castle Peak's partially filled crater is thought to be 323 +/- 50 years old (*Young*

et al., 1996). Soufrière Hills Volcano followed a 30 year cyclic pattern in seismic activity, with an increase in earthquakes recorded in 1890's, 1930's and 1960's, none of which led to an eruption. There is no record of seismicity recorded prior to 1890. An increase in seismicity in the early 1990s led to the beginning of the eruption in July 1995 (*Young et al.*, 1998).

1.4 Current Eruptive History

Soufrière Hills Volcano began erupting on the 18^{th} July 1995 after three years of increased seismicity; it has since undergone five main phases of eruptions (*Odbert et al.*, 2014; *Shepherd et al.*, 2003). 18 earthquake swarms lasting from hours to days were recorded from 1992 to the beginning of the eruption in 1995 (*Ambeh and Lynch*, 1996). Changes in seismicity have been recorded throughout the eruption with a decrease in volcano-tectonic (VT) earthquakes as the eruption has progressed (Figure 1.4). VT seismicity at the start of the eruption was common due to the conduit forming (*Aspinall et al.*, 1998), this then changed to hybrid and Long Period earthquakes once the system had stabilised. More information on the types of volcanic signals recorded on Montserrat is explained in Section 2.1. Soufrière Hills Volcano has undergone several phases of dome growth and collapses, resulting in many Pyroclastic Density Currents (PDC's), that have destroyed the majority of south Montserrat. A timeline highlighting the key events throughout the eruption is shown in Figure 1.6. Soufrière Hills Volcano is still thought to be active, although no main dome growth has been recorded since 2010. Phases throughout the eruption have been defined by MVO as time periods with active extrusion.

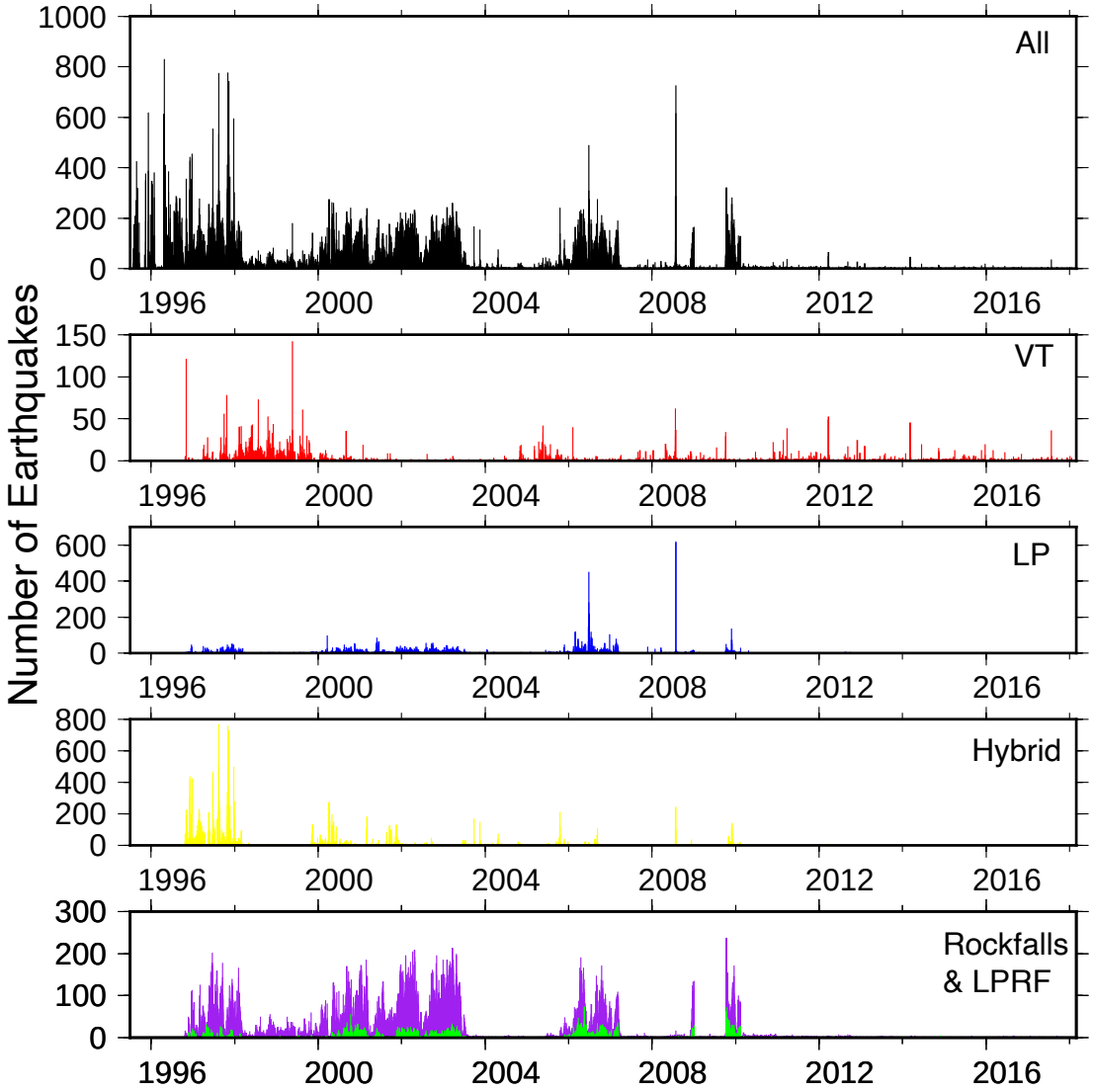

Figure 1.4: Histogram showing the number of earthquakes recorded by MVO per day recorded from 1995 to 2018. Types of seismicity are not known prior to October 1996. Red = VT, blue = LP, yellow = hybrid, green = LPRF, purple = rockfall.

Pre-1995

Earlier seismicity in 1933–1937, and 1966–1967 recorded earthquakes beneath St George's Hills, however, seismicity was not recorded there in the lead up to the eruption in 1995 (*Powell*, 1938; *Shepherd et al.*, 1971).

Figure 1.5: Figure taken from (*Powell*, 1938). Figure shows epicentre estimates for earthquakes located between 28^{th} April 1936 to 26^{th} May 1937; location estimates were calculated using the amplitudes of recorded earthquakes on the island.

Phase 1

The phreatic phase began on the 18^{th} July 1995, which transitioned to the magmatic phase later on the 15^{th} September (*Wadge et al.*, 2014). Phreatic explosions with 3 km ash columns were common during the first few months of Phase 1, with high SO_2 levels of 300 tonnes/day (*Young et al.*, 1998). Phase 1 was subject to several cycles of continuous dome growth and collapse, resulting in several large scale PDC's. A large dome collapse on the 25^{th} June 1997 resulted in a PDC travelling 6 km to the north-east, reaching Bramble Airport and killing 19 people (*Loughlin et al.*, 2002). A large PDC in August 1997 destroyed Montserrat's capital Plymouth, which had previously been evacuated (*Wadge et al.*, 2014).

Seismicity during the first few months of the eruption was located across most of southern Montserrat, and was recorded beneath St George's Hill, Windy Hill and to the NE near Long Ground (*Aspinall et al.*, 1998; *Miller et al.*, 2010). From summer 1996 the majority of seismicity was then recorded beneath the main crater. There are several hypotheses for the reason seismicity was recorded beneath St George's Hill, such as a response to stress change from a magmatic intrusion, or from the triggering of local fault and hydrothermal systems (*Miller et al.*, 2010). Seismicity was also recorded to the NE near Long Ground and was interpreted as stress changes as a result of a secondary intrusion that ascended as a NE/NNE dyke (*Miller et al.*, 2010; *Roman et al.*, 2008). *Aspinall et al.* (1998) showed a migration of seismicity to the SW over a two-day period, but this was discounted by *Roman et al.* (2008) due to large hypocenter errors.

Overall seismicity was located widely across south Montserrat during the first year of the eruption, highlighting the complex environment, and the effect that a magmatic intrusion can have on seismicity in the region. Lava extrusion ceased on the 10^{th} March 1998 marking the start of an 18 month pause in activity (*Wadge et al.*, 2014). Higher levels of activity were noticed every 5–6 weeks, with a partial dome collapse on the 3^{rd} July 1998; increased seismicity, ash and explosions reached a climax in November 1999 marking the start of Phase 2 (*Norton et al.*, 2002; *Wadge et al.*, 2014).

Phase 2

Phase 2 was the longest period of continuous lava extrusion lasting 3.5 years with two short breaks in extrusion: March–May 2001, and June–July 2002 (*Wadge et al.*, 2014). There were three main dome collapses: 20^{th} March 2000 resulting in a PDC down the Tar River Valley and a 9 km ash column (*Carn et al.*, 2004); 29^{th} July 2001 where rainfall is thought to have triggered a large volume dome collapse (*Matthews et al.*, 2002); and a major collapse on the 12^{th} July 2003 (*Herd et al.*, 2005). There was very little seismicity recorded with the first two dome collapses; these were both preceded by heavy rainfall, which was thought to have destabilised the dome (*Carn et al.*, 2004; *Matthews et al.*, 2002).

The 12^{th} July 2003 dome collapse lasted for over 18 hours, ending with a Vulcanian explosion, marking the onset of Pause 2 (*Edmonds et al.*, 2006). PDC's to the east of the island formed lobes and turbidite deposits off the coast (*Herd et al.*, 2005; *Trofimovs et al.*, 2006). A swarm of 9500 hybrid earthquakes that merged intro tremor were recorded in the lead up to the dome collapse (Figure 1.4); this was interpreted as an indicator of magma pressurisation in the upper conduit (*Wadge et al.*, 2014). Activity during Pause 2 was limited to ash venting, SO_2 pulses and hybrid earthquake swarms (*Wadge et al.*, 2014).

Phase 3

Three and a half months of phreatic explosions began on the 15^{th} April 2005, with dome growth restarting a few months later on the 8^{th} August 2005; the increase in activity in April marked the start of Phase 3. A series of Volcano-Tectonic and Long Period earthquakes on the 7^{th} and 9^{th} February 2006 marked an opening of a NNE trending fissure (*Wadge et al.*, 2014). On the 20^{th} May 2006, a three hour dome collapse removed all prior dome growth from Phase 3; the collapse was gas rich resulting in a high energy PDC down Tar River Valley, and a small tsunami (*Trofimovs et al.*, 2012; *Wadge et al.*, 2014). Dome growth continued throughout 2006 with a small dome collapse on the 8^{th} January 2007 triggering a PDC down Belham Valley (*De Angelis et al.*, 2007; *Wadge et al.*, 2014). Dome growth slowed, with Phase 3 finishing on the 20^{th} April 2007. Activity during Pause 3 was limited to mostly gas flux from Gages wall and long period seismicity.

Phase 4

Phase 4 consisted of mainly short duration periods of activity with a high degree of cyclicity and explosivity; this marked a different pattern to observations seen in earlier phases. An increase in volcano-tectonic earthquakes on the 21^{st} to 26^{th} July preceded the start of Phase 4; this was followed by a two-day swarm of hybrid and long period earthquakes (*Wadge et al.*, 2014). On the 29^{th} July, a vulcanian explosion resulted in an ash column and several pumice flows to the East and West of the island (*Chardot et al.*, 2010; *Komorowski et al.*, 2010). Over 1800 earthquakes were recorded in the 10-day period leading up to the vulcanian explosion, with a continuous change from high frequency to low frequency earthquakes. Both volcano-tectonic and long period seismicity was relatively shallow, and was inferred to be the ascent of decoupled magmatic fluid and gas which triggered earthquakes in this shallow region (*Rodgers et al.*, 2016). Original MVO locations show a pattern of seismicity to the SE, but these events have large associated errors, and therefore are not included for intepretations.

Phase 4 was divided into two short episodes of explosions and extrusion (named 4a and 4b). Lava extrusion halted in September 2008 marking the end of Phase 4a. Little surface activity was observed until the beginning of December, where an increase in seismicity and dome growth was recorded (*Komorowski et al.*, 2010). Several PDCs occurred throughout December 2008, with a PDC on Christmas Eve reaching the sea at Plymouth (*Wadge et al.*, 2014). Two large explosions on the 3^{rd} January 2009 resulted in a 11 km ash cloud marking the end of Phase 4b.

Phase 5

A swarm of 24 volcano-tectonic earthquakes were recorded prior to ash venting on the 5^{th} October 2009, marking the start of Phase 5 (*Wadge et al.*, 2014). Lava extrusion began on the 9^{th} October 2009, with dome growth mostly focussed to the SW. Dome growth switched to the NE later in November after an increase in hybrid and volcano-tectonic earthquakes, and shifted again to the NW in December (*Wadge et al.*, 2014). Three vulcanian explosions occurred on the 8^{th}, 10^{th} and 11^{th} January 2010, all of which resulted in fountain collapse PDCs through several valleys. On the 11^{th} February, a large dome collapse resulted in

several PDC's, extending the shoreline by 650 m, and leaving a horseshoe-shaped scar open to the north at the crater (*Wadge et al.*, 2014). Two terminal vulcanian explosions resulted in tephra plumes reaching a height of 15 km (*Wadge et al.*, 2014).

Although little surface activity has been recorded since the 11^{th} February 2010, marking the end of Phase 5, Soufrière Hills Volcano still shows signs of an ongoing eruption with changes in seismicity, deformation and gas flux being recorded daily. However, no dome growth has been recorded since the end of Phase 5. VT strings were recorded during and after Phase 4, but were dominant in Phase 5; these are a series of VT earthquakes which occur over a short period of time (*Smith*, 2013). VT strings on the 22^{nd} and 23^{rd} March 2012 were followed by a strong gas and strain signal, which correlated with ash venting at the surface (*Smith*, 2013). A Very Long Period signal was recorded on Montserrat on the 23^{rd} March 2012 which coincided with outgassing at Soufrière Hills Volcano (*Šindija et al.*, 2021). A gradual deepening of seismicity has been recorded since 2012 which was first highlighted in a MVO report in 2018; an increase in hypocenter depth correlated with the installation of the Spider stations (portable vertical component seismometers) (*MVO*, 2018).

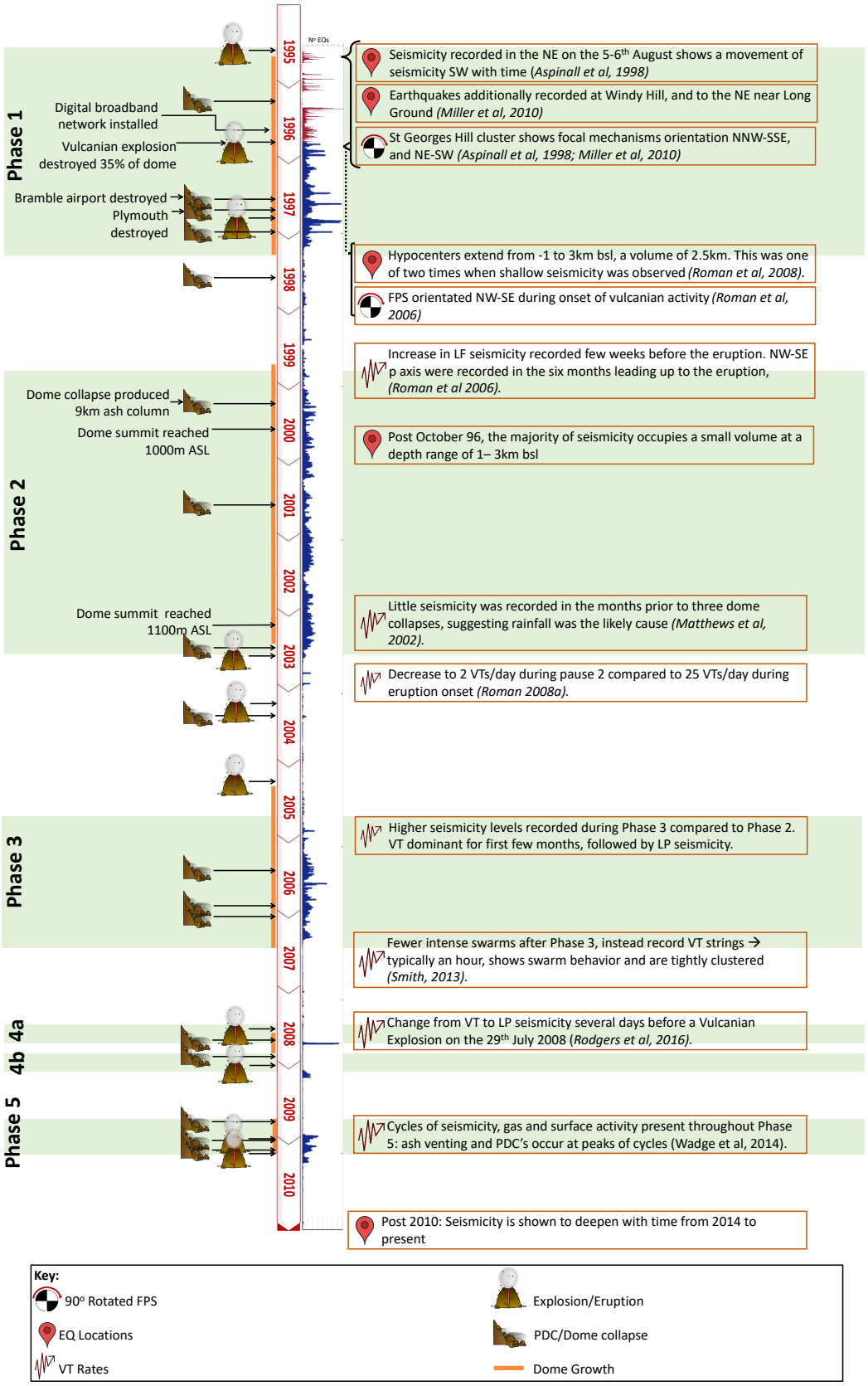

Figure 1.6: Schematic showing key events throughout the first five phases of the eruption. Red histogram shows the number of earthquakes before October 1996 using events by *Aspinall et al.* (1998); blue histogram shows MVO counts from October 1996 to February 2018. Green regions represent times during the active phases. Max number of daily events in the histograms is 800 earthquakes.

1.4.1 Seismicity at Volcanic Settings

Eruptions are generally preceded by an increase in seismic activity, driven by the fracturing of crust as magma migrates to the surface (*Matthews*, 2009). Signals throughout the eruption vary in frequency and amplitude depending on the source and location that they originate from. Differences in frequency signals can be explained by source parameters and different volcanic processes. For example high frequency earthquakes are representative of fracturing of the local country rock as magma rises to the surface (*McNutt*, 1996), whereas lower frequency events are thought to be related to degassing and pressurisation of the magmatic system (*Neuberg*, 2000). Different seismic signals are explained in more detail in Section 2.1

Earthquakes recorded in volcanic settings are usually related to magma movement, and can provide details on the magmatic chamber, dyke location and magmatic processes. Differences observed in the temporal pattern of seismic events can be explained by variation in parameters such as flow rate, volatile content and groundwater composition (*McNutt*, 1996). An increase in earthquakes were recorded in the 8 months prior to the Augustine Volcanic eruption in January 2006; this intensified in the days leading up to the eruption with an increase in low frequency earthquakes suggestive of magma ascent (*McNutt and Roman*, 2015).

Volcanic earthquakes generally occur at shallow depths of 1-9 km bsl, events generally occur in swarms with similar locations and magnitudes (*McNutt and Roman*, 2015). There is a general background level of seismicity which varies at different volcanoes across the world; an increase in seismicity above the background level can suggest reactivation of the volcanic systems, such as a fresh influx of magma, or magma movement which usually precedes a volcanic eruption.

Earthquakes are mainly located beneath the final eruption site, but can also be recorded at 'distal clusters' away from the final eruption. These distal clusters are thought to occur on previous faults in the region that are triggered by an increase in pressure beneath the volcano, resulting in earthquakes along previous faults that may be distal to the final eruption site (*Baird et al.*, 2015). Seismicity in the lead up to the 2004 eruption at Mount St Helens were located in a small cluster at 1 km depth; the eruption then occurred directly

above this location. Whereas, initial seismic activity at Mount Pinatubo in 1991 was located 5 km NW of the final eruption site, in what is thought to be a distal cluster (*McNutt and Roman*, 2015).

Earthquakes have also seen to migrate with time which can be interpreted as a propagating dyke. The 2014–2015 Brdharbunga–Holuhraun event recorded over 30,000 earthquakes that migrated a total of 50 km over a 13 day period, ending at the location of the new eruption. The direction of the dyke followed regions of pre-existing weaknesses, and the seismicity allowed the tracking of magma giving an idea of the final eruptive location (*Woods et al.*, 2019). Similarly, seismicity in the Red Sea prior to a new volcanic island being formed showed a migration of earthquakes along a NW orientated dyke prior to the final eruption (*Eyles et al.*, 2018)

1.4.2 Seismicity Cycles

Cyclicity of geophysical measurements at silicic volcanoes is thought to be related to the periodic slowing of the magma flow due to an increased viscosity resulting from shallow degassing (*Sparks*, 1997; *Voight et al.*, 1998, 1999). Viscosity increases as volatiles escape from rising magma due to microlite crystallisation; this can result in a magma plug forming, stopping the flow of more volatile rich magma at deeper levels, and hence a decrease in recorded SO_2 (*Lensky et al.*, 2008). This leads to an increase in pressure of magma beneath the magma plug which is recorded at the surface as hybrid seismicity and inflation around the dome. The pressure increases to a critical threshold where it then overcomes the resistance of the plug, pushing it out of the dome. This leads to deflation at the surface and an increase in SO_2 as the fresh magma is able to degas, marking the start of a new cycle (*Voight et al.*, 1998; *Watson et al.*, 2000).

Cyclic patterns in SO_2, seismicity and tilt measurements are commonly recorded at Soufrière Hills Volcano, and are thought to be correlated to each other. Repetitive inflation and deflation cycles of 6–8 hours were recorded in December 1996 to January 1997, and cycles of 12–18 hours were recorded in May 1997 to August 1997 (*Voight et al.*, 1998). *Watson et al.* (2000) found a strong correlation of 0.73–0.9 between ground deformation and SO_2 which was consistent with a rise in magma and flow rate. This was broadly correlated to an increase in hybrid seismicity, thought to be triggered by an increase in pressure as a

result of the rise of magma (*Voight et al.*, 1998, 1999; *Watson et al.*, 2000). An increase in hybrid seismicity is recorded with an increase in inflation; later in the cycle this turns into a tremor signal, which is shortly followed by explosions (*Voight et al.*, 1998, 1999).

Cycles of seismicity, tilt and SO_2 have also been recorded at other active volcanoes including Mount Pinatubo in 1991, and Sakurajima volcano in 2008–2010. Low frequency seismicity turned into long period events at Mount Pinatubo that lasted 7 to 10 hours; seismicity was often accompanied with intermittent explosive activity, similar to Soufrière Hills Volcano (*Newhall and Punongbayan*, 1996). Inflation at Sakurajima volcano often culminated with a slight decrease in gas emissions before explosions several hours later; this was interpreted as an increase in gas and magma accumulation beneath a sealed surface such as a magma plug (*Yokoo et al.*, 2013). Work by *Michaut et al.* (2013) shows that magma ascent can yield gas expansion; this along with magma compaction can result in pressurised gas waves. This would be recorded at the surface as cyclic low frequency seismicity with cycles repeating every 1 to 100 hours (*Michaut et al.*, 2013).

The cyclic behaviour was used for actively monitoring the volcano; once inflation began to flatten, an increased likelihood of rockfalls and PDC's would occur within the following few hours. As a result, volcanologists were sent out at the beginning of the inflationary cycles to take any measurements needed, when the risk of rockfalls were lower (*Voight et al.*, 1998).

1.5 Monitoring

Several seismic networks were deployed at the beginning of the eruption in 1995 by the University of West Indies Seismic Research Centre (SRC), the USGS Volcano Disaster Program and the British Geological Survey (*Aspinall et al.*, 1998; *Neuberg et al.*, 1998). Following the first phreatic explosions in July 1995, the SRC were the first to establish a base in Montserrat to monitor the eruption; this was then followed by the USGS which visited Montserrat for 6 weeks establishing a new seismic network and data acquisition system (*Aspinall et al.*, 2002). By 1996 several institutions were employed to monitor the volcano on a daily basis, forming the Montserrat Volcano Observatory (MVO). MVO has been moved several times from its original location in Plymouth from 1996–1997, to its purpose-built observatory in Flemmings in January 2003.

Routine monitoring of Soufrière Hills Volcano falls into four main techniques: visual observations, seismic monitoring, ground deformation and gas monitoring. Videos and photos are regularly taken from helicopters and permanent cameras to help assess changes in dome volume and morphology of the surrounding region. In addition, research looking at environmental monitoring of groundwater, deposit mapping, gravity surveys, and geochemical and petrological analysis has been completed to understand more about volcanic processes occurring at Soufrière Hills (*Aspinall et al.*, 2002; *Barclay et al.*, 1998; *Hautmann et al.*, 2013; *Murphy et al.*, 2000).

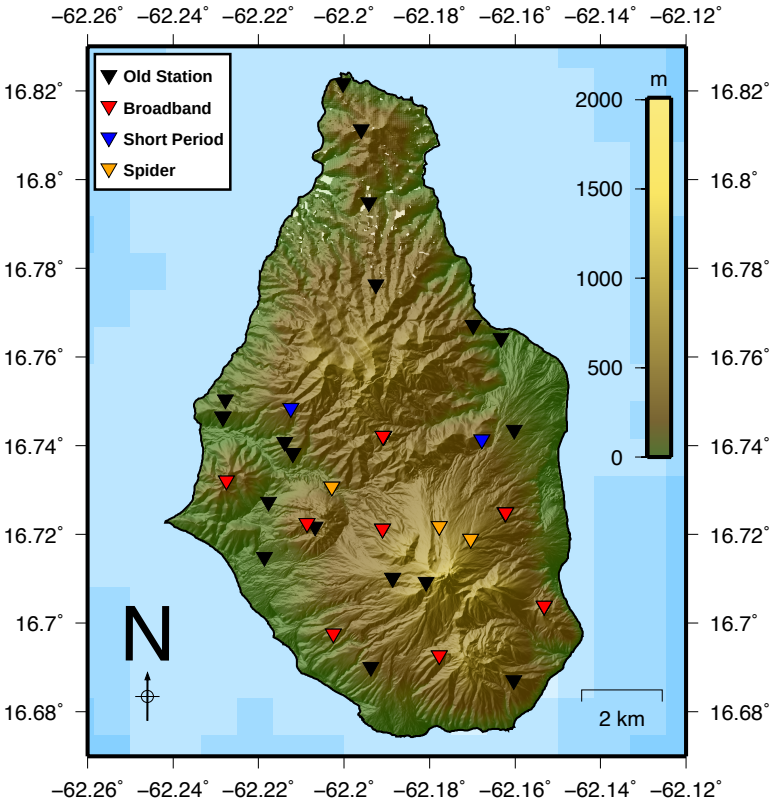

Figure 1.7: Locations of seismometers active from 1995-2020 (black) and seismometers active in January 2021 (coloured) shown by an inverted triangle; current seismic stations are coloured by type.

The seismic network on Montserrat has changed several times since the beginning of the eruption. There have been over 30 seismic stations deployed by MVO since 1995 with a maximum of 12 stations being active at any one time (Figure 1.7. Three main types of seismic stations are used on Montserrat: Short Period seismometers (vertical component), Broadband three component seismometers and Spider Stations. Spider stations are portable

vertical component seismic stations that can be easily deployed and orientate themselves in the field. These were provided by USGS, and were particularly useful for deploying in remote regions, due to their ability to self-orientate. Seismic data is monitored daily by MVO staff and is used as the main monitoring technique.

Ground deformation monitoring began in 1995 with three tilt stations installed on the western flank of Soufriere Hills Volcano; this was to monitor Gages crater wall and Castle Peak dome. In 1999, additional sites were added to the network to monitor the eastern flanks (*Aspinall et al.*, 2002). A differential GPS system was installed across Montserrat in April 1996 to be used in conjunction with the tiltmeters.

Gas monitoring on Montserrat was taken via remote sensing using a COSPEC correlation spectrometer and Infra-Red Spectroscopy during the early stages of the eruption (*Oppenheimer et al.*, 1998; *Young et al.*, 1998). Gas monitoring is now from two permanent Differential Optical Absorption Spectroscopy (DOAS) stations based downwind of the plume (*Edmonds et al.*, 2003). Direct sampling from the dome was rarely taken, but direct samples from hydrothermal vents were taken during the beginning of the eruption before conditions became too dangerous (*Hammouya et al.*, 1998). Samples were used to monitor SO_2 and CO_2 release; this gives an insight into deeper processes occurring in the magmatic system (*Aspinall et al.*, 2002).

1.5.1 Seismic Data Acquisition

Each seismometer on Montserrat is connected to a digitiser and GPS (for time stamp); this is transmitted over freewave radio back to the observatory. MVO use the Guralp software *SCREAM!* which allows communication with the digitisers, before being passed to *Earthworm* for analysis. *Earthworm* has several built in programs that are able to collect, process and analyse the data (*Johnson et al.*, 1995). It is formed through multiple modules which can communicate with each other, allowing each module to be independent but still able to interact with each other (*Luckett et al.*, 2007). Earthworm has the ability to do routine processing and calculations including RSAM which calculates the mean amplitude of the signal, normally over a 60 second window. This is used as MVO's alert system: when an amplitude threshold is recorded at three or more stations, an alert is sent to MVO staff so that they can analyse the signal. A back-up alert on *SCREAM!* is also present incase

Earthworm was to fail.

MVO locates earthquakes using the location program *Hypocenter* (*Lienert et al.*, 1986); this is built into the program *Seisan* which allows the user to pick arrival times, locate earthquakes and do further analysis. Events are handpicked by an analyst for arrival time phases and are classified by type before being located; locations are kept inside the S-files inside of *Seisan*. MVO currently uses a basic 1D seismic velocity model based on Guadeloupe and adapted for Montserrat; the velocity model is comprised of five layers and does not account for topography. More information on the velocity model and *Hypocenter* program can be found in Section 4.1.2 and 3.2.1 respectively.

1.6 Plumbing System

Island arc volcanoes are complex systems that can display irregular distributions of seismic velocities, making it difficult to accurately represent this in velocity models (*Paulatto et al.*, 2010b). If the seismic velocity model used for earthquake location does not represent the main changes in seismic velocity, then this can affect the located hypocenters. Previous research on Montserrat has produced conflicting results of the depth and size of the magma chamber. This section compares different techniques and interpretations used to constrain the magmatic system beneath Soufrière Hills Volcano.

1.6.1 Geological Models

Petrological observations are often used alongside geophysical techniques to constrain the location and dimensions of magma reservoirs. Petrological experiments performed by *Barclay et al.* (1998) concluded that magma stored at Soufrière Hills Volcano was stored at a P_{H20} (the partial pressure of water in stored melt) of 115–130 MPa. This corresponds to a water-saturated magma chamber at a depth of 5–6 km bsl (*Barclay et al.*, 1998). This is consistent with depths calculated via geochemical analysis of hornblende phenocrysts, which suggested a depth of 5 km to the top of the reservoir (*Rutherford and Devine*, 2003).

Geological evidence also suggests a secondary deeper source of magma. Small amounts of basalt are found mixed into the andesite, implying that the upper reservoir may tap into

a deeper source of mafic magma (*Annen et al.*, 2006; *Murphy et al.*, 2000). In agreement with this, *Devine et al.* (2003) has shown that crystal phases from erupted lavas suggest a deeper reservoir at depths greater than 10 km. Chemical concentrations and the longevity of the eruption suggests that the upper reservoir is voluminous with a calculated volume of 4 km^3 (*Voight et al.*, 2006); this has been suggested to be an extensive zone of magmatic mush beneath Soufrière Hills (*Christopher et al.*, 2015).

1.6.2 Seismic Models

The SEA-CALIPSO (Seismic Experiment with Airgun-source — Caribbean Andesitic Lava Island Precision Seismo-geodetic Observatory) project in December 2007 used a combination of land and ocean based seismometers, with a sea-based airgun source to image variations in seismic velocity around Montserrat (*Voight et al.*, 2014). The project aim was to image the upper crust at Montserrat with the hope to further constrain the magmatic system beneath Soufrière Hills (*Paulatto et al.*, 2010a). However, due to seismic velocities being higher than expected and the short distance between source and receivers, the project was limited by the maximum depth of ray penetration resulting in unreliable data at depths greater than 5 km (*Shalev et al.*, 2010).

A 3D seismic velocity model of Montserrat was produced from seismic tomography of P wave first arrivals produced from the SEA-CALIPSO project, further described in *Shalev et al.* (2010). The seismic model highlights high velocity anomalies beneath all three volcanic centres at 2–3 km depth, and low velocity anomalies on the volcanic centres' flanks — particularly around Centre Hills (*Shalev et al.*, 2010). High velocity anomalies are thought to correspond to solid andesitic cores that are made up of multiple sill and dyke intrusions (*Paulatto et al.*, 2010a). This is consistent with crystalline cores found by *Harford and Sparks* (2001), suggesting that intrusions beneath the volcanic centre solidify at 3 km depth (*Shalev et al.*, 2010). Interpretations for low velocity anomalies are more disputed, and are thought to be due to several reasons: syn-volcanic apron deposits from previous eruptions (*Shalev et al.*, 2010), and hydrothermal alteration (*Carlson*, 2001).

A subset of the SEA-CALIPSO data (four land and four ocean seismometers) was used to create a 2D seismic velocity cross section orientated NW/SE across Montserrat. The 2D velocity model extends to a depth of 10 km, and suggests a two layered model with

a velocity change at 2–2.8 km bsl (*Paulatto et al.*, 2010a). The upper layer has seismic velocities ranging from 1.5–5.5 km/s, whilst the lower layer increases from 4 km/s to a maximum of 6.5 km/s at the base of the model (*Paulatto et al.*, 2010a).

The upper layer is thought to consist of a sedimentary cover composed of a calcareous and volcaniclastic composition (*Paulatto et al.*, 2010a), and an island structure divided into a volcanic core and a lower velocity volcanic apron, similar to results found in *Shalev et al.* (2010). The lower layer is interpreted as the upper part of the crust, composed of an intrusive network of sills and dyke of intermediate composition. Petrological studies show the upper crust to be dominated by granitoid intrusions produced from silicic magma, supporting *Paulatto et al.* (2010a)'s interpretation. The interface between the upper and lower layer is interpreted as a paleoseabed, formed prior to volcanic activity of the inner Lesser Antilles arc 22 Ma years ago (*Bouysse and Westercamp*, 1990).

Paulatto et al. (2012) combined seismic tomography from SEA-CALIPSO with numerical models of magma chamber growth to further constrain the size and depth of the magmatic chamber beneath Soufrière Hills Volcano. The seismic velocity model produced was generated using a regularised inversion of first arrival times (*Hobro et al.*, 2003). The model shows the three volcanic centres share a similar shallow structure up to 4 km bsl, before beginning to differ (*Paulatto et al.*, 2012). A low velcocity zone beneath Soufrière Hills Volcano has a maximum seismic velocity reduction of 0.7 km/s compared to Centre Hills (*Paulatto et al.*, 2012), and is estimated to be 6–8 km wide and 4 km high, resulting in a volume over 100 km^3 . However, this is likely an overestimate due to the model not taking into account the presence of melt in the magma which reduces seismic velocity. Petrological observations indicate that the magma contained 35% melt prior to eruption (*Murphy et al.*, 2000). Including this in the model suggests a magma chamber of 13 km^3 at a depth of 5.5–7.5 km bsl (*Paulatto et al.*, 2012). This is supported by early seismicity in the region during Phase 1, which showed the magma chamber must be at depths greater than 5 km (*Aspinall et al.*, 1998). This is shown by the reduction in earthquakes recorded at depths greater than 5 km; this lack of seismicity suggests that the region is too warm for brittle failure proposing the start of a magma chamber.

1.6.3 Geodetic Models

Tilt measurements from the flanks of volcanoes can provide information on shallow processes that contribute to dome growth and collapse (*Voight et al.*, 1998, 1999). Three tiltmeters deployed on Chances Peak from December 1996 to August 1997 were analysed to provide constrains on the size, depth and pressure of the shallow magmatic system beneath Soufrière Hills Volcano (*Widiwijayanti et al.*, 2005). A calculated pressure of 1–4 Mpa suggests a source depth of 740–840 m with radius 200–340 m (*Widiwijayanti et al.*, 2005). These dimensions are considerably larger for conduit size than estimates calculated from magma flux (*Voight et al.*, 1999). This suggests that the conduit size is likely to be much smaller, with overpressures measured accounted for by a fluid saturated, heavily fractured rock mass surrounding the conduit (*Christopher et al.*, 2015; *Widiwijayanti et al.*, 2005).

The CALIPSO project involved four 200 m boreholes consisting of a dilatometer, seismometer, tiltmeter and surface GPS (*Mattioli et al.*, 2004). Volume changes were used to estimate the dimensions of the magmatic system using data from the dilatometers for the 12^{th} July 2003 dome collapse. The results modelled an oblate spheroid at 6 km depth, radius 1 km and an overpressure of 1 MPa (*Voight et al.*, 2006), providing similar results to seismic and geological studies (*Aspinall et al.*, 1998; *Barclay et al.*, 1998).

Geodetic and efflux records can provide information into deeper processes contributing to volcanic behaviour (*Elsworth et al.*, 2008). Geodetic and efflux data (used data from extrusion record on Soufrière Hills) from three eruptive periods over a 12 year duration at Soufrière Hills Volcano show that surface efflux levels respond to a pressure and volume change at a large depth, rather than deflation of the shallow reservoir (*Elsworth et al.*, 2008). Therefore, *Elsworth et al.* (2008) suggests that there are two reservoirs at 6 and 12 km bsl. Data indicates that during eruptive periods magma is depleted from the deeper reservoir, with the shallower reservoir inflating slightly due to inflow exceeding outflow. During pauses in eruption, the deeper reservoir re-inflates from a source deeper than 12 km, but at half the rate that it was depleted during an eruption; this results in the deeper reservoir having been slowly depleted since the start of the eruption in 1995 (*Elsworth et al.*, 2008).

A gravity survey over Montserrat aimed to understand the islands subsurface density distribution. The survey showed high density material beneath Silver Hills and Centre Hills to a

depth of 500 m, and low density anomalies beneath Soufrière Hills Volcano, and the flanks of Silver and Centre Hills, which were angled at 30–45° to a depth of 1 km (*Hautmann et al.*, 2013). This correlates with the results from seismic studies during the SEA-CALIPSO project (*Paulatto et al.*, 2010a; *Shalev et al.*, 2010). High density anomalies are interpreted as subsurface volcanic domes, and low density anomalies are interpreted as either hydrothermally altered rocks or melt accumulation (*Hautmann et al.*, 2013). A low velocity and low resistivity zone at 1–4 km depth was also confirmed by a magnetotellurics study (*Shalev et al.*, 2010).

1.6.4 Summary

Accumulating information from geophysical and geological studies suggests that the magmatic system beneath Soufrière Hills Volcano is comprised of four main elements (Figure 1.8):

- The strato-volcano, combining the solid andesitic cores from multiple dyke intrusions, and volcanic deposits from previous eruptions such as debris from PDC's, lahars and avalanches (*Carlson*, 2001; *Harford and Sparks*, 2001; *Paulatto et al.*, 2010a; *Shalev et al.*, 2010). Low density and low seismic velocity anomalies are recorded on the flanks of Silver and Centre Hills, and beneath Soufrière Hills; this is interpreted to be a result of hydrothermal alteration and/or melt accumulation (*Hautmann et al.*, 2013). Evidence from tiltmeters suggests the area surrounding the conduit is heavily fractured and fluid saturated (*Widiwijayanti et al.*, 2005).

- A large zone of magma mush is thought to be beneath Soufrière Hills complex (*Christopher et al.*, 2015). This is broken into two regions where different signals are recorded: an upper and lower zone which magma transfers between. *Barclay et al.* (1998) showed that water saturated magma is stored at depths of 5-6 km bsl, with *Murphy et al.* (2000) supporting that the region beneath 5 km is where andesitic magma resides prior to eruptions. Seismic tomography and the depth of VT earthquakes suggests the upper extent of the magma mush region extends from 5 km depth (*Aspinall et al.*, 1998; *Paulatto et al.*, 2012).

- A deeper subregion of melt at 12 km depth where andesitic magma is generated from

fractionation of basalt (*Elsworth et al.*, 2008). Evidence from crystal phases and inclusions of basalt in erupted andesite confirm the presence of a region of increased melt deeper than 10 km (*Annen et al.*, 2006; *Devine et al.*, 2003; *Murphy et al.*, 2000). This region is thought to feed eruptions, and inflates the shallower mush zone located at 5 km during periods of unrest (*Elsworth et al.*, 2008).

- A primary source of mafic magma deeper than 12 km, which refills the deeper reservoir, and is thought to originate from the mantle wedge (*Elsworth et al.*, 2008; *Zellmer et al.*, 2003).

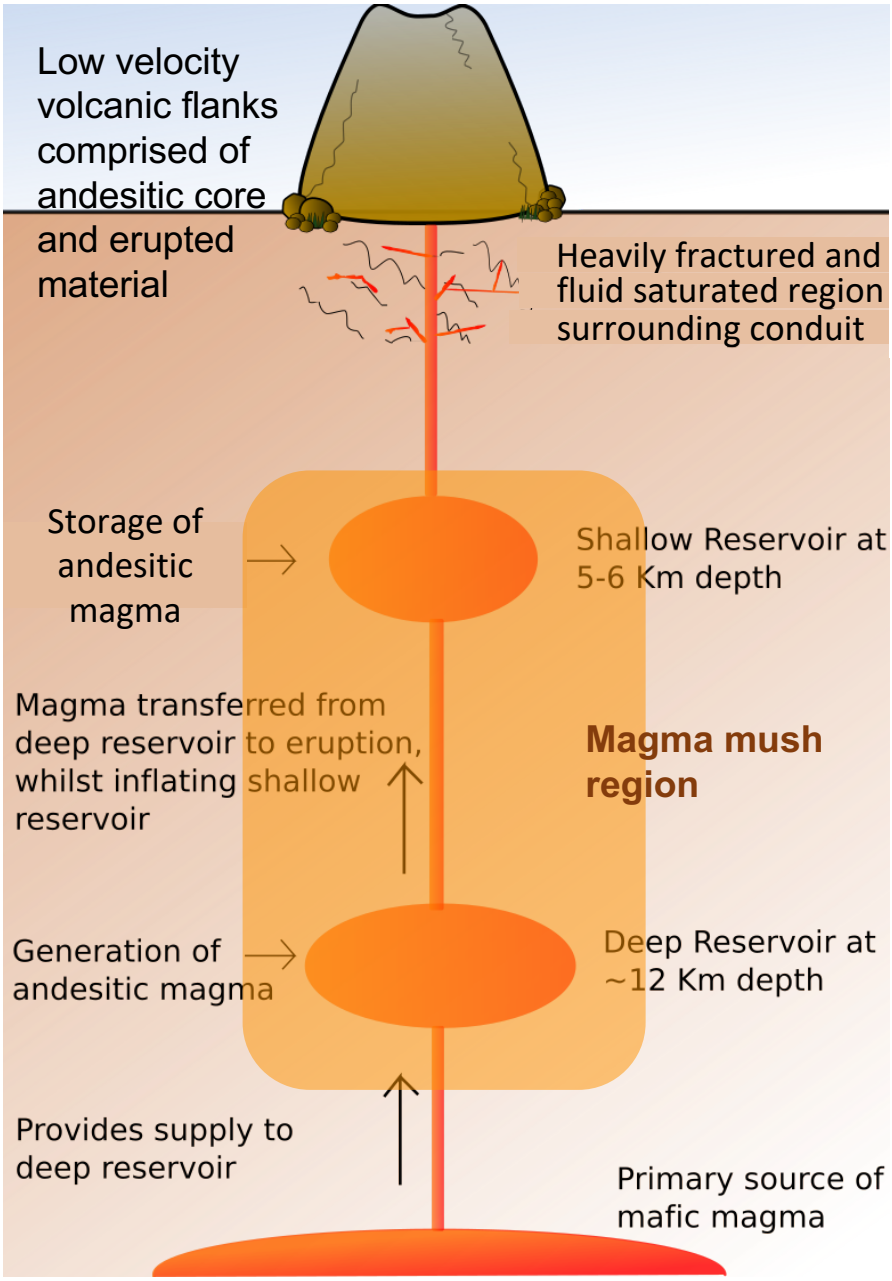

Figure 1.8: Summarised schematic of the four main elements of the magmatic system beneath Soufrière Hills Volcano.

Chapter 2

Seismicity

Volcanic seismicity is a useful indicator for current and future activity at active volcanoes, and can be used to map the extent and evolution of magmatic regions (*Chouet*, 1996; *Luckett et al.*, 2007). Different types of seismic signals can give an insight into the internal dynamics of the volcano (*Luckett*, 2005). Changes in seismicity have been recorded prior to and during increased volcanic activity at volcanoes worldwide including Soufrière Hills Volcano; as a result seismic monitoring is one of the primary short term methods currently used by MVO in monitoring Soufrière Hills Volcano (*Luckett et al.*, 2007).

There are over 1500 volcanoes worldwide, but only the minority of these are actively monitored by an observatory. Volcanoes close to large population in well developed countries tend to be more closely monitored than those in developing countries. For example, the Hawaii Volcanic Observatory seismic network covers the majority of the island of Hawai'i and is able to accurately record earthquakes greater than magnitude 1 (*Okubo et al.*, 2014). Volcanic activity is forecasted by analysing rates, types and location of earthquakes, including how seismic signals may differ in frequency throughout time. Swarms and tremors are common precursors to volcanic activity, whereas the difference between volcano-tectonic and long period seismicity can give an indication of the internal state of the volcano (*Thompson et al.*, 2015).

The start of the eruption in July 1995 resulted in several seismic networks being deployed, and the establishment of the Montserrat Volcano Observatory (MVO) (*Aspinall et al.*, 1998). MVO had 12 seismic stations in use across the island in January 2020; however, due to timing issues and frequent power outages, it is not common to have all 12 stations receiving data.

The terms seismicity, earthquake location and hypocenter are sometimes used interchangeably in seismology. The location of an earthquake is the point where the main seismic energy is released, and in the case of volcano-tectonic earthquakes, the point of local displacement. In this study earthquake location and hypocenter are used to define the location of one or several earthquakes, whereas seismicity refers to a group of earthquakes that form a particular trend in either time or location. For example, 'seismicity during the 1966 seismic crisis', would refer to all earthquakes in this time period, and would be talking about the trends seen as a whole, not focussing on just locations. Whereas, relocated hypocenters refers to the location of that subset of earthquakes only. All earthquakes referred to in this study are volcanic related earthquakes, and are thought to have originated in the volcanic and magmatic system.

2.1 Signal Types

The type of seismic signal and the frequency of earthquakes are used as tools to help understand physical processes and the potential severity of eruptions at volcanoes (*Lahr et al.*, 1994). Volcanic earthquakes can originate in either fluids such as magma or gas (thought of as a triggered resonance signal), and in solids such as the surrounding country rock (*Chouet*, 1996); these give different seismic signals which give an indication on the source process. A change in signal type has been recorded at a number of volcanoes prior and during ongoing eruptions such as Mount St Helens (1980), Pinatubo (1991), and Ito-oki (1989) (*McNutt*, 1996).

On Montserrat, seismicity was predominantly Volcano-Tectonic (high-frequency) earthquakes at the start of the eruption in 1995; this was interpreted as shear failure in the surrounding country rock (*Aspinall et al.*, 1998). As the eruption progressed, a switch to low frequency earthquakes was observed, suggesting a change in trigger mechanism or environment that the earthquakes were originating from (*Miller et al.*, 1998). Low frequency earthquakes, such as long period and hybrid earthquakes, provide an important link between processes observed at the surface, and physical processes acting within the magmatic system (*Neuberg et al.*, 2006).

The classification of seismic events on Montserrat was first described by *Miller et al.* (1998),

who adapted a broad classification scheme used at other volcanoes to fit signals recorded on Montserrat (*Lahr et al.*, 1994; *Latter*, 1981). Examples of different seismic signals recorded on Montserrat can be seen in Figure 2.1. There has been debate over the differences between hybrid and long period earthquakes, with *Neuberg et al.* (2006) and *Rodgers et al.* (2016) suggesting that these should be under the same classification of Low Frequency earthquakes. *Neuberg and Pointer* (2000) suggests that long period and hybrid seismicity share the same source process, with the only difference due to the depth of the initial trigger of the earthquake. This is agreed with by *Rodgers et al.* (2016) who suggests that both long period and hybrids are end members of the same spectrum, and therefore can be classified as the same category.

This thesis uses the classification system used by MVO which follows that of *Miller et al.* (1998), where hybrid and LP earthquakes are classified as two separate families. The following sections describe the signals and their interpretations generally and specifically at Montserrat. These classifications are based on waveforms and are used in subsequent chapters when looking at seismicity through different phases in the eruption to aid understanding of processes that were occurring during these timeframes.

2.1.1 Volcano-Tectonic Earthquakes

Generally, Volcano-Tectonic (VT) earthquakes have clear P and S wave arrivals with frequencies mostly between 5–10Hz, and generally occur in swarms (*McNutt and Roman*, 2015). These are interpreted as rock fracture, double-couple earthquakes in country rock, or slip on pre-existing faults — similar to earthquakes seen at active fault lines (*Chouet*, 2003; *McNutt*, 1996). In volcanic settings, this is a response to stresses imposed by the movement of fluids at volcanoes, and magma intruding into country rock resulting in localised fractures and increased stress (*Lahr et al.*, 1994; *Latter*, 1979; *Luckett et al.*, 2007). VT seismicity can be used to map stress concentrations in the area surrounding the magma conduit, giving an estimate of the magma source (*Chouet*, 1996). It is commonly one of the first signs of renewed volcanic activity at volcanoes (*Endo et al.*, 1981; *Lockwood et al.*, 1985; *Power et al.*, 1995; *Team*, 1991).

VT earthquakes recorded at Montserrat have been located throughout southern Montserrat at depths shallower than 7 km (*Aspinall et al.*, 1998). Interpretations of VT seismicity on

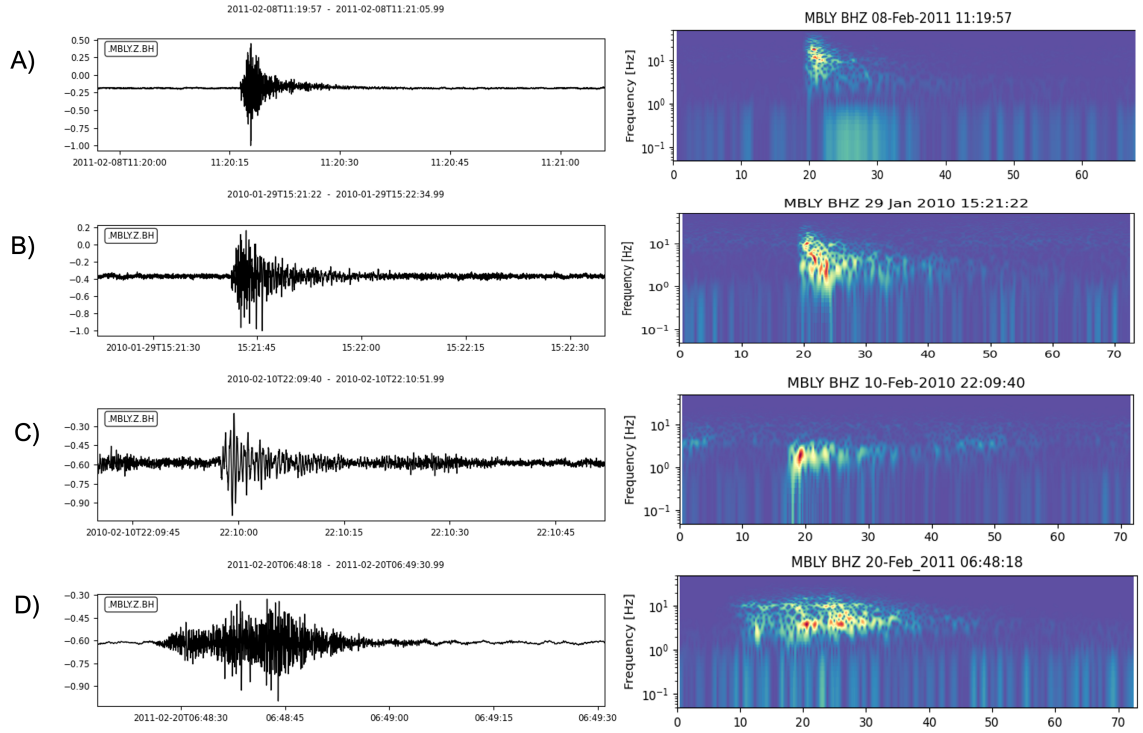

Figure 2.1: Examples of different seismic signals recorded at Soufrière Hills Volcano, and the associated spectrograms showing frequency variation throughout the signal. A) Volcano-Tectonic earthquake, B) Hybrid earthquake, C) Long Period earthquake, D) Rockfall event.

Montserrat suggest these are a result of rock fracture from intruding magma, and increased stress around a magma conduit. A recent feature at Montserrat is VT strings; these are short intense swarms of VT earthquakes that have a duration up to an hour (*Smith*, 2013). A quarter of these VT strings have been related to increased degassing and ash venting. Correlation with SO_2 flux data suggests there is a relationship of increased gas release generating the VT strings (*Smith*, 2013).

2.1.2 Low Frequency

Low Frequency (LF) earthquakes include Long Period and hybrid earthquakes defined by *Miller et al.* (1998), but some researchers combine these into one category (*Neuberg et al.*, 2000, 2006; *Rodgers et al.*, 2016; *Rowe et al.*, 2004). These have frequencies ranging from 0.2–10 Hz (*Neuberg et al.*, 2006). Generally, LF earthquakes originate from a fluid-rock boundary (*Chouet*, 1988; *Neuberg et al.*, 2000), with trigger mechanisms including: ascent of magma in a conduit (*Neuberg et al.*, 2006; *Rodgers et al.*, 2016), pressurisation of fluid filled cracks (*Chouet*, 1996), interaction of magma and water (*Zimanowski*, 1998), shear

fracture due to stick-slip motion of magma plugs in the conduit (*Goto*, 1999), and degassing processes within the conduit (*Stix et al.*, 1997).

Rowe et al. (2004) suggests that LF events on Montserrat in 1996 during dome growth were initiated by rapid bubble formation, the continued creation and destruction of fluid filled cavities within the magma conduit. The majority of the energy from LF earthquakes is trapped within the conduit due to the high impedance contrast with the surrounding rock (*Neuberg et al.*, 2006). This results in conduit resonance, and can make arrival picks more difficult at seismic stations. The majority of LF swarms show a high correlation between events suggesting the trigger mechanism is a stable non-destructive source (*Neuberg et al.*, 2006).

MVO classifies Low-Frequency events into Hybrid and Long Period — which are described in more detail below. Although both show similar processes, this study will keep the terms Hybrid and Long Period seismicity separate to help differentiate between different changes in seismicity at Soufrière Hills Volcano.

Long Period Earthquakes

Long Period (LP) earthquakes are emergent with monochromatic waveforms (*Neuberg et al.*, 1998); LP's recorded at Montserrat generally have less clear P and S waves with frequencies between 1–2.5 Hz (*Fehler and Chouet*, 1982). At Galeras volcano, LP seismic coda can last up to 1.5 minutes (*Cruz and Chouet*, 1997). Shallow LP events are related to the resonance of fluid filled cavities whilst deeper LP events are thought to relate to magma movement (*Kumagai et al.*, 2003, 2005). LP earthquakes are a result of short term pressure disturbances occurring within fluid filled conduits, such as bubble formation and collapse (*Aki et al.*, 1977; *Chouet*, 1985; *Koyanagi et al.*, 1987; *McNutt and Roman*, 2015). Shear failure of rock or non-linear flow processes that occur at very shallow depths are also thought to cause LP events, due to path effects changing the seismic signature (*McNutt and Roman*, 2015). Modelling by *Tuffen et al.* (2008) shows that earthquakes may occur in crystal rich and crystal free silicic magmas, suggesting that LP earthquakes could originate from processes in erupted magma. This fits observations seen where growing lava spines have coincided with small earthquake swarms locating in the lava dome (*Cooper et al.*, 2008; *Nakada et al.*, 1999).

On Montserrat, there is still some debate on interpreting LP events. They are thought to be related to strong pressurisation of the volcanic plumbing system, which is seen in a sealed system (*Chouet*, 1996; *Neuberg et al.*, 2000). This is the result of volumetric changes within the magma conduit, involving the movement of fluids within a resonating magma conduit (*Chouet*, 1996; *De Angelis*, 2009). The similarity in coda between events in the same LP swarm suggests that there is a repetitive excitation of the same source (*Lahr et al.*, 1994; *Qamar et al.*, 1983; *Stephens et al.*, 1994). The lack of high frequency content in the seismic signal is thought to be due to the interaction with the free surface, where surface waves dominate (*Neuberg and Pointer*, 2000). LPs generally show the same polarisation at all stations (*Lahr et al.*, 1994), and are frequently associated with ash venting from the dome (*Neuberg*, 2000).

The restart of dome growth in March 1997 resulted in PDC's to the South of Soufrière Hills. LP seismicity increased in mid-March with 50% of LP earthquakes preceding rockfall events by a few seconds (*Miller et al.*, 1998). No movement on the dome during LP seismicity suggests that the LP signal was not caused by a surface process, and instead shallow magma movement (*Neuberg et al.*, 1998).

Hybrid Earthquakes

Hybrid earthquakes are a mixture of VT and LP events; seismic signals have an impulsive, high frequency P wave arrival (similar to a VT event), followed by a low frequency, monochromatic coda (seen in LP events) (*Luckett et al.*, 2007). Hybrid earthquakes can occur in repetitive swarms which show similar waveforms and magnitude, suggesting a repetitive source mechanism (similar to LP) (*White et al.*, 1998). At Galeras volcano, hybrid earthquakes were recorded but not classified as a separate family to LP earthquakes, similar to some researchers when looking at hybrid events on Montserrat (*Cruz and Chouet*, 1997). It is thought hybrid earthquakes represent a mixture of processes such as an earthquake occurring adjacent to a fluid filled cavity resulting in oscillations, or that hybrids are shallower than LF earthquakes and hence are able to preserve more higher frequency energy (*McNutt*, 1996).

On Montserrat, hybrid earthquakes are thought to be triggered by shear faulting on an interface between a fluid filled crack and country rock (*Chouet*, 1996; *Lahr et al.*, 1994),

violent degassing into cracks (*White et al.*, 1998), and the build up of pressure resulting in stick-slip motion along conduit walls (*Voight et al.*, 1998, 1999). Repetitive hybrid earthquakes preceded the first magma extrusion in September 1995 (*White et al.*, 1998). Similar swarms were noted once dome growth began, with over 8000 events recorded during the first eight months (*Miller et al.*, 1998). This changed to non-repetitive swarms which merged into tremor lasting roughly an hour on the 20^{th} July 1996, accompanied by an increase in steam emission from the dome (*Sparks et al.*, 1998).

To clarify the difference between hybrid and LP seismicity, a hybrid earthquake is a result of an earthquake occurring on a interface between a fluid filled system and the local country rock, or through the build up of pressure, but normally resulting on a boundary along a liquid-solid interface. Where LP earthquakes are a result of the movement of fluids as a result of either a resonating conduit, increased pressure or magma movement.

2.1.3 Very Long Period and Ultra Long Period Signals

Very and Ultra Long Period (VLP and ULP) earthquakes have been recorded at different types of volcanoes across the world (*Chouet and Matoza*, 2013). They can last from seconds to several minutes and have very low frequencies; these form a continum ranging from LP signals to ULP signals which show the lowest frequencies (*Šindija et al.*, 2021). They are thought to originate from a fluid-rock interaction such as magma or gas movement in the volcanic system (*Chouet and Dawson*, 2011), and are commonly observed prior to caldera collapses and phreatic explosions (*Kawakatsu et al.*, 2000; *Kumagai et al.*, 2001). A VLP signal was recorded on Montserrat on the 23^{rd} March 2012 during an outgassing event.

2.1.4 Tremor

Volcanic tremor on Montserrat is a continuous signal that can last for several minutes (or days in some locations) with similar frequencies to hybrid earthquakes (*Miller et al.*, 1998); these signals have emergent onsets making first arrivals difficult (*Konstantinou and Schlindwein*, 2003). Experimental simulations by *Burlini et al.* (2007) show that long lasting volcanic tremor is related to melt migration. Tremor is closely related to LP earthquakes and reflects the response of fluid filled conduits to sustained periods of pressure fluctuations

(*Cruz and Chouet*, 1997). Tremor can be preceded by repetitive hybrid or LP events that start to occur more frequently until they combine into a tremor signal (*McNutt*, 1996; *Miller et al.*, 1998; *Sparks et al.*, 1998; *Voight et al.*, 1998, 1999). An example of this is shown in Figure 2.2.

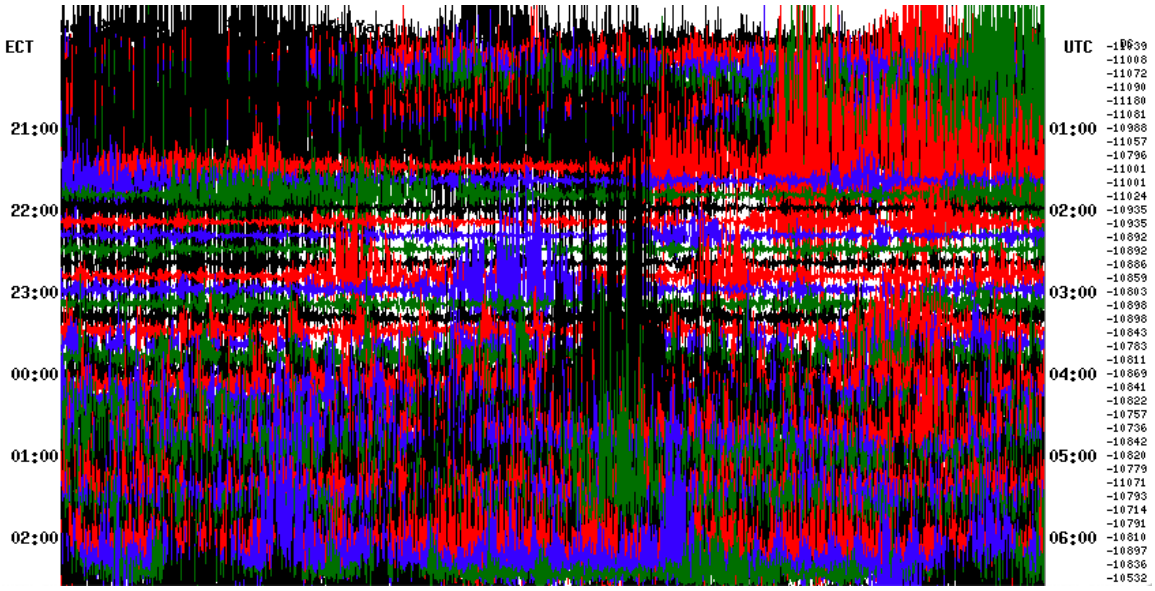

Figure 2.2: An example of cyclic tremor that was recorded during Phase 5 of the eruption; image provided by Paddy Smith.

2.1.5 Rockfalls

Rockfall signals have an emergent waveform of a longer duration which contains a wide range of frequencies (*Luckett et al.*, 2007). Rockfall signals are normally visually correlated with rockfalls or pyroclastic density currents from the dome (*Miller et al.*, 1998). The number of rockfall events can give an indication to the dome growth rate (*Calder et al.*, 2005); this is important as the view of Soufrière Hills Volcano can sometimes be restricted due to poor visibility.

2.1.6 Explosions

A vulcanian explosion has a long period signal up to 2 Hz; this is then followed by a higher amplitude and higher frequency signal, resulting from the formation of pyroclastic flows (*Miller et al.*, 1998).

A phreatic explosion is from a steam-blast eruption and is characterised by an impulsive

broadband signal that lasts a few minutes (*Miller et al.*, 1998).

2.2 Current Earthquake Locations

At present, earthquake locations on Montserrat are from two main catalogues: MVO computed locations from October 1996 to 2018, and hypocenters computed by *Aspinall et al.* (1998) for earthquakes prior to October 1996. Both catalogues use the same 1D seismic velocity model, with a similar location method for earthquake location: *HypoEllipse* (before October 1996), and *Hypocenter* (post October 1996).

Locations are concentrated around Soufrière Hills Volcano, with the majority of seismicity located from 1 km asl to 5 km bsl. Figure 2.4 shows a histogram representing the depths of VT earthquakes; two peaks at 1.5 and 3 km depth are recorded; this does not correlate with a velocity model boundary at those depths. Seismicity is recorded across the southern half of Montserrat, with an increase in earthquakes being located to the west beneath St George's Hill and Windy Hill during 1995–1996.

Over the past 25 years earthquake rates, types and the location of seismicity has provided an insight into the magmatic system, and processes that occur in the lead up to lava extrusion. A change in type of seismicity to lower frequency earthquakes can be suggestive of the shallowing of magma, which in turn increases the likelihood of eruption. Similarly, seismicity at other locations, such as St George's Hill could be suggestive of magma migration, a secondary intrusion site, or the reactivation of previous faults as a result of increased stress from uprising magma beneath Soufrière Hills Volcano. A complete and accurate earthquake catalogue aids current hazard assessment but also improves understanding of the volcanic system as a whole.

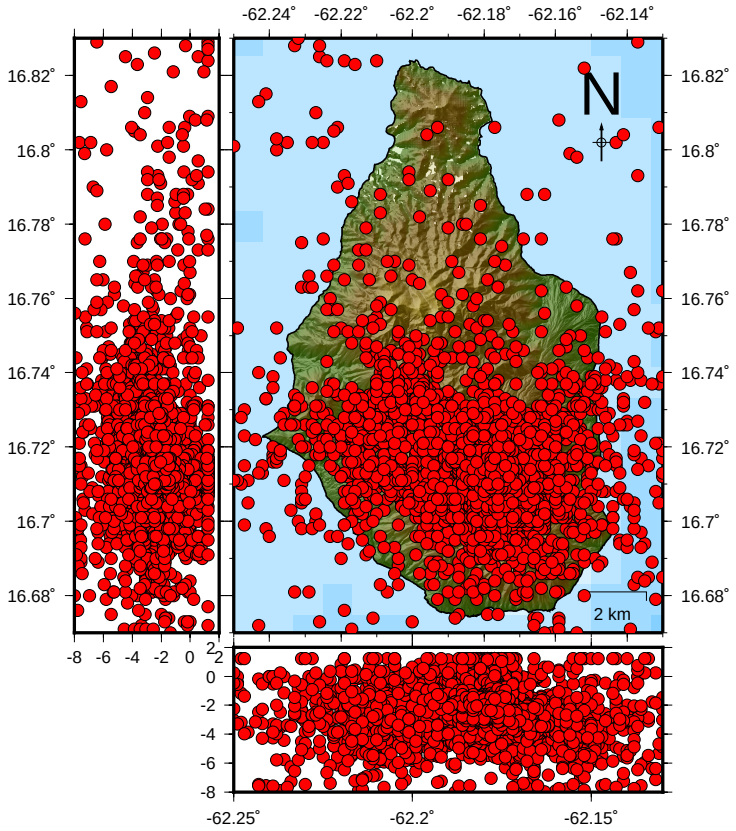

Figure 2.3: Map showing earthquake hypocenters from July 1995 to February 2018: earthquakes were located by the Montserrat Volcano Observatory for events post October 1996 and by *Aspinall et al.* (1998) before October 1996. Only locations with errors less than 5 km are plotted.

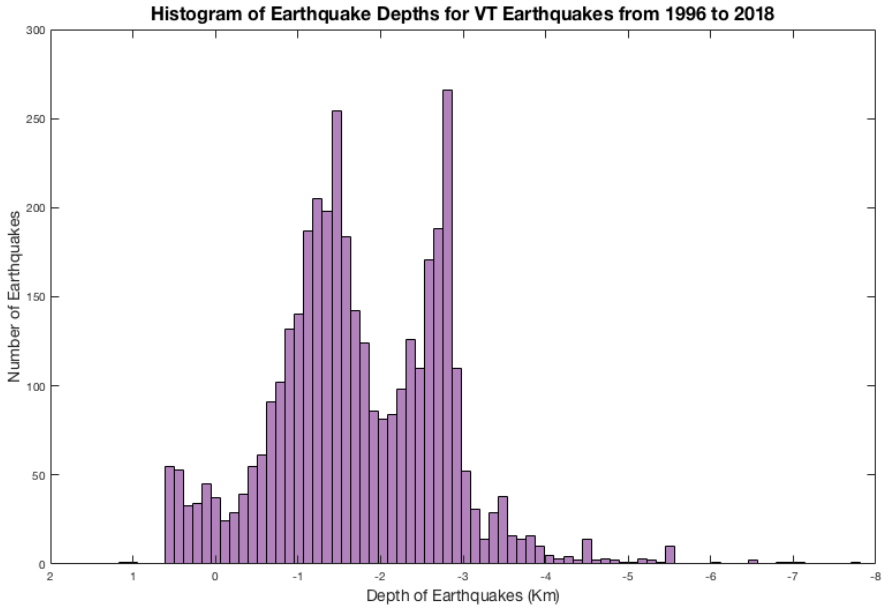

Figure 2.4: Histogram to show the range of depths located by MVO for VT earthquakes from October 1996 to February 2018. VT earthquakes are only displayed here due to other seismicity types generally being associated with larger depth errors.

2.3 Seismic Stations

The number of seismic stations on Montserrat has varied over the past 25 years with the network being continuously revised and updated and stations being destroyed during the eruption; the network from 1995 to 2020 is shown in Figure 2.5. This section looks at the evolving network over the past 25 years, and highlights periods where there was low station coverage. This is particularly important to understand, as time periods with fewer stations may have an additional impact on the accuracy of earthquake locations. This is explored in more detail in Chapter 6, which looks at the impact of using only four seismic stations for earthquake location.

Pre-1995

Prior to the start of the eruption in 1995 there had been several seismic networks deployed on Montserrat to monitor activity. Increased seismicity in November 1935 led to an expedition to Montserrat by the Royal Society of London, and a seismic network of eight seismic stations was established by *Powell* (1938). This network operated until 1951 and recorded over 200 earthquakes during 1937 to 1938 which were located beneath Soufrière Hills and St George's Hill (Figure 1.5).

In 1966 the Seismic Research Centre (SRC) installed four seismic stations across the island to record increased seismicity; this was reduced to a short period vertical seismic station from 1967 to 1980 before being swapped to a telemetered station at St George's Hill (*Smith*, 2013). Two additional seismometers were installed in 1989 to help distinguish between local and tectonic events (*Shepherd et al.*, 1971). The island was damaged by Hurricane Hugo in 1989; this led to the seismic station not being fully restored until 1992 (*Shepherd et al.*, 2002). There were only two seismic stations being operated by SRC prior to the start of the eruption in 1995 (*Luckett*, 2005).

1995–1996

Two stations previously provided by SRC were supplemented by an additional seven 1 Hz seismic stations in 1995s by the USGS Volcano Disaster program (*Aspinall et al.*, 1998).

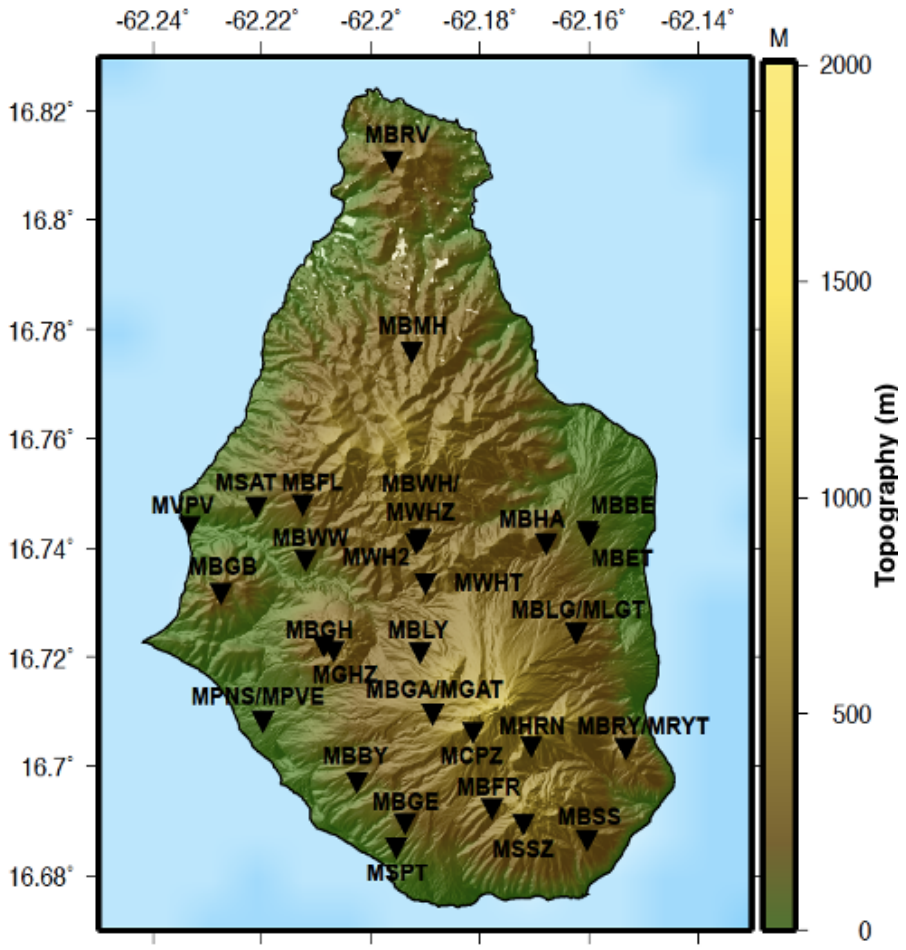

Figure 2.5: Diagram showing the locations and names of the seismic stations used from 1995 to 2020 by the Montserrat Volcano Observatory. Seismometers deployed during SEA-CALIPSO and from other institutions are not shown. Station codes are as follows: MB = Montserrat Broadband deployed since 1996, MS = Montserrat Spider Stations. The rest of the station codes were from the 1995-1996 setup and had a different naming system. Here, the first letter 'M' refers to Montserrat, the second and third character refer to the location name, with the last letter representing the type of seismometer. V or Z refer to vertical, T stands for high gain data, and L stands for Low gain data.

The narrow range in amplitude signals of the analogue system resulted in some events in this time period being clipped; this led to the installation of two radio links: high gain data (MLGT) and low gain data (MLGL) at Long Ground (*Luckett*, 2005). The seismic stations were telemetered to a PC-SEIS acquisition system (*Murray et al.*, 1996). Before October 1996 only event data, such as arrival times and locations, were stored on the IRIG database (*Luckett*, 2005).

1996–1997

In October 1996, the British Geological Survey (BGS) installed five 3-componet broadband seismometers (Guralp CMG-40T) and three vertical seismometers (Integra LA100 1Hz) (*Neuberg et al.*, 1998) (Figure 2.6). The data were digitised at the site to 75 Hz and sent to the observatory via either UHF radio links, or the Bethel telephone exchange — which sent the data along a dedicated telephone line for the observatory (*Luckett*, 2005). Data were synchronised with a time signal from the GPS clock based at MVO; this was then passed through an Interpolating Line Interface supplied by *Earth Data Ltd*, allowing different stations to be synchronised (*Luckett*, 2005). Data acquisition was processed through the program *SEISLOG* (*Utheim and Havskov*, 1997).

In June 1997 volcanic activity resulted in the destruction of the Bethel telephone line, resulting in loss of communications with three stations; an additional station was then destroyed by pyroclastic flows (*Luckett*, 2005). Relocation of the observatory to the north of the island in September 1997 resulted in the loss of communication with two other stations, taking the network down to two operating seismic stations by the end of the year (*Luckett*, 2005).

1998–2002

Telemetry problems between stations and the temporary site for the observatory were solved by installing repeater sites at Centre Hills and Silver Hills, alongside a telephone line to transmit data from the old observatory. This resulted in the network being rebuilt in April 1998, and consisted of six seismic stations (*Luckett*, 2005). Two new 1 Hz vertical seismometers were installed, and station MBRY was updated from a vertical component to a broadband seismometer (*Luckett*, 2005) (Figure 2.7). An additional broadband station was added to the network at Brodericks Yard in March 1999 to improve the azimuthal coverage (*Luckett*, 2005). The eight stations continued throughout 1999–2002, with some stations seeing the odd month offline due to weather and battery problems. Acquisition changed to a combination of SA24 and *Earthworm* (*Johnson et al.*, 1995) in 2001 to replace the original *SEISLOG* software (*Luckett*, 2005).

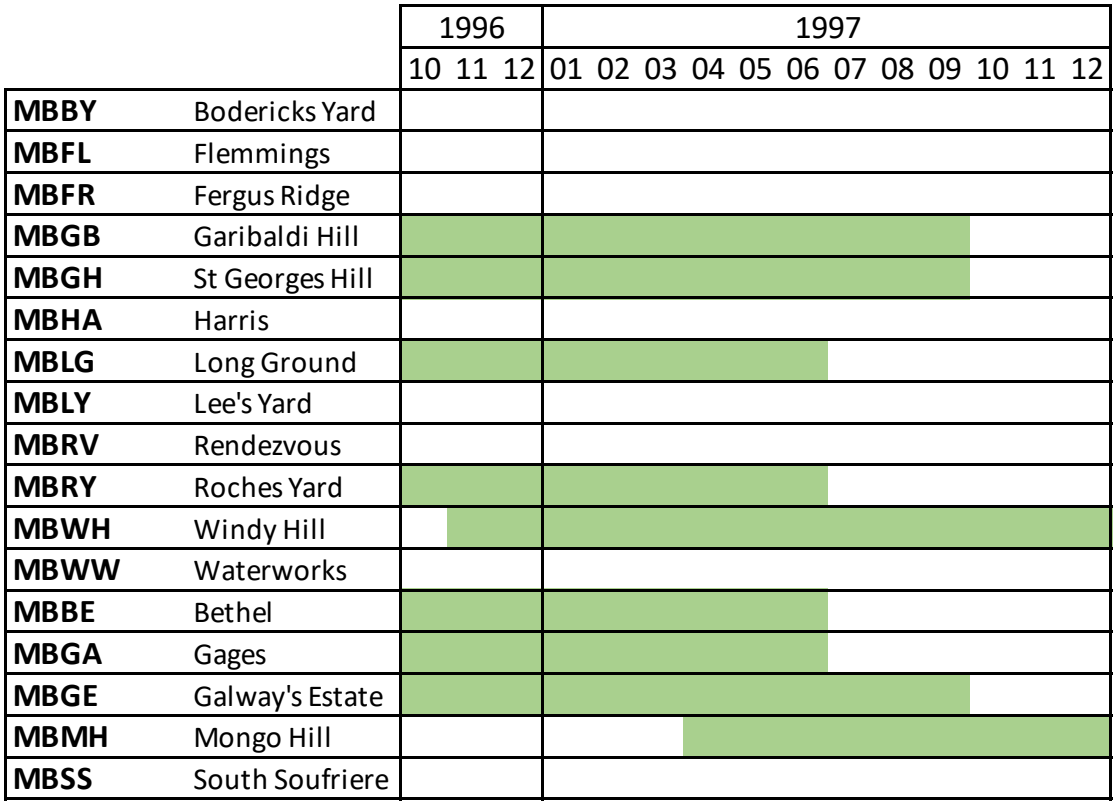

Figure 2.6: Time plot showing which seismic stations were active (green) on Montserrat from 1996–1997.

2003–2005

MVO moved to its purpose built site in Flemmings in January 2003; this resulted in the loss of the station at the old observatory and a reorganisation of the network. The seismic station from the old observatory was moved to a new site further north at Rendezvous in March 2003 (*Luckett*, 2005). Two additional broadband seismometers were installed at Lees Yard (June 2003) and Harris (September 2004) by MULTIMO Consortium (*Green and Neuberg*, 2005) and Pennsylvania State University respectively (Figure 2.8). During 2003–2004 there was a minimum of eight seismometers online in the network. Brodericks Yard was replaced in September 2004, marking the start of the 2005 upgrade (*Luckett*, 2005).

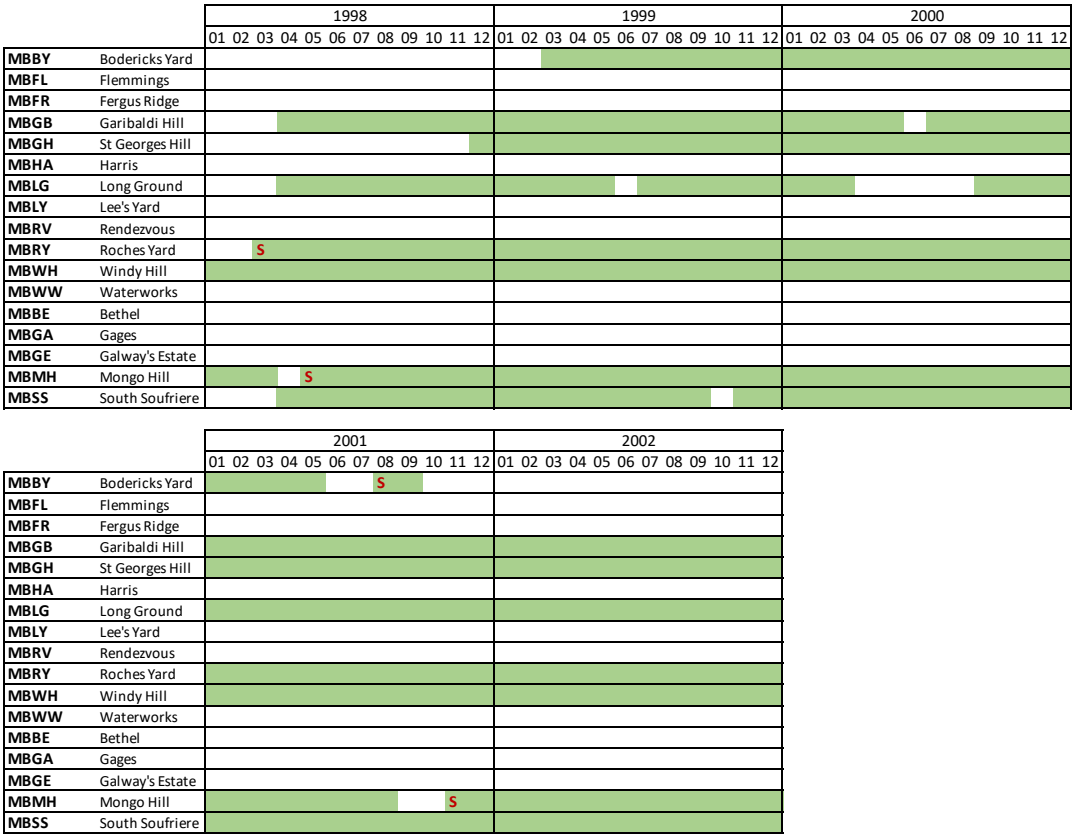

Figure 2.7: Time plot showing which seismic stations were active (green) from 1998 to 2002. S denotes a change in seismometer.

2005–2007

The network was upgraded in March 2005 with each seismometer being updated with a Guralp DM24 digitiser; this meant that each station was time stamped independently (*Luckett*, 2005). Interference between the UHF radios and marine band signals became problematic; as a result, the communications were changed to spread-spectrum radio modems (freewave) (*Luckett*, 2005). The software *SCREAM* was introduced allowing two way communication with the digitisers; this data could then be then fed into *Earthworm* to check any timing issues with the GPS clocks. Stations MBLG and MBWH were upgraded in March 2005 to 3 component broadband seismometers, and two new stations were installed in June 2005 (MBFR) and September 2005 (MBFL) to include a station at the observatory (*Luckett*, 2005). This resulted in a network of 11 seismic stations over the two-year period (Figure 2.9).

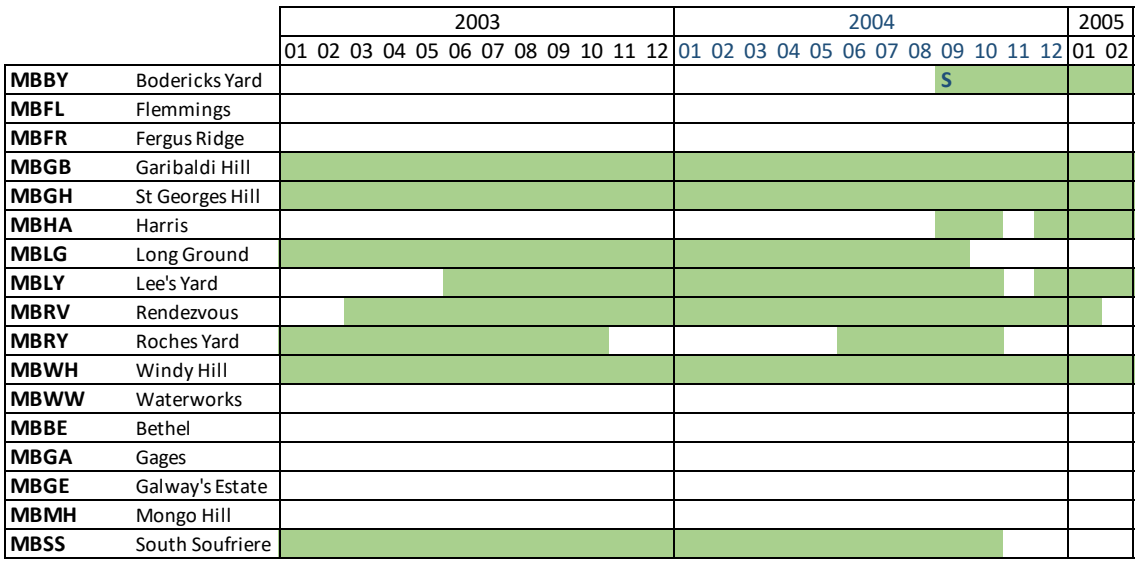

Figure 2.8: Time plot showing which seismic stations were active (green) from 2003 to 2005. S denotes a change in seismometer.

2007–2010

There is very little information on this time period, due to a lack of papers and station notes not being published on MVO's website. However, by looking at helicorders online an idea of which stations were active can be estimated. The 11 seismic stations continued to work throughout the period, with some stations being off for a month or two at a time, which can be assumed as needing repair, or due to timing issues with the GPS clock. An additional station was added to the west of the island in May 2009 by Jurgen Neuberg from the University of Leeds (Figure 2.10).

2010–2018

From June 2010 onwards, station notes were uploaded onto the MVO internal website, allowing easier recognition of station problems and any change in seismometer type and location. No additional seismic stations have been added to the network since 2009, although two stations (MBHA + MBGB) were moved 30 m due to logistical purposes. Stations MBRV, MBFR, MBWW and MBLG were removed due to logistical issues in April 2012, November 2014, June 2015 and December 2015 respectively (Figure 2.11 and 2.12).

There have been several issues with some stations, notably MBLG which had intermittent

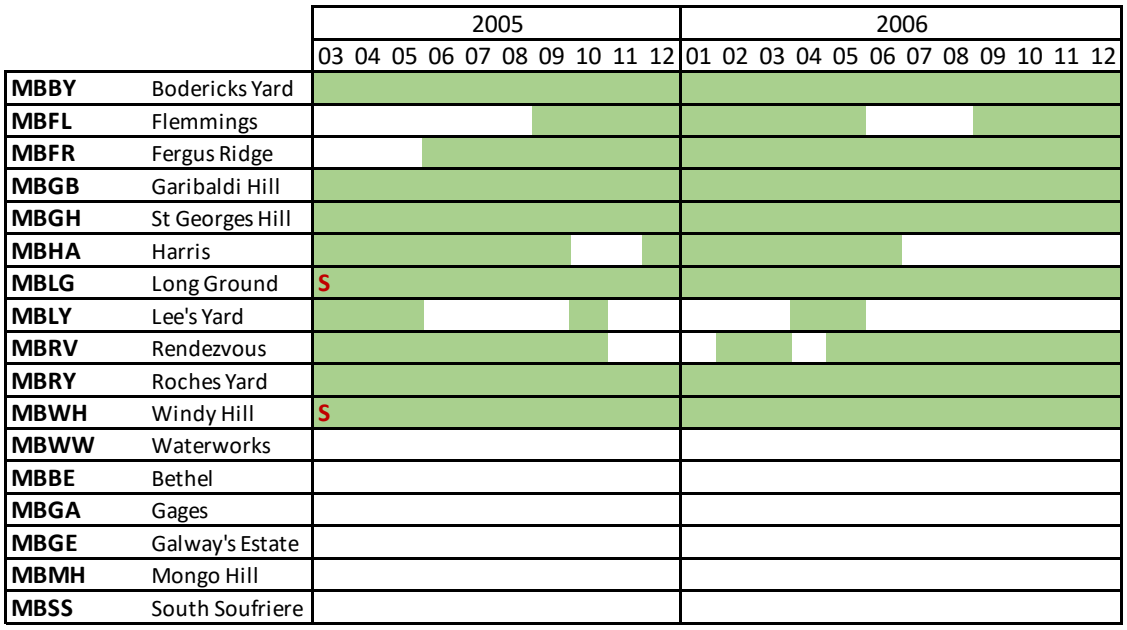

Figure 2.9: Time plot showing which seismic stations were active (green) from 2005 to 2007. S denotes a change in seismometer.

data gaps from 2010 until 2015 when the station was removed. A lot of the station problems have been related to minor repairs due to animal damage, flooding of stations and battery outage. Timing issues with the digitisers have effected all the seismic stations at some point during the past 7 years, notably MBFR, MBGB, MBHA and MBRV which had several months of incorrect time stamps. These timing issues vary from a few seconds up to several minutes and result in the station not being able to be used for arrival picks. Timing issues were the result of an error with the GPS time stamp which would slowly drift, becoming further out of sync with time (starting at a few seconds, and increasing to several minutes after a few months).

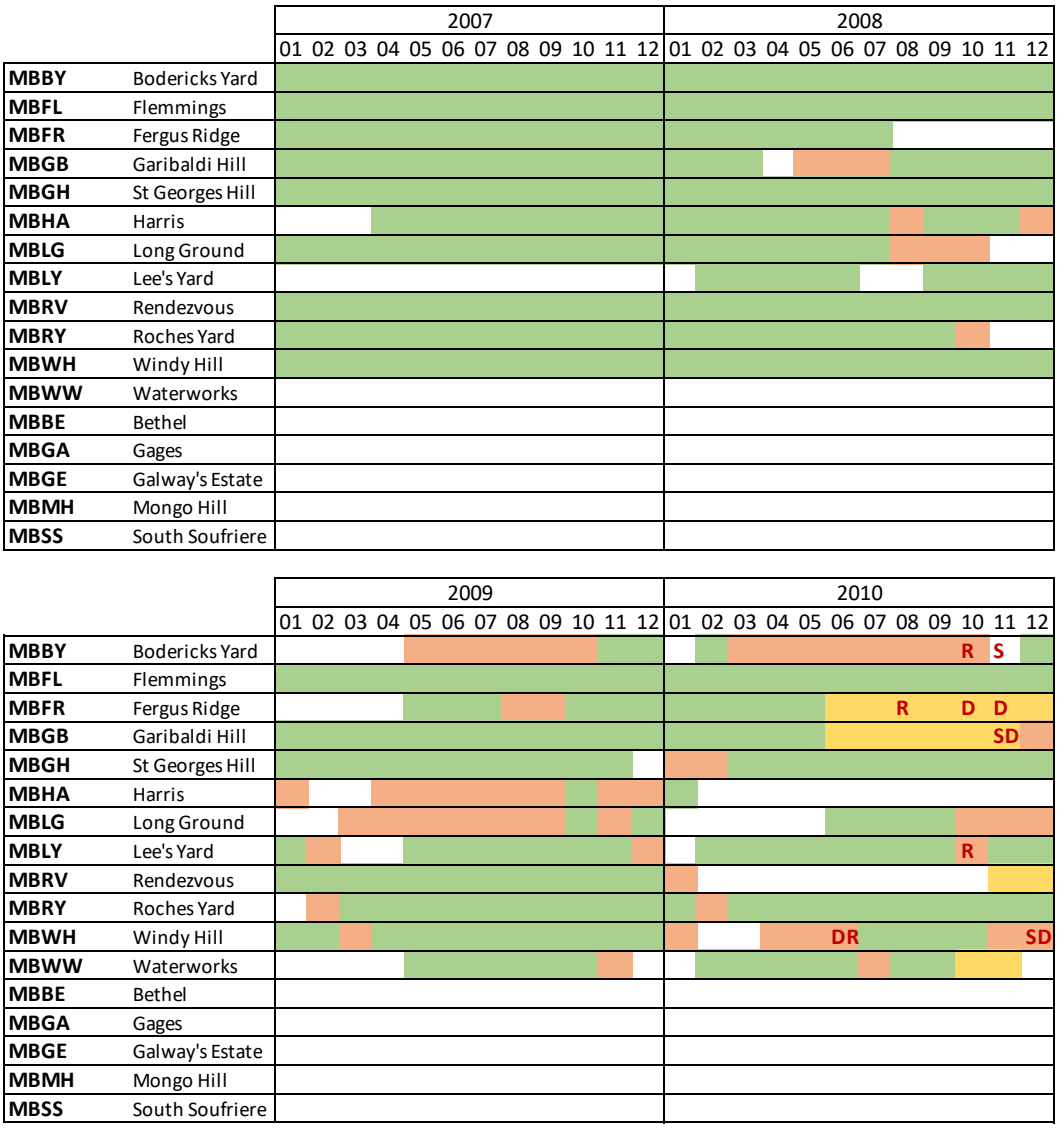

Figure 2.10: Time plot showing which seismic stations were active (green) from 2007 to 2010. S denotes a change in seismometer, R denotes a repair taken place, D denotes a change in Digitiser. Orange sections represents months when the station was off for a few days or weeks, or had other issues. Yellow sections represent months when the seismic station had a timing issue.

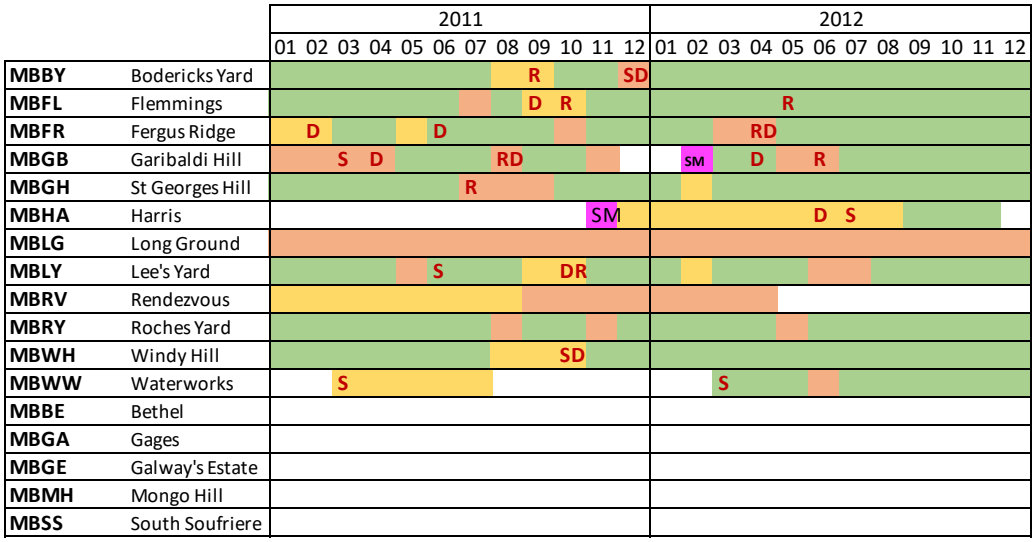

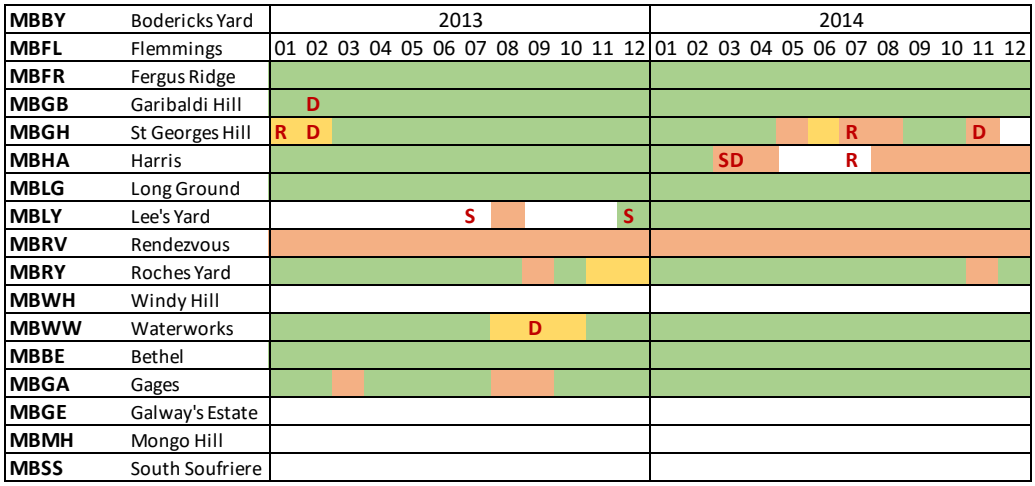

Figure 2.11: Time plot showing which seismic stations were active (green) from 2011 to 2014. S denotes a change in seismometer, R denotes a repair taken place, D denotes a change in Digitiser. Orange sections represents months when the station was off for a few days or weeks, or had other issues. Yellow sections represent months when the seismic station had a timing issue. Pink months represent a time when the seismic station moved to a new location.

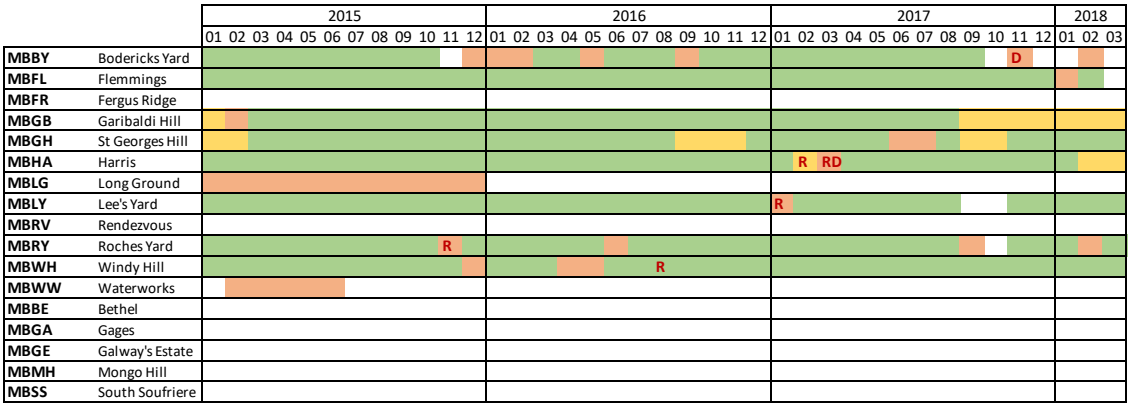

Figure 2.12: Time plot showing which seismic stations were active (green) from 2014 to 2018. S denotes a change in seismometer, R denotes a repair taken place, D denotes a change in Digitiser. Orange sections represents months when the station was off for a few days or weeks, or had other issues. Yellow sections represent months when the seismic station had a timing issue.

2.4 Summary

This chapter gives an overview to the main seismic signals recorded on Montserrat, and how the seismic stations have varied over the past 25 years. This helps to understand the variation in seismicity on Montserrat, which is key for interpretations throughout Chapter 5 and 6. These chapters use the relocated seismic catalogue alongside differing types of seismicity to understand changes in the volcanic system throughout the course of the eruption. Understanding how seismic stations have varied throughout the seismic catalogue is key when comparing earthquake location, as a variation in seismic network can have an impact on accuracy of the calculated hypocenter. Further, understanding which stations had timing issues, or were undergoing repairs highlights which timeframes may have results that are less trustworthy. The change in seismic network through time is used in Chapter 4 to understand how different seismic stations affect outputted earthquake locations.

Chapter 3

Earthquake Location

3.1 Earthquake Location Methods

An earthquake can be described by its hypocenter, origin time, faulting style and a measure of its size; however the accuracy of earthquake location is still a prominent geophysical problem. Earthquake hypocenters are of great importance in society: firstly, to understand the locality of the damage from large earthquakes; and secondly, for assessing future earthquake hazards in the region (*Lomax et al.*, 2009). In volcanic regions an increase in seismicity can indicate magma movement; tracking earthquake locations and frequency through time is a useful tool in monitoring volcanoes (*McNutt*, 1996).

Earthquake location is an inverse problem, with both origin time (t_o) and the location (x_o, y_o, z_o) unknown. Arrival times (t_i), of the P and S wave, are recorded at a minimum of four seismometers in the region of the earthquake. The time for the seismic waves to reach the seismic station is proportional to the distance from the earthquake's hypocenter. Arrival times recorded at each station can be written as:

$$t_i = T_i(x_o, x_i) + t_o \tag{3.1}$$

where $T_i(x_o,x_i)$ is the travel time from the origin to the seismic station, and t_o is the earthquake's origin time (*Menke*, 2018). If the origin time is known, distance (d) can be calculated by:

$$d = (t_i - t_o)V_P \tag{3.2}$$

where V_P is the average seismic P wave velocity for the region. However, we rarely have the origin time of an earthquake (except in anthropogenic cases), and therefore need another way to measure distance. A simple approach may be taken by assuming a constant ratio ($\sqrt{3}$) between P and S wave velocities, and then using the difference between P (t_P) and S (t_S) arrival times to calculate a distance from each station to the earthquake:

$$d = \frac{(t_S - t_P)V_P}{\sqrt{3} - 1} \tag{3.3}$$

Using calculated distances from three or more stations, the epicentre of the earthquake can be calculated by triangulation (four stations are needed to additionally calculate depth). However, the earth is not homogenous and has spatial variations in seismic velocity within the earth. Therefore Equation 3.3 is a simplified calculation for distance between seismometer and earthquake, and hence an estimate of the hypocenter. Arrival times at each seismic station are then:

$$t_i = t_o + \int_{r_o(s)} \frac{1}{V}(r_o)ds \tag{3.4}$$

where $r_o(s)$ denotes a point at distance s along ray path r_o between receiver and earthquake (*Lomax et al.*, 2009). Hence, earthquake location is an under-constrained problem. We rarely know the true velocity distribution for a given area, and therefore the velocity model brings an additional uncertainty into computed earthquake hypocenters. Velocity models can be estimated from seismic tomography and other inversion techniques producing 1D, 2D and 3D models with a range of complexity, increasing the accuracy of calculated travel times (*Lomax et al.*, 2009).

Earthquake locations can be absolute or relative depending on the location method used. Absolute locations are determined in a fixed geographic co-ordinate system and time base (*NonLinLoc (Lomax, 2001), Hypocenter (Lienert et al., 1986), HypoEllipse (Lahr, 1999)*); whereas relative locations are located with respect to another spatial-temporal object, such

as a group of earthquakes, examples of this are *HypoDD* (*Waldhauser*, 2001a) and *Bayesloc* (*Myers et al.*, 2011).

To minimise the misfit between calculated and recorded arrival times, some methods involve linearisation of equations, through Taylor expansions, these are called linearised methods. As computers have advanced, direct search methods (non-linearised methods) have been further developed; these create a grid of all possible solutions, and produces a complete probabilistic solution (*Lomax et al.*, 2009).

3.2 Linearised methods

The earthquake location problem can be solved using an iterative least squares approach. The *Geiger* (1912) method linearises the problem by considering the geometry of seismic rays as they leave the source. This formed the basis for all numerical earthquake algorithms (*Jordan and Sverdrup*, 1981). As computing power increased in the 1960's it led to the formation of an iterated linearised approach, following on from Geiger's method.

Equation 3.4 is approximated by a Taylor series expansion around an initial estimated location $\mathrm{m}_o = (\mathrm{x}_o,\mathrm{y}_o,\mathrm{z}_o)$:

$$f(m) = f(m_o) + (m - m_o)f'(m_o) + \frac{(m - m_o)^2}{2}f''(m_o) + ... \tag{3.5}$$

where f(m) is the forward problem that calculates the arrival time (d_{calc}), given a prior location m. If the forward problem for all d_{calc} values are calculated using the first two values from the Taylor expansion [Equation 3.5], then the matrix can be solved to find the origin location by linear algebraic methods. This is then reiterated by re-setting m_o in equation 3.5 to the new location found from the matrix (*Lomax et al.*, 2009). The linear problem is solved again by algebraic methods, and this method is repeated several times until either it reaches a set number of iterations, or a minimum misfit. The final result produces a single hypocenter, origin time and associated errors (*Lomax et al.*, 2009). Linear methods are known to perform less accurately for earthquakes located in complex environments (such as volcanic settings) than for direct search methods (*Presti et al.*, 2008).

3.2.1 Hypocenter

Hypocenter follows Geiger's method, which uses a centred and scaled, linearised least squares approach with adaptive damping to solve earthquake location and origin time (*Lienert and Havskov*, 1995; *Lienert et al.*, 1986). *Hypocenter* combines two location programs: *HYPO71* and *Hypoinverse*, due to issues and limitations with the two methods, and has shown to improve residual times (*Lienert et al.*, 1986). Residual times are the difference between the observed travel time (at the seismometer) and the calculated travel time when choosing the optimal hypocenter; the aim is to reduce residuals so that there is a minimal difference between calculated and observed arrival times for P and S waves. One issue was *HYPO71*'s tendency to keep the depth of the earthquakes at the starting location (*Wesson et al.*, 1971). The origin time is determined as the mean arrival time minus the mean travel time, allowing the x,y,z co-ordinates to be solved iteratively by changing the damping factor before each inversion (*Lienert et al.*, 1986).

A 1D layered seismic velocity model can be defined for local events, or the user can use the IASPEI91 model which is built into *Hypocenter* (*Lienert and Havskov*, 1995). Calculations for location include station elevations, which improves the ability to locate earthquakes at shallow depths (*Lienert et al.*, 1986). *Hypocenter* also uses a starting location algorithm which analyses phase data information, and selects a starting location for the inversion based on the minimum RMS (*Lienert and Havskov*, 1995). The location is first calculated with the depth fixed; depth is then unconstrained for the second convergence which produces the final location (*Buland*, 1976). The main limitation of *Hypocenter* is the restriction to using a 1D seismic velocity model, and its ability to converge near a local solution, potentially missing out on the true location.

3.3 Non-linearised methods

The earliest earthquake locations used direct search methods including simple grid searches (*Lomax et al.*, 2009), and graphical and algebraic methods (*Milne*, 1886). Direct search methods determine a 4D probability density function (PDF) over a given region for all possible solutions. This provides a grid of PDF values, with the optimal solution taken as the maximum value of the PDF. Modern direct search methods can be exhaustive where

every grid cell is checked in a specified region, or it can be directed and evolutionary, where the algorithm learns as it searches for the optimal solution (*Lomax et al.*, 2009). *NonLinLoc* is an example of such a technique and has several search methods available which the user can choose depending on their location site, and computer capability. There are three main types of direct search which will be explored in more detail.

3.3.1 Regular, deterministic search

These searches include grid searches, nested grid searches and Monte Carlo searches using a distributed sampling of a specified region to estimate a complete location PDF (*Lomax et al.*, 2009). The grid search algorithm performs a search on every node inside the grid to obtain an estimate of the PDF at that point; further nested grid searches perform successively smaller grid searches (with nodes closer together), centred around the maximum PDF value from the previous grid (*Lomax*, 2005). Grid searches are computationally demanding and hence provide a restriction on the initial search region (*Lomax*, 2005).

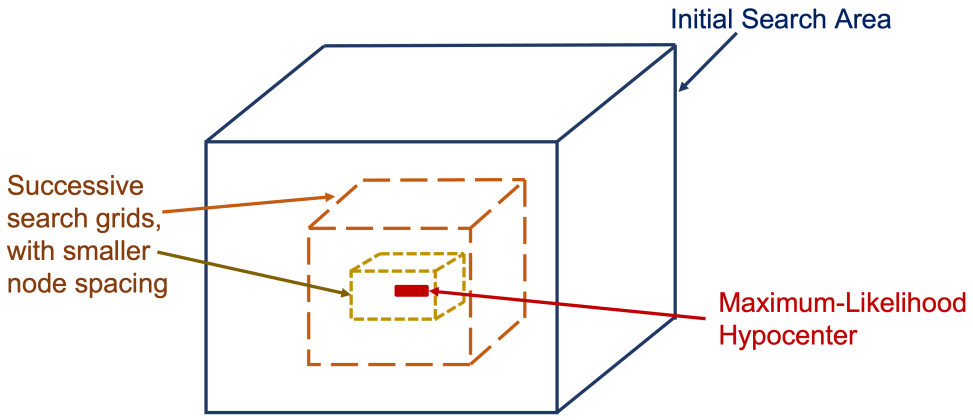

Figure 3.1: Schematic showing how nested grid searches are used for earthquake location. In each successive grid, the node spacing is reduced to get a finer detail PDF for the search region.

3.3.2 Directed Search

A directed search is an evolutionary, directed location method that is non-linearised and can identify local maxima in the PDF. An example of a directed search is the random walk

method which uses a stochastic search throughout the search region, leaning towards areas of higher PDF values. These searches are very efficient and maps the PDF as it moves, but do not always sample all of the region, which can result in the algorithm converging on a local minimum providing an incorrect solution (*Lomax et al.*, 2009).

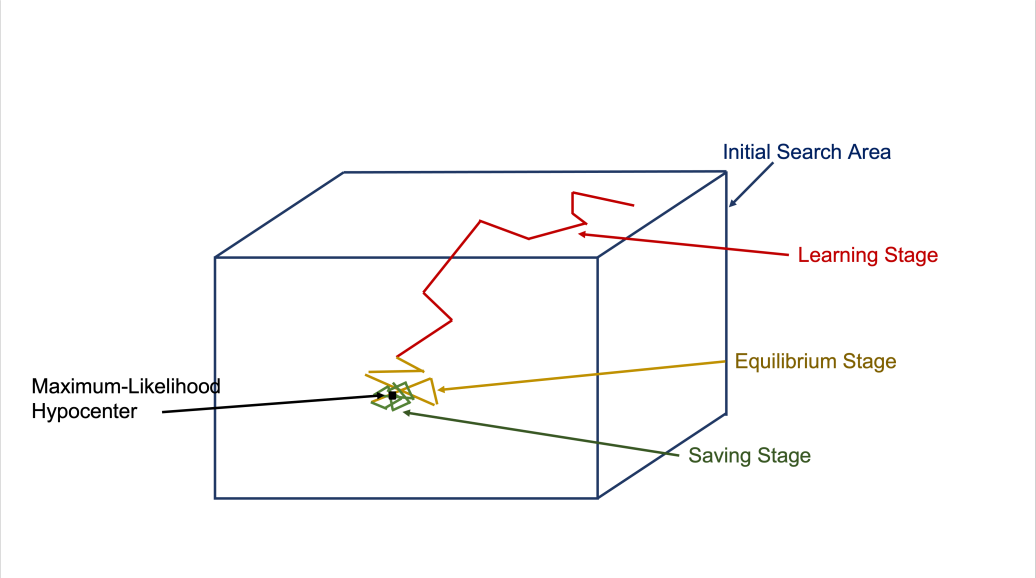

Figure 3.2: The random walk method displayed with its three stages of mapping the PDF throughout the initial search region. The saving stage maps the PDF accurately for a localised region; but therefore can converge in local minimums if the learning stage does not adequately sample the search area.

3.3.3 Importance Sampling

Importance sampling is a learning algorithm that follows a target function using information from previous samples (*Lomax et al.*, 2009). The metropolis algorithm is similar to that of the random walk directed search, but instead a prior PDF is defined. This prior PDF includes all information about the region, including active fault zones, previous earthquake locations and damage reports (*Lomax et al.*, 2009). As the algorithm performs the random walk, it trials samples and compares the PDF value to the prior PDF before being accepted (walk moves to new location) or rejected (walk trials another location). This reduces the effect of the algorithm being stuck in a local solution, by always comparing PDF values with values from higher up in the hierarchy.

The Oct-Tree algorithm uses recursive subdivision and sampling of cells in 3D space to generate a cascade of PDF values (*Lomax et al.*, 2009). A coarse, regular grid is created

throughout the entire search region (pre-defined depending on region of study) and the probability (P_i) that the earthquake location is in that 3D cell (x_i) is calculated:

$$P_i = V_i PDF(x_i) \tag{3.6}$$

Where V_i is the volume of the 3D cell x_i. P_i is calculated throughout the grid and is ranked. The cell with the highest probability is then subdivided into eight sub-cells, and again P_i is calculated for each cell. These eight values are then added to the original list, before choosing the highest probability cell. This technique continues until it reaches a pre-determined number of samples or a maximum probability. Advantages of this technique mean that it can map multiple PDF peaks, resulting in the solution not being stuck in a local solution, and is 100 times faster than grid search (*Lomax*, 2005). However this algorithm is dependent on initial grid size and can run slowly for large 3D velocity models.

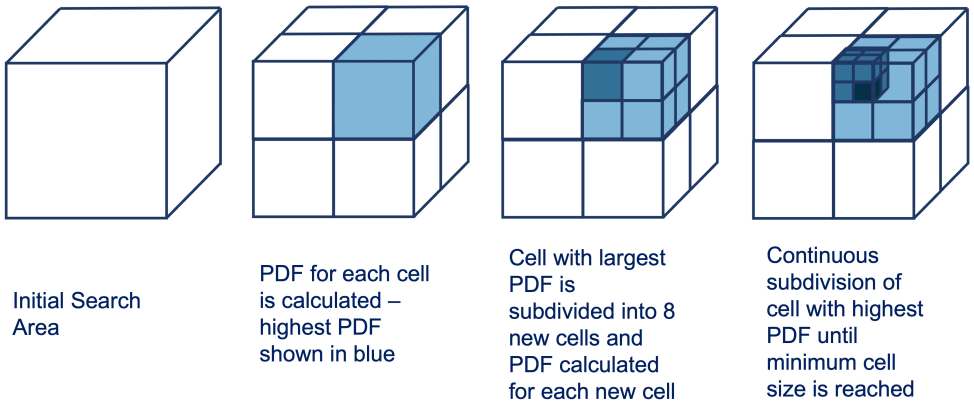

Figure 3.3: Schematic showing Oct-Tree method converging on the highest PDF. Darker blues represent higher PDF values, with successive subdivisions finding the area of highest PDF.

3.3.4 NonLinLoc

For *NonLinLoc*, synthetic travel times are calculated from a search region to each seismic station, using a given velocity model. These are then compared to the arrival times recorded on seismic stations, and the match between the calculated and observed arrival times are maximised to produce the 'best estimate' of the earthquake's location (*Lomax et al.*, 2009). *NonLinLoc* has the ability to use several search methods including: Grid Search, Random

Walk, and Oct-Tree. There are 2 main location methods built inside *NonLinLoc* that also can be chosen by the user: Gaussian analytical inversion and the Equal Differential Time method.

GAU

The Gaussian Analytical location method follows the inversion approach of *Tarantola and Valette* (1982) with a LS-L2 likelihood function. For this method the PDF has the form of:

$$pdf(X, t_0) \propto k\, exp\left(-\frac{1}{2}\sum_{obs_i}\frac{[Tobs_i(X) - Tcalc_i(X)]^2}{\sigma_i^2}\right) \tag{3.7}$$

where X is a point in 3D space, t_0 is an estimate of origin time, k is a normalisation factor, Tobs_i and Tcalc_i are observed and calculated times respectively for observation (obs_i) and σ_i is the assigned error for obs_i.

EDT

The Equal Differential Time (EDT) likelihood function is based on the inversion approach of *Tarantola and Valette* (1982). For this EDT method (EDT OT WT — EDT origin time weighted) the EDT sum probabilities are weighted by the variance of origin time estimates over all pairs of readings; this has been shown to reduce the probability at points with inconsistent origin time estimates leading to a more compact location PDF (*Lomax*, 2001). The EDT method is very robust if outliers are present (*Lomax et al.*, 2009), and provides an alternative to the standard LS-L2 likelihood function that is normally used in location methods (*Lomax*, 2001).

For the EDT location method, the PDF takes the following form:

$$pdf(X) \propto k\left[\sum_{obs_a,obs_b}\frac{1}{\sqrt{\sigma_a^2+\sigma_b^2}}exp\left(-\frac{\{[Tobs_a(X)-Tobs_b(X)]-[TTcalc_a(X)-TTcalc_b(X)]\}^2}{\sigma_a^2+\sigma_b^2}\right)\right]^N \tag{3.8}$$

where Tobs_a and Tobs_b are the observed arrival times, TTcalc_a and TTcalc_b are the calculated travel times for two observations obs_a and obs_b, and N is the total number of observations.

Weighted

It is possible to weight the stations in *NonLinLoc* so that they are all equally weighted. The EDT and GAU methods both apply a weighting to the stations which represents how the observation contributed to the maximum likelihood hypocenter. With the Gaussian method the travel time error is fixed using the LOCGAU command, but varies with observation travel time. To allow the stations to be equally weighted, the location method can be set to GAU and the CorrLen set to equal zero, resulting in no travel time error being applied. This resulted in all stations showing a weighting of 1.

3.4 Summary

This chapter gives an oversight to the main location algorithms used in earthquake location, and how these differ mathematically. *Hypocenter* is the location method currently used by the Montserrat Volcano Observatory for locating earthquakes on Montserrat, and uses a linearised mathematical approach. Whereas, *NonLinLoc* is an example of another location method, which uses a non-linearised approach. The mathematics behind both of these methods are explored in detail to help understand the differences between them, and the advantages of using different methods. *Hypocenter* and variations of *NonLinLoc* (GAU, EDT and Weighted) are used in Chapter 4 to compare different location methods and velocity models, to understand if the current location method on Montserrat can be improved.

Chapter 4

Comparison of Location Methods

4.1 Introduction

Location algorithms provide an estimate of an earthquake's hypocenter using several pieces of data. However, calculated locations will always be a best estimate due to there being too many unknowns to provide an absolute location. Location algorithms solve for four unknowns: origin time and X, Y, Z location. The user inputs arrival times at several seismic stations alongside an estimate of the seismic velocity structure for the local region. However, one of the fundamental uncertainties that impacts the earthquake's calculated location comes from the velocity model itself. This is also an estimate of the velocity structure and is rarely precisely known for a region. More often, a simplified 1D seismic velocity model is used for earthquake location. Some programs allow for more complex models in 2D and 3D, however these in themselves can add more uncertainties as they carry their own errors. Different velocity models will result in different calculated hypocenters, which could alter interpretations.

Several location methods are available ranging from basic triangulation used originally, to non-linear and linearised techniques (see Chapter 3). Each method will provide an estimate for the location and associated error for each earthquake, and these will differ slightly between location methods. Finally, the seismic arrival times that are collected can vary greatly between regions. Some areas are densely populated in seismic stations, resulting in good azimuthal coverage and a large amount of input data to further constrain hypocenters. However, some regions may be limited by the number of seismic stations that can be used, and more importantly the range of azimuthal coverage. For example, in Montserrat, it is

difficult to get stations along the SE due to the frequent number of PDC's and the lack of access to these areas (Figure 2.5).

There are several features that can impact the accuracy of locating earthquakes, and these can vary greatly between regions depending on the amount of pre-existing information known, and the availability/accessibility of seismic stations. It is therefore important that the station configuration and location methodology are tested to see if there are areas of poor accuracy in the region that may impact results, and therefore interpretations. This can also give an indication of how well the current methodology performs, and if this could be improved.

This chapter aims to compare several velocity models, location methods and seismic station configurations on Montserrat to understand which method optimises an earthquake's location by increasing the number of earthquakes whose locations can be trusted, whilst also reducing hypocenter errors so that locations can be used for interpretation. First the velocity model and location method are compared to see 1) how well the current setup on Montserrat works and what errors are associated with this, and 2) if this can be improved by changing the location method or using a different seismic velocity model. This new methodology is then used to compare different station configurations that have been active on Montserrat over the past 25 years, and if this ongoing evolution of station configurations has impacted located hypocenters, and therefore interpretations of the volcanic system.

4.1.1 Montserrat Volcano Observatory Methodology

The Montserrat Volcano Observatory (MVO) was established in October 1996 by several institutions after increased activity in July 1995 (*Aspinall et al.*, 2002). Several organisations, including USGS, had equipment including seismometers in place from the beginning of the eruption. However, it was not until October 1996 when MVO was established, that the main monitoring and data collection began. In January 2003, MVO was moved to its new permanent observatory based in Flemmings after several temporary locations due to Plymouth being destroyed by a Pyroclastic Density Current in 1997. MVO currently use a simple 1D seismic velocity model with the location program *Hypocenter* for earthquake location.

4.1.2 Velocity models

The current 1D seismic velocity model used by MVO is comprised of five layers, as shown in Figure 4.1, with the top layer of the velocity model corresponding to a height of 1.241 km. The velocity model was created using a starting model based on Guadeloupe before being adapted with trial and error modifications to make it applicable to Montserrat (*Power et al.*, 1998); the model does not take into account topography.

An additional three seismic velocity models of Montserrat (two 1D, and one 3D), are compared in this research to understand which model performs best at constraining seismicity on Montserrat (1D models are shown in Figure 4.1). *Rowe et al.* (2004) produced a 1D seismic velocity model using 3914 arrival times of shallow seismicity from July 1995 to September 1996, with the tomography program VELEST and Simul2000. Data from the SEA-CALIPSO project in 2007 was used to produce 1D and 3D seismic velocity models of Montserrat using active source seismology.

A 3D model by *Shalev et al.* (2010) was determined by P wave first arrivals at 58 stations on land and sea, and using the tomography code of *Shalev and Lees* (1998). This was then converted to a 1D model by *Miller* (2011), using the Levenberg-Marquarat non-linear minimisation procedure (*Press et al.*, 1992), and this accounts for the 1D SEA-CALIPSO model used in this study. The 3D seismic velocity model from *Paulatto et al.* (2012) was generated from over 4000 airgun shots with a mixture of 10 ocean bottom seismometers and 244 land seismometers taken from the SEA-CALIPSO project; the model was inverted using a tomography code from *Hobro et al.* (2003). The 3D velocity model takes into account topography, and is determined with spacing of 0.5 km (in X,Y and Z) extending to a depth of 10 km bsl.

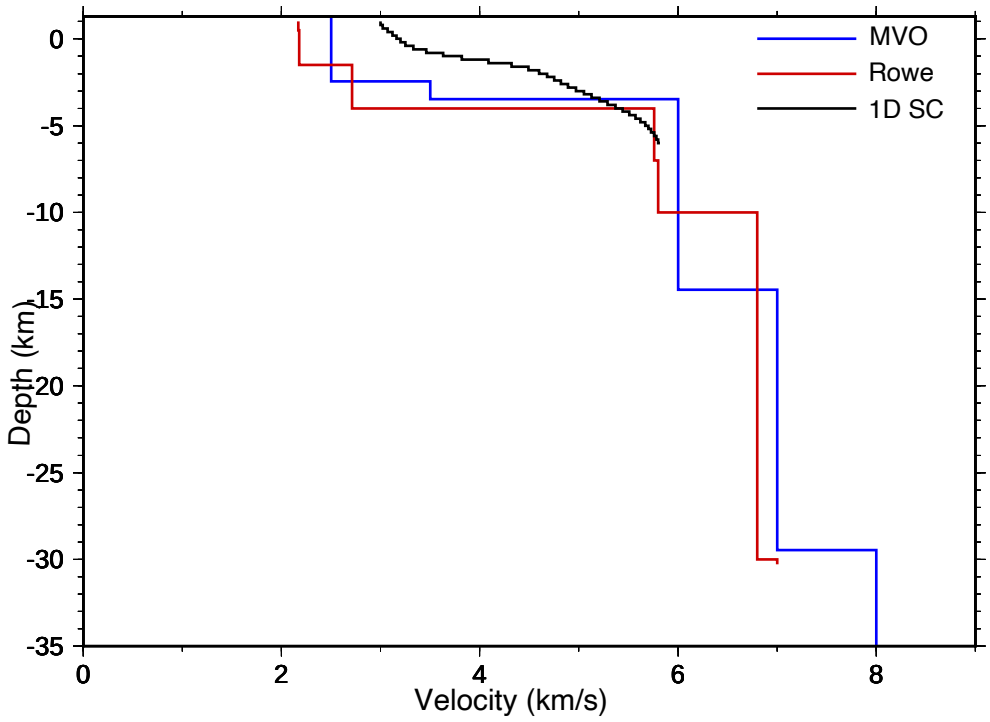

Figure 4.1: P wave seismic velocities for the three different 1D seismic velocity models tested. Blue line represents the velocity model currently used by the Montserrat Volcano Observatory. The red line is the velocity model proposed by *Rowe et al.* (2004), and the black line is the 1D velocity model created from the SEA-CALIPSO project in 2007 (*Shalev et al.*, 2010)

4.1.3 Station Variability

Station variability on Montserrat has varied considerably over the past 25 years, with a total of 31 seismic stations deployed since 1995 (excluding temporary stations), shown in Figure 2.5. Prior to October 1996 when BGS installed three-component broadband seismometers, only single component seismometers were available on the island. Station variability can have an impact on the accuracy and the associated errors of earthquake locations. By comparing the time series of stations and grouping together time periods when station layout was similar, ten time periods were formed, shown in Figure 4.2. For the time period July 1995 to September 1996, not all 16 stations were constantly active at any one time. However, not enough information is known for this time period to separate the section further. For the comparison of velocity models and location methods, the most current time period (December 2014–2018) was chosen as this represents the current configuration.

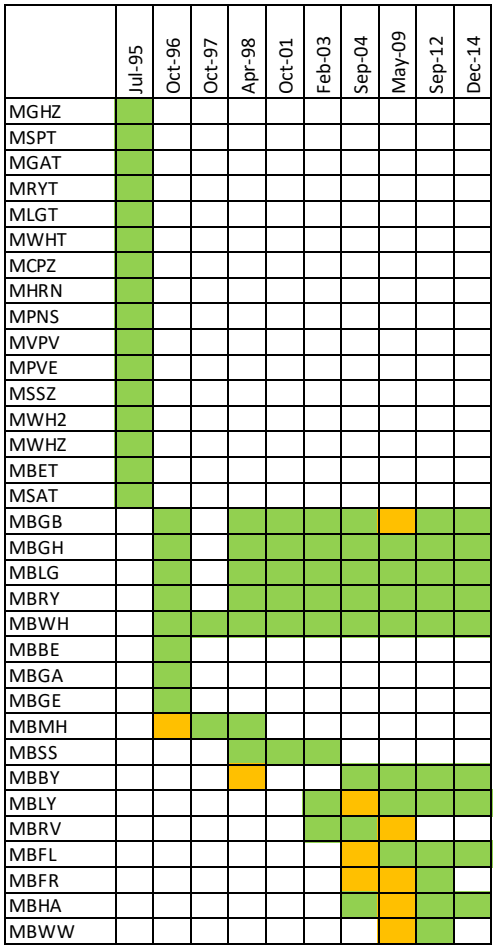

Figure 4.2: Station variability throughout the 10 times periods used in this study. Green represents when a station is fully active, and orange represents a station that was only active for some of the time period. Time periods range from date at top of table inclusive to the next time period (exclusive).

4.2 Methodology

Three main aspects that affect the accuracy of locating earthquakes are looked at: velocity model, location method and station configuration. Four velocity models, four location methods and ten time periods are tested and compared to decide which is the optimal setup for MVO in locating earthquakes on Montserrat. The ten time periods represent varying station configurations on Montserrat from 1995 to 2018, and can be seen in Section 4.1.3. The four velocity models that will be tested are shown in Section 4.1.2. Velocity models are inputted into each location method with the exception of *Hypocenter* which can not use 3D models in the location program. Each velocity model extends to a different depth, ranging from 6 to 35 km bsl. Extending or reducing the models so that they all extend to the same depth would create a false model that would not be representative of Montserrat. In order to test the applicability of the model the velocity models were kept with their current end depth. The velocity model is only important for depths shallower than the deepest earthquakes. On Montserrat, earthquakes are mostly shallower than 8 km, but events have been located up to 30 km.

Two location programs were used for this study: *Hypocenter* (*Lienert et al.*, 1986) which is currently used by MVO, and *NonLinLoc* (*Lomax*, 2001), which has been proven to work well in complex environments. Current MVO settings and parameters were used with the location method *Hypocenter*; this was to keep it consistent when comparing different velocity models and location methods to present day MVO locations. *NonLinLoc* has several search methods (GRID, Metropolis-Gibbs Random Walk, and Oct-Tree) and location methods (Gaussian Analytical and Equal Differential Time) that can be used when running the program. More information on the different location methods of *NonLinLoc* is explained in Section 3.3.4.

Multiple minima in the PDF are readily detected with the Grid and Oct-Tree method, but are more commonly missed by the Metropolis-Gibbs Random Walk (*Lomax and Curtis*, 2001). Test runs using the GRID search method with the synthetic data showed the method to be too computationally intensive; *Lomax and Curtis* (2001) shows the grid search to be 100 times more computationally expensive that the Oct-Tree algorithm. The Oct-Tree sampling method is known for its high efficiency and reliable mapping of Probability Density

Functions (PDF) (*Lomax*, 2001; *Mostaccio et al.*, 2005, 2013; *Turino et al.*, 2009). Therefore the Oct-Tree sampling method was chosen as the search method for *NonLinLoc* for all three variations. Three different location methods were used in *NonLinLoc* for relocation with the Oct-Tree search algorithm: Equal Differential Time (EDT) likelihood function, Gaussian Analytical approach, and a weighted method using the Gaussian Analytical search method but forcing all stations to be weighted equally.

All earthquakes were located using the UTM 20N projection grid so that errors were reduced when transforming between Cartesian and Geographic co-ordinate systems during relocation. This was shown to have a small effect on overall locations, on average reducing errors by 50 m (Appendix A).

4.2.1 Synthetic Earthquakes

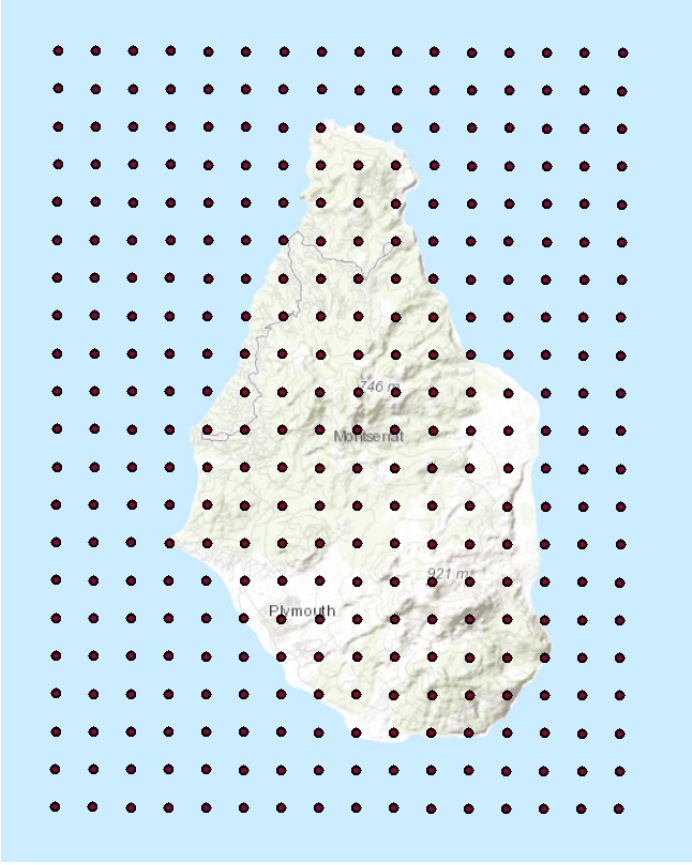

Figure 4.3: Location of the synthetic earthquakes used for relocation: synthetic earthquakes are spaced 1 km apart and cover a 15 by 20 km grid.

To compare relocations from each velocity model and location method, a 15 by 20 km grid of synthetic earthquakes was created over Montserrat, shown in Figure 4.3. Synthetic

earthquakes were generated every 1 km resulting in a total of 336 synthetic earthquakes. Changing the depth of the synthetic earthquakes forces the ray paths to pass through different layers of the velocity model, improving the tests on velocity models and station configuration. Synthetic earthquakes were set at depths of 0.5 km asl, 0, 1, 3, 5, 5.8 and 10 km bsl to make sure that the velocity model was adequately sampled throughout. Depths of 1 and 3 km were chosen due to the majority of seismicity being located at these depths beneath Soufrière Hills Volcano. A depth of 5.8 km bsl was chosen to test the 1D SEA-CALIPSO model when earthquakes were positioned near the edge of the velocity model, due to the model only extending to a depth of 6 km.

Synthetic P and S wave arrival times were calculated to each synthetic earthquake from the active seismic stations in that time period, for each of the velocity models, using the predetermined travel time grids. The synthetic arrival times did not include any picking errors, or noise when calculating the travel times, and hence represent optimal travel times. Synthetic arrival times were then used to relocate the synthetic earthquakes using each velocity model, location method and time period (representing station configuration). A schematic of this procedure is shown in Figure 4.4.

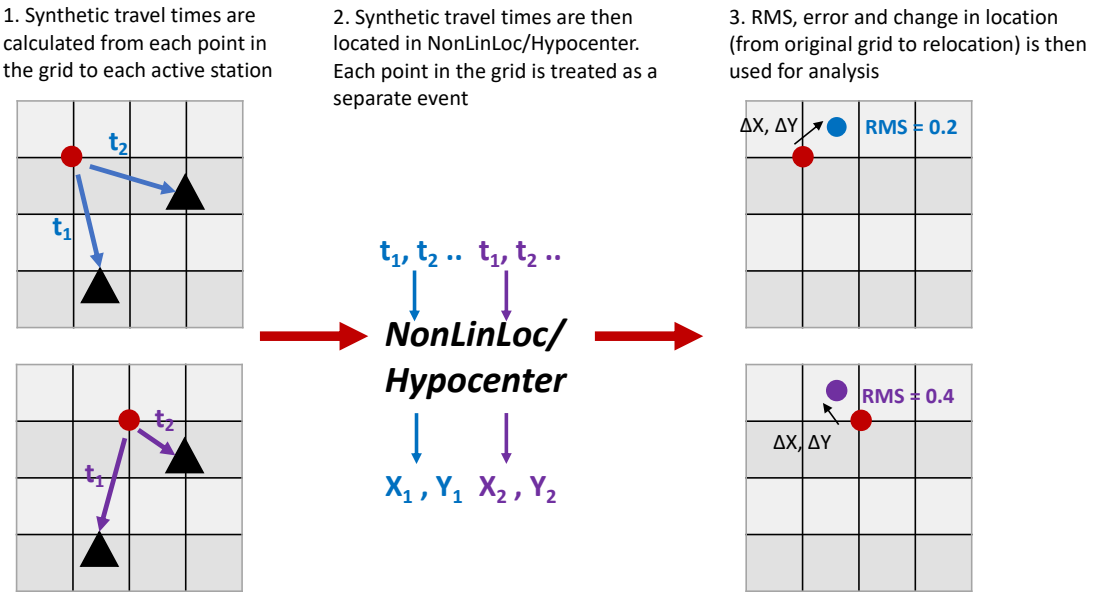

Figure 4.4: Schematic explaining the methodology used to relocate the synthetic earthquakes. The red dot represents the synthetic grid location, with the blue and purple dot representing the relocated hypocenter. t_1 and t_2 are travel times from each station, and X_1, Y_1, and X_2, Y_2 are the relocated locations for each synthetic earthquake.

4.2.2 Time2EQ calculation

Arrival times were calculated from all active stations to each synthetic earthquake in the grid using the TIME2EQ function in *NonLinLoc*. This is calculated by looking up the location of the synthetic earthquake in the pre-created travel time grids which are produced for each station, and reading the time it would take to get to that station.

Travel time grids are created for each station and contain travel times from that station to every point in a pre-defined X,Y,Z grid. These are saved in a sub-folder so that they do not need to be generated for each location. The travel time grids are created using the *Grid2Time* function in *NonLinLoc*, which uses the Eikonal finite-difference scheme of *Podvin and Lecomte* (1991). This uses a systematic application of Huygens principle with finite difference approximation. The method takes into account varying propagation modes and local discontinuities when calculating travel times; it is also very robust compared to other techniques and therefore performs well with complex velocity models (*Podvin and Lecomte*, 1991). Although these tools are built into *NonLinLoc* they are not using *NonLinLoc*'s search method and therefore can be used to calculate arrival times for the synthetic data which can be inputted into both *Hypocenter* and *NonLinLoc*.

4.2.3 Trusting Earthquakes

To compare how well the synthetic earthquakes were relocated with each method and velocity model, a parameter was created to test if the relocated earthquakes could be trusted. This looked at the distance that the relocated earthquake moved compared to the original synthetic location, and whether this distance was within the error calculated for that individual event. A trusted event is an earthquake that is relocated to a location within the error calculated — ie the 68% confidence ellipsoid covers the original synthetic location. This error is calculated by each location method. Whereas an untrusted location is an earthquake that is relocated to a distance greater than the calculated error. This is shown in Figure 4.5.

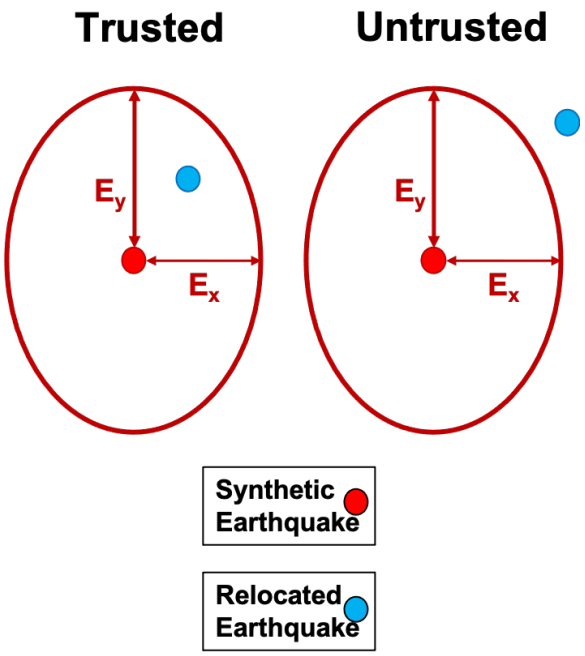

Figure 4.5: Schematic showing the criteria for True (trusted) and False (untrusted) relocated earthquakes. The red ellipsoid shows the 68% confidence ellipsoid, with the earthquakes being compared to the X,Y, Z calculated errors.

4.2.4 Measures of Uncertainty

RMS

RMS is calculated by *NonLinLoc* and *Hypocenter* and is stored inside the hypocenter files created for each event. The RMS is defined as the 'root-mean-square of time residuals at maximum likelihood or expectation hypocenter' (*Lomax et al.*, 2009), where the residual is the difference between the predicted and calculated travel times, shown in Equation 4.1.

$$X_{rms} = \sqrt{\frac{1}{n}(X_1^2 + X_2^2 ... X_n^2)} \tag{4.1}$$

where n is the number of travel times used in the calculation, and X is the residual. The residual is t - t_o - ie the actual travel time (observed) minus the predicted travel time.

Covariance calculation

Covariance values: CovXX, CovYY and CovZZ are outputted in the Statistics line of hypocenter files (.hyp) produced by *NonLinLoc*. *Hypocenter* produces errors in the files in terms of E_h, E_x and E_z. These can be converted to covariances in XX, YY and ZZ using the following equations:

$$CovXX = (E_x)^2 \tag{4.2}$$

$$CovYY = \sqrt{(E_h)^2 - (E_x)^4)} \tag{4.3}$$

$$CovZZ = (E_z)^2 \tag{4.4}$$

Hypocenter Error

The error was calculated using the following equations, taken from *Lomax* (2001):

$$X_{error} = \frac{\sqrt{(3.53 * CovXX)}}{2} \tag{4.5}$$

$$Y_{error} = \frac{\sqrt{(3.53 * CovYY)}}{2} \tag{4.6}$$

$$Z_{error} = \frac{\sqrt{(3.53 * CovZZ)}}{2} \tag{4.7}$$

where CovXX, CovYY and CovZZ are the covariance values of the PDF calculated by *NonLinLoc*. These equations were also used to calculate error for *Hypocenter* locations using CovXX, CovYY and CovZZ calculated in section 4.2.4. This was used to keep the errors compared between *NonLinLoc* and *Hypocenter* consistent.

4.3 Results

4.3.1 Analysis of Location Data

When comparing velocity models and location methods, only the station configuration representing December 2014 to January 2020 was used. This allows the most accurate velocity model and location method for Montserrat to be chosen, before looking at the impact of station configuration on earthquake location. This time period was chosen as this represented MVO's station configuration in 2020 and therefore would aid in any recommendations given to MVO's data processing.

The mean values calculated for RMS, and change in location (X,Y,Z) for each relocation are shown in Figure 4.6, and the mean errors for each relocation are shown in Figure 4.7. Errors relate to the outputted hypocenter errors produced by each program, converted to the same type of error using the equations shown in Section 4.2.4. The light green cells represent the lowest value for each variable per depth (looking at both velocity model and location method). The Rowe and 1D SEA-CALIPSO velocity models produce the lowest mean values (for RMS, change in location and error), accounting for 47% and 33% of the relocations respectively. The Rowe model performs better at shallower depths of 0 and 1 km, whereas the 1D SEA-CALIPSO performs better at greater depths — although this is limited to a maximum depth of 6 km bsl.

The weighted *NonLinLoc* method produces the lowest errors consistently out of all of the location methods, although this is only a small difference (order 10 m) from the GAU *NonLinLoc* search method. The lowest RMS values are shown with the EDT *NonLinLoc* search method. Mean changes in location for X, Y, and Z show that the EDT *NonLinLoc* and GAU *NonLinLoc* search methods produce 43% and 33% of the lowest values respectively. The mean change in location for Gaussian, EDT and weighted vary by tens of metres per model; this is looked at in more detail in section 4.3.3. The *Hypocenter* location method with the MVO velocity model consistently underperforms and all velocity models used with *Hypocenter* show higher RMS, changes in location and errors compared to other location methods in *NonLinLoc*.

Figure 4.8 shows the percentage of earthquakes that were classified as 'trusted' using the

definition in section 4.2.3 for each relocation. This has been coloured to highlight relocations with the highest amount of trusted locations, with dark green representing 90% of locations that are trusted, and orange representing 60%. Red boxes highlight the search method and velocity model that produce the highest percentage of trusted locations for each depth.

The EDT *NonLinLoc* method has the highest percentage of trusted locations (mostly over 80%) with the majority of velocity models and depths. The MVO model with the location method *Hypocenter* performs well for X and Y locations but produces a low percentage of trusted earthquakes for the Z location. The 1D SEA-CALIPSO model with the *NonLinLoc* EDT method performs best overall, however it cannot be used for depths greater than 6 km bsl. The 3D model has more trusted locations when using the EDT *NonLinLoc* method compared to the Rowe and MVO model. However, the 3D model produces larger errors equal to 200 m compared to other models, and this is likely the reason that there is a greater percentage of trusted locations.

			Velocity Model																									
			0.5hkm				0km				1km				3km				5km				5.8km				10km			
			MVO	Rowe	1D SC	3D	MVO	Rowe	1D SC	3D	MVO	Rowe	1D SC	3D	MVO	Rowe	1D SC	3D	MVO	Rowe	1D SC	3D	MVO	Rowe	1D SC	3D	MVO	Rowe	1D SC	3D
RMS	HYPO	MVO settings	0.094	0.794	0.123	X	0.095	0.746	0.129	X	0.093	0.588	0.136	X	0.100	0.300	0.146	X	0.092	0.154	0.150	X	0.091	0.149	0.151	X	0.090	0.152	X	X
	NonLinLoc	GAU OCT	0.089	0.089	0.088	0.095	0.088	0.088	0.088	0.094	0.088	0.088	0.088	0.095	0.088	0.088	0.088	0.095	0.088	0.088	0.088	0.093	0.088	0.088	0.090	0.093	0.088	0.088	X	0.117
		EDT OCT	0.081	0.081	0.081	0.081	0.081	0.081	0.081	0.081	0.081	0.081	0.081	0.081	0.081	0.081	0.081	0.081	0.081	0.081	0.081	0.081	0.081	0.081	0.083	0.081	0.081	0.081	X	0.082
		weighted	0.089	0.089	0.088	0.095	0.088	0.088	0.088	0.094	0.088	0.088	0.088	0.095	0.088	0.088	0.088	0.095	0.088	0.088	0.089	0.093	0.088	0.088	0.090	0.093	0.089	0.088	X	0.117
Loc X	HYPO	MVO settings	0.378	144.0	0.945	X	0.398	142.56	8.536	X	0.455	139.32	7.865	X	0.640	131.53	6.608	X	0.896	123.79	5.510	X	0.570	122.5	2.223	X	0.603	112.6	X	X
	NonLinLoc	GAU OCT	0.190	0.147	0.211	0.429	0.226	0.180	0.235	0.406	0.293	0.208	0.249	0.500	0.343	0.279	0.221	1.020	0.340	0.321	0.254	1.464	0.331	0.311	0.264	1.578	0.362	0.330	X	2.561
		EDT OCT	0.195	0.144	0.222	0.369	0.233	0.187	0.243	0.368	0.303	0.201	0.252	0.283	0.342	0.278	0.227	0.277	0.343	0.328	0.260	0.301	0.336	0.316	0.271	0.317	0.373	0.339	X	0.426
		weighted	0.191	0.147	0.214	0.426	0.226	0.181	0.235	0.412	0.294	0.208	0.249	0.501	0.345	0.278	0.221	1.024	0.335	0.321	0.254	1.465	0.327	0.313	0.264	1.580	0.361	0.330	X	2.568
Loc Y	HYPO	MVO settings	0.544	137.6	1.623	X	0.9352	137.88	1.8621	X	1.049	139.58	2.293	X	1.0789	144.93	2.8026	X	1.7612	151.86	3.1608	X	0.729	153.7	3.258	X	0.834	169.7	X	X
	NonLinLoc	GAU OCT	0.267	0.165	0.269	0.611	0.332	0.233	0.298	0.618	0.452	0.280	0.298	0.642	0.485	0.404	0.242	1.152	0.502	0.485	0.287	1.737	0.492	0.455	0.301	1.913	0.478	0.397	X	3.610
		EDT OCT	0.268	0.148	0.281	0.455	0.336	0.236	0.309	0.416	0.465	0.271	0.305	0.300	0.491	0.401	0.245	0.266	0.512	0.494	0.286	0.305	0.492	0.464	0.301	0.334	0.481	0.403	X	0.450
		weighted	0.267	0.167	0.269	0.607	0.331	0.233	0.298	0.603	0.455	0.279	0.298	0.643	0.485	0.403	0.242	1.156	0.495	0.485	0.287	1.737	0.477	0.444	0.301	1.911	0.471	0.398	X	3.649
Loc Z	HYPO	MVO settings	1.283	1.113	3.686	X	2.9412	0.6503	4.1905	X	3.464	1.3649	3.3524	X	3.8414	3.2214	1.8149	X	1.9598	5.161	0.9801	X	1.428	5.886	0.936	X	1.012	9.435	X	X
	NonLinLoc	GAU OCT	1.116	0.993	0.996	1.435	0.537	0.324	0.343	0.388	0.590	0.284	0.452	0.751	0.806	0.578	0.433	1.247	1.059	0.954	0.459	1.488	1.010	0.976	0.289	1.657	0.521	0.434	X	0.351
		EDT OCT	1.101	0.993	0.997	0.996	0.524	0.314	0.350	0.114	0.613	0.269	0.453	0.307	0.816	0.574	0.443	0.446	1.060	0.967	0.462	0.613	1.016	0.999	0.291	0.653	0.525	0.442	X	0.350
		weighted	1.112	0.993	0.991	1.434	0.535	0.322	0.343	0.383	0.591	0.283	0.452	0.750	0.800	0.578	0.434	1.244	1.055	0.952	0.457	1.484	0.991	0.977	0.286	1.656	0.512	0.433	X	0.354

Figure 4.6: Table shows mean RMS and change in X, Y and Z location of the 336 relocated earthquakes for each relocation for the time period December 2014 to February 2018. Green cells highlight lowest value for that depth and variable. 1D SC represents 1D SEA-CALIPSO; 3D represents the 3D SEA-CALIPSO model; GAU EDT represents Gaussian Analytical Oct-Tree; EDT OCT represents Equal Differential Time Oct Tree; and weighted is the Gaussian Weighted method with Oct-tree.

			Velocity Model																									
			0.5hkm				0km				1km				3km				5km				5.8km				10km			
			MVO	Rowe	1D SC	3D	MVO	Rowe	1D SC	3D	MVO	Rowe	1D SC	3D	MVO	Rowe	1D SC	3D	MVO	Rowe	1D SC	3D	MVO	Rowe	1D SC	3D	MVO	Rowe	1D SC	3D
Error X	HYPO	MVO settings	1.212	51.378	0.661	X	1.244	51.866	0.658	X	1.032	50.676	0.636	X	0.804	49.764	0.640	X	0.714	40.571	0.663	X	1.626	42.381	0.676	X	1.597	40.782	X	X
	NonLinLoc	GAU OCT	0.289	0.239	0.355	0.499	0.308	0.263	0.375	0.512	0.346	0.297	0.396	0.612	0.475	0.390	0.417	0.626	0.487	0.456	0.453	0.702	0.502	0.469	0.470	0.743	0.632	0.593	X	1.016
		EDT OCT	0.342	0.291	0.428	0.653	0.362	0.316	0.449	0.677	0.412	0.354	0.464	0.552	0.560	0.469	0.490	0.548	0.564	0.530	0.539	0.607	0.585	0.545	0.563	0.641	0.773	0.723	X	0.899
		weighted	0.284	0.235	0.348	0.494	0.302	0.258	0.369	0.506	0.340	0.292	0.388	0.606	0.466	0.383	0.407	0.615	0.476	0.446	0.442	0.690	0.490	0.458	0.457	0.729	0.617	0.578	X	0.995
Error Y	HYPO	MVO settings	1.402	51.459	0.914	X	1.015	51.893	0.913	X	0.992	50.773	0.915	X	0.995	49.730	0.933	X	0.976	40.630	0.952	X	1.446	42.394	0.962	X	1.143	40.772	X	X
	NonLinLoc	GAU OCT	0.349	0.262	0.377	0.582	0.384	0.305	0.401	0.611	0.407	0.335	0.427	0.687	0.541	0.434	0.449	0.671	0.580	0.524	0.493	0.734	0.611	0.548	0.518	0.783	0.844	0.758	X	1.037
		EDT OCT	0.407	0.332	0.444	0.756	0.435	0.367	0.467	0.791	0.464	0.389	0.489	0.576	0.619	0.504	0.532	0.532	0.660	0.599	0.602	0.609	0.701	0.630	0.637	0.654	1.034	0.934	X	0.965
		weighted	0.345	0.258	0.370	0.577	0.380	0.301	0.394	0.604	0.402	0.331	0.420	0.678	0.533	0.428	0.439	0.662	0.571	0.516	0.482	0.722	0.604	0.540	0.507	0.771	0.838	0.750	X	1.017
Error Z	HYPO	MVO settings	1.782	1.467	1.140	X	4.135	1.767	1.015	X	3.311	1.560	0.908	X	0.907	1.726	0.897	X	0.791	2.349	0.892	X	2.397	2.538	0.882	X	2.145	2.218	X	X
	NonLinLoc	GAU OCT	0.522	0.344	0.410	0.153	0.570	0.390	0.491	0.183	0.513	0.352	0.589	0.338	0.730	0.442	0.750	0.675	0.903	0.777	0.685	1.046	0.982	0.856	0.595	1.171	1.280	1.250	X	1.285
		EDT OCT	0.598	0.414	0.496	0.205	0.642	0.465	0.591	0.342	0.597	0.441	0.687	0.570	0.824	0.529	0.864	0.786	0.964	0.831	0.842	0.952	1.059	0.915	0.772	1.005	1.646	1.558	X	1.184
		weighted	0.519	0.343	0.406	0.151	0.568	0.388	0.487	0.180	0.507	0.347	0.585	0.333	0.726	0.438	0.741	0.668	0.898	0.773	0.676	1.036	0.977	0.850	0.587	1.164	1.266	1.235	X	1.271

Figure 4.7: Table shows mean error of the 336 relocated earthquakes for each relocation for time period December 2014 to February 2018. Green cells highlight lowest value for that depth and variable. 1D SC represents 1D SEA-CALIPSO; 3D represents the 3D SEA-CALIPSO model; GAU EDT represents Gaussian Analytical Oct-Tree; EDT OCT represents Equal Differential Time Oct-Tree; and weighted is the Gaussian Weighted method with Oct-Tree

		MVO Hyp	Rowe Hyp	1D SC Hyp	MVO OCT GAU	Rowe OCT GAU	1D SC OCT GAU	3D OCT GAU	MVO OCT EDT	Rowe OCT EDT	1D SC OCT EDT	3D OCT EDT	MVO Weighted	Rowe Weighted	1D SC Weighted	3D Weighted
	x	86.90	10.42	55.06	84.52	82.44	84.82	65.18	88.69	88.39	91.37	86.61	82.44	82.74	84.23	64.29
	y	92.86	14.88	51.79	81.85	82.74	79.17	58.63	87.50	89.29	85.71	84.52	80.36	81.25	78.57	59.52
0.5hkm	z	86.90	10.42	55.06	84.52	82.44	84.82	65.18	88.69	88.39	91.37	86.61	82.44	82.74	84.23	64.29
	x	83.63	11.01	37.20	83.63	83.63	82.44	66.67	87.50	89.88	89.29	88.10	82.14	82.14	81.55	66.67
	y	95.54	14.58	45.83	80.65	81.25	75.89	61.01	85.71	86.61	81.85	86.90	80.36	80.06	75.60	61.31
0km	z	38.99	18.45	10.42	70.24	72.92	77.98	16.96	77.68	78.57	83.93	93.75	68.75	1.49	78.27	16.96
	x	78.87	11.61	27.98	81.25	82.44	79.46	65.48	86.90	90.77	88.10	91.67	79.76	81.55	77.38	64.58
	y	90.48	10.71	32.14	73.81	82.74	78.57	58.63	80.36	87.50	81.55	88.99	72.92	81.85	77.68	58.63
1km	z	25.60	14.58	10.12	77.08	84.82	73.51	11.31	84.23	89.88	80.06	86.01	76.79	84.82	74.11	10.71
	x	81.85	15.18	18.15	77.98	79.76	84.23	34.23	83.93	87.50	89.88	88.99	77.08	78.87	83.33	34.23
	y	75.30	5.36	21.13	74.70	69.35	83.33	26.79	77.98	76.19	89.29	88.10	74.11	69.05	82.14	25.89
3km	z	29.17	16.96	36.31	72.32	75.30	83.04	27.38	75.00	84.23	86.90	83.93	72.92	74.11	82.44	27.08
	x	73.51	13.39	16.37	77.38	77.38	84.82	25.89	83.33	82.44	88.99	88.39	76.19	76.49	83.63	25.60
	y	58.33	5.36	17.56	75.30	70.54	83.93	15.48	79.46	75.89	88.99	88.10	75.30	68.75	83.63	15.18
5km	z	63.10	21.13	62.80	55.06	48.21	75.60	38.69	57.74	50.89	84.52	78.87	55.95	47.92	75.89	37.80
	x	93.45	16.67	15.77	78.57	78.87	83.63	24.70	85.42	84.52	89.58	88.69	78.27	76.79	83.33	24.40
	y	78.27	5.36	15.77	76.19	73.81	83.93	17.56	82.14	80.36	89.88	86.31	77.08	74.70	83.93	16.37
5.8km	z	79.17	26.79	50.60	70.24	60.71	86.01	35.71	70.83	60.71	90.48	79.17	70.24	60.42	85.71	35.71
	x	95.24	16.96	X	83.33	85.42	X	22.32	89.58	88.69	X	89.88	81.85	84.52	X	22.32
	y	71.73	1.49	X	84.23	85.71	X	7.74	88.99	91.67	X	89.29	84.82	85.71	X	7.44
10km	z	84.23	6.55	X	86.90	86.90	X	94.05	95.54	95.54	X	93.45	86.61	85.71	X	93.75

Figure 4.8: Table shows the percentage of trusted earthquakes for the X,Y,Z location, for each velocity model and location method. Orange shows percentages higher than 60%, yellow higher than 70%, light green higher than 80% and dark green higher than 85%. The red outlined cells show the best velocity model/location method for that depth.

4.3.2 Error Testing

Error testing is plotted to show if there are areas of Montserrat which are impacted by using certain location methods or velocity models. An example of this is the error testing for the X location at 0 and 5 km depth shown in Figures 4.9 and 4.10 respectively. All the *NonLinLoc* search methods perform well with the three 1D models, with just a few untrusted locations. However, the 3D model produces more untrusted locations which is seen clearer at depths of 5 km; the *NonLinLoc* EDT method removes this effect producing a better coverage of trusted locations across the whole of the island. *Hypocenter* produces a low number of trusted locations for both the Rowe and the 1D SEA-CALIPSO models, which show a thick strip of trusted locations that run through the centre of Montserrat. The MVO model performs well with *Hypocenter*, with similar trusted locations to other *NonLinLoc* methods.

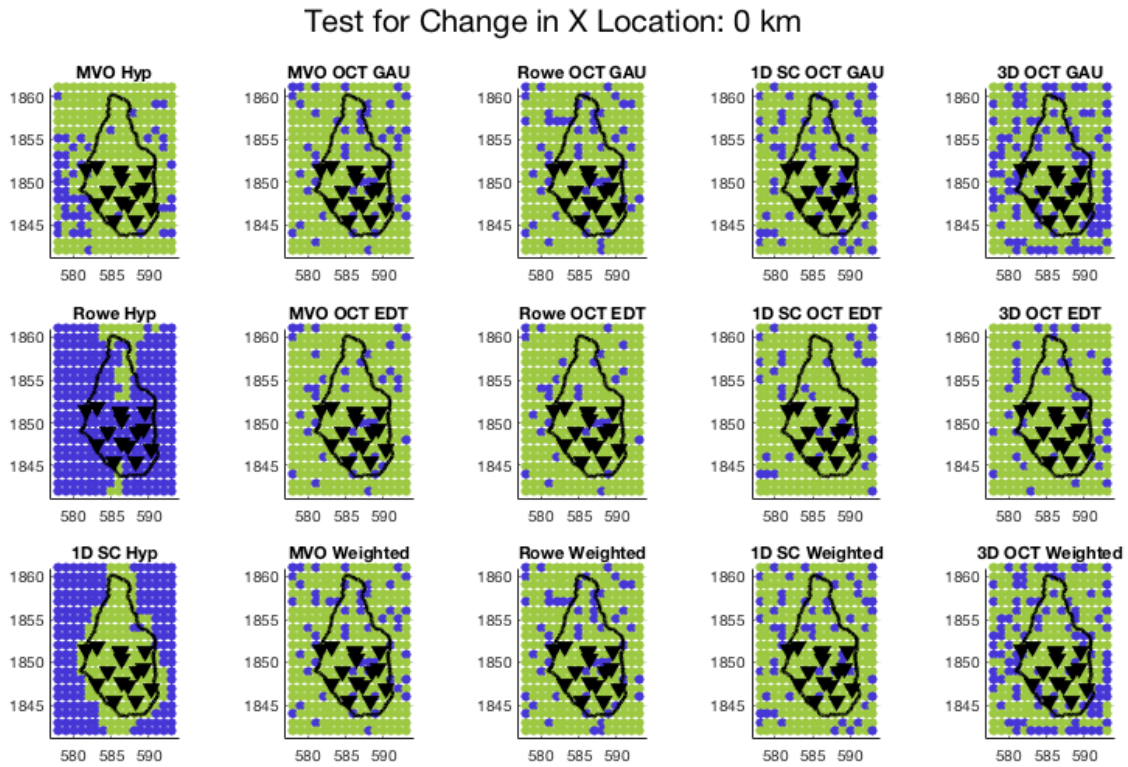

Figure 4.9: Error testing for the X location during the time period December 2014 to 2018 at 0 km depth. Green represents a trusted location, and blue represents an untrusted location. Inverted triangles represent seismic stations used in relocation. 1D SC represents 1D SEA-CALIPSO.

Error testing for the Y location shows similar results and patterns to the X and Z location. The Rowe model produces a high percentage of trusted locations at shallow depths for the

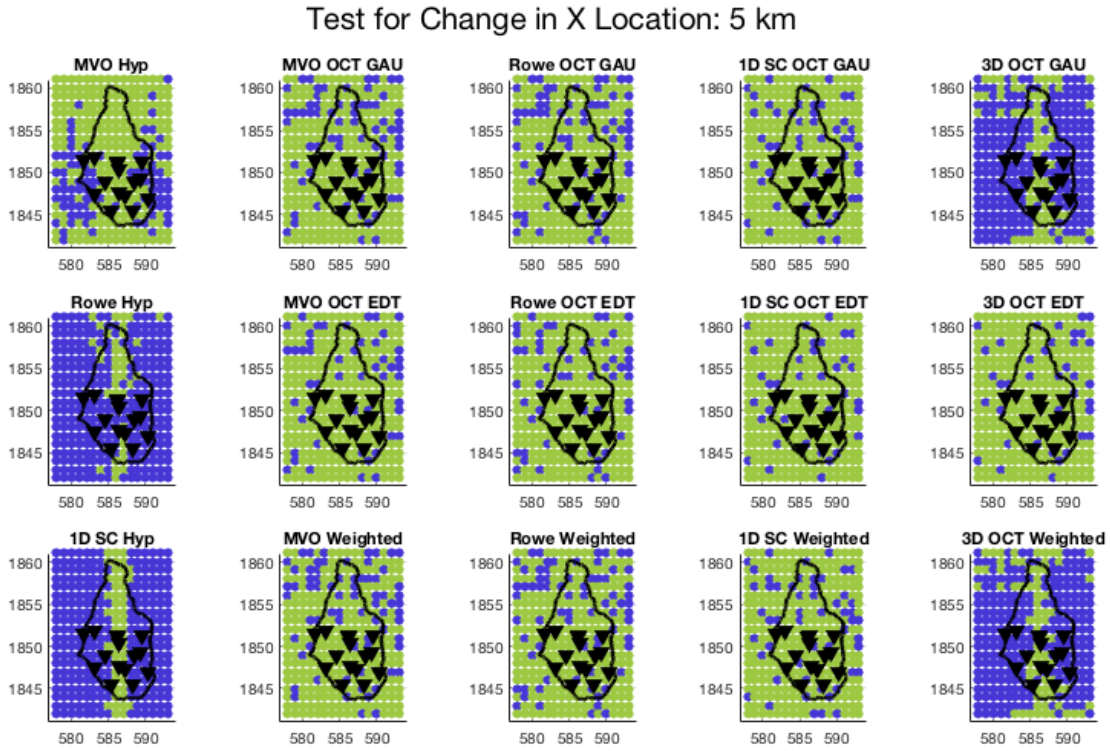

Figure 4.10: Error testing for the X location during the time period December 2014 to 2018 at 5 km depth. Green represents a trusted location, and blue represents an untrusted location. Inverted triangles represent seismic stations used in relocation. 1D SC represents 1D SEA-CALIPSO.

Z location (Figure 4.11), but does not perform as well with deeper earthquakes. At 5 km depth, the 1D SEA-CALIPSO model has a significant increase in trusted locations compared to the other models at this depth (Figure 4.12), which was also seen with the percentage of trusted earthquakes in Figure 4.8. The 3D model performs poorly for the Z location up to 5 km depth where a slight increase in trusted locations is recorded. *Hypocenter* also performs poorly for all models at shallow depths, but this improves with depths greater than 5 km.

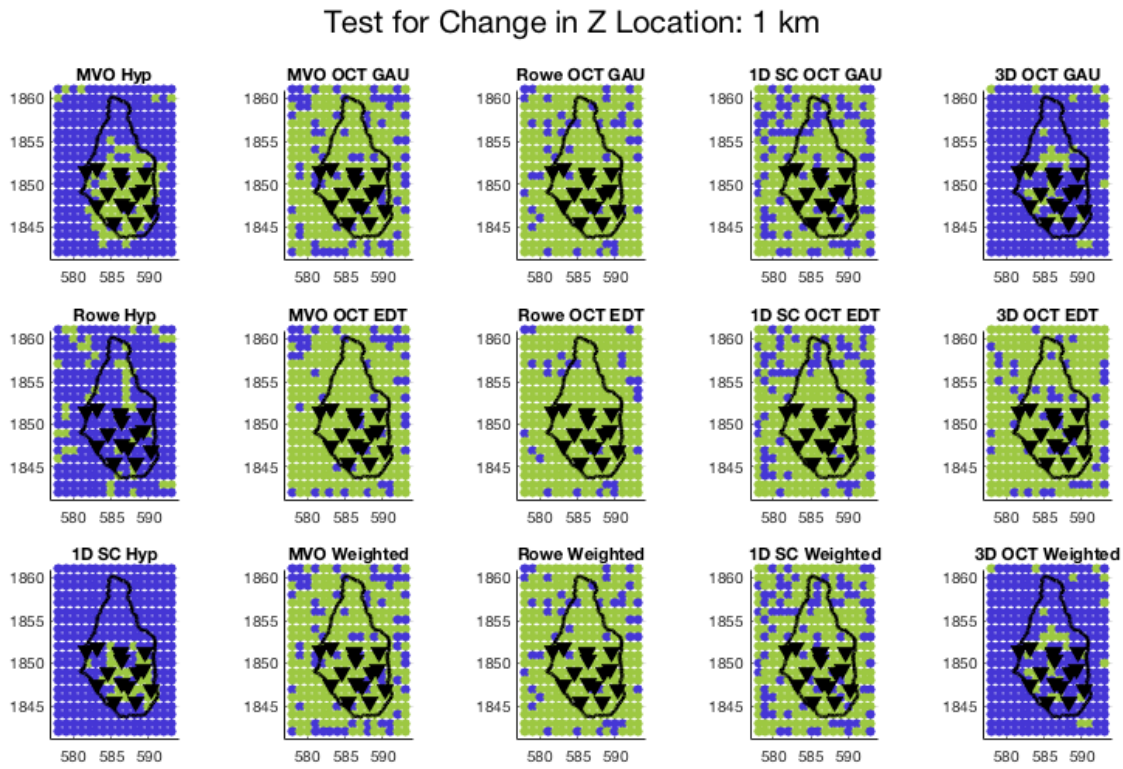

Figure 4.11: Error testing for the Z location during the time period December 2014 to 2018 at 1 km depth. Green represents a trusted location, and blue represents an untrusted location. Inverted triangles represent seismic stations used in relocation. 1D SC represents 1D SEA-CALIPSO

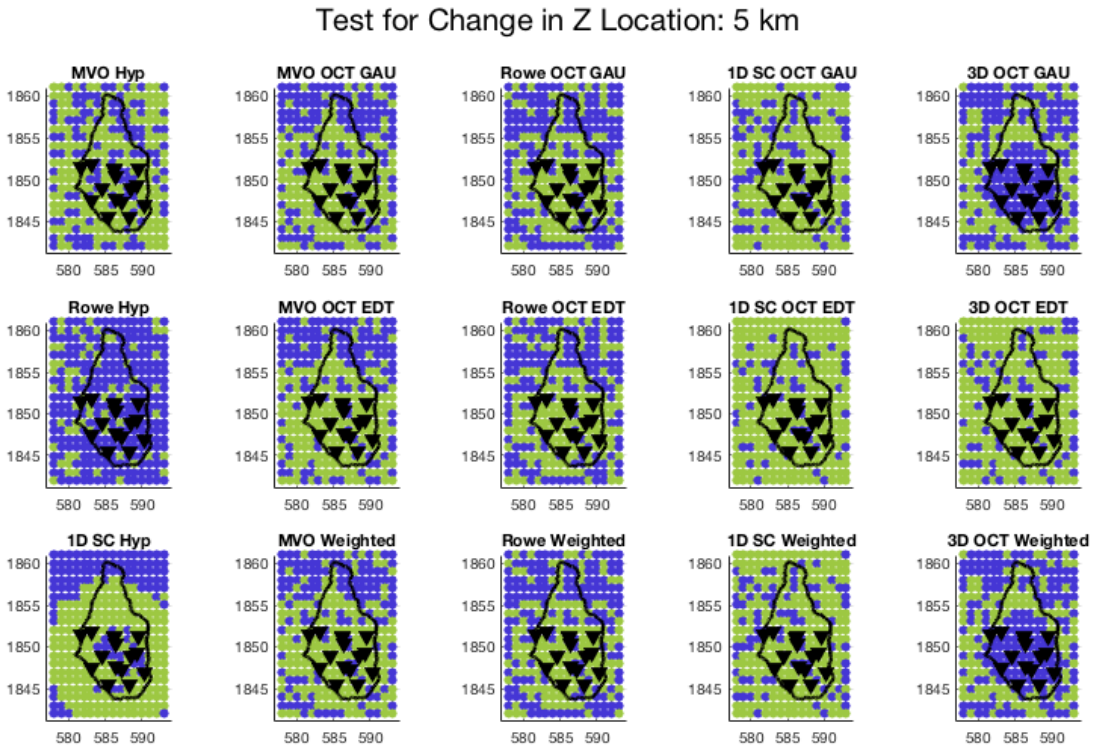

Figure 4.12: Error testing for the Z location during the time period December 2014 to 2018 at 5 km depth. Green represents a trusted location, and blue represents an untrusted location. Inverted triangles represent seismic stations used in relocation. 1D SC represents 1D SEA-CALIPSO

4.3.3 RMS, Change in Location and Error

Boxplots help to visualise the range of values attributed to either error or change in location; this can give more information when comparing different relocations. The range in RMS values for each velocity model and location method is shown in Figure 4.13. Relocations with *Hypocenter* have larger medians and ranges than relocations with *NonLinLoc*; this is very clear when used in conjunction with the Rowe model. Relocations in *NonLinLoc* have similar mean and ranges with all velocity models, with the EDT method producing slightly lower values. This same trend is seen at all depths.

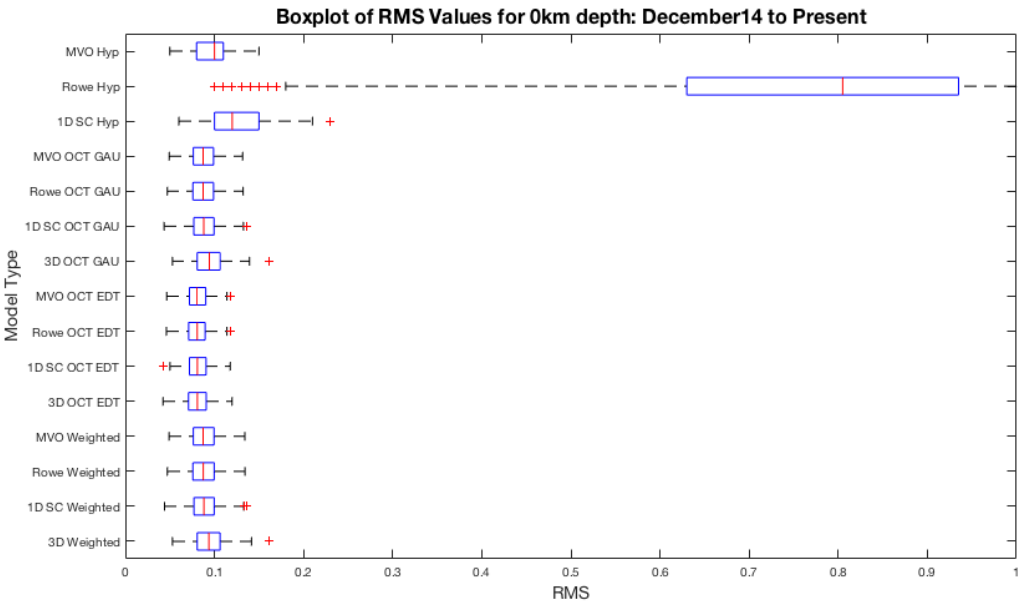

Figure 4.13: Boxplots of RMS values at 0 km depth for the time period December 2014 to February 2018. Red central line represents median, edges of box represent 25^{th} and 75^{th} percentile, black dashed line represents the range in values, and red crosses represent outliers. 1D SC represents 1D SEA-CALIPSO

The change in X location (between the original synthetic location and the relocated location) for 0 and 5 km depth is shown in Figure 4.14 and 4.15 respectively. Relocations with *Hypocenter* have a wide range of changes in location for all velocity models. This is also seen with the 3D model with all location methods in *NonLinLoc* at depths greater than 5 km. At 5 km depth the three 1D velocity models with *NonLinLoc* all have a similar median and range, with the 1D SEA-CALIPSO velocity model having marginally lower values. At 0 km depth, the Rowe and MVO velocity model have much smaller ranges and medians than the 1D SEA-CALIPSO velocity model. A similar pattern is seen for the

change in Y location.

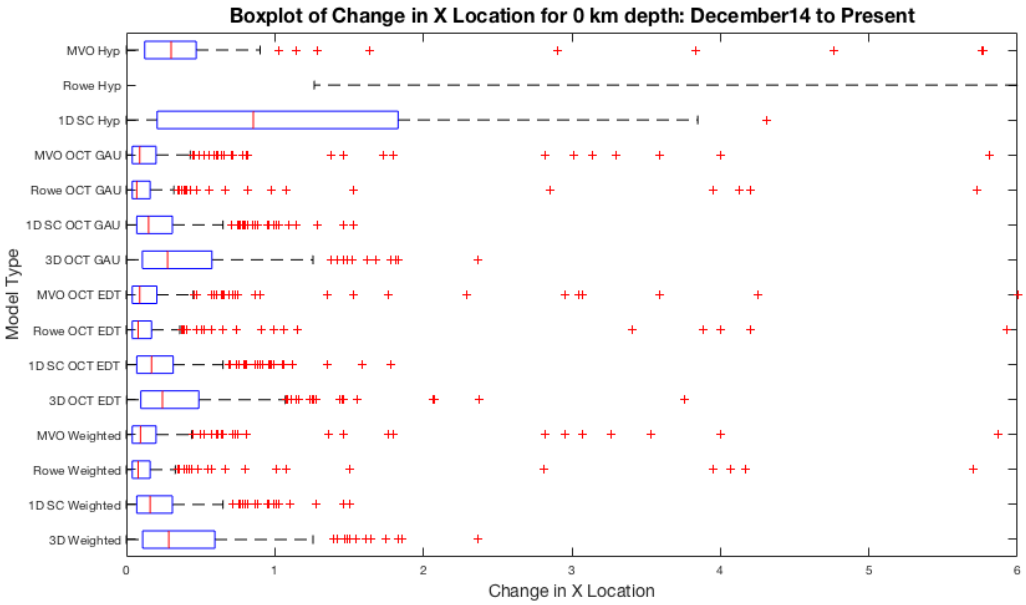

Figure 4.14: Boxplots of Change in X Location at 0 km depth for the time period December 2014 to February 2018. Red central line represents median, edges of box represent 25^{th} and 75^{th} percentile, black dashed line represents the range in values, and red crosses represent outliers. 1D SC represents 1D SEA-CALIPSO

The change in Z location had a similar pattern to the X and Y locations, with the median being lower for the majority of *NonLinLoc* relocations than with *Hypocenter* at 0 km depth. The change in Z location is more varied at depths of 5 km; the 1D SEA-CALIPSO model has a low mean and small range for all location methods, whereas the Rowe model has a larger range at greater depths.

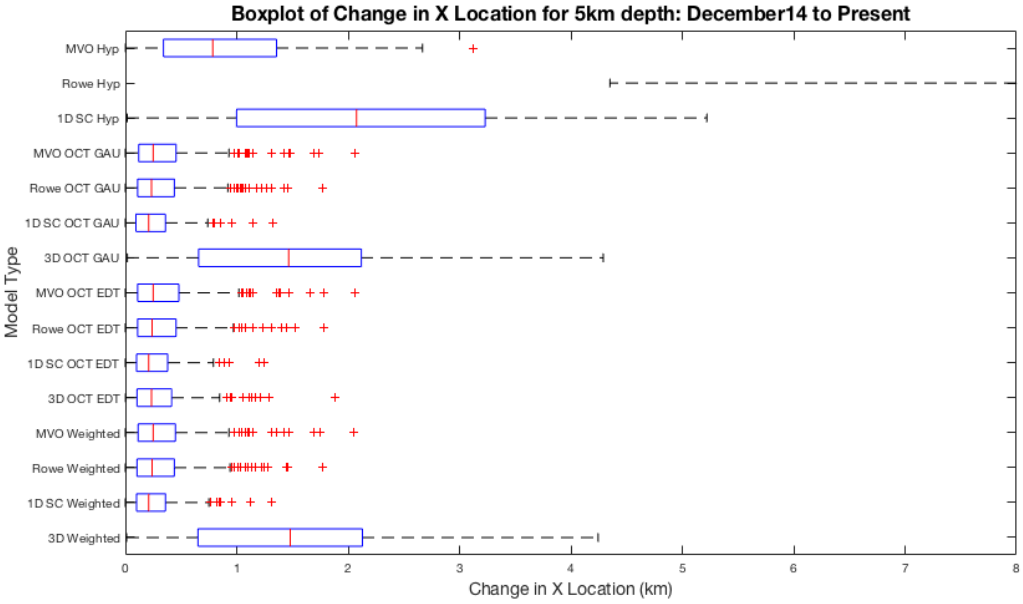

Figure 4.15: Boxplots of Change in X Location at 5 km depth for the time period December 2014 to February 2018. Red central line represents median, edges of box represent 25^{th} and 75^{th} percentile, black dashed line represents the range in values, and red crosses represent outliers. 1D SC represents 1D SEA-CALIPSO

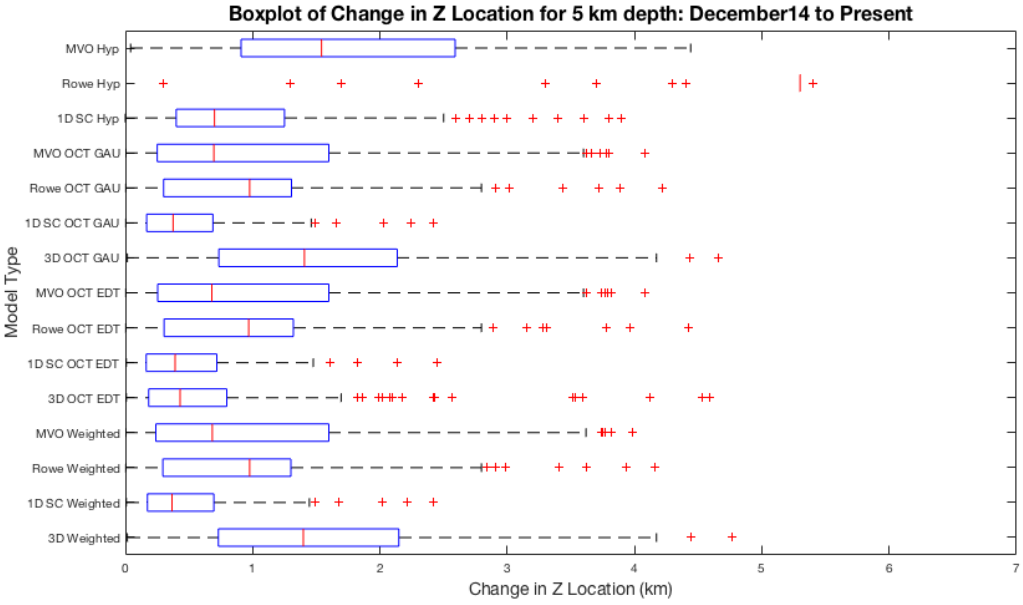

Figure 4.16: Boxplots of Change in Z Location at 5 km depth for the time period December 2014 to February 2018. Red central line represents median, edges of box represent 25^{th} and 75^{th} percentile, black dashed line represents the range in values, and red crosses represent outliers. 1D SC represents 1D SEA-CALIPSO.

Calculated X, Y and Z errors for relocations have similar results at all depths. *Hypocenter* relocations have consistently higher errors compared to *NonLinLoc* relocations for all velocity models. The MVO and Rowe velocity model have small median errors and ranges for the X error for all location methods at shallow depths (Figure 4.17). However, there is a large amount of outliers associated with these models compared to the 1D SEA-CALIPSO and 3D models. As the depth increases, the Rowe and 1D SEA-CALIPSO models show similar error ranges. The main difference with the Y error is at depths greater than 3 km: the 1D SEA-CALIPSO model produces smaller ranges in error compared to the Rowe model. However, the median value for the Rowe model is lower than the 1D SEA-CALIPSO model (Figure 4.18).

The 3D model produces consistently lower Z errors for all location methods (Figure 4.19). There is little difference between location methods within *NonLinLoc*, as the differences in error appear to be a result of the velocity model. The Rowe velocity model produces lower Z errors than the 1D SEA-CALIPSO model at all depths.

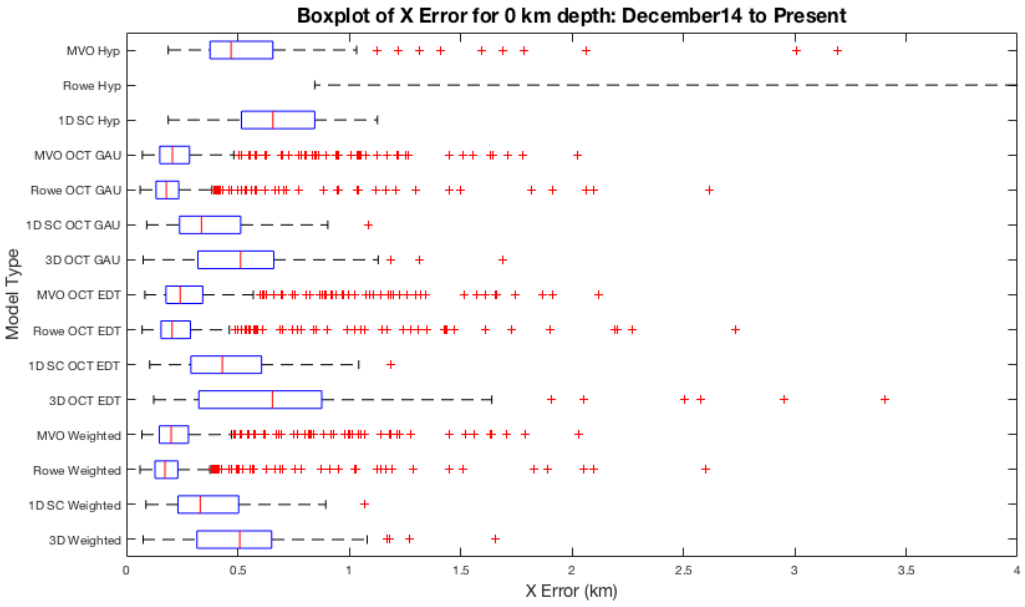

Figure 4.17: Boxplots of X Error at 0 km depth for the time period December 2014 to February 2018. Red central line represents median, edges of box represent 25^{th} and 75^{th} percentile, black dashed line represents the range in values, and red crosses represent outliers. 1D SC represents 1D SEA-CALIPSO

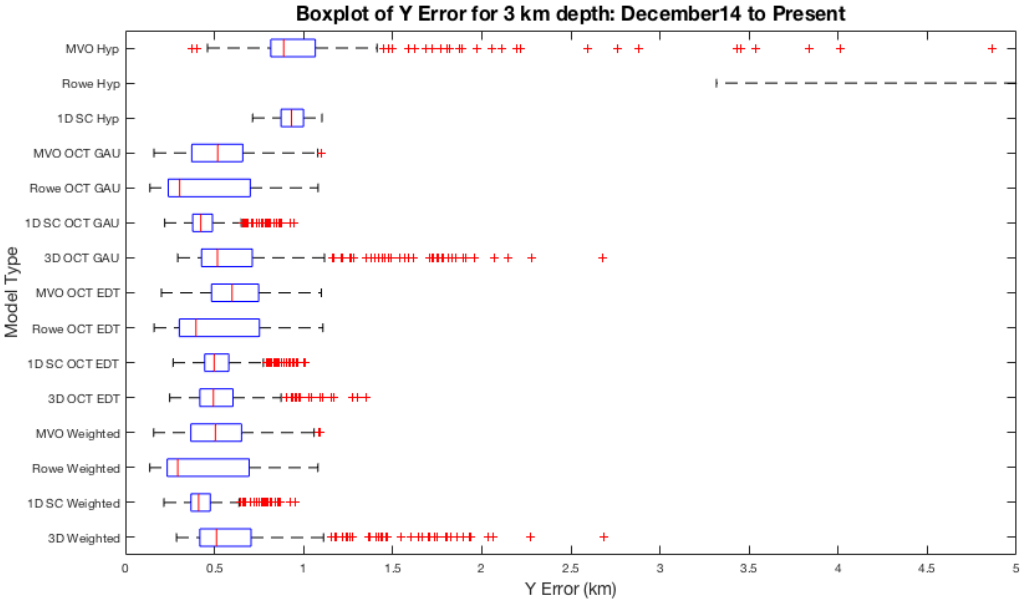

Figure 4.18: Boxplots of Y Error at 3 km depth for the time period December 2014 to February 2018. Red central line represents median, edges of box represent 25^{th} and 75^{th} percentile, black dashed line represents the range in values, and red crosses represent outliers. 1D SC represents 1D SEA-CALIPSO

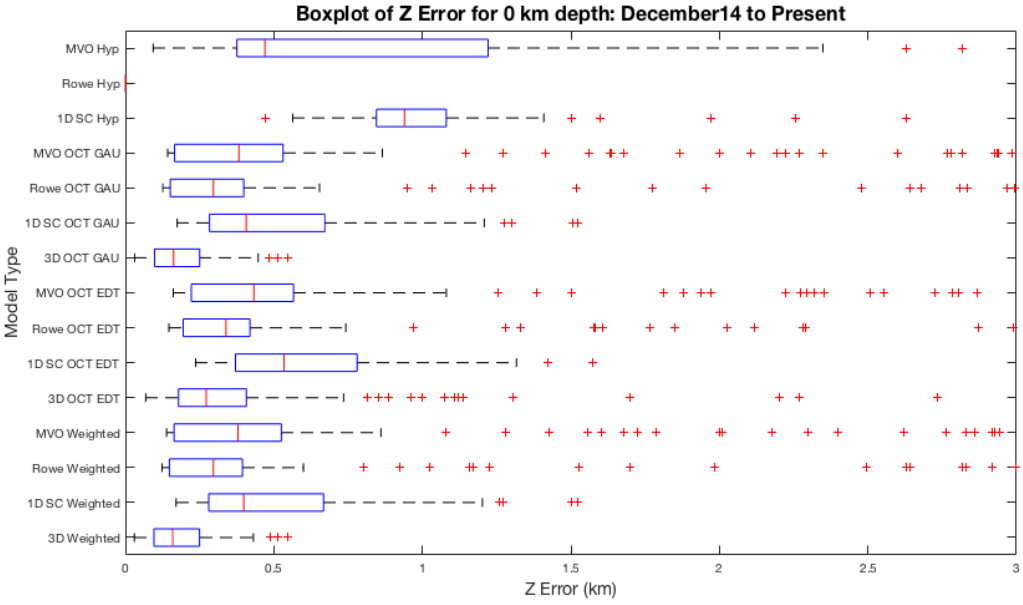

Figure 4.19: Boxplots of Z Error at 0 km depth for the time period December 2014 to February 2018. Red central line represents median, edges of box represent 25^{th} and 75^{th} percentile, black dashed line represents the range in values, and red crosses represent outliers. 1D SC represents 1D SEA-CALIPSO. Note: for the Rowe Hyp model, the majority of errors calculated were either 0 or 999km by Hypocenter. As a result the boxplot is centered around 0 km and therefore is not clearly seen.

4.3.4 Statistics

Comparison of relocations shows a variation between calculated errors and changes in locations when using different velocity models and location methods. To check that the results for each relocation were significantly different to each other, a Dunn statistical test was performed. This tests between each pair of relocations to calculate the probability of observing a randomly selected value from the first group that is larger than a randomly selected value from the second group. The Dunn test was used with the Berronni method and adjusted P values, which was computed in *R*. The Dunn test used data comprising of all synthetic earthquakes for four depths; 0,1,3 and 5 km, so that each model and method had 1344 points. The raw data for this can be found in Appendix C.

Figures 4.20 and 4.21 show if there is any significance between two sets of relocations for both change in location and error respectively. For example, the change in X location with the MVO model and *Hypocenter* method are significantly higher than the change in X location with the MVO model using the *NonLinLoc* EDT method. The significance means that if there is a statistical significance of 0.05 that the values are from the same datasets, ie, that the locations are significantly different between two methods.

Hypocenter has significantly higher changes in X,Y and Z locations compared to *NonLinLoc* for all velocity models, with the exception of the 3D model, where the MVO model with *Hypocenter* produces significantly lower values. The 3D model performs poorly with all location methods which is shown by having significantly greater changes in location compared to other velocity models. The Rowe model has significantly lower changes in locations compared to all other velocity models, especially when comparing with the 1D SEA-CALIPSO model.

Similar to changes in location, a significant increase in error is seen for all *Hypocenter* relocations compared to *NonLinLoc* (Figure 4.21). The Rowe model has significantly lower errors compared to other velocity models, although this is more clearly shown for the weighted and GAU *NonLinLoc* method. The trusted locations in Figure 4.8 show the EDT method to have the highest percentage of trusted locations, but Figure 4.21 shows the errors are significantly larger; this could be the reason more events were trusted.

Overall, the statistical test shows that the Rowe model produces significantly smaller

changes in locations and errors than other velocity models. However, Figures 4.20 and 4.21 are comparing all four depths at once. It is therefore important to run a statistical test per depth to make sure there are no differences in significance at each depth. This is particularly important given the 1D SEA-CALIPSO model has shown to be more suited at greater depths. The statistical test was run again separately at depths of 0, 1, 3 and 5 km.

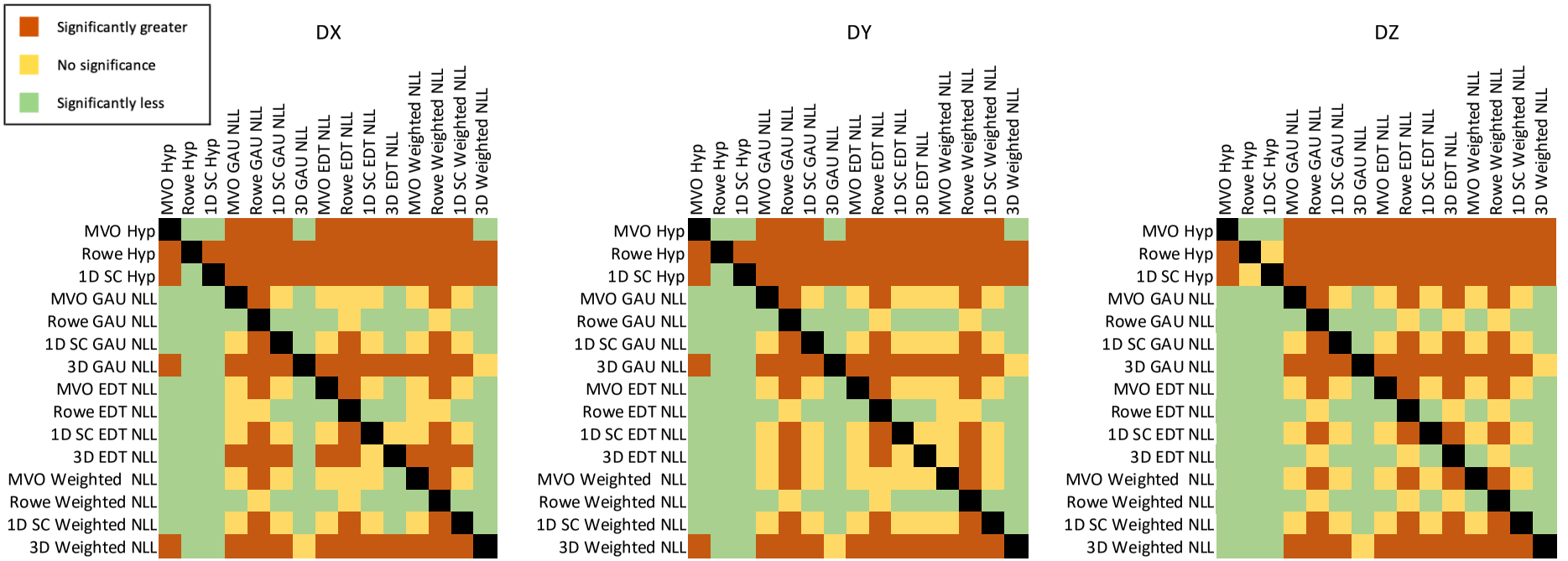

Figure 4.20: Significance checkerboards showing if different runs are more or less significant than other runs. To be read down (Y) and then across (X) when interpreting. Green represents Y is significantly less than X, Orange represents Y is significantly greater than X, and yellow means there is no statistical significance between the two runs. 1D SC represents 1D SEA-CALIPSO.

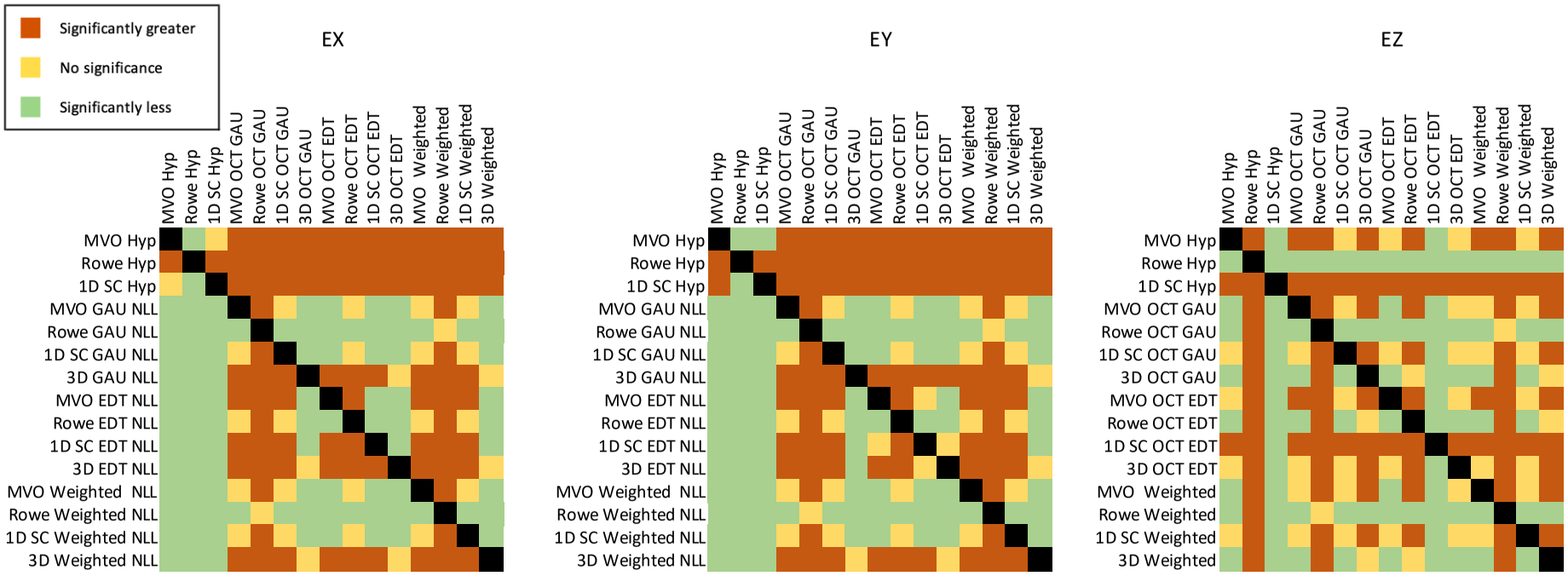

Figure 4.21: Significance checkerboards showing if different runs are more or less significant than other runs. To be read down (Y) and then across (X) when interpreting. Green represents Y is significantly less than X, Orange represents Y is significantly greater than X, and yellow means there is no statistical significance between the two runs. 1D SC represents 1D SEA-CALIPSO.

At 0 km depth (Figure 4.22), the MVO and Rowe model produce significantly smaller changes in X and Y location with *NonLinLoc* compared to the other velocity models. But, for the Z location, the 3D model with the EDT *NonLinLoc* method outperforms all other relocations. At all depths *Hypocenter* has significantly greater changes in location than the other location methods. The Rowe model has significantly lower changes in X, Y and Z location compared to the 1D SEA-CALIPSO and 3D model at 1 km depth; there is little difference between location method used with the Rowe model (Figure 4.23).

This changes at 3 km depth where the 1D SEA-CALIPSO model has significantly lower changes in X and Y location values than the MVO and 3D model (Figure 4.24). There is no significant difference seen between the 1D SEA-CALIPSO and Rowe model, suggesting that both models work adequately at this depth. The Rowe model has significantly lower changes in Z location compared to other velocity models at 3 km depth. At greater depths of 5 km there is no significant difference in X and Y location between the Rowe and 1D SEA-CALIPSO model (Figure 4.25). But the 1D SEA-CALIPSO model has significantly lower changes in Z location compared to the Rowe model, supporting the data in Section 4.3.3 and 4.3.2.

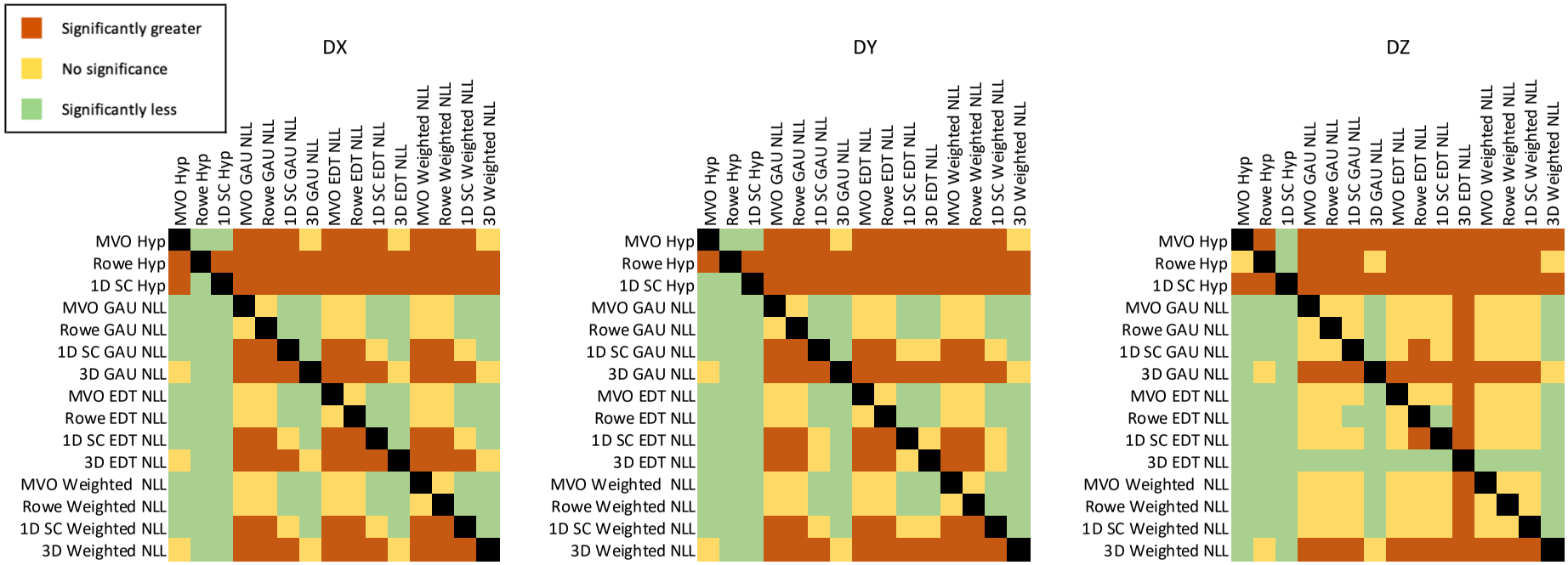

Figure 4.22: Significance checkerboards for 0 km showing if different runs are more or less significant than other runs. To be read down (Y) and then across (X) when interpreting. Green represents Y is significantly less than X, Orange represents Y is significantly greater than X, and yellow means there is no statistical significance between the two runs. 1D SC represents 1D SEA-CALIPSO.

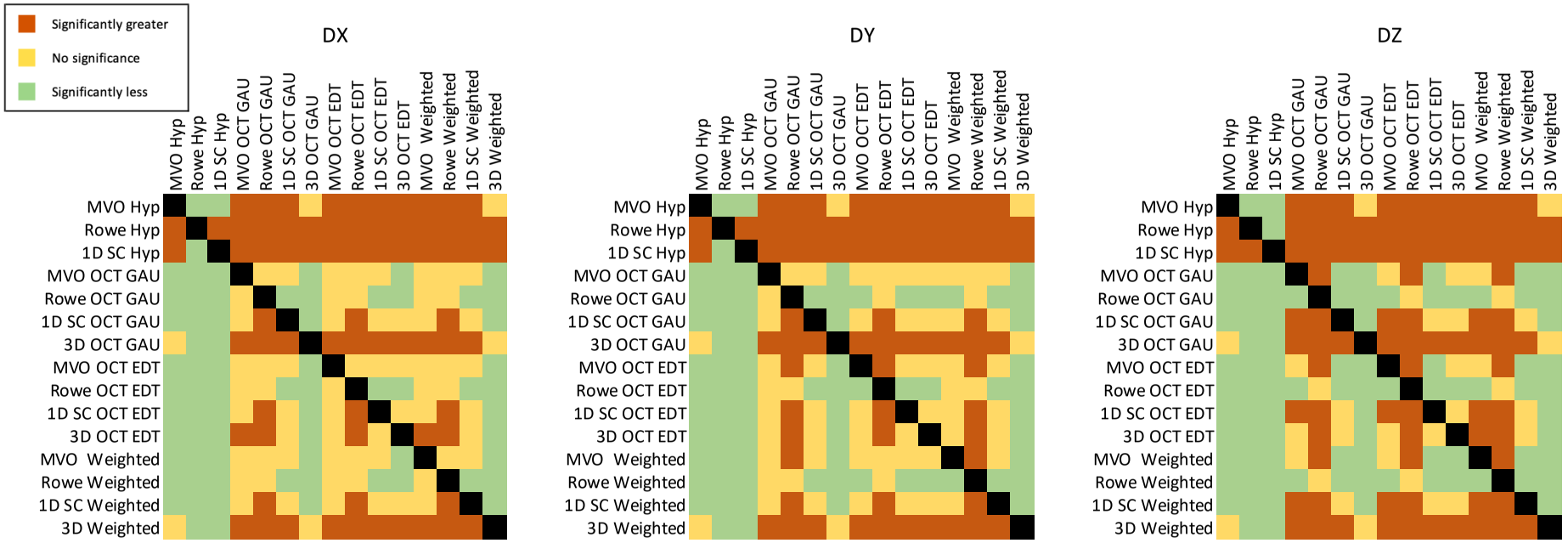

Figure 4.23: Significance checkerboards for 1 km depth showing if different runs are more or less significant than other runs. To be read down (Y) and then across (X) when interpreting. Green represents Y is significantly less than X, Orange represents Y is significantly greater than X, and yellow means there is no statistical significance between the two runs. 1D SC represents 1D SEA-CALIPSO.

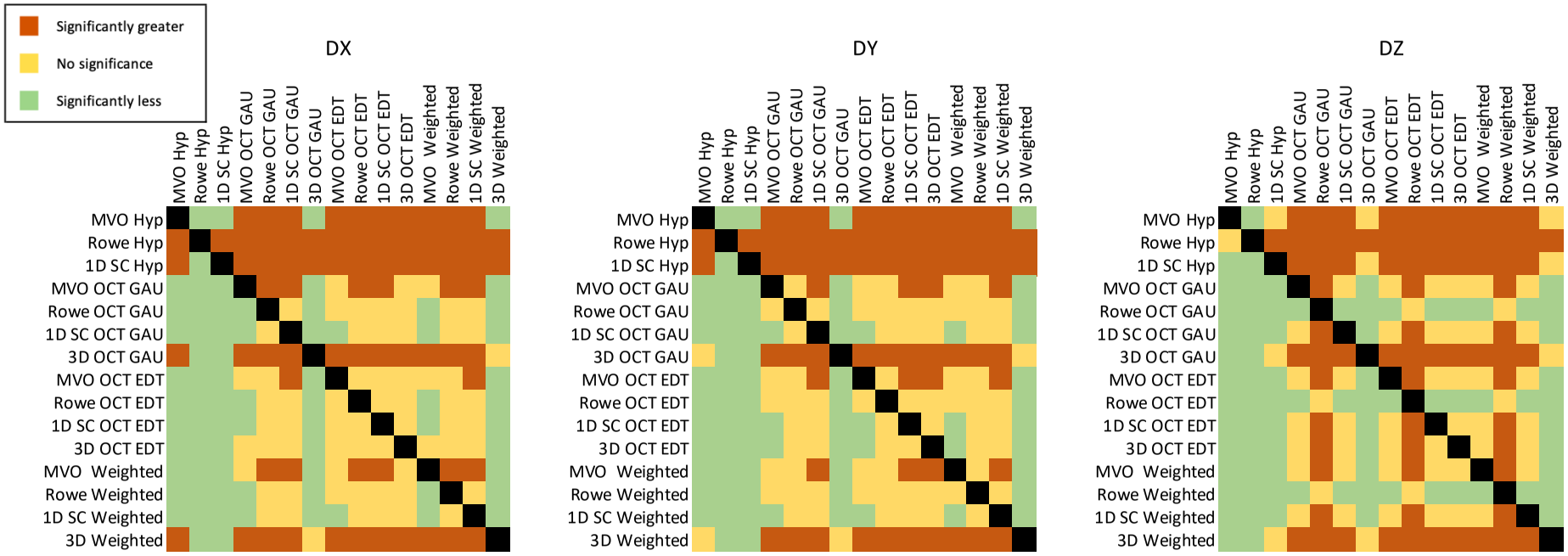

Figure 4.24: Significance checkerboards for 3 km depth showing if different runs are more or less significant than other runs. To be read down (Y) and then across (X) when interpreting. Green represents Y is significantly less than X, Orange represents Y is significantly greater than X, and yellow means there is no statistical significance between the two runs. 1D SC represents 1D SEA-CALIPSO.

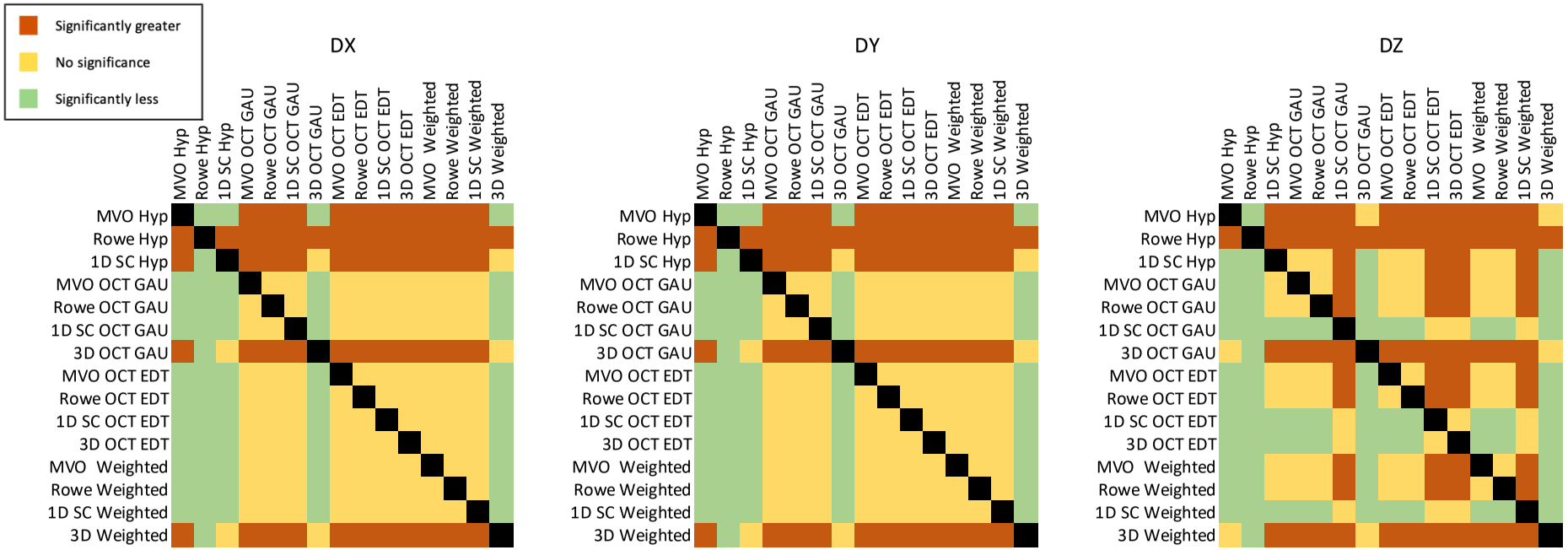

Figure 4.25: Significance checkerboards for 5 km depth showing if different runs are more or less significant than other runs. To be read down (Y) and then across (X) when interpreting. Green represents Y is significantly less than X, Orange represents Y is significantly greater than X, and yellow means there is no statistical significance between the two runs. 1D SC represents 1D SEA-CALIPSO.

4.3.5 Method Conclusion

Hypocenter relocations for the Rowe and 1D SEA-CALIPSO velocity model produce large errors and changes in locations. Use of the MVO velocity model with *Hypocenter* (MVO's current setup), produce a high percentage of trusted locations for X and Y, but fail on constraining the depth (Z) location. Errors produced when using *Hypocenter* are much larger than relocations using *NonLinLoc*. The MVO velocity model performs poorly in *NonLinLoc* for the majority of variables compared to other 1D velocity models available.

The Rowe velocity model performs best at depths of 0, 1 and 3 km, with the 1D SEA-CALIPSO velocity model performing better at depths greater than 5 km. However, the 1D SEA-CALIPSO velocity model is limited to a depth of 6 km. The Rowe velocity model performs well at additional depths up to 10 km with changes in location of 200–300 m compared to the 1D SEA-CALIPSO model at 5 km depth. Therefore the Rowe model is more useful for relocating earthquakes on Montserrat, given a) its ability to locate deeper events which may be indicators of future unrest episodes, and b) producing significantly smaller changes in locations and errors compared to other models at shallower depths, where the majority of seismicity is currently located on Montserrat.

There is not much difference between the three methods in *NonLinLoc* when using the Rowe velocity model. The Gaussian and Weighted method produce smaller errors, but the number of trusted earthquakes is greater with the EDT method. The difference in errors between the EDT and Gaussian method are on the order of 30–50 m, and so produce similar results. It is more important to have a greater number of trusted earthquakes, especially when the difference in errors is minimal. Therefore the Rowe velocity model will be used with the *NonLinLoc* EDT method for relocations of the Montserrat seismic catalogue.

4.4 Station Configuration

Ten different station configurations were compared to understand the effect the seismic network has on calculating earthquake locations. Synthetic earthquakes were relocated using the Rowe velocity model with the EDT location method in *NonLinLoc*, as decided in Section 4.3.5. The ten station configurations used are shown in Section 4.1.3; this were run at depths of 0,1,3,5 and 10 km.

4.4.1 RMS

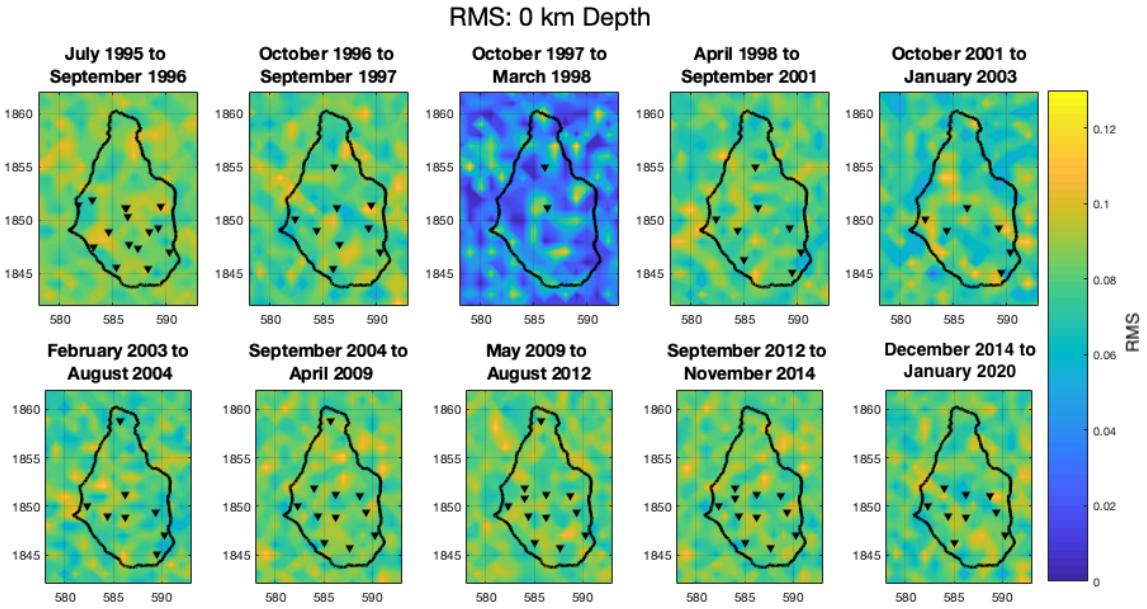

Figure 4.26: RMS values at 0 km across Montserrat for each time period; black inverted triangles represent seismic stations active during the time period.

RMS values were relatively low ranging from 0.08 to 0.12 seconds across the majority of the island for all station configurations (Figure 4.26); results were similar at all depths. The only difference in RMS is for the time period October 1997 to March 1998 when values are significantly lower; this is likely a result of there being only two stations and hence fewer arrival times to fit with the location, resulting in artifically lower RMS values.

4.4.2 Change in Location

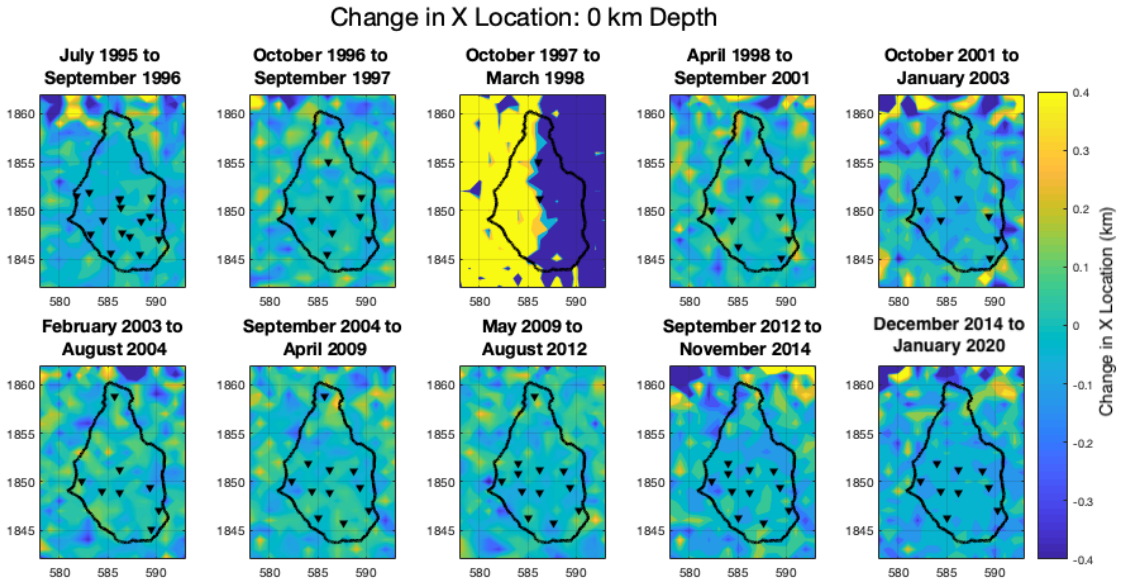

Figure 4.27: The change in X location at 0 km depth for each synthetic earthquake over Montserrat with 10 different time periods; black inverted triangles represent seismic stations active during the time period.

The change in location is defined as the change in X distance (km) from the original synthetic location to the new relocated location. The change in X and Y location showed similar results, with an increase in change in location with an increase in depth. At 0 km (Figure 4.27) and 10 km (Figure 4.28) there is little difference in values for each station configuration; but an increase in change in location is shown with an increase in depth. High values for the October 1997 to March 1998 time period are recorded for all changes in location, and this is a result of there being two stations active at this time.

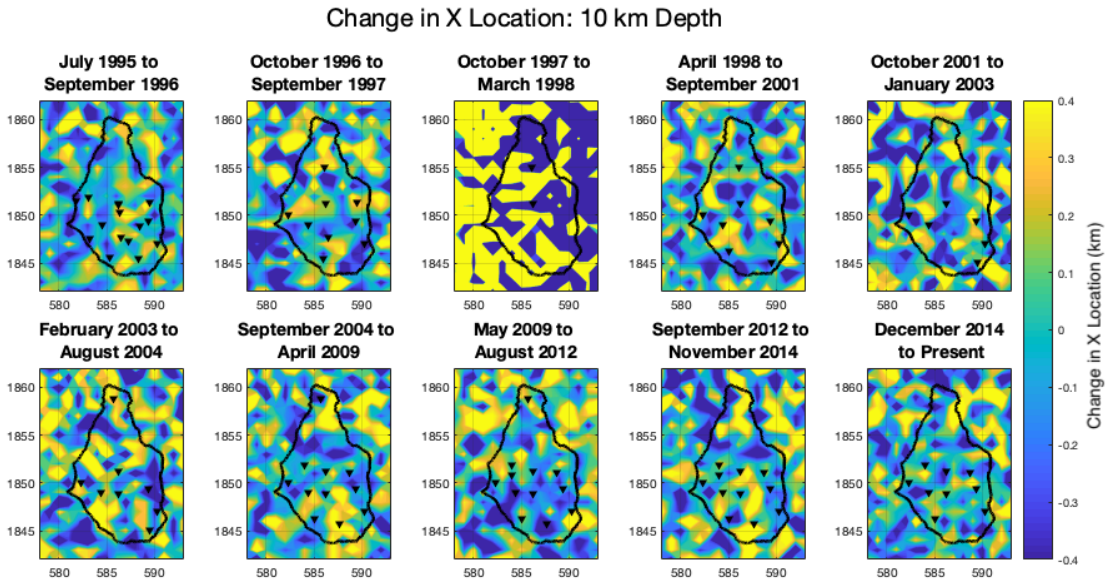

Figure 4.28: The change in X location at 10 km depth for each synthetic earthquake over Montserrat with 10 different time periods; black inverted triangles represent seismic stations active during the time period.

4.4.3 Errorcheck

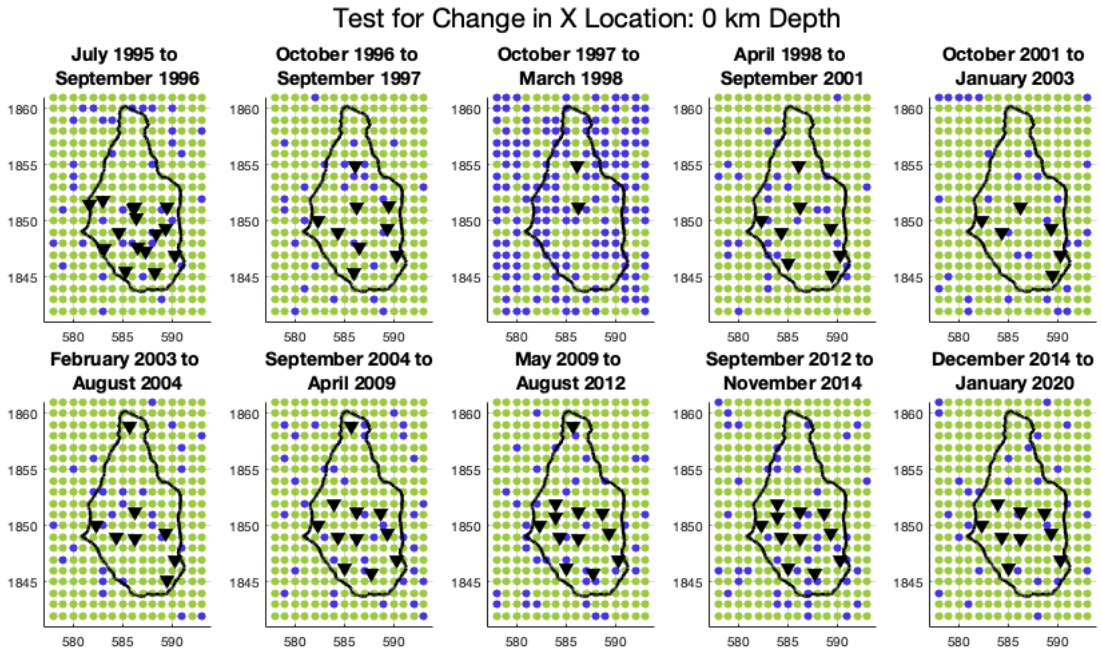

Figure 4.29: Error testing for X location at 0 km depth for 10 time periods; inverted triangle represents seismic stations active during that time period. Green represents a trusted location, and blue represents an untrusted location.

For X and Y locations there is a large proportion of trusted earthquakes for all time periods with more than two stations. No link between the percentage of trusted earthquakes and station configuration is shown. The same pattern is across all depths, with Figure 4.29 showing an example for the X location at 0 km depth.

For the Z location there is a decrease in the number of trusted locations with depth, an example of this is shown at 0 and 5 km (Figure 4.30 and 4.31 respecitvely). At 5 km depth, there is a slight increase in trusted earthquakes in the north with the presence of station MBMH (situated in the North of the island: Figure 2.5).

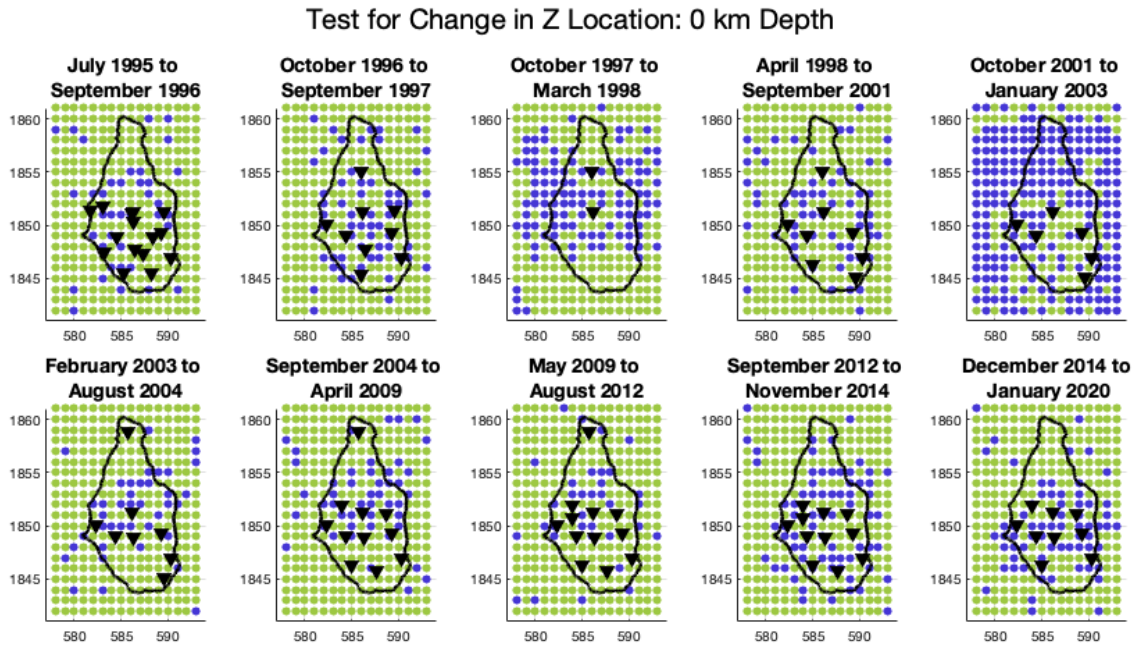

Figure 4.30: Error testing for Z location at 0 km depth for 10 time periods; inverted triangle represents seismic stations active during that time period. Green represents a trusted location, and blue represents an untrusted location.

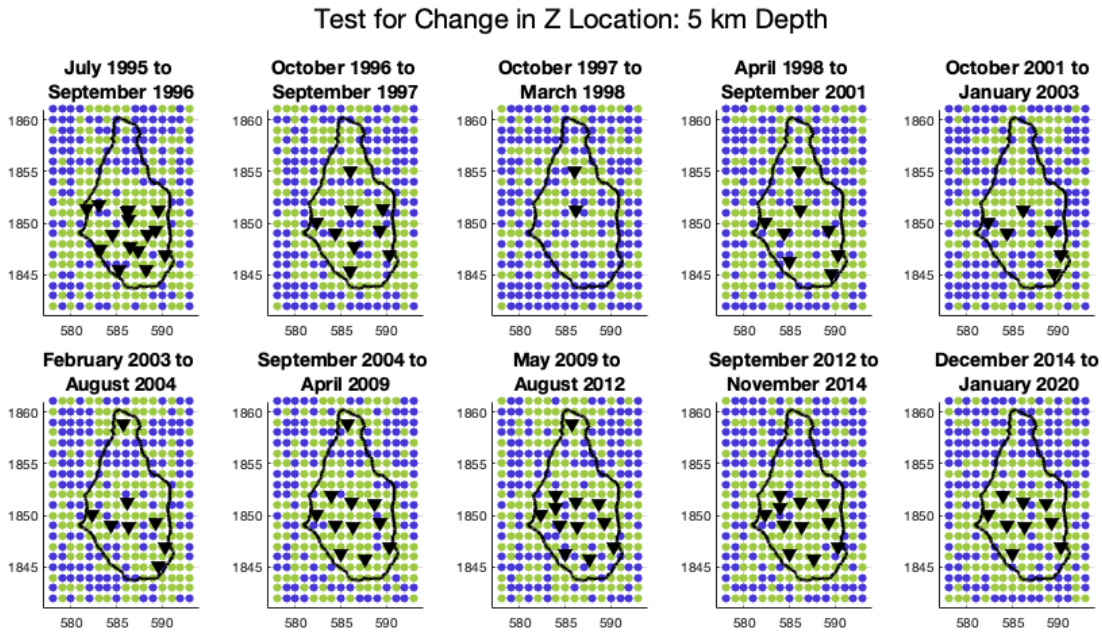

Figure 4.31: Error testing for Z location at 5 km depth for 10 time periods; inverted triangle represents seismic stations active during that time period. Green represents a trusted location, and blue represents an untrusted location.

4.4.4 Seismic Station Configuration Conclusion

There is little difference between the ten different station configurations when using the EDT method in *NonLinLoc* with the Rowe velocity model. The main difference is for the time period October 1997 to March 1998 when there were only two stations active. This was a time period when previous stations had been wiped out, resulting in only two stations operated by MVO. This shows the importance of having multiple seismic stations across Montserrat operating to provide redundancy in cases of failure and to keep a high percentage of trusted hypocenters alongside low errors. Overall, when using multiple seismic stations, the network performs well, with no areas of low accuracy clearly identified. The impact on the number of seismic stations active is explored further in Chapter 6, when only four seismic stations were used to locate earthquakes in the days prior to a Vulcanian explosion in July 2008.

4.5 Conclusion

Synthetic earthquakes were relocated with several velocity models and location methods to determine the most suitable setup for earthquake location on Montserrat. Results show that the current earthquake location method used at Montserrat Volcano Observatory could be improved. Earthquake locations located using *Hypocenter* with the MVO velocity model (MVO's operational setup) yielded low percentages of trusted earthquakes for the depth location, and on average had higher errors than earthquakes located using the *NonLinLoc* location method. The *NonLinLoc* EDT method performed well with all velocity models. The Rowe velocity model worked best at shallower depths up to 3 km, and the 1D SEA-CALIPSO was more suited for depths greater than 5 km; however this model was limited to locating earthquakes up to a depth of 6 km. As a result, the *NonLinLoc* EDT location method was chosen with the Rowe velocity model as it produced a high percentage of trusted locations, alongside low errors, and changes in locations at all depths. This setup is used to relocate the whole seismic catalogue from 1995 to 2018 in Chapter 5.

Comparison of different station configurations shows little difference when using the *NonLinLoc* EDT method with the Rowe velocity model. High errors and changes in location were recorded when using only two stations, although this is expected due to a low number of arrival times. Most of the time periods have greater than 8 stations, and therefore would be expected to perform well. It would be expected that times when there are fewer stations would be more problematic. This is looked at in Chapter 6, which looks at the accuracy of locations when using only four seismic stations.

Chapter 5

Catalogue Relocation: 1995–2018

Volcanic seismicity is one of the main short term monitoring methods used by volcanic observatories (*Luckett et al.*, 2007) and can give an indication on the location and size of magmatic eruptions (*White and McCausland*, 2016). Accurate earthquake locations have been used worldwide to help locate the migration of magma beneath the surface (*Ebinger et al.*, 2008; *Eyles et al.*, 2018; *Woods et al.*, 2019). Relocating past seismic catalogues with improved accuracy can lead to new analysis of volcanic systems.

This chapter aims to understand differences in locations of the relocated earthquakes and the implications this has on interpretations of the volcanic system at Soufrière Hills Volcano leading up to and during the five phases of the eruption. More information on each phase of the eruption is detailed in Section 1.4. For each phase in the eruption, hypocenters from the original MVO catalogue are compared with the relocated hypocenters located using *NonLinLoc* with the *Rowe et al.* (2004) seismic velocity model, the method defined in Chapter 4. This is then compared with other geophysical and geological studies to understand if differences in the locations can provide additional information about the volcanic system. This is important as there are time periods in the eruption where there are conflicting interpretations from different studies; refining the seismic catalogue will help in understanding the system, and elucidate which interpretations may be more plausible.

5.1 Relocated Catalogue

All earthquakes recorded from July 1995 to February 2018 by the Montserrat Volcano Observatories Network were relocated using the *NonLinLoc* OctTree Equal Differential Time

(EDT) sampling method with the *Rowe et al.* (2004) seismic velocity model (Figure 4.1). This relocation method was shown in Chapter 4 to produce a high percentage of trusted locations whilst keeping calculated hypocenter errors low. Synthetic data using the original location method by MVO (*Hypocenter* with MVO model) showed large calculated errors at some depths, with an overall low percentage of trusted locations. This new methodology was shown to significantly improve the accuracy of locations when compared to the original MVO method (Section 4.3.5).

Relocating the catalogue with *NonLinLoc* resulted in a total of 13,610 relocated earthquakes, compared to 13,239 earthquakes that were previously located by MVO using *Hypocenter*. Relocations used P and S arrivals (with weightings) for all event types from 1995-2018; these were picked by several analysts at MVO. More earthquakes were able to be relocated due to *NonLinLoc* being able to locate with four arrival phases, whereas *Hypocenter* needs a minimum of 5 arrival phases. Original and relocated earthquakes are shown in Figure 5.1. The majority of seismicity is located in South Montserrat but earthquakes are recorded across the whole island.

Figure 5.2 shows the number of earthquakes located at each latitude, longitude and depth, with most earthquakes located in the vicinity of Soufrière Hills Volcano. The majority of earthquakes are above 5 km depth but do extend to a depth of 30 km, with increased seismicity recorded at depths of 1 and 3.5 km bsl. Earthquakes greater than 8 km depth are infrequent and likely to be a result of poor earthquake locations; for this reason only earthquakes shallower than 8 km are looked at in this Chapter. Table 5.1 and Figure 5.3 display the range of errors on the relocated earthquakes. The majority of relocations (99%) have errors less than 5 km, with mean values all under 2 km.

	X (km)	**Y (km)**	**Z (km)**
Minimum Value	0.101	0.111	0.185
Maximum Value	15.056	16.975	13.181
Mean	1.904	1.731	1.884
Standard Deviation	1.180	0.994	1.064
25^{th} Percentile	1.025	1.076	1.256
75^{th} Percentile	2.536	2.259	2.151
99^{th} Percentile	4.756	4.659	5.168

Table 5.1: Table showing statistics of calculated errors for the relocated earthquakes.

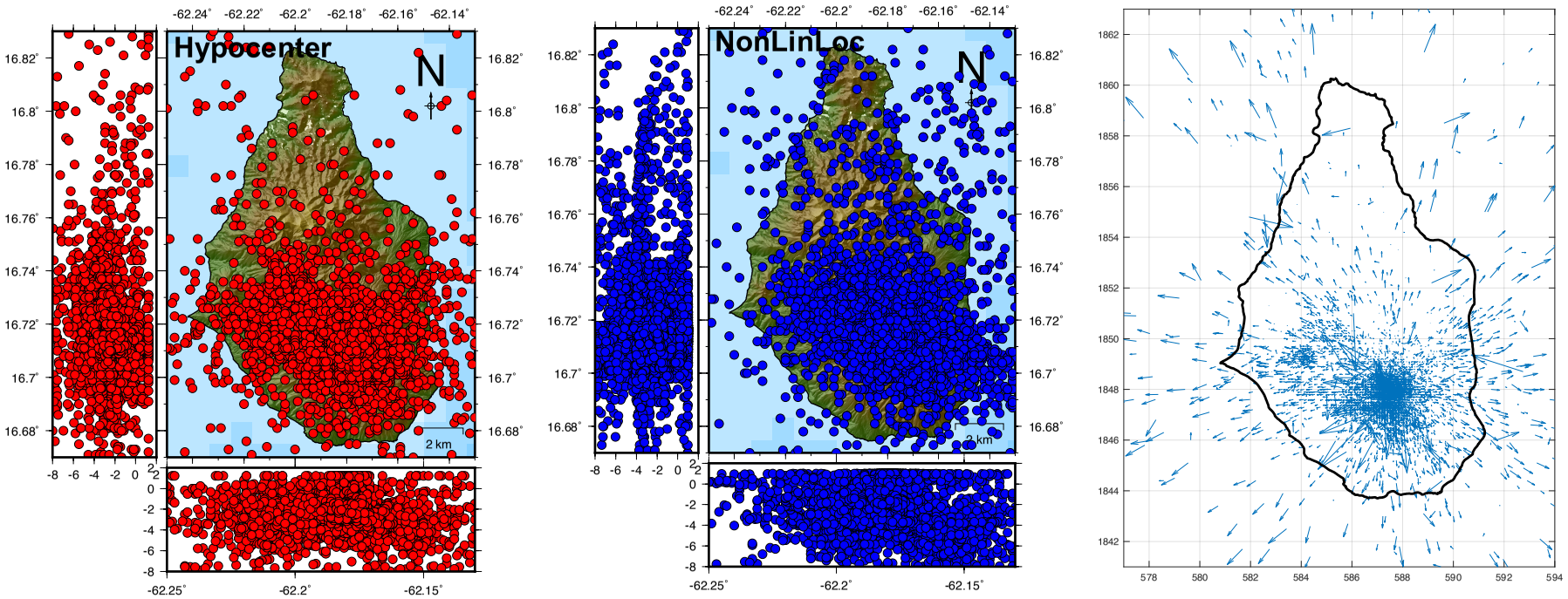

Figure 5.1: Locations of all relocated earthquakes from July 1995 to February 2018 for *Hypocenter* (red) and *NonLinLoc* (blue); only earthquakes up to 8 km depth are shown, but earthquakes are located up to 30 km in depth. Vector plot shows change in location from original *Hypocenter* location (start of arrow) to *NonLinLoc's* relocation (arrow head).

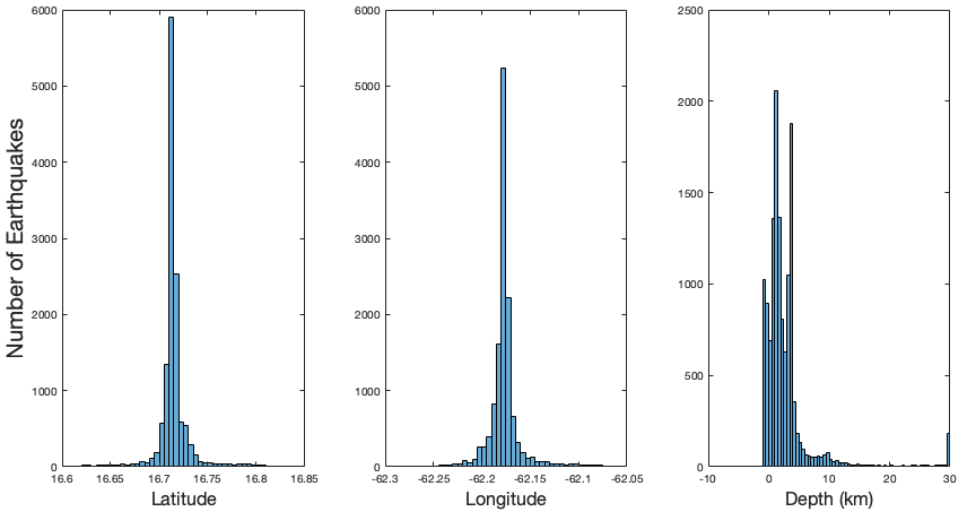

Figure 5.2: Histogram showing the latitude, longitude and depth locations of the relocated catalogue.

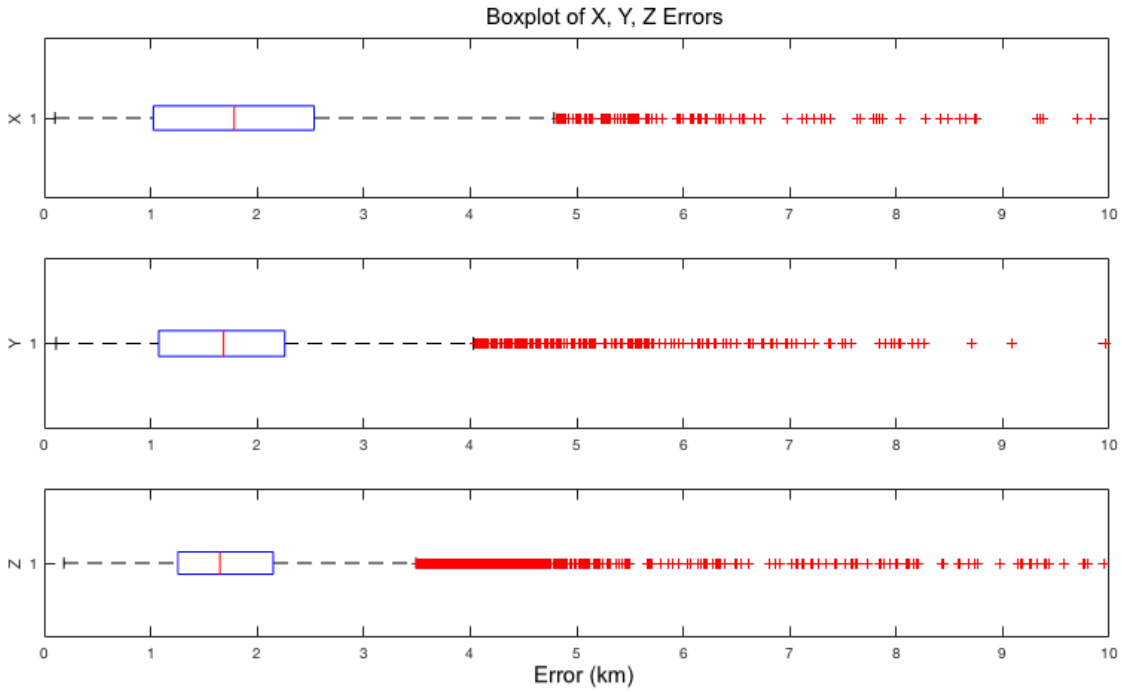

Figure 5.3: Boxplots of the X, Y and Z Errors associated with the relocated earthquakes. Sides of box define 25^{th} and 75^{th} percentile, with red line representing the median value. Red crosses are outliers of the data, with the black dashed line representing the range of values.

The number of daily recorded earthquakes from 1995 to 2018 is shown in Figure 5.4a. Over 272,000 earthquakes have been recorded since 1995, however only a small fraction of these contain arrival times that can then be used for location, shown in Figure 5.4b. Figure 5.4a shows that seismicity was generally higher in 1995–1996 during Phase 1, although there is also a strong increase in seismicity in July 2008 when over 700 earthquakes were recorded in a day. Magnitude data is incomplete for the whole time period, and therefore this was not included in the research. This means the magnitude of completeness is not known for the 1995-1996 dataset, and how this may have varied over the years with the change in seismic stations. This also could affect the number of earthquakes that are being recorded, and hence this needs to be accounted for when interpreting number of events throughout different phases. Increased VT seismicity at the start of the eruption is interpreted as the conduit forming with stresses equilibrating in the surrounding region (*Aspinall et al.*, 1998). Increases in seismicity were recorded prior to each phase in the eruption, making this time period of particular interest to understand the plumbing system. Hence, relocated seismicity during these time periods will be examined in more detail in Section 5.2

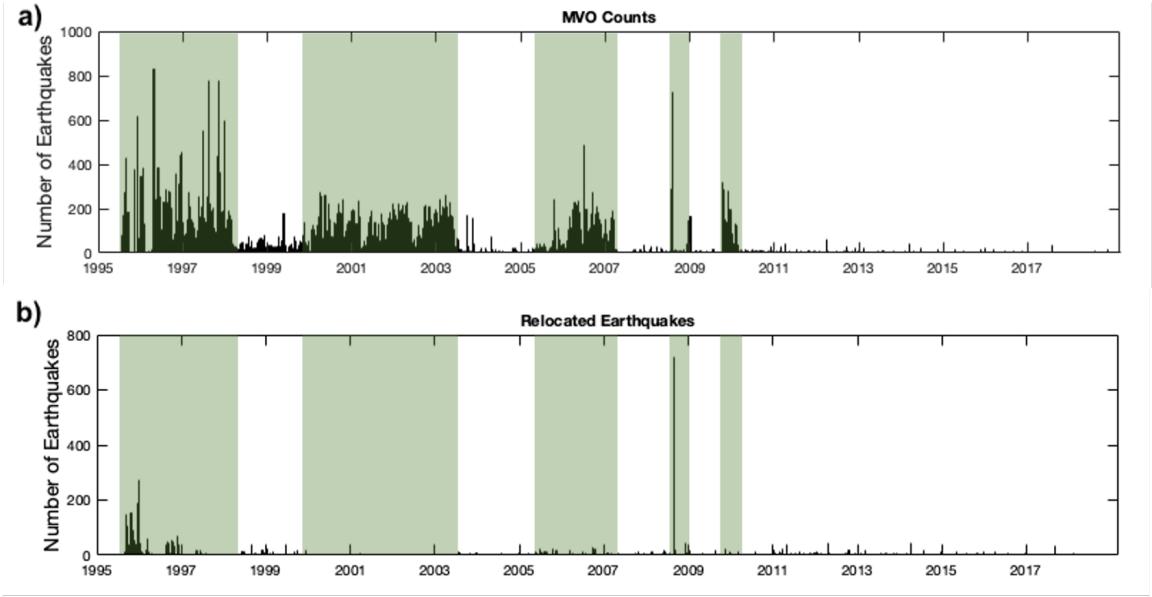

Figure 5.4: Histogram showing the number of earthquakes per day throughout 1995 to 2018, inclusive of all types. Top histogram shows the number of earthquakes recorded at MVO (not all recorded events were located with MVO). And the bottom histogram shows the number of earthquakes that were relocated with *NonLinLoc*. Green boxes represent different phases of the eruption.

The latitude, longitude and depth position of the relocated earthquakes throughout the past 25 years are shown in Figures 5.5, 5.6 and 5.7 respectively; this helps in viewing any changes in location throughout the eruption. The location settles after 2008 where it stays mostly

beneath Soufrière Hills (located at 16.72^{o}N and 62.18^{o}W). Prior to 2009, the locations are a lot more scattered, with periods where seismicity is recorded across the island such as in July 2008 and early 2005; this correlates to a time period when there were fewer arrival times (shown as events coloured in red), and therefore events may not have been as well constrained. Seismicity was initially deeper, extending to depths of 6 km bsl during 1995. Over time seismicity mostly shallowed to 0–4 km bsl.

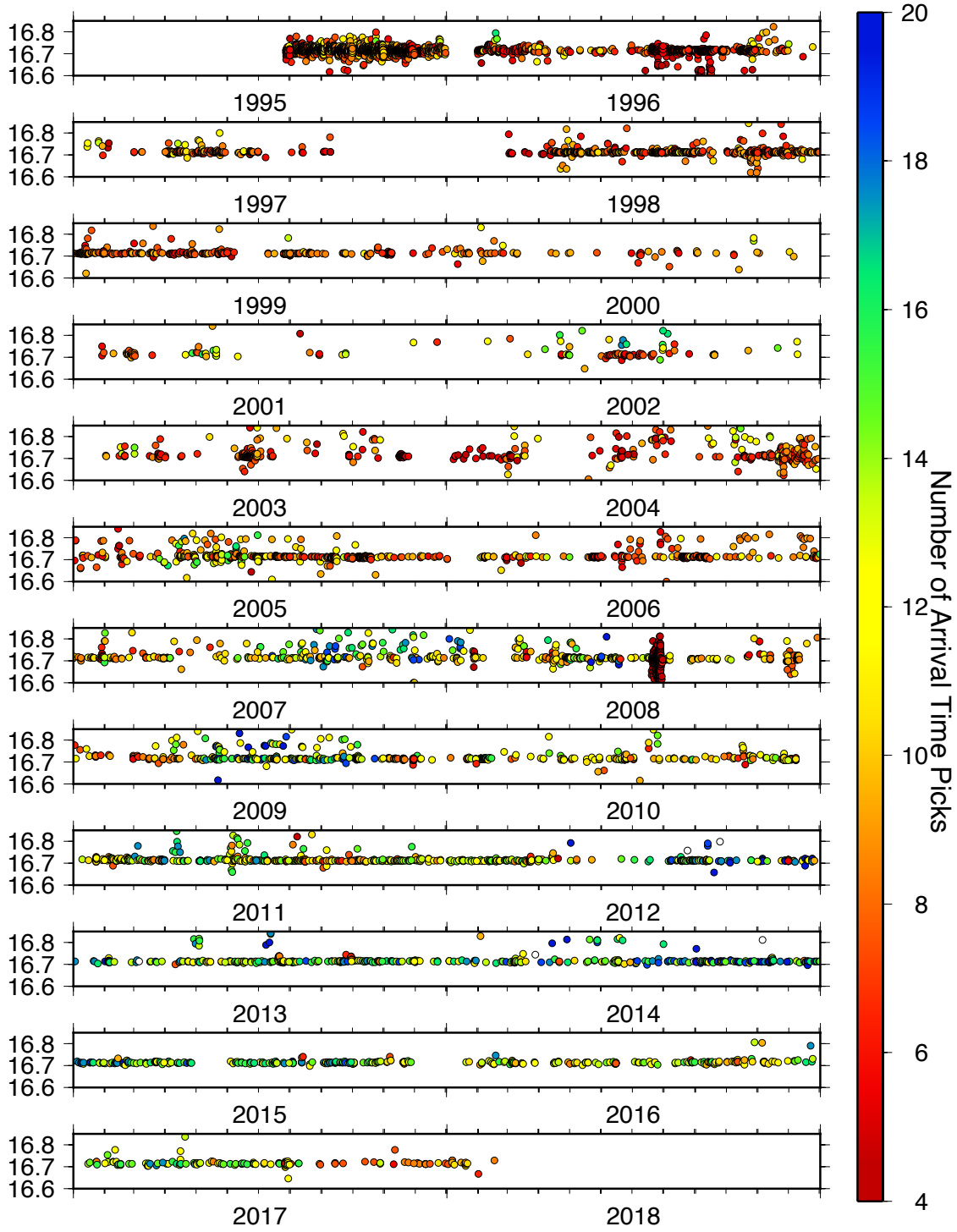

Figure 5.5: Plot showing the latitude location of earthquakes throughout the course of the eruption. Earthquakes are coloured by the number of picks used to locate the earthquake.

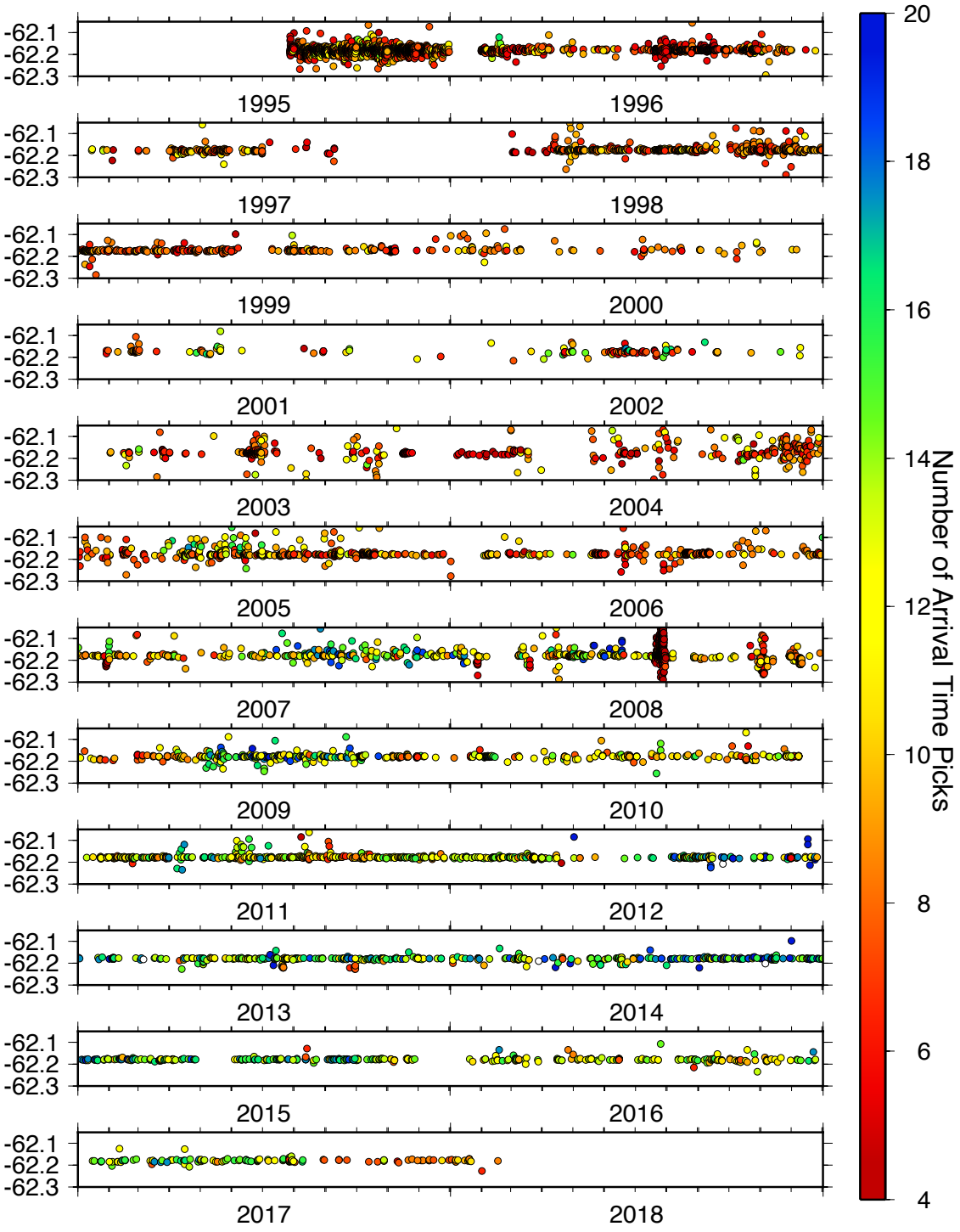

Figure 5.6: Plot showing the longitude location of earthquakes throughout the course of the eruption. Earthquakes are coloured by the number of picks used to locate the earthquake.

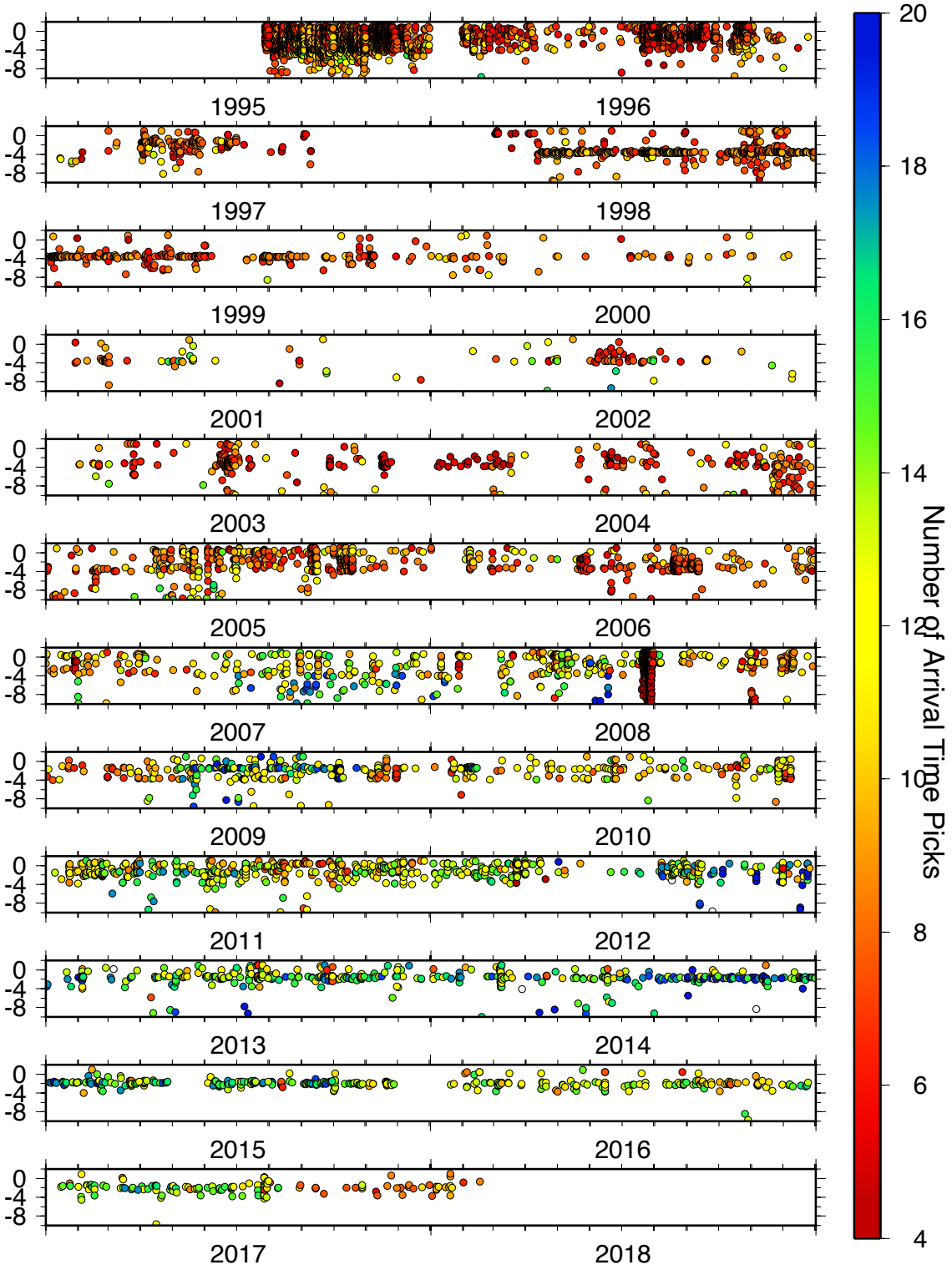

Figure 5.7: Plot showing the depth location of earthquakes throughout the course of the eruption. Earthquakes are coloured by the number of picks used to locate the earthquake.

5.1.1 Comparison with *Hypocenter*

Relocated earthquakes located with *NonLinLoc* were compared with the original MVO catalogue to see if there were significant changes in location. Earthquakes from MVO's catalogue for November 1996–February 2018 were located using the method *Hypocenter* with the MVO 1D seismic velocity model (Section 4.1.2). Earthquake locations from July 1995 to October 1996 were taken from *Aspinall et al.* (1998), where earthquakes were located using the same MVO 1D model but with the location method *HypoEllipse* (*Lahr*, 1999). These locations were used due to MVO not being formed during this time period, and hence did not compute their own locations for this period. It was decided to keep the locations that had previously been computed at the time so that there was a fair comparison between the new method and previous earthquake locations on Montserrat.

The spread in change in X, Y and Z locations are shown in Figures 5.8, 5.9, and 5.10 respectively; X, Y and Z location are used due to locating earthquakes in *NonLinLoc* with the NONE transformation, more information is shown in Appendix A. Mean values for each year can be found in Appendix D. For 1999 to 2008, there is a large change in location with an average of 50 km difference for some years. Whereas, for time periods such as 2011 to 2018 there is very little change in location for all the earthquakes that were relocated, represented by the small ranges shown in the boxplots.

A reason for the large change in locations observed during 1999 to 2008 could be due to a larger proportion of long period or hybrid earthquakes; these generally have fewer arrival time picks due to more emergent onsets. The average number of picks per event show an increase in mean number of arrival time picks from 2008 onwards with mean values generally above 10, whereas for 1999–2008 mean arrival picks are around 5–8 (Figure 5.11). This is a likely reason that the decrease in change in location is observed from 2008 onwards, however large changes in location could also be a result of a timing issue with one of the seismometers. This suggests that with some methods, the number of picks has a large influence on outputted locations; either the number of arrival time picks needs to be increased in future. Alternatively using an improved velocity model and location method also reduces the associated errors and improves locations, reducing the need for additional arrival time picks. This would also account for the large changes in location as *Hypocenter*

would include the station with a timing error in location, whereas *NonLinLoc* is able to pick out outliers in arrival phases (*Lomax et al.*, 2009).

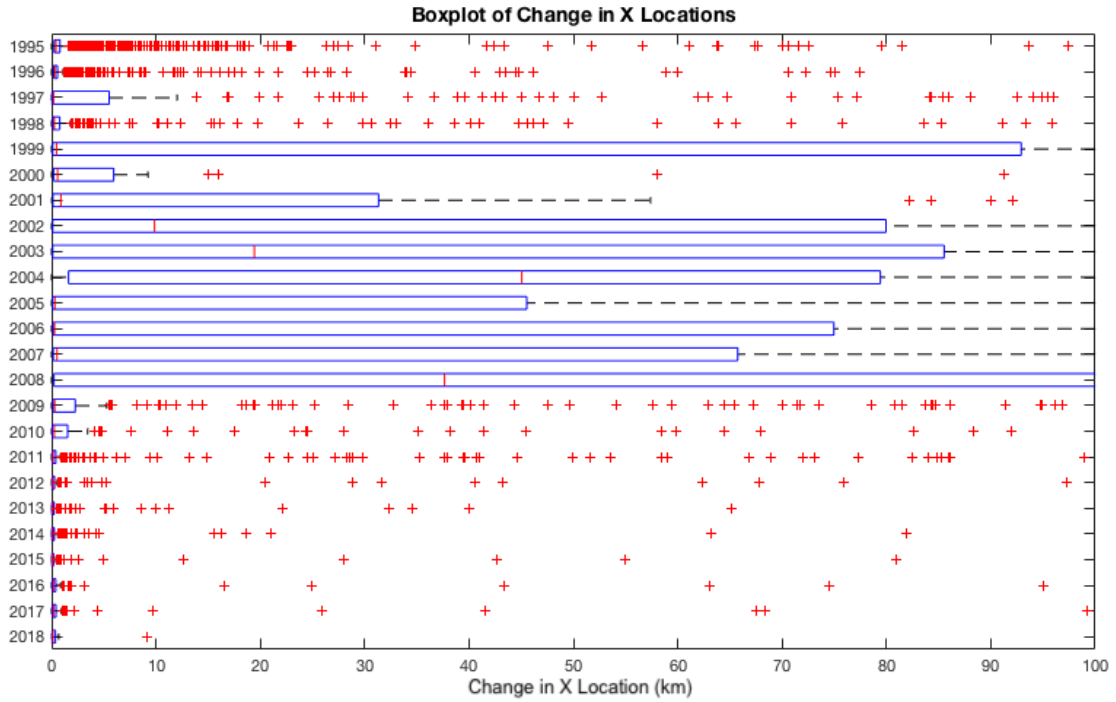

Figure 5.8: Boxplot showing the change in X location between *Hypocenter* and *NonLinLoc* locations. Red central line represents median, edges of box represent 25^{th} and 75^{th} percentile, black dashed line represents the range in values, and red crosses represent outliers.

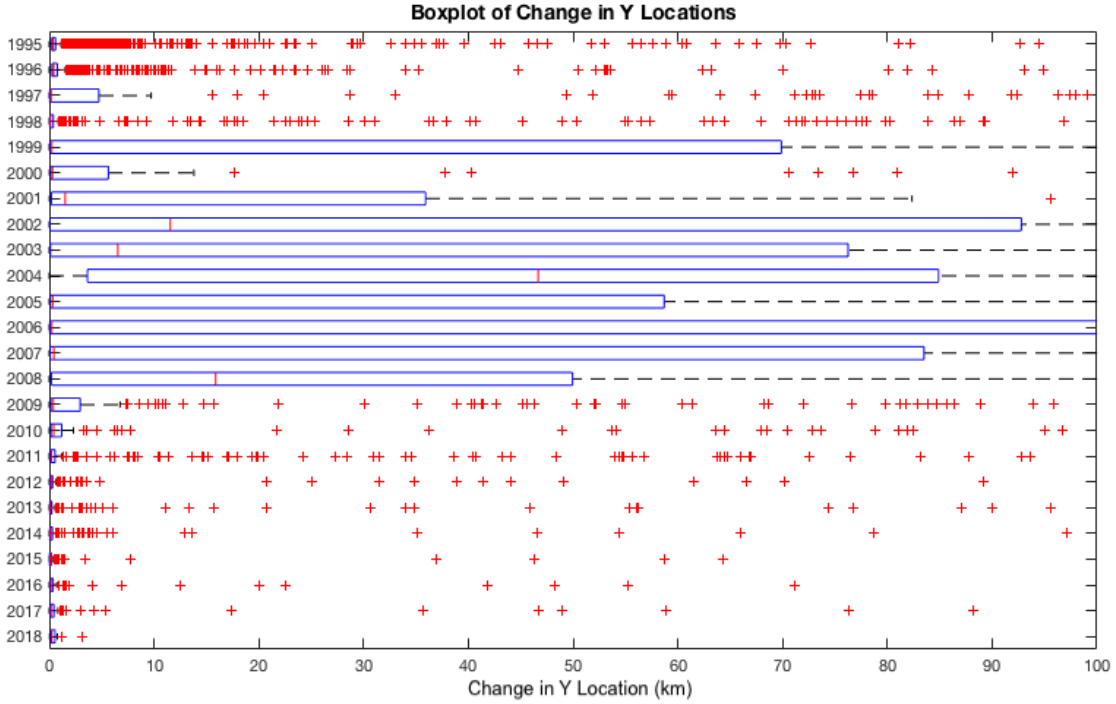

Figure 5.9: Boxplot showing the change in Y location between *Hypocenter* and *NonLinLoc* locations. Red central line represents median, edges of box represent 25^{th} and 75^{th} percentile, black dashed line represents the range in values, and red crosses represent outliers.

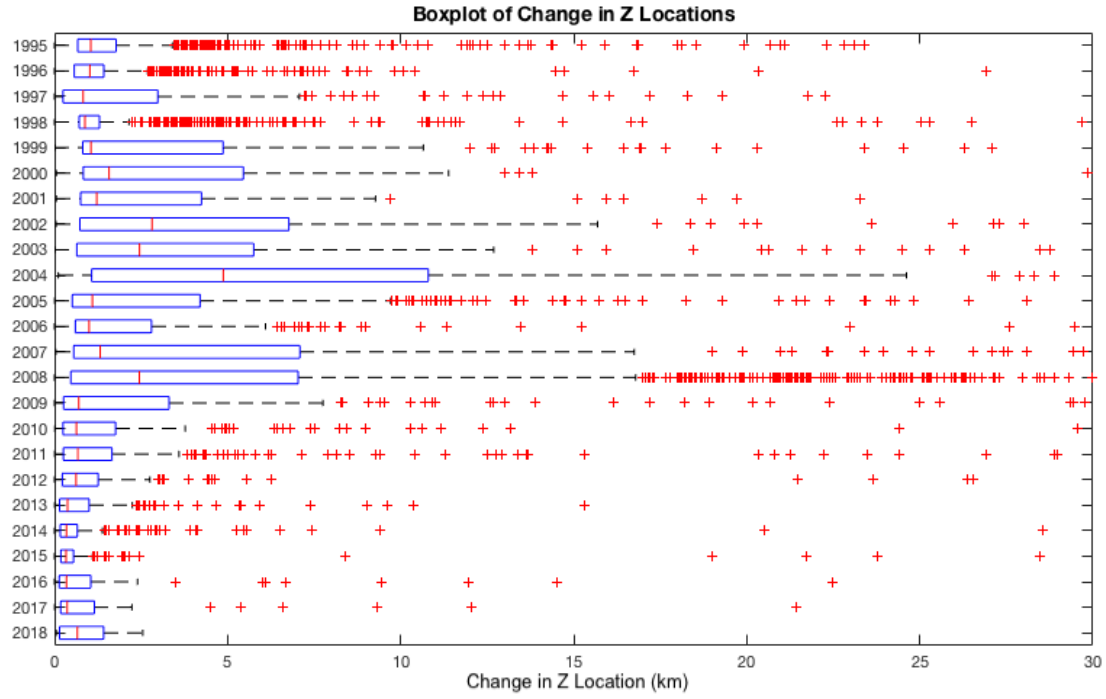

Figure 5.10: Boxplot showing the change in Z location between *Hypocenter* and *NonLinLoc* locations. Red central line represents median, edges of box represent 25^{th} and 75^{th} percentile, black dashed line represents the range in values, and red crosses represent outliers.

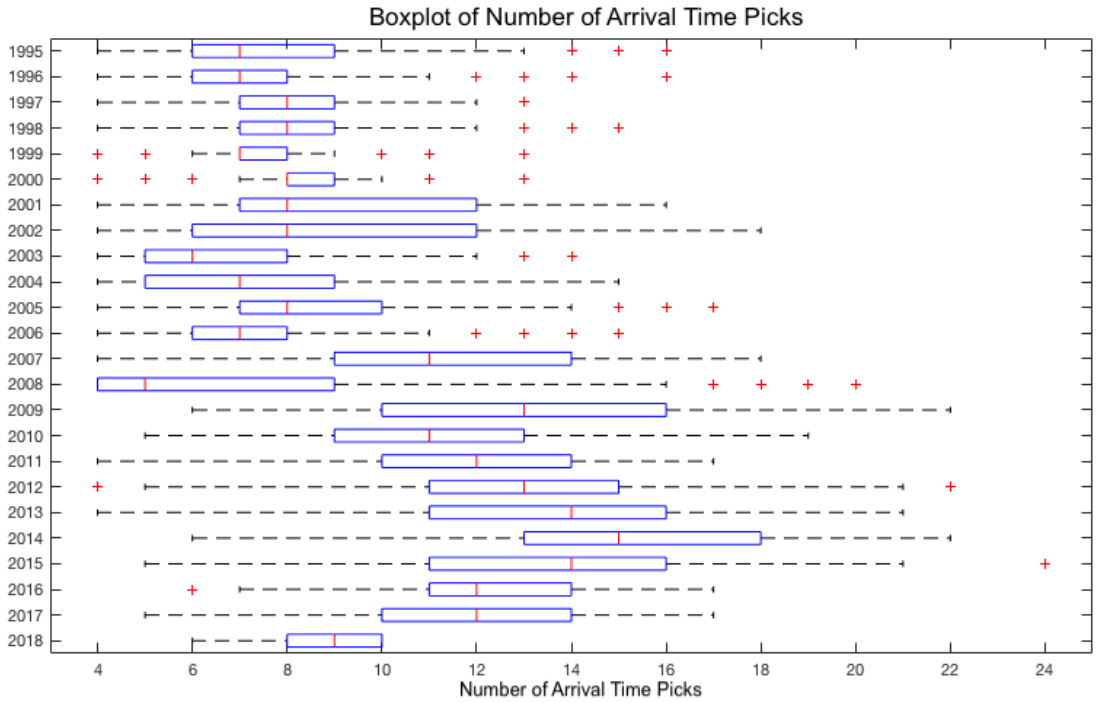

Figure 5.11: Boxplot of the number of arrival phases used to relocate each earthquake per year. Red central line represents median, edges of box represent 25^{th} and 75^{th} percentile, black dashed line represents the range in values, and red crosses represent outliers.

Figure 5.12 shows the number of earthquakes per type that were relocated from 1996 to 2018 in NonLinLoc using the MVO seismic catalogue (there is no data for types of seismicity in 1995). There is no clear pattern between type of seismicity and change in location: i.e. no prominent increase in a type of seismicity from 2008 is shown. There is a decrease in hybrid seismicity after 2008, but this is with LP and LPRF as well, and so is unclear if this is just a reduction in seismicity or has impacted the change in location. This suggests that the increase in change in location from 1999 to 2008 was likely down to the decrease in number of arrival time picks. No significant change in the number of seismic stations was recorded during this time, and so a reason for the lower number of arrival time picks could be due to time constraints by analysts at MVO; in times of heightened seismicity only a few stations are constantly used for picking arrival phases.

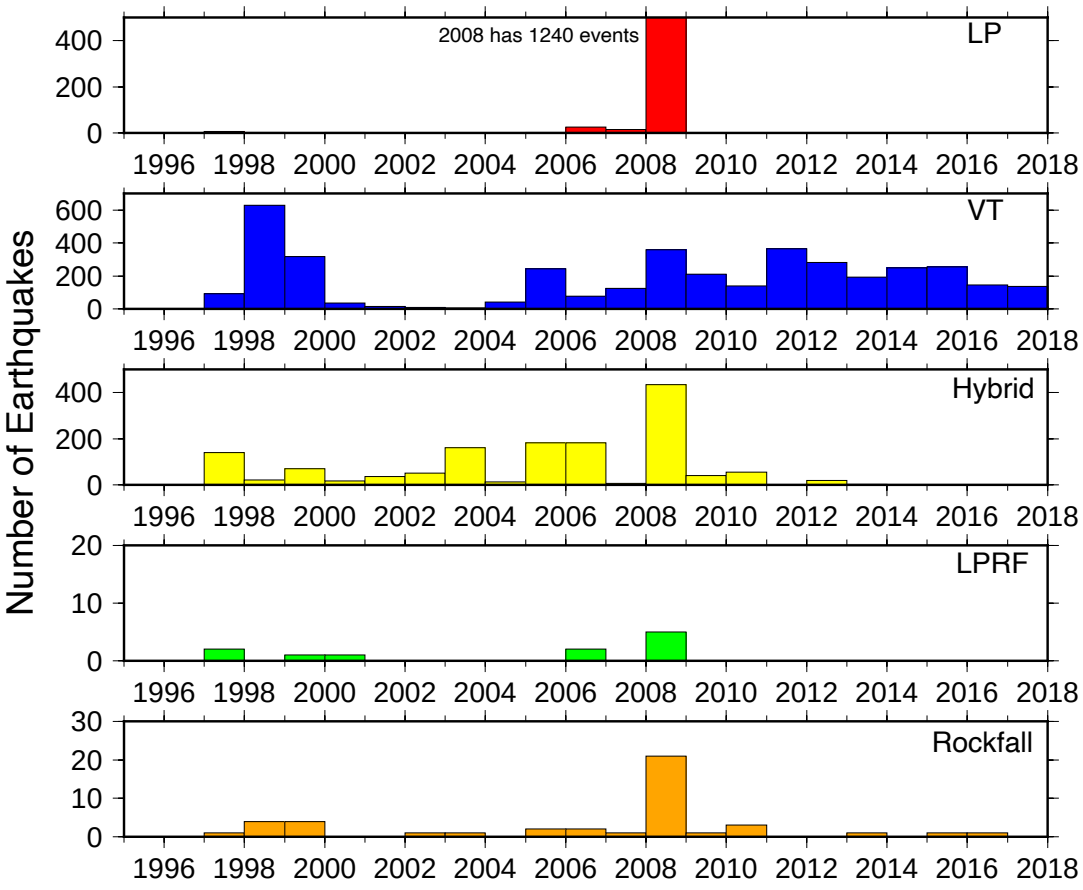

Figure 5.12: Histogram showing the types of seismicity through each year taken from the MVO catalogue. This is for located events only in *NonLinLoc*, so that this can be compared with the large changes in location recorded from 1999 to 2008.

The average hypocenter error calculated for each year for both location methods is shown in Figure 5.13. The error is calculated for each earthquake from each location method; this has then been converted into the standard error using the computed covariances, and equations defined in Section 4.2.4 and 4.2.4. An increase in error for *Hypocenter* locations is recorded from 1999 to 2009; average errors per year (the average from each calculated hypocenter location) reach up to 50 km with individual earthquakes having latitude and longitude errors up to 70 km. These errors were outputted from MVO's earthquake catalogue, and have been converted to a standard error matching NonLinLoc using equations in Section 4.2.4. This time period is when there was a reduction in arrival time picks for earthquake locations and correlates with the large change in locations between *NonLinLoc* and *Hypocenter*. *NonLinLoc*'s computed errors are not affected as severely by this time period, and maintain average errors less than 3 km for all time periods. Further, large changes in location recorded during this time period are likely a result of inaccurate locations provided by *Hypocenter* due to the large errors associated with events during this time.

The Longitude, Latitude and Depth locations for *Hypocenter* (blue) and *NonLinLoc* (red) are plotted as histograms in Figures 5.14, 5.15 and 5.16 to understand if there is a systematic shift in location between each method. Longitude shows a similar location for both methods, but with time periods 2002, 2005 and 2006 having a greater number of earthquakes located beneath Soufrière Hills with *NonLinLoc*. This suggests that some *Hypocenter* located earthquakes, which were located further from Soufrière Hills have been better constrained with *NonLinLoc*. The latitude location shows a similar result, with the majority of years having the same display of locations, but with some years such as 2008 and 2009 having a higher number of earthquakes being located beneath Soufrière Hills Volcano.

The depth locations show a greater spread for both *NonLinLoc* and *Hypocenter*. Neither method seems to consistently locate earthquakes at a shallower or greater depth than the other. Earlier time periods show a greater variation in depth values; whereas later time periods such as 2012 to 2017 show similar values. Depth locations from 1998 to 2001 were located much shallower with *Hypocenter* compared to *NonLinLoc*; this correlates with time periods shown earlier that have large changes in locations during this time.

The majority of seismicity is around Soufrière Hills Volcano, but the 1995 and 2008 period show a greater spread in locations across Montserrat. This could be related to volcanic

processes occurring during this time frame, which is similar to results that were seen in Figures 5.5 and 5.6.

	Hypocenter			NonLinLoc		
	X	Y	Z	X	Y	Z
1995	1.91	1.97	2.74	1.85	1.87	1.62
1996	2.21	2.32	1.92	1.58	1.79	1.68
1997	16.14	16.25	2.39	1.32	1.37	1.69
1998	9.63	9.65	1.92	1.97	1.7	1.85
1999	26.79	26.86	1.94	1.87	1.58	1.97
2000	16.79	16.8	2.42	2.23	1.75	2.22
2001	20.69	20.74	2.43	2.33	1.94	2.1
2002	38.8	38.88	3.98	2.35	2.22	2.66
2003	37.02	37.11	3.65	2.51	2.42	2.48
2004	49.13	49.18	4.66	2.73	2.62	2.48
2005	25.98	26.09	3.66	1.56	1.47	1.92
2006	33.47	33.56	1.75	2.5	1.74	2.25
2007	29.44	29.51	2.82	1.48	1.52	1.76
2008	41.2	41.31	3.22	2.65	1.76	2.5
2009	15.83	15.94	2.39	1.12	1.17	1.29
2010	8.6	8.89	1.75	1.03	1.09	1.24
2011	7.97	8.2	2.3	1.14	1.1	1.72
2012	3.91	4.14	2.49	1.34	1.31	1.68
2013	4.7	4.92	2	1.84	1.89	1.99
2014	3.26	3.46	1.67	1.3	1.31	1.64
2015	2.47	2.67	1.43	1.44	1.48	1.67
2016	5.79	5.95	1.75	1.61	1.56	1.67
2017	5.63	5.81	1.62	1.53	1.66	1.66
2018	1.99	2.03	1.14	1.28	1.51	1.39

Figure 5.13: Table showing the mean error for X, Y and Z locations per year for *Hypocenter* and *NonLinLoc* locations. Light blue represent errors greater than 5 km, yellow greater than 10 km and orange greater than 20 km.

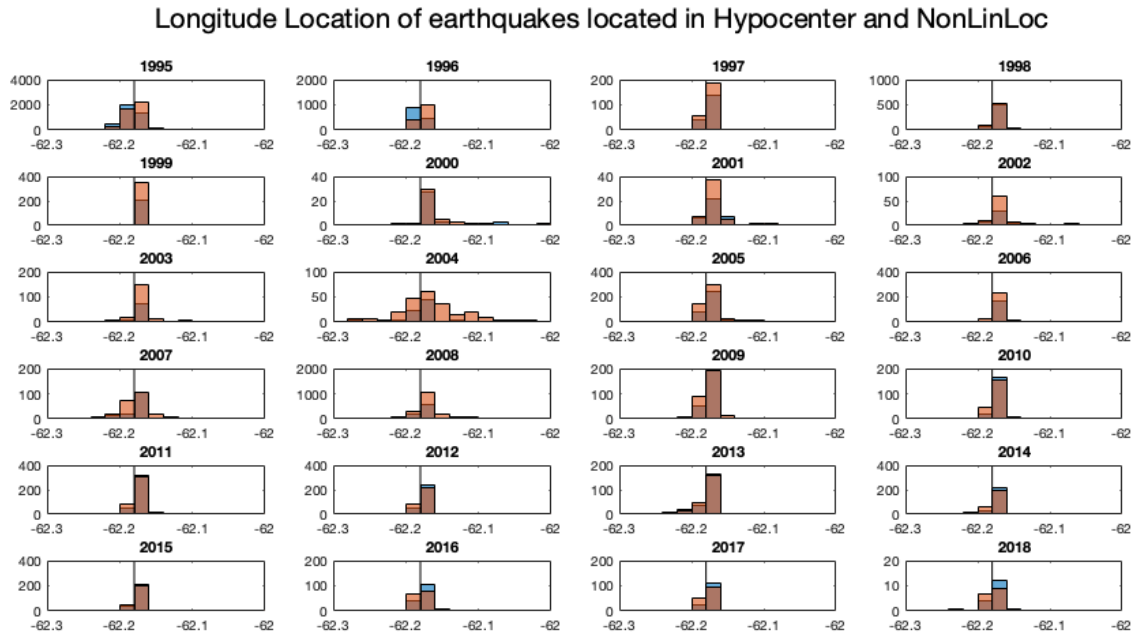

Figure 5.14: Histogram showing longitude location for *Hypocenter* (blue) and *NonLinLoc* (red) locations. Black line denotes location of Soufrière Hills Volcano

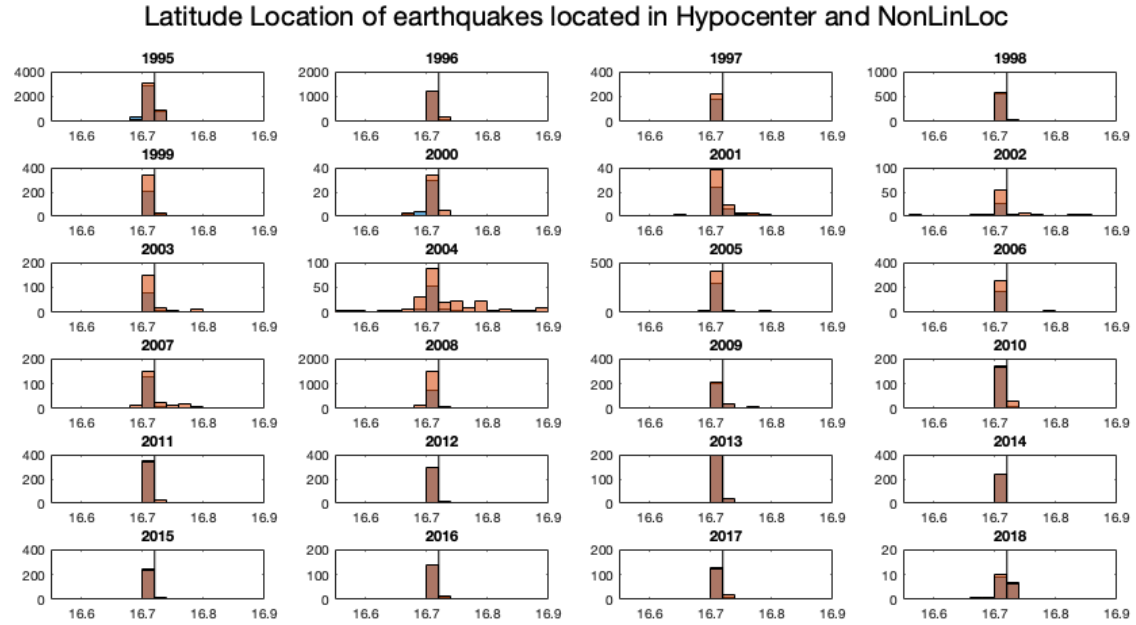

Figure 5.15: Histogram showing latitude location for *Hypocenter* (blue) and *NonLinLoc* (red) locations. Black line denotes location of Soufrière Hills Volcano.

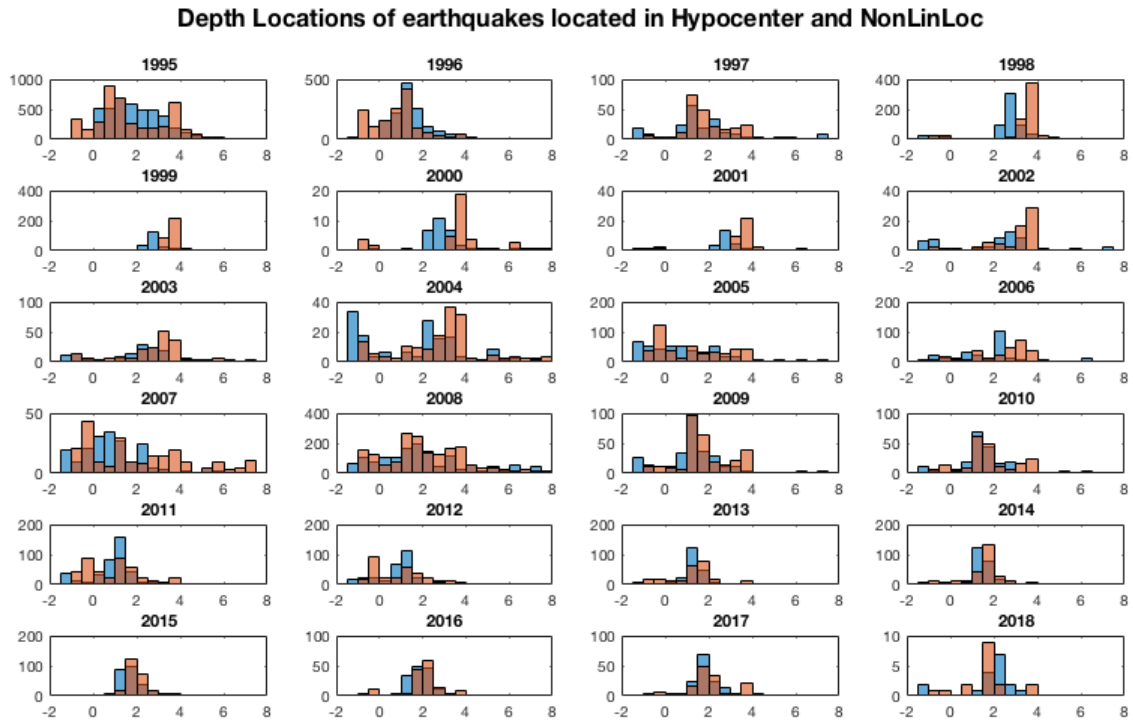

Figure 5.16: Histogram showing Depth location for *Hypocenter* (blue) and *NonLinLoc* (red) locations

5.2 Interpretations of Relocated Seismic Catalogue

5.3 Phase 1: 17^{th} July 1995 to 10^{th} March 1998

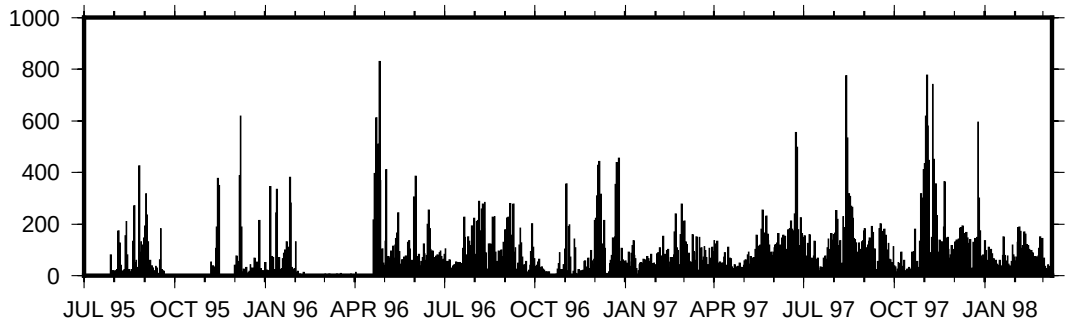

Figure 5.17: Histogram showing the number of earthquakes per day in Phase 1. Data up to October 1996 uses earthquakes located by *Aspinall et al.* (1998). Locations after October 1996 use the number of earthquakes recorded by MVO.

The eruption at Soufrière Hills Volcano began on the 18^{th} July 1995 after three years of elevated seismicity; the extrusion lasted until the 10^{th} March 1998 and is known as Phase 1 of the eruption. Phreatic explosions and 3 km high ash columns dominated the first few months of the eruption, and were accompanied by high SO_2 levels reaching 300 tonnes/day (*Young et al.*, 1998). Seismicity was recorded across southern Montserrat from July–September 1995, with earthquakes being located in 'distal clusters' away from the eruptive activity (*White and McCausland*, 2016). Dome building then began after September, when a change in seismicity to more repetitive hybrid cycles, LP and banded tremor were recorded (*Gardner and White*, 2002; *Miller et al.*, 1998; *White et al.*, 1998). Three distinct pulses in discharge rate were all preceded by earthquakes swarms between February 1996 to May 1997 (*Sparks et al.*, 1998).

Several changes were made to the seismic network during Phase 1, with a large upgrade occurring in October 1996 when MVO was first established. Seismometers prior to this were mainly one component with arrival time data from July 1995 to October 1996 being provided by personal communication with Willy Aspinall. Original locations during this period were taken from *Aspinall et al.* (1998). This data did not contain seismicity type and hence no interpretation of differing seismicity is looked at for Phase 1. High levels

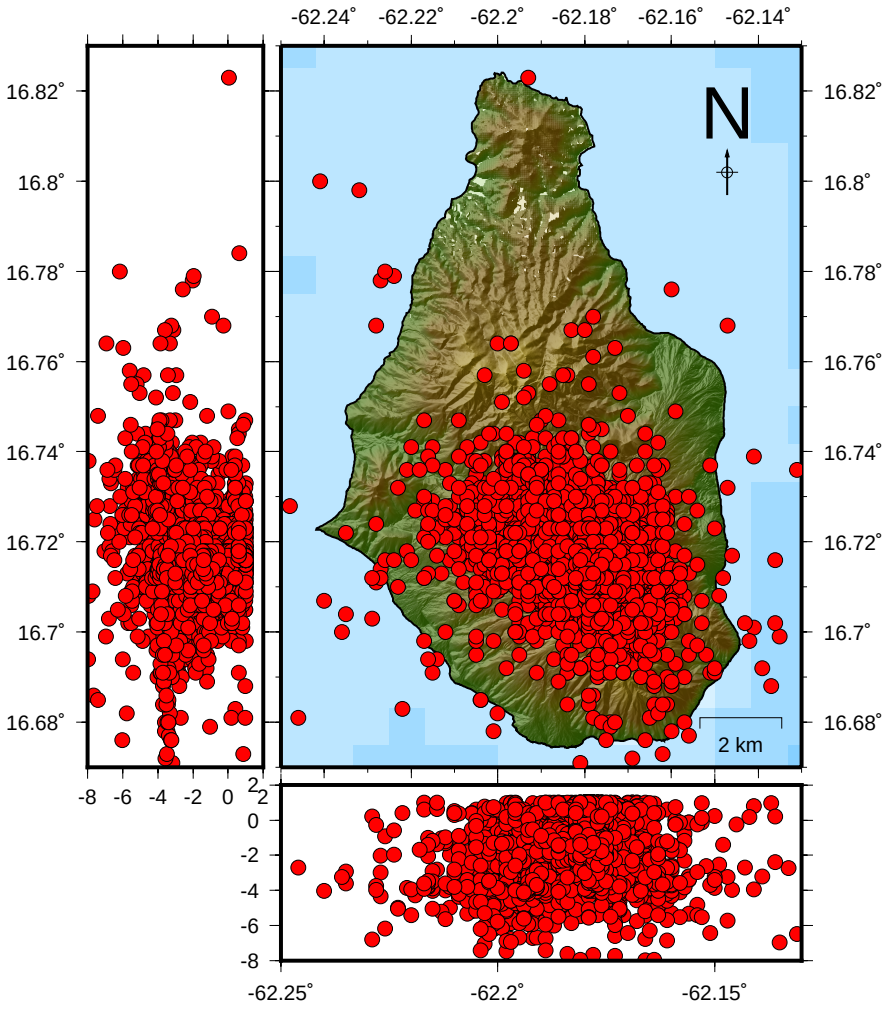

Figure 5.18: Earthquake relocations during Phase 1: earthquakes with errors greater than 3 km have been removed.

of seismicity were recorded during the start of the eruption, with over 200 earthquakes recorded per day (Figure 5.17).

Seismicity throughout Phase 1 covers the majority of south Montserrat (Figure 5.18). Due to the large number of events, it is hard to see any individual trends or clusters in seismicity. Previous research shows seismicity to not just be concentrated beneath Soufrière Hills Volcano, but to extend to other regions such as St George's Hill, Windy Hill and to the NE near Long Ground (*Aspinall et al.*, 1998; *Miller et al.*, 2010; *Roman et al.*, 2008; *White and McCausland*, 2016). The locations of these complexes alongside other faults in the region is shown in Figure 5.19. These periods of seismicity are described in more detail in the following sections, where original locations computed by MVO/*Aspinall et al.* (1998) are compared with relocated earthquakes from this study.

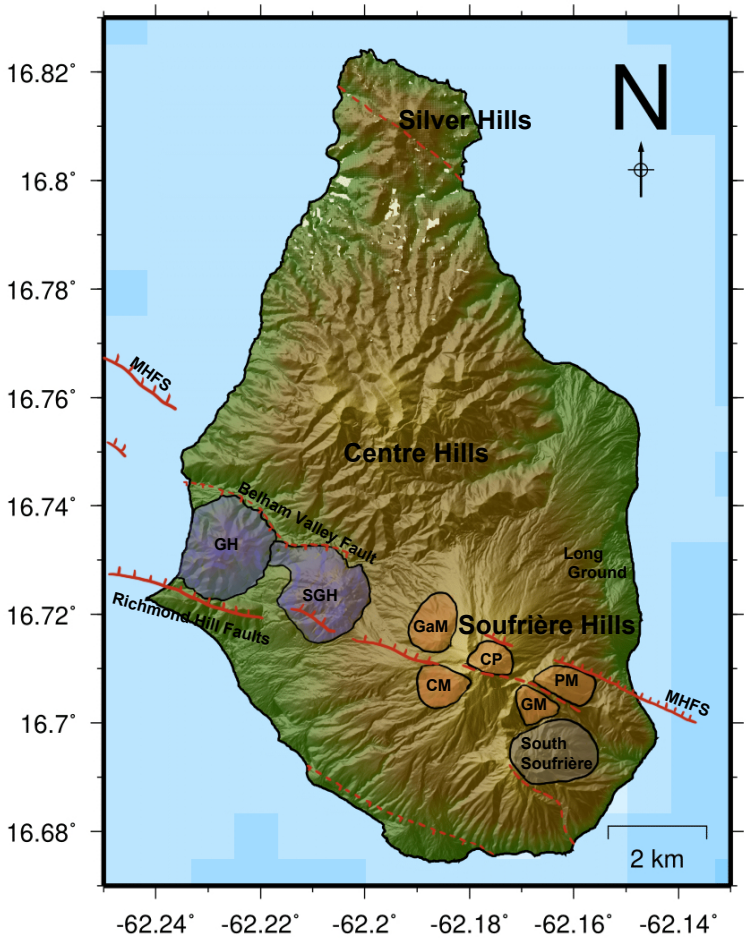

Figure 5.19: Figure showing the faults and geological complexes on Montserrat. Locations of faults and geological features are taken and adapted from *Baird et al.* (2015). Coloured regions represent volcanic complexes grouped by age; orange areas represent complexes relating to Soufrière Hills. Annotations: GH = Garibaldi Hill, SGH = St George's Hill, MHFS = Montserrat-Havers Fault System, CP = Castle Peak, GM = Galways Mt, CM = Chances Peak, PM = Perches Mt and GaM = Gages Mt.

5.3.1 St George's Hill

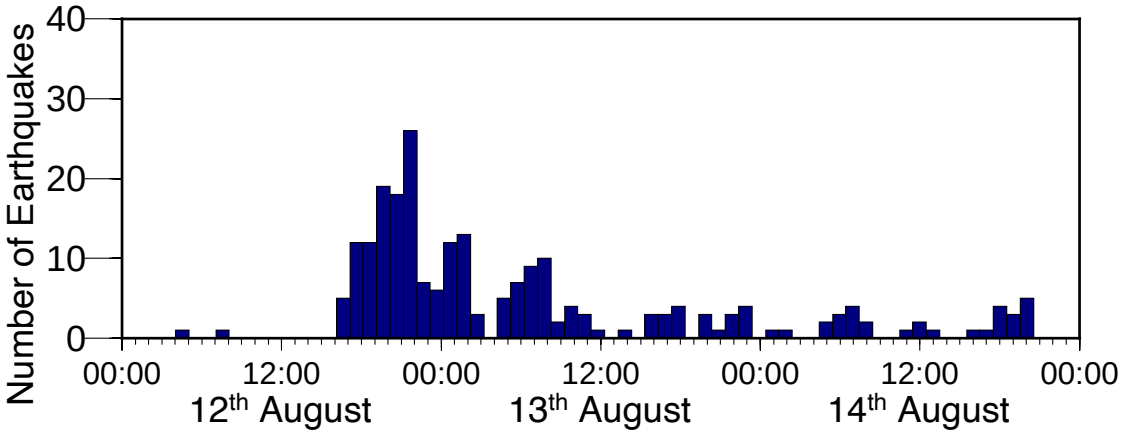

Figure 5.20: Histogram showing the number of earthquakes per hour from the 12^{th}–14^{th} August 1995 that were located by *Aspinall et al.* (1998)

A distal cluster of earthquakes was recorded from the 12^{th}–14^{th} August 1995 underneath St George's Hill located to the NW of Soufrière Hills Volcano. The majority of seismicity during this period occurred in the first 24 hours (Figure 5.20). St George's Hill is comprised of volcanic deposits, but there is little evidence for a volcanic system underneath (*Harford et al.*, 2002). A low resistivity anomaly was recorded beneath St George's Hill that was interpreted as a hydrothermally-altered smectic clay cap (*Ryan et al.*, 2009); this, alongside increased seismicity in the area, suggests that there is a separate geothermal system beneath St George's Hill (*Ryan et al.*, 2013).

Seismicity was recorded at St George's Hill and Soufrière Hills in 1933–1937 during an earlier seismic crisis; hypocenters at St George's Hill were estimated to be at depths of 1–2 km bsl (*Powell*, 1938). In 1966–1967 seismicity was located along the southern flanks of Soufrière Hills Volcano, with hypocenters along a 4 km belt extending WNW/ESE towards St George's Hill (*Shepherd et al.*, 1971). No seismicity beneath St George's Hill was recorded in the few years leading up to the eruption in 1995 (*Shepherd et al.*, 2002).

Relocated seismicity from the 11^{th}–14^{th} August 1995 is shown in Figure 5.21 alongside original locations by *Aspinall et al.* (1998). *Aspinall et al.* (1998) locations are mostly beneath St George's Hill with some events extending towards Garibaldi Hill and Soufrière Hills Volcano. Relocations show a tighter clustering of earthquakes around St George's

Hill at depths of 2–4 km, with no earthquakes recorded beneath Garibaldi Hill. A link in hypocenters is now seen between the western flanks of Soufrière Hills Volcano and St George's Hill, which was not seen in the original dataset. This seismicity follows a similar trend to the Belham Valley Fault, and proposed dyke orientations for the region (*Hautmann et al.*, 2009; *Mattioli et al.*, 1998).

Previous Research

Miller et al. (2010) relocated this period using *Hypocenter* and the *Rowe et al.* (2004) velocity model with station corrections. Results showed seismicity 3.5 km WNW of Soufrière Hills and at depths of 3–4 km (this used earthquakes that had horizontal and depth errors less than 1 km and 2 km respectively). Focal mechanisms on the 12^{th} August at 18:30 and 19:46 showed normal faulting with WNW-ESE extension, and 2 events later in the day at 20:18 and 20:21 showed NE-SW extension (*Miller et al.*, 2010). Focal mechanisms on the 13^{th} August by *Aspinall et al.* (1998) showed reverse slip and strike slip under St George's Hill, with a NE-SW strike. This is similar to field outcrops in the region, which show a NE orientation (*Miller et al.*, 2010), but different to main fault complexes across Montserrat, which are orientated NNW (*Feuillet et al.*, 2010).

90 degree rotations in focal mechanisms can be interpreted as an inflating dyke (*Roman and Cashman*, 2006); in this case a 90 degree rotation would be a result of stresses induced by inflation of a NW-SE orientated dyke beneath Soufrière Hills (*Smith*, 2013). This would account for the NE-SW extension recorded by *Miller et al.* (2010) and NE-SW strike by *Aspinall et al.* (1998). Later seismicity on the 12^{th} August have p axis parallel to σ_1 (NE/SW), which is suggestive of a propagating dyke (*Ukawa and Tsukahara*, 1996). There is debate between the orientation of the dyke responsible for the Soufrière Hills intrusion, although due to the orientation of geological faults and other research, it is thought the most likely orientation is WNW-ESE (*Baird et al.*, 2015; *Hautmann et al.*, 2009; *Mattioli et al.*, 1998). This is looked at in more detail in section 5.8.3.

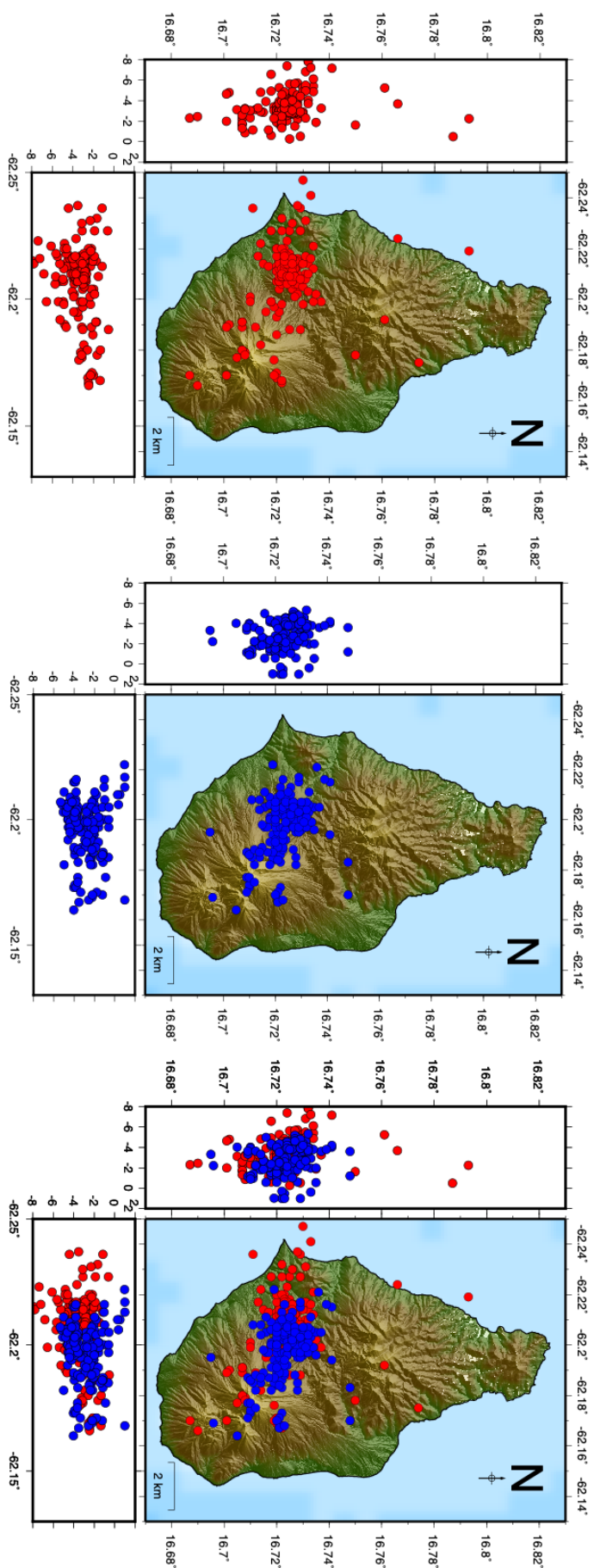

Figure 5.21: Diagram showing relocations from the 11^{th}–14^{th} August 1995 with locations computed by *Aspinall et al.* (1998) (red) and *NonLinLoc* (blue) locations. Diagram shows all locations, and not restricted by errors.

There are several hypotheses for the cause of seismicity under St George's Hill: 1) a response to stress change from a magmatic intrusion, 2) triggering of pre-existing fault structures such as the Belham Valley Fault and Montserrat-Havers Fault System, and 3) disturbance of hydrothermal systems (*Aspinall et al.*, 1998; *Miller et al.*, 2010; *White and McCausland*, 2016). St George's Hill is likely to have less fractures and has undergone thermal alterations, meaning it is more likely to support larger earthquakes, shown by the low b values recorded (*Power et al.*, 1998). V_p gradients extending from Garibaldi Hill to Soufrière Hills are parallel to the Belham Valley Fault, suggesting possible structures in this region (*Miller et al.*, 2010). The most likely cause of the distal seismicity was determined by *Miller et al.* (2010); *Roman et al.* (2008); *Smith* (2013) to be stress changes resulting from an intruding dyke, which altered stress distributions and promoted localised fault movements; although the orientation of the responsible dyke is still argued.

Distal VT seismicity clusters have been shown to occur prior to the onset of the main eruption at volcanoes around the world (*White and McCausland*, 2016). *White and McCausland* (2016) suggested that distal VT clusters are 1) at a distance from the eruption site that is equal to the depth of the distal cluster; 2) activity occurs several months before the onset of the eruption; 3) no systematic migration of hypocenters is recorded through time; and 4) hypocenters align with regional fault lines (*Chicangana*, 2005; *Jones et al.*, 2001; *Legrand et al.*, 2011; *Roman et al.*, 2008). Seismicity at St George's Hill occurred in the months leading up to the effusive part of the eruption where dome building began in September 1995, and is located along the Belham Valley Fault at a distance of 4–5 km from the main eruptive site. This fits with the main criteria proposed by *White and McCausland* (2016).

Interpretations

The relocated seismicity shows a connection between the NW of Soufrière Hills to St George's Hill, suggesting a link between these two locations. Figure 5.22a shows the location of the earthquakes coloured by time to see if there is a migration of seismicity over this 3-day period. Seismicity starts to the NW of Soufrière Hills, and by the 13^{th} August seismicity is predominantly underneath St George's Hill. Looking closer at the 12^{th} August we can see that a large number of earthquakes migrate towards St George's Hill from 4–9pm, after the majority of earthquakes recorded are located beneath St George's Hill (Figure

5.22b).

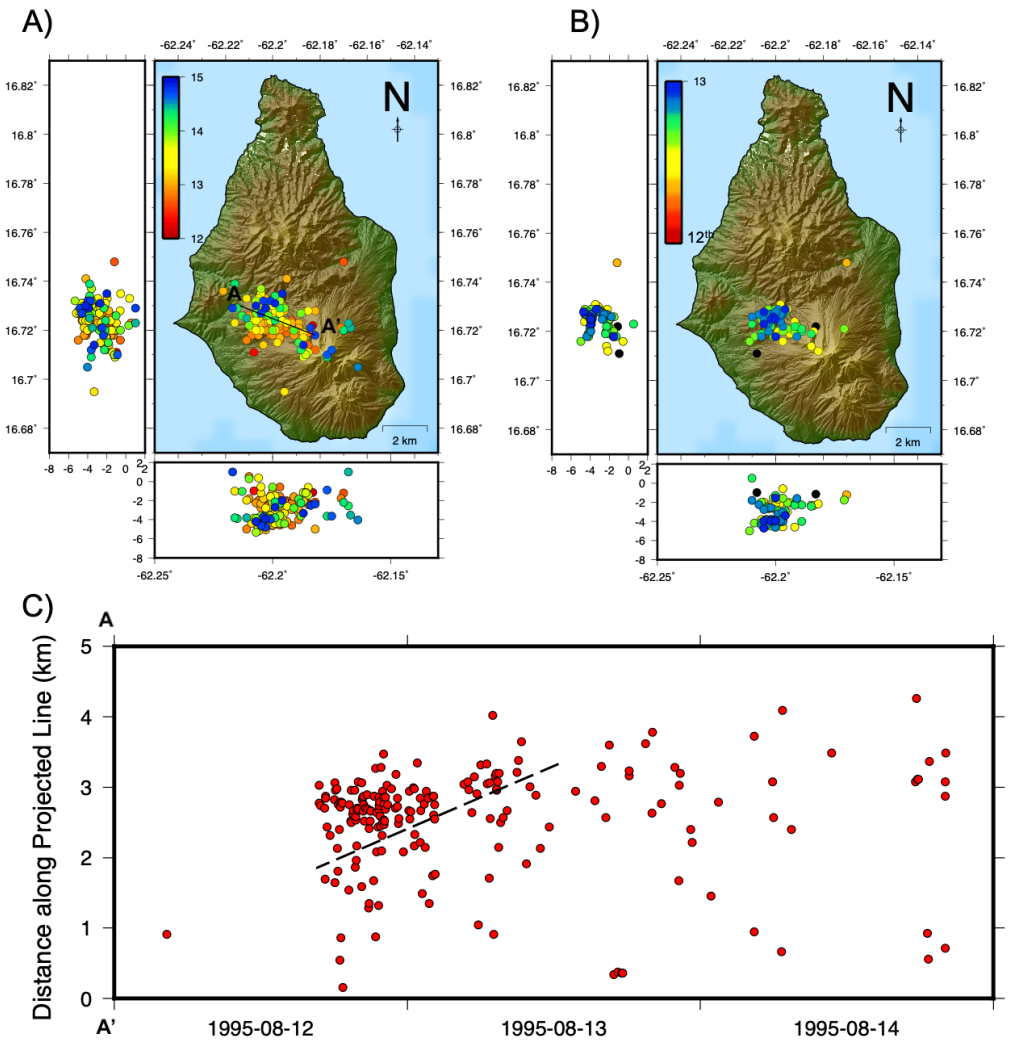

Figure 5.22: A) Diagram showing relocations from the 12^{th}–14^{th} August 1995; locations only shown with errors less than 3 km. Locations are colour coded by time. Black line represents projection taken to plot Figure C; projection taken by eye. B) Reocations coloured by time for the 12^{th} August only; black dots represent events that occurred before 12pm on the 12^{th}. C) Distance along the projected dyke with time to see if there is any correlation in seismicity along the path. All relocations have errors less than 3 km.

A suggestive dyke orientation is plotted in Figure 5.22a; earthquakes along this line within 1 km are plotted in Figure 5.22c to see if there is a propagation of seismicity with time. This dyke orientation was determined by eye to follow the main trend in seismicity during this time period. This follows similar trends found by *Baird et al.* (2015); *Hautmann et al.* (2009) and *Mattioli et al.* (1998), which suggested a dyke orientation varying from NW to WNW. This also follows the trend in volcanic complexes recorded at Soufrière Hills, and

the Belham Valley Fault which extends towards St George's Hill. A slight trend is seen with time, with more seismicity to the NW after the 13^{th} August. A black dashed line shows an estimate for the speed of dyke propagation throughout this time period, with propagation rates estimated to be 0.02 m/s. Propagation rates are likely to be faster as the majority of seismicity moved on the 12^{th} August.

Relocations show a connection of seismicity from Soufrière Hills Volcano towards St George's Hill, which may migrate with time. The location of this seismicity follows faults in the region such as the Belham Valley Fault. It has been shown that VTs on regionally aligned faults, such as the Belham Valley Fault, can be easily triggered by low internal pressures produced by an intruding magmatic body (*Vargas-Bracamontes and Neuberg*, 2012). This could be a plausible reason for the seismicity seen along the fault and at St George's Hill. However, the presence of migration of seismicity with time alongside rotated focal mechanisms are indicative of an inflating dyke (*Roman and Cashman*, 2006). *White and McCausland* (2016) originally proposed that this distal cluster was a result of the local stress field triggering seismicity along faults, however, this assumed no propagation in seismicity.

Focal mechanisms computed by *Aspinall et al.* (1998); *Miller et al.* (2010) show a mixture of dyke inflation and dyke propagation, which could be suggestive of a stalling dyke as it progresses towards St George's Hill. There is a separate geothermal system beneath St George's Hill, which has been shown by increased well temperatures, increased seismic velocities and recent magmatic intrusions (*Ryan et al.*, 2013). St George's Hill is also located at an intersection of two fault systems, which produces zones of crustal weakness that can act as preferential paths for magmatic intrusions (*Faulds et al.*, 2011; *Ryan et al.*, 2013).

Therefore it is likely that this seismicity could be a result of dyke propagation in this region, with an eruption not occurring due to the magma finding a different area of weakness at the final eruptive site of Soufrière Hills. However, it can not be ruled out that seismicity was triggered by changes in local stress fields activating localised faults as suggested by *White and McCausland* (2016). More work further constraining seismicity during this time period, alongside looking at the helicorders to see if there are additional events that could be included, such as microseismic events would be beneficial.

Subsequent seismicity at St George's Hill

In previous research, only the 12^{th}–14^{th} August 1995 were looked at with seismicity underneath St George's Hill, however earthquakes were recorded in the area throughout the rest of August through to October 1995 (Figure 5.23). Sporadic events were seen in the few days after the main migration of seismicity in August, with most of these centred on St George's Hill. Earthquakes in September are eastward of St George's Hill, and in October earthquakes are located between St George's Hill and Windy Hill. Hypocenters on the 13^{th}–14^{th} November 1995 also showed a migration from Soufrière Hills Volcano towards St George's Hill; this is very similar to seismicity seen in August 1995. A small ash cloud was recorded on the 13^{th} November at Soufrière Hills Volcano.

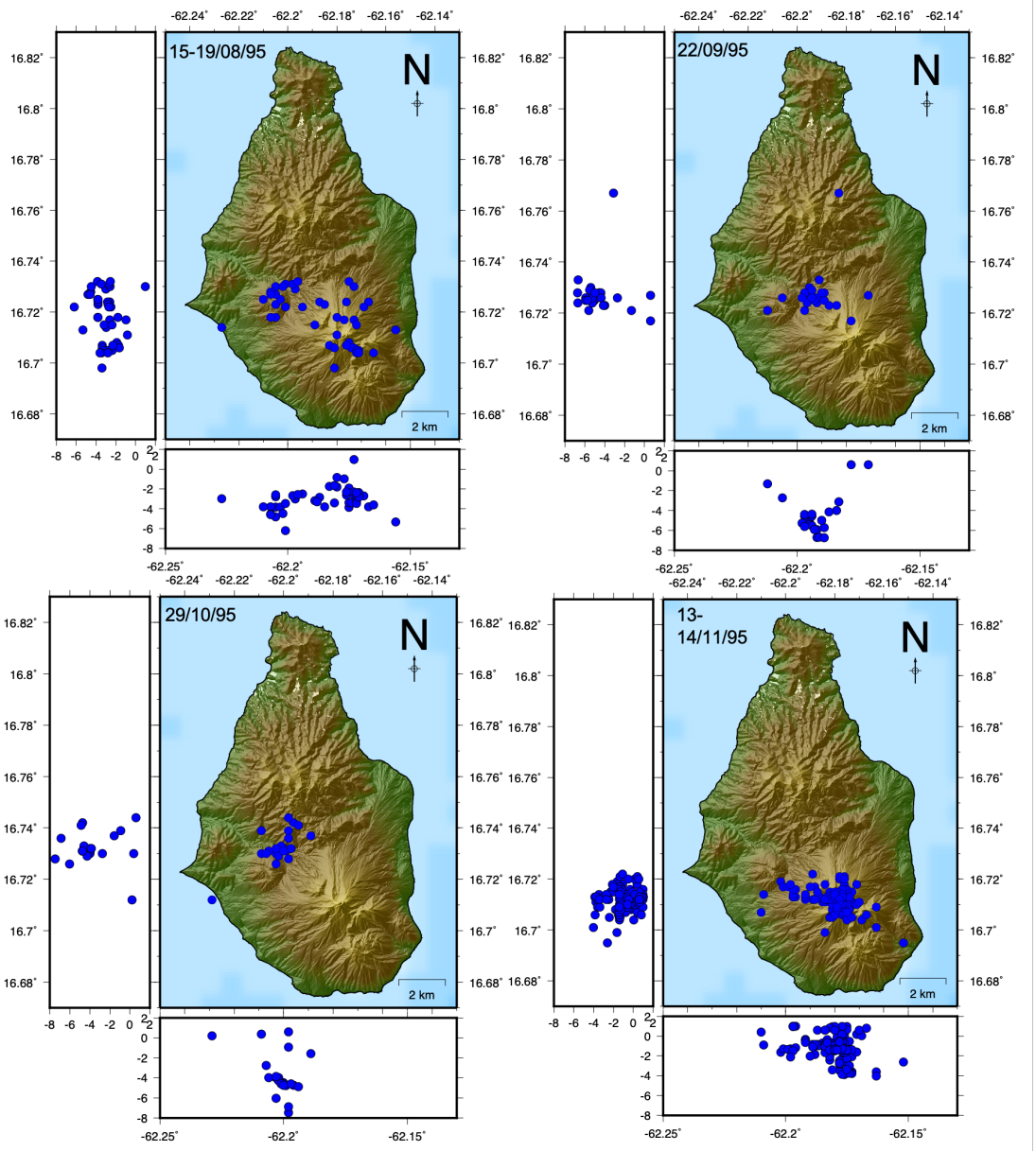

Figure 5.23: Diagrams show relocation of seismicity in 1995 that showed locations in a similar region as the St George's Hill original sequence. Dates are inclusive, and only locations with errors less than 3 km are plotted.

5.3.2 Seismicity to the WNW of Soufrière Hills

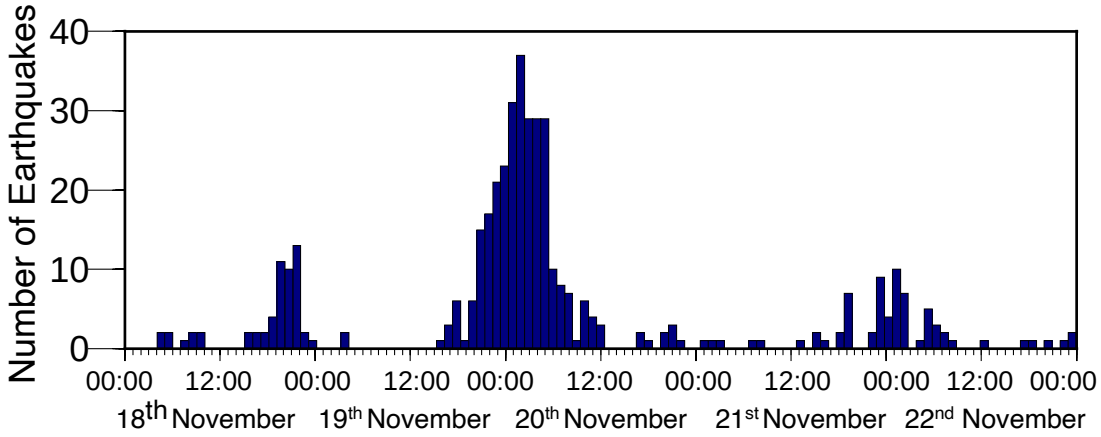

Figure 5.24: Histogram showing the number of earthquakes per hour from the 18^{th} to 22^{nd} November 1995 that were located by *Aspinall et al.* (1998)

A group of earthquakes extending to the WNW from the summit of Soufrière Hills Volcano was recorded from the 18^{th}–22^{nd} November 1995, which was labelled as a separate cluster to St George's Hill by *Miller et al.* (2010); this seismicity was recorded as dome growth initiated. A regional earthquake was recorded on the 19^{th} November at 7.54pm of magnitude 3.5, followed by an increase in local seismicity (Figure 5.24). Relocations show a similar trend in earthquakes to those recorded on the 12^{th}–14^{th} August at St George's Hill (Figure 5.25). Comparison with locations by *Aspinall et al.* (1998) show that relocations are shallower, and located more to the north. Locations do not extend all the way to St George's Hill and instead culminate around Gages village, but still follow a similar trend to the Belham Valley Fault. Hypocenters get shallower as they move towards the south of the island reaching a depth of 2.5 km bsl.

Earthquakes during this time period occurred several hours after activity beneath Soufrière Hills Volcano, but no migration in seismicity was recorded (*Miller et al.*, 2010). *Miller et al.* (2010) interpreted this seismicity as a potential zone of structural weakness resulting from magma ascent. This is a similar interpretation for the St George's Hill seismicity, suggesting these two clusters of earthquakes could have similar mechanisms in the subsurface. However, the two clusters appear to be spatially different, and therefore could be formed from different processes. To understand if these two clusters are from statistically different locations, further analysis is computed in Section 5.3.6.

No migration in seismicity is recorded with time, which was shown for the St George's Hill cluster. This suggest that seismicity in this region could be a result of external pressures reactivating old faults in the region (*Miller et al.*, 2010; *White and McCausland*, 2016). This could be more plausible due to the correlation with dome growth initiation, suggesting there was magma ascent during this time.

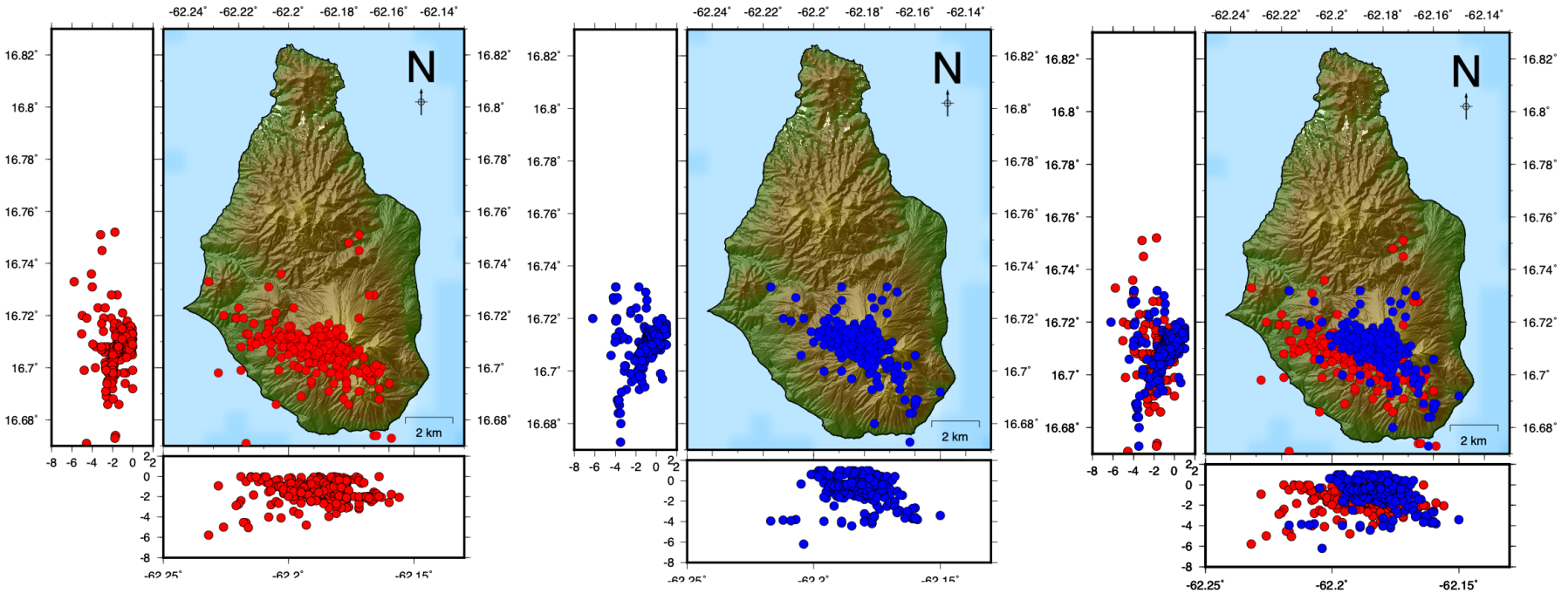

Figure 5.25: Diagram showing earthquake locations from the 18^{th}–22^{nd} November 1995 with *Hypocenter* (blue) and *NonLinLoc* (red) locations, all earthquakes are plotted.

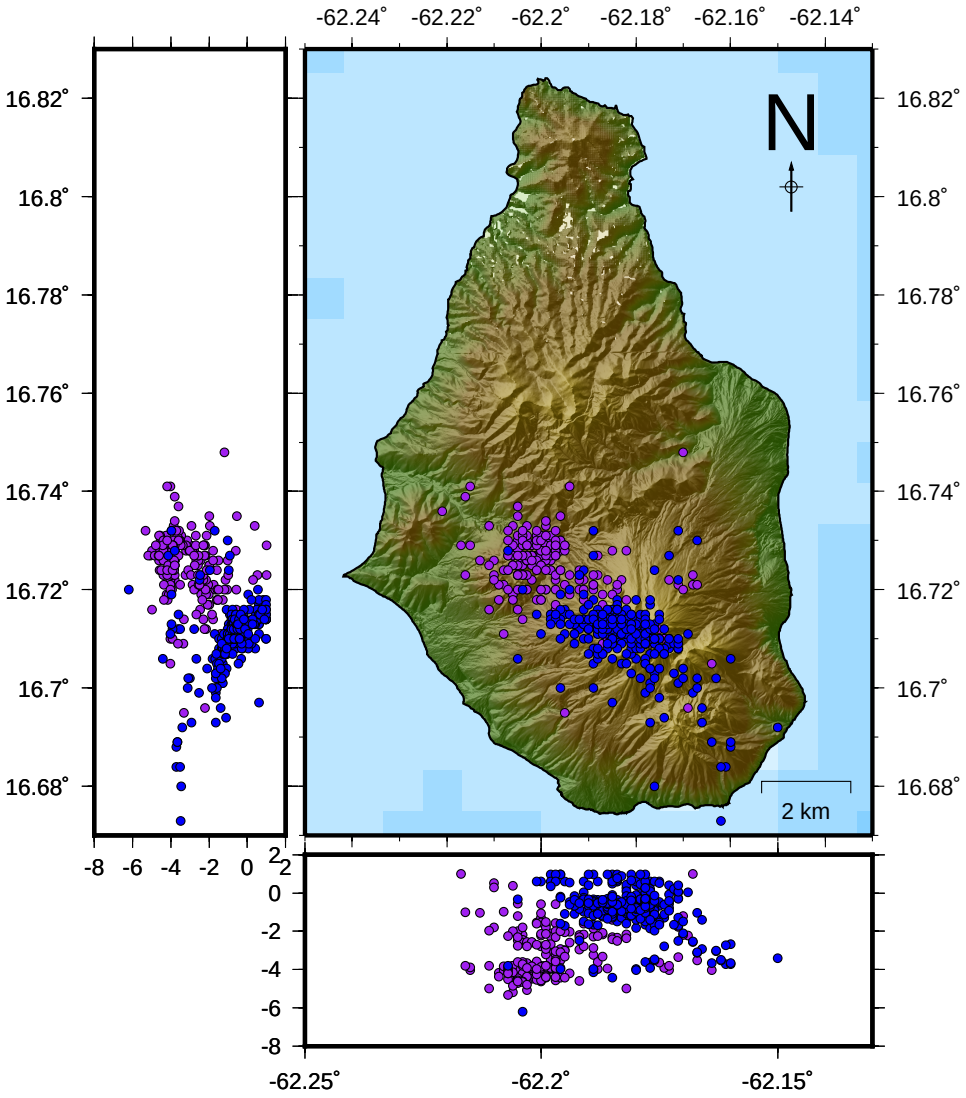

Figure 5.26: Diagram showing relocations from the 18^{th}–22^{nd} November 1995 (blue) and Seismicity from the St George's Hill cluster on the 12^{th}–14^{th} August 1995 (purple). Only earthquakes with errors less than 3 km included.

5.3.3 Windy Hill

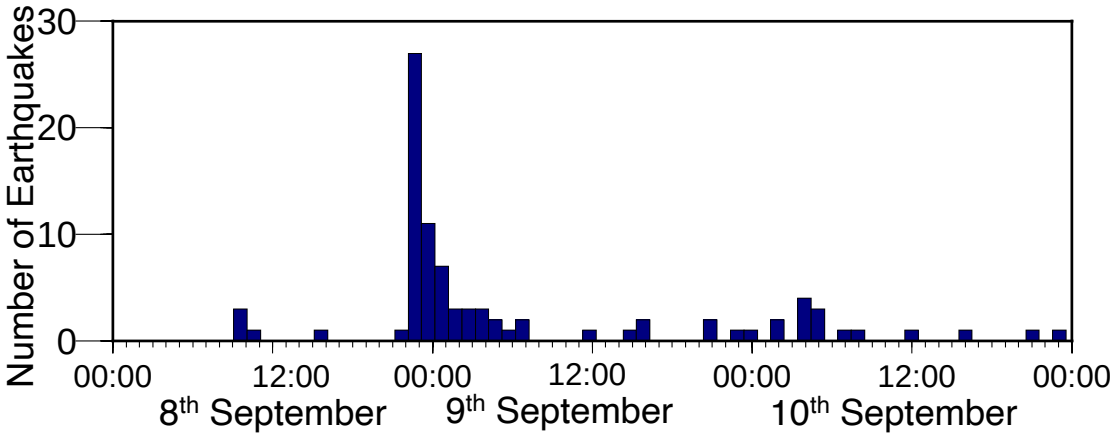

Figure 5.27: Histogram showing the number of earthquakes recorded by *Aspinall et al.* (1998) per hour from the 8^{th} –10^{th} September 1995.

An increase in earthquakes was recorded from the 8^{th}–10^{th} September 1995, centred around Windy Hill. The majority of this seismicity occurred late on the 8^{th} September (Figure 5.27) and locations by *Aspinall et al.* (1998) show this to extend from Soufrière Hills Volcano to the NNW in between St George's Hill and Windy Hill at 2–4.5 km depth (Figure 5.28). Locations by *Miller et al.* (2010) show similar locations with earthquakes located at 2–3 km NNW of Soufrière Hills Volcano, and at depths of 2–4 km. Focal mechanisms computed by *Miller et al.* (2010) are consistent with a N-S orientated fault.

Relocations show hypocenters to be more easterly, directly south of Windy Hill, and extending more to the north; this is deeper at 3–5.5 km depth. There is no progression of earthquakes to the north with time, with only a few earthquakes linking the cluster to Soufrière Hills summit. This makes this cluster quite distinct as the previous two clusters have all originated from the flanks of Soufrière Hills Volcano. This suggests that the distal cluster could have been a result of increased stress due to a magmatic intrusion resulting in localised seismicity on nearby faults (*White and McCausland*, 2016).

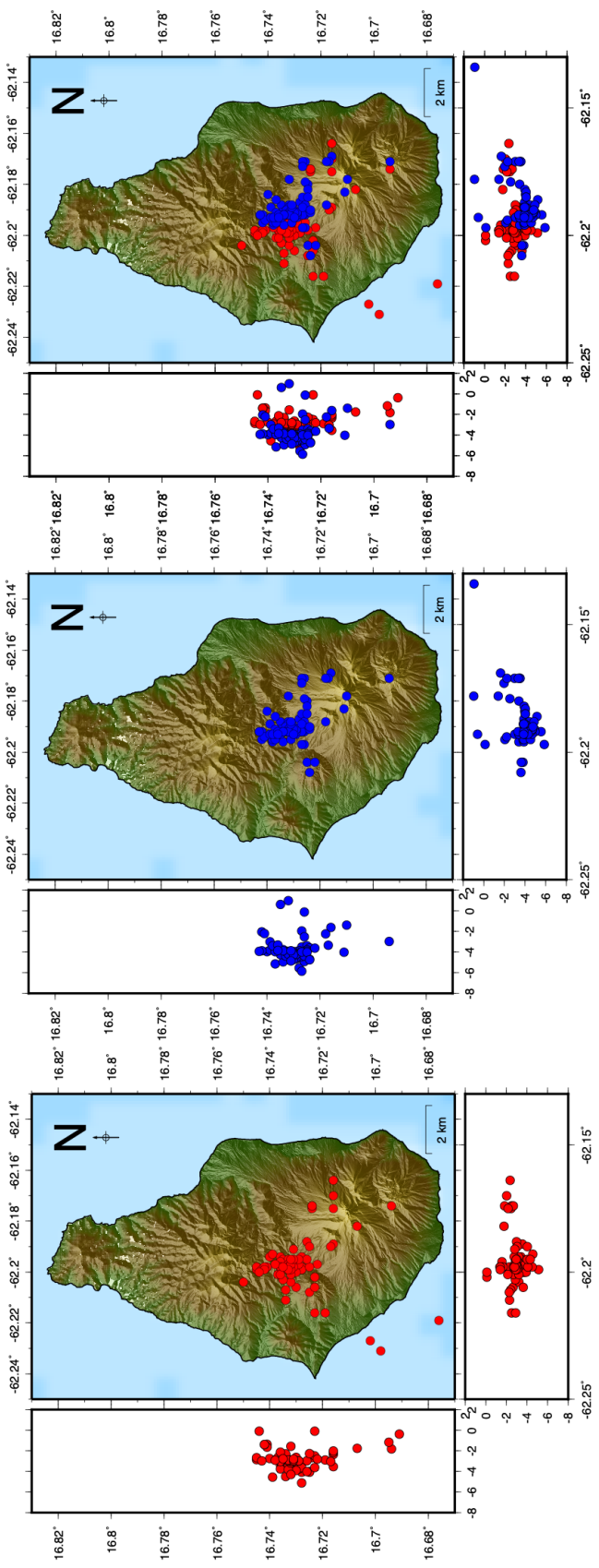

Figure 5.28: Diagram showing locations from the 8^{th}–10th September 1995 for *Hypocenter* (blue) and *NonLinLoc* (red) relocations. All earthquakes are plotted during this time period.

Further seismicity at Windy Hill

Earthquakes were also recorded at Windy Hill during February and July 1996 (Figure 5.29). Earthquakes on the 11^{th} February 1996 shows hypocenters to be in a similar location to September 1995 with locations south of Windy Hill, but with shallower depths of 1–4 km. Two short bursts of activity were recorded in late July, with earthquakes trending from Soufrière Hills Volcano towards Windy Hill. Both of these bursts originate from the southern edge of Soufrière Hills, and extend towards Windy Hill, however hypocenters do not reach as far north as seen in September 1995. On the 20^{th}–21^{st} July earthquakes were relatively shallow at depths 0–2 km, with earthquakes a couple of days later reaching up to 4 km depth. Over 560 small VT earthquakes were recorded on the 20^{th} July from 6–8pm, but these were too small to be located due to difficulties in picking arrival times.

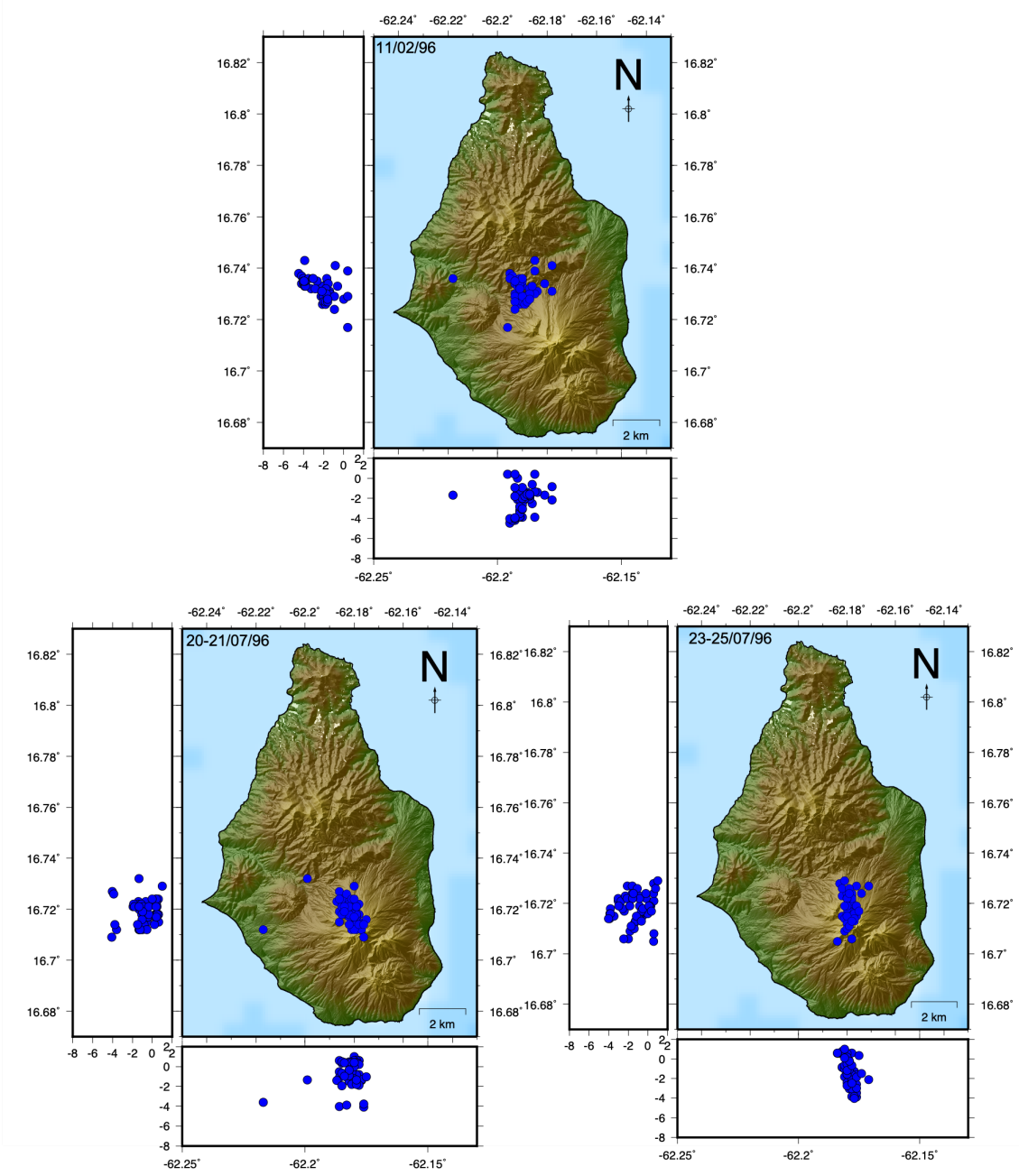

Figure 5.29: Diagram showing relocations from seismicity clusters also seen at Windy Hill. All earthquakes plotted have errors less than 3 km.

5.3.4 NE cluster

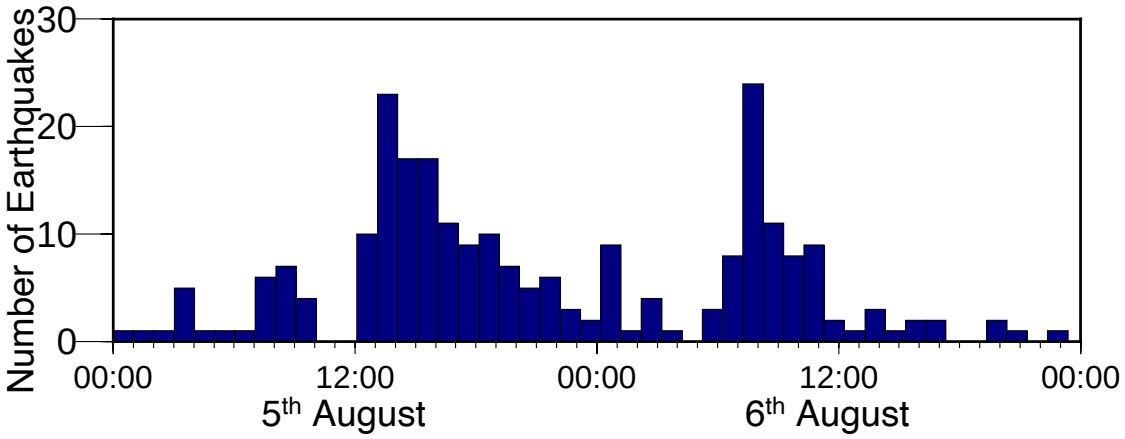

Figure 5.30: Histogram showing the number of earthquakes per hour from the 5^{th}–6^{th} August 1995 that were located by *Aspinall et al.* (1998).

A small cluster of earthquakes that are located extending to the north-east from Soufrière Hills Volcano was recorded on the 5^{th}–6^{th} August 1995. There were two small peaks in seismicity that gradually decreased with time over the two days (Figure 5.30). Original locations by *Aspinall et al.* (1998) suggest a migration of hypocenters from the NE towards Soufrière Hills Volcano (Figure 5.31). This 2-day cluster of earthquakes was repicked by *Roman et al.* (2008) and relocated using the MVO velocity model with *Hypocenter*; locations show a dense cloud of seismicity at 3.5–4.5 km bsl, 2 km NE from Soufrière Hills. *Roman et al.* (2008) did not show a migration in seismicity unlike *Aspinall et al.* (1998); however this was due to *Roman et al.* (2008) using higher quality events with errors less than 1.5 km, compared to events with errors less than 5 km used by *Aspinall et al.* (1998). Locations by *Miller et al.* (2010) (using the Rowe velocity model with *Hypocenter*) show a 4–5 km cluster at 2 km bsl declining in depth towards the NE. Focal mechanisms during this period show dextral strike-slip motion suggestive of a WNW-ENE compression (*Miller et al.*, 2010).

Relocations in *NonLinLoc* show a tighter cluster of hypocenters extending to the NE towards Long Ground (location of Long Ground is shown in Figure 5.19). Depths are constrained to 0.5 km height to 5 km bsl, with a slight deepening to the NE, similar to locations found by *Miller et al.* (2010). Earthquakes do not extend as far to the NE as previously recorded by *Aspinall et al.* (1998); this is likely a result of events being located outside of the station coverage — an issue also seen for the July 2008 dataset, and explored in more detail in

Chapter 6.

Aspinall et al. (1998) proposed that there was a migration in seismicity to the SW towards Soufrière Hills over the two-day period. Figure 5.32 shows the relocated seismicity coloured by time. Initially earthquakes were located near Long Ground and concentrated at depths of 1–4 km. On the 6^{th} August, earthquakes migrated towards the SW, remaining just NW of Soufrière Hills Volcano. *Roman et al.* (2008) proposed that the horizontal error was larger than the radius of the cluster, and so no migration could be justified. Relocated events show the same migration of seismicity using events with errors less than 1.5 km, concluding that this trend is real.

Surface faults at Long Ground show orientations of 68 degrees similar to the trend of seismicity during this period, but perpendicular to regional faults (*Miller et al.*, 2010). A zone of low seismic velocity to the NE is observed, which could be interpreted as an old or active geothermal system (*Ryan et al.*, 2013). This cluster was interpreted as stress changes produced from an ascending NE/NNE trending dyke (*Miller et al.*, 2010; *Roman et al.*, 2008), and could have been a result of a secondary intrusion (*Roman et al.*, 2008). An intruding dyke would have altered stress distributions, promoting localised fault movements, and resulting in distal VT seismicity at Long Ground (*Smith*, 2013; *White and McCausland*, 2016). However, it is unclear why the migration of seismicity moved towards Soufrière Hills, and was not triggered as an increase in seismicity from Soufrière Hills towards Long Ground, as would be expected with a NE trending dyke.

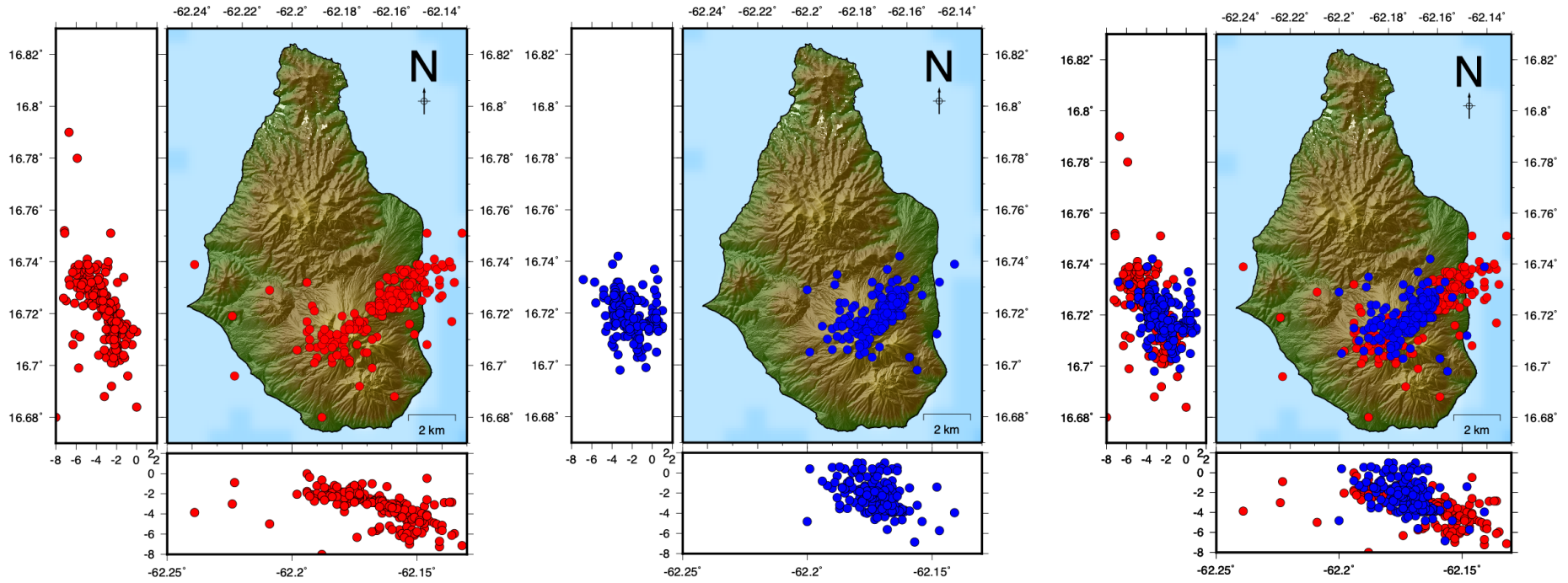

Figure 5.31: Diagram showing locations from the 5^{th}–6^{th} August 1995 with *Hypocenter* (blue) and *NonLinLoc* (red) locations. All earthquakes recorded during this time period are plotted.

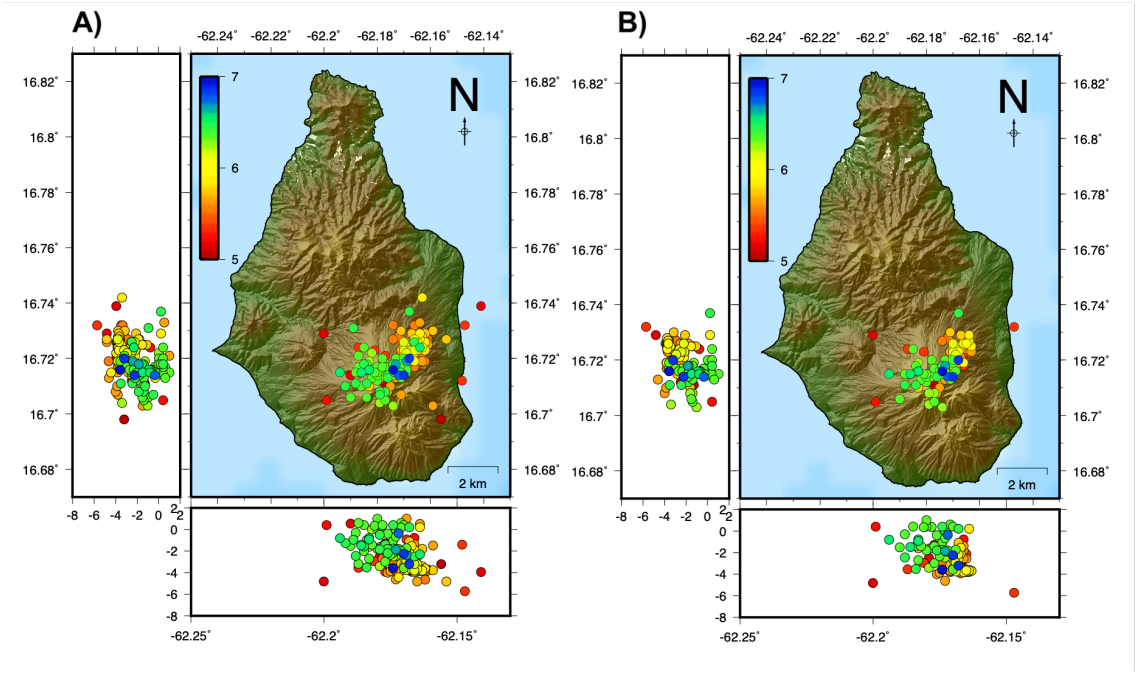

Figure 5.32: Locations of earthquakes from the 5^{th}–6^{th} August 1995 colour coded by time. A) All earthquakes plotted have errors less than 3 km, B) all earthquakes have errors less than 1.5 km.

Further seismicity to the NE

A small cluster of earthquakes were recorded on the 11^{th} October 1995, shown in Figure 5.33. This shows a small number of hypocenters to the north-east, but due to the small number of events, and lack of migration this could not be interpreted as clearly.

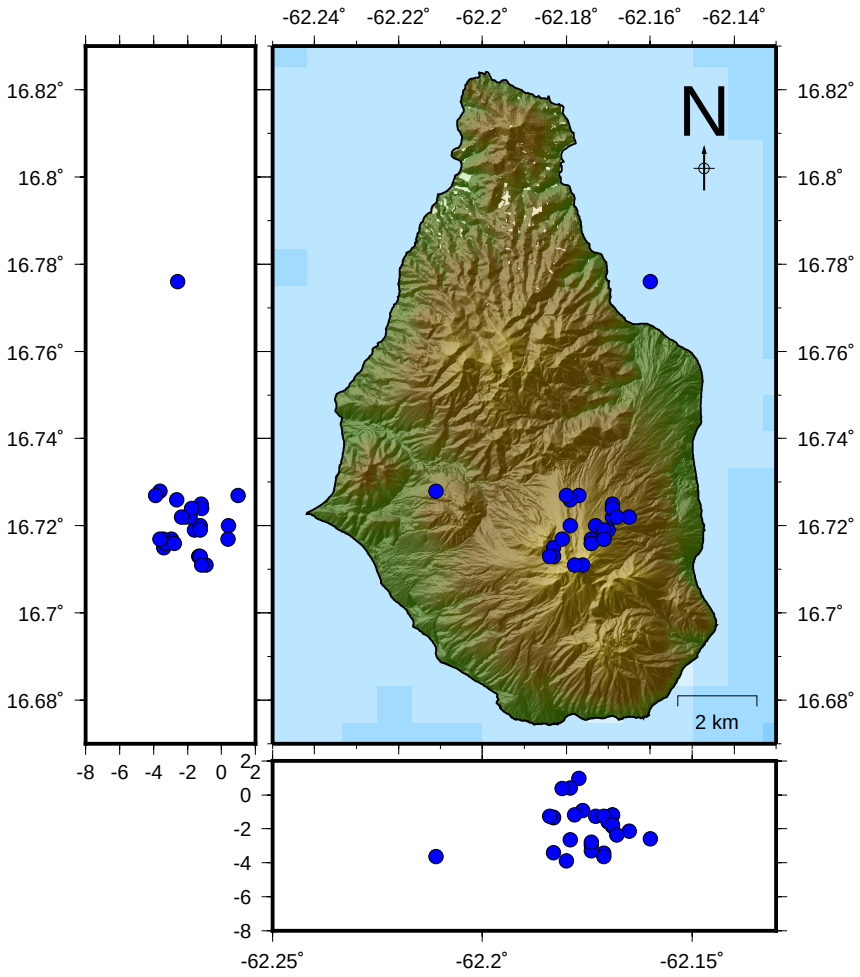

Figure 5.33: Diagram showing locations from the 11^{th} October 1995. All events plotted have errors less than 3 km.

5.3.5 Comparison of Seismicity at Windy Hill and St George's Hill

Seismicity has been analysed at St George's Hill and Windy Hill by *Aspinall et al.* (1998), *Roman et al.* (2008), and *Miller et al.* (2010). However, these have always been interpreted as isolated clusters with no links between the two locations. Relocations in this study have highlighted other time periods where earthquakes are located between St George's Hill and Windy Hill (e.g. 29^{th} October 1995 and 22^{nd} September 1995 (Figure 5.23)). Comparison between the two main clusters of Windy Hill and St George's Hill are shown in Figure 5.34. The two clusters are distinct, with the Windy Hill cluster focussed at 3–5 km and located much further to the east. The St George's Hill cluster is mostly beneath St George's Hill, with some migration in hypocenters towards Soufrière Hills Volcano.

These main clusters were compared with four other clusters that were previously highlighted to be located between St George's Hill and Windy Hill (Figure 5.35). The four clusters are different to each other but do overlap with the St George's Hill and Windy Hill clusters. In particular the white cluster representing the 29^{th} October 1995 in Figure 5.35 has hypocenters located between St George's Hill and Windy Hill. This is very distinct and is the only time period where a clear link between the two is seen. Earthquakes on the 22^{nd} September 1995 (yellow) shows locations to be centred to the east border of the St George's Hill cluster, and on the southern edge of the Windy Hill cluster. The two clusters in 1996 (blue and purple) show no link with St George's Hill, and extend from Windy Hill to Soufrière Hills almost in two segments. This could suggest there is a similar mechanism here to the Windy Hill cluster.

The presence of seismicity linking the two main clusters together, alongside seismicity between these two regions suggests that these may be linked. Seismicity at St George's Hill is thought to be either a result of stress changes from a magmatic intrusion at Soufrière Hills Volcano, or dyke propagation in this geothermally active region (*Aspinall et al.*, 1998; *Miller et al.*, 2010). Pre-existing structures such as the Belham Valley Fault are likely to be triggered by internal pressures from an intruding magmatic body, resulting in seismicity seen along this fault (*Vargas-Bracamontes and Neuberg*, 2012). The link in seismicity between Windy Hill and St George's Hill is looked at in more detail in Section 5.3.6.

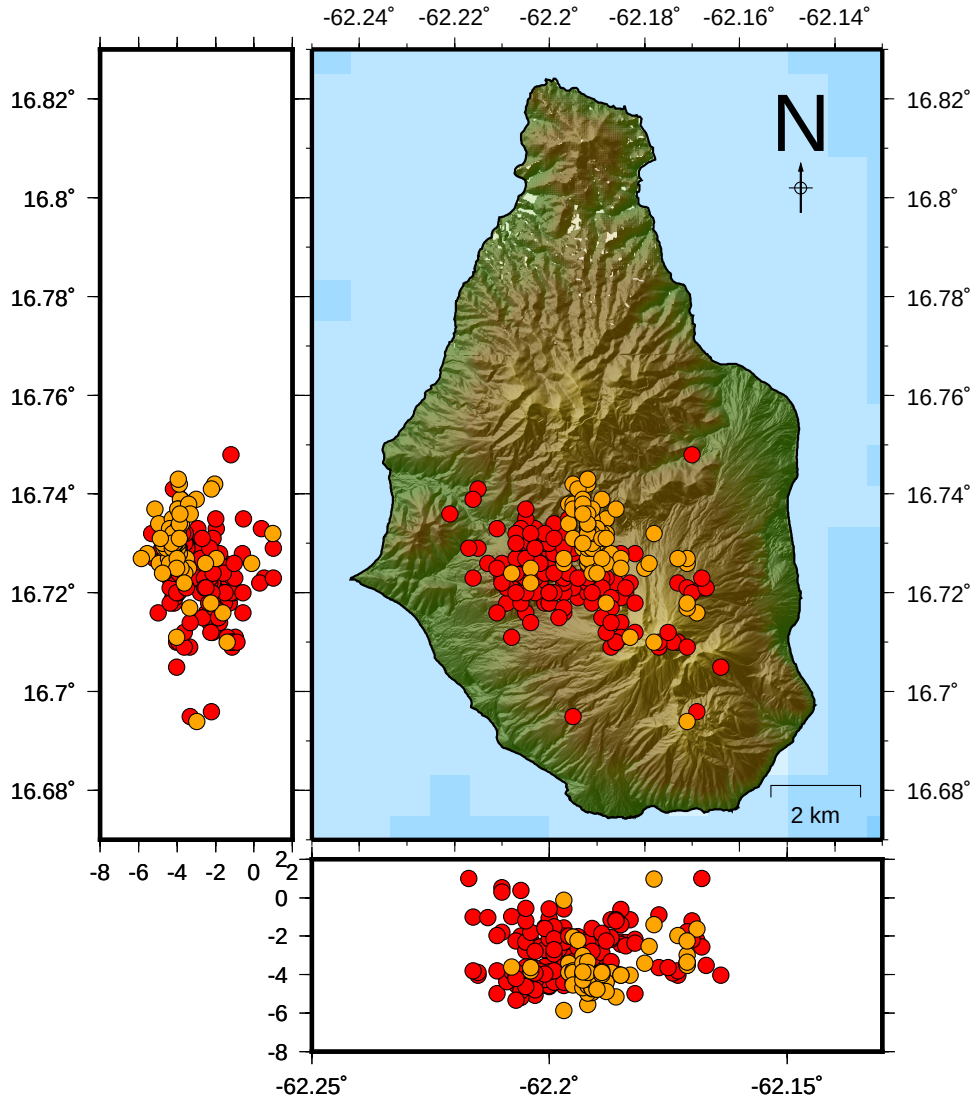

Figure 5.34: Location of seismicity colour coded per cluster for seismicity at SGH and WH. Red — 11^{th}–14^{th} August 1995; orange — 8^{th}–10^{th} September 1995. Only earthquakes with errors less than 3 km are plotted.

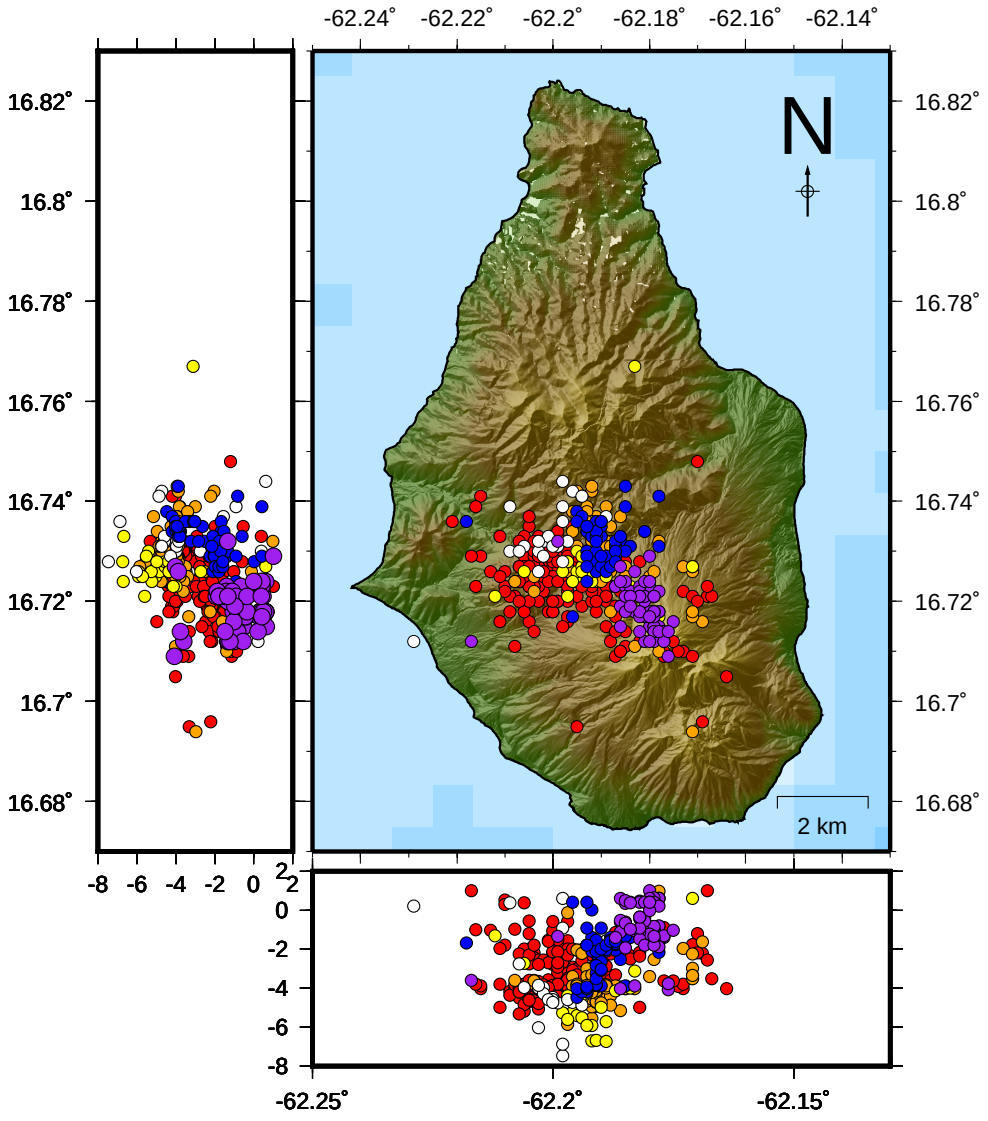

Figure 5.35: Location of seismicity colour coded per cluster for seismicity at SGH and WH. Red —11^{th}–14^{th} August 1995; orange — 8^{th}–10^{th} September 1995; yellow — 22^{nd} September 1995; white — 29^{th} October 1995; blue — 11^{th} February 1996; purple — 20^{th}–21^{st} July 1996. Only earthquakes with errors less than 3 km are plotted.

5.3.6 Cluster Analysis

In section 5.3.5, several distal clusters of earthquakes were highlighted, with clusters having shared locations between St George's Hill and Windy Hill. A statistical test was run to compare every distal cluster that has been highlighted so far from 1995 to 1996, to see if any locations are statistically similar. Clusters have been determined by time only, which have been highlighted in Sections 5.3.1 to 5.3.4; a cluster is defined as having over 10 earthquakes in a 1–2 day period that are located in a region distal to Soufrière Hills Volcano. This means time is the only factor separating earthquakes in these locations, removing any human preference of events. All locations within the dates are kept, including time frames when earthquakes were also recorded elsewhere during the same time window. Each cluster is tested against each other to see if they are significantly different. Any two periods that are shown to be statistically the same can then be grouped together for further analysis.

The following time periods are defined as individual distal clusters:

- Cluster 1: 11^{th}–14^{th} August 1995 (SGH cluster)
- Cluster 2: 8^{th}–10^{th} September 1995 (WH cluster)
- Cluster 3: 22^{nd} September 1995
- Cluster 4: 29^{th} October 1995
- Cluster 5: 11^{th} February 1996
- Cluster 6: 20^{th}–21^{st} July 1996
- Cluster 7: 15^{th}–19^{th} August 1995
- Cluster 8: 13^{th}–14^{th} November 1995
- Cluster 9: 18^{th}–22^{nd} November 1995
- Cluster 10: 23^{rd}–25^{th} July 1996
- Cluster 11: 5^{th}–6^{th} August 1995
- Cluster 12: 11^{th} October 1995

Data was not normally distributed, and therefore a non-parametric ANOVA test is most suitable so that each cluster could be compared with each other: for this a Kruskall-Wallis test was used. This is a non-parametric method which tests if samples from each subset originate from the same distribution; in this case it tests if earthquakes in each cluster are from the same region. This test compares each X, Y and Z component of the location separately, and all together to see if there was any significant difference in location between the clusters. If no significant change in location is shown by the statistical test then it can be assumed that the two clusters are from the same location.

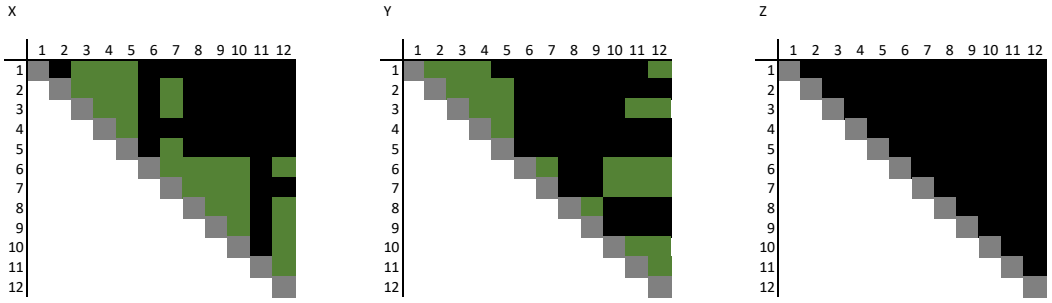

Figure 5.36: Diagram showing the results from the statistical test for the X, Y and Z locations. Green represents an area of no statistical difference, and black represents an area of significantly different locations.

Results from the statistical test are shown in Figure 5.36, with black representing clusters that have a statistical difference in location, and green no statistical difference — i.e that the two clusters are from the same location. For the Z location we see that there is a statistical difference between every cluster, where there are some similarities between clusters for the X and Y location. The reason for this could be that the Z location is harder to constrain, and is normally associated with larger errors. It is likely that the depth locations would overlap when accounting for errors, but with the statistical test it does not take this into account. To aid viewing which clusters have similar locations, the results were combined for X and Y locations, so that only those that show no statistical significance in location between X and Y are coloured as green: this is shown in Figure 5.37.

Results using the combined XY statistical test show that the following clusters can be put into three groups where there are statistical similarities in locations. These are defined as mega-clusters; the timings of these are shown in Figure 5.38:

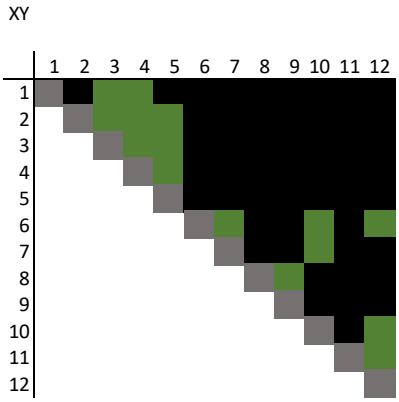

Figure 5.37: Diagram showing the results from the statistical test for the X and Y location combined. Green represents an area of no statistical difference, and black represents an area of significantly different locations.

- Mega-Cluster 1: Clusters 1, 2, 3, 4 and 5
- Mega-Cluster 2: Clusters 6, 7, 10, 11 and 12
- Mega-Cluster 3: Clusters 8 and 9

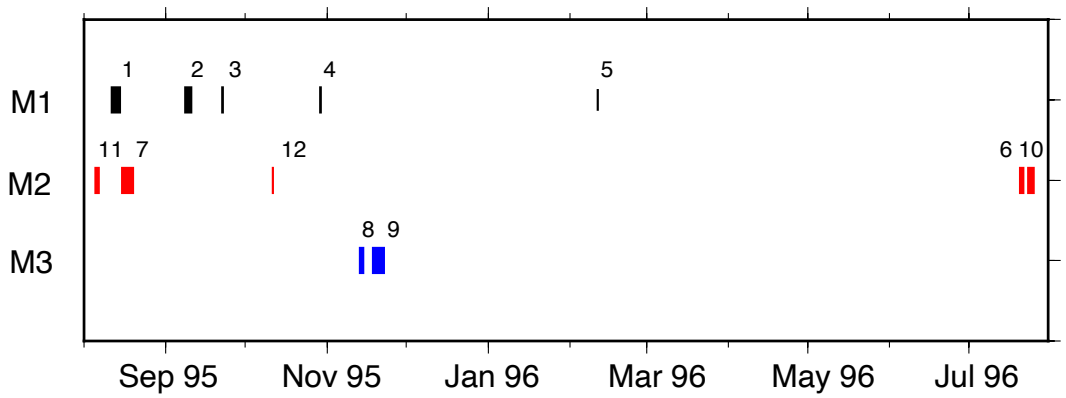

Figure 5.38: Timeline showing when each distal cluster occurred for each megacluster. Numbers represent cluster ID, and M1–M3 represent Mega-Cluster 1 to Mega-Cluster 3.

If these three mega-clusters are statistically distinct from each other, then we can group all clusters in a mega-cluster together to say that these are from a statistically similar location, and hence may have the same source or process causing them. The same statistical test was performed but using grouped locations from each cluster responsible for the mega-cluster, so that there were 3 groups being compared against each other. Results showed that all

three mega-clusters are statistically significant in all three components; this means we are able to interpret the mega-clusters with confidence that these are distinct clusters.

As the depth locations showed statistical significance for all clusters, it was decided to look at the ranges in depths to see if there were any overlaps for this. Depth locations normally have larger errors and are not as well constrained as X and Y locations. Mega-cluster 1 (clusters 1–5) show depths that are relatively similar to each other with the exception of cluster 2, which is slightly deeper (Figure 5.39). Clusters 8 and 9 from mega-cluster 3 have mostly overlapping depths but do have a strong difference in the mean value. Mega-cluster 2 shows a strong variety in depths mostly seen from cluster 7.

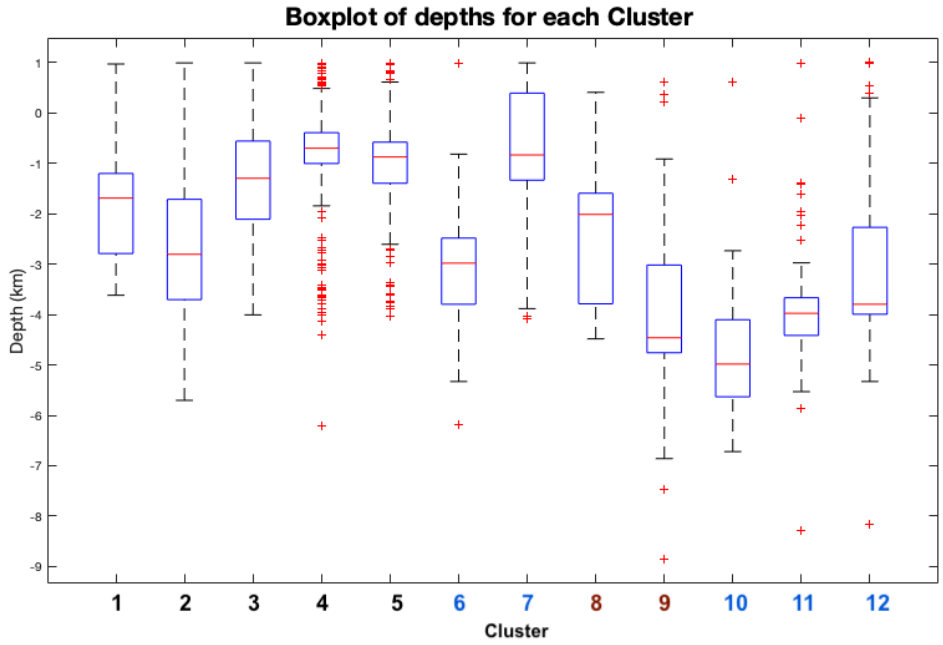

Figure 5.39: Boxplots showing the range in depth locations for each cluster. Red line represents the median value, with outer edges of the box relating to the 25^{th} and 75^{th} percentile. Black Numbered clusters refer to Mega-Cluster 1, Blue numbered clusters refer to Mega-Cluster 2, Red numbered clusters refer to Mega-Cluster 3.

Interpretation of Mega-clusters

Figure 5.40 shows how the different clusters are linked to each other from the statistical test. Not every cluster in a mega-cluster is linked to every other cluster, which can make interpreting the results more complex.

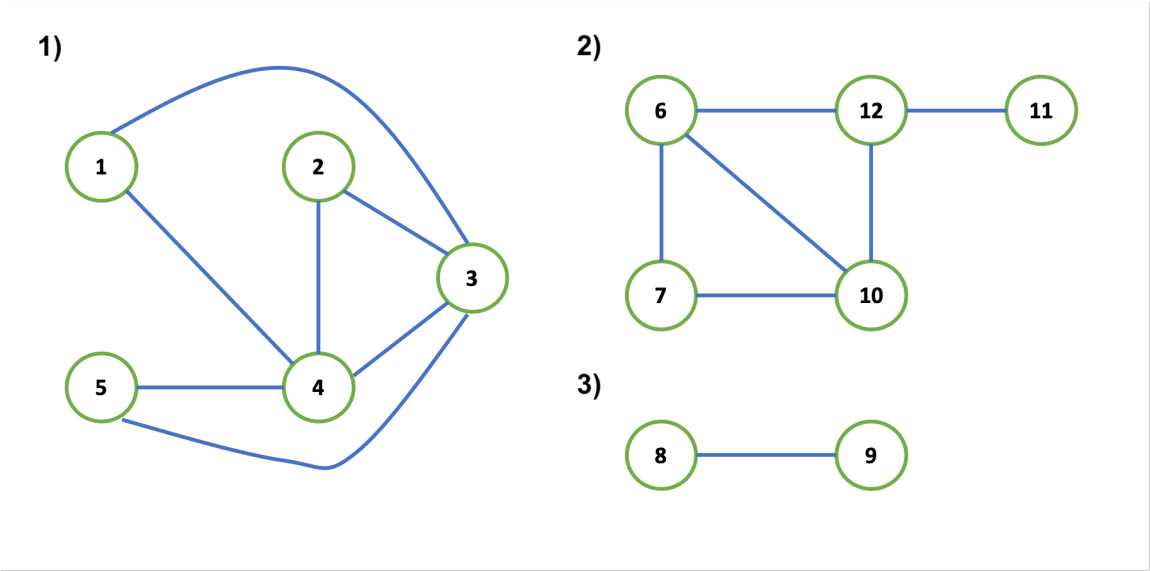

Figure 5.40: Diagram showing the links between different clusters for each mega-cluster. A connection between two clusters shows that there is no statistical difference between these.

Mega-Cluster 1

Mega-cluster one contains five time periods of seismicity from August 1995 to February 1996. Cluster 1 relates to the main St George's Hill cluster recorded on the 11^{th}–14^{th} August 1995, and Cluster 2 relates to the main Windy Hill cluster on the 8^{th}–10^{th} September 1995. Clusters 3 and 4 were both thought to be related to St George's Hill, and this has been shown through the statistical test. Cluster 5 was thought to be related to Windy Hill. The analysis shows that Cluster 5 does have similar locations to the Windy Hill cluster (cluster 2), but also to Clusters 3 and 4, which were related to St George's Hill. Locations for these five clusters are shown in Figure 5.41.

Earthquake locations are mostly between St George's Hill and Windy Hill, with only a few events located on the flanks of Soufrière Hills Volcano (Figure 5.42). Combining the five clusters does not highlight any additional features when looking in map view. Comparing the depth of earthquakes from the five clusters only, we can see that depths are mostly consistent, with a potential shallowing for the last cluster recorded in February 1996. Depths

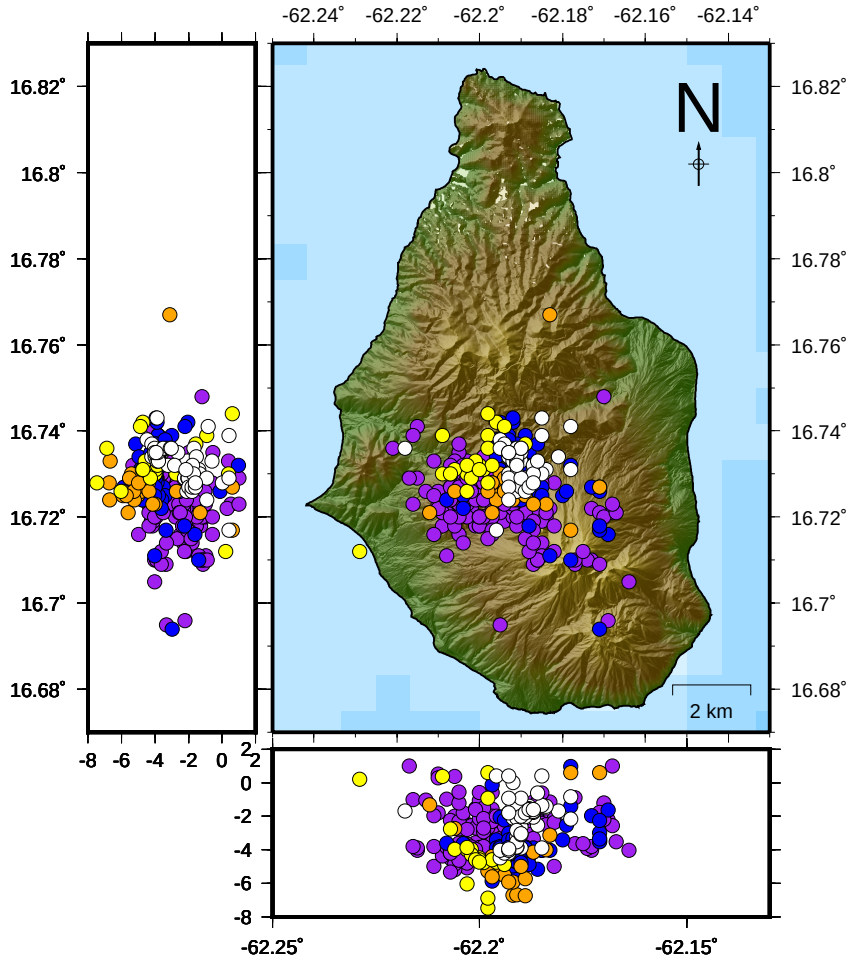

Figure 5.41: Location of seismicity for mega-cluster 1. Purple = Cluster 1 (11^{th}–14^{th} August 1995), Blue = Cluster 2 (8^{th}–10^{th} September 1995), Orange = Cluster 3 (22^{nd} September 1995), Yellow = Cluster 4 (29^{th} October 1995), White = cluster 5 (11^{th} February 1996). All earthquakes with errors greater than 3 km are removed.

are mostly on the range of 1–5 km bsl, although this extends towards 6 km bsl in some clusters (Figure 5.43).

The results were studied in 3D to see if any additional features were highlighted; a screenshot from this is shown in Figure 5.44. Most notably, it can be seen that not many events are being located beneath Soufrière Hills, with the majority of earthquakes located at distal zones at a wide range of depths. There is an increased concentration of seismicity at 3–4.5 km depth; comparing this with Figure 5.42, a band of seismicity is seen at this depth, that extends towards the NW flanks of Soufrière Hills Volcano. This could be indicative of seismicity being triggered along faults that are orientated in this zone. However, this could also be seismicity only recorded in the St George's Hill original cluster, that showed a propagation in seismicity with time along this path, suggestive of dyke propagation.

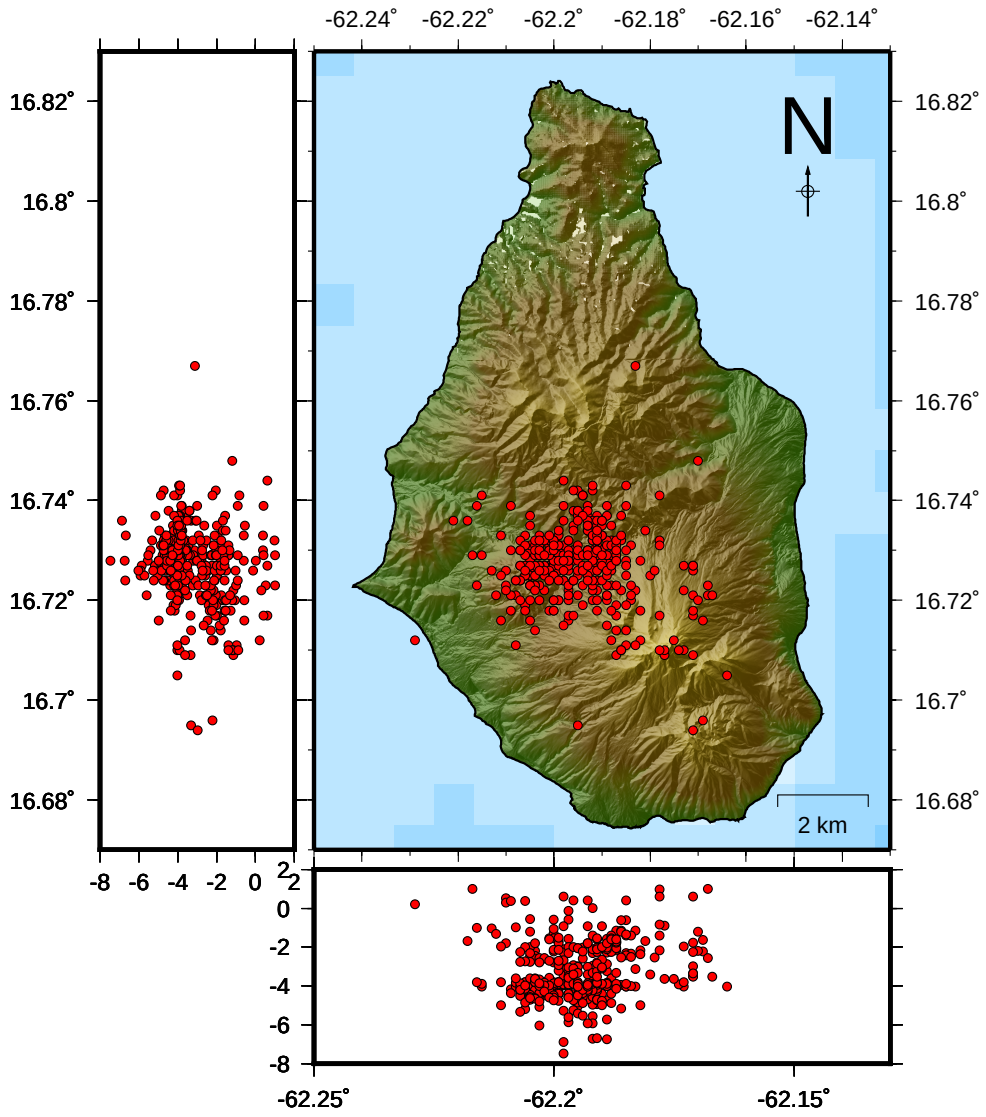

Figure 5.42: Location of seismicity for mega-cluster 1; earthquakes with errors greater than 3 km have been removed

Comparison of locations with the 3D tomography model from the SEA-CALIPSO project (*Shalev et al.*, 2010) show that seismicity at Windy Hill is located along a high V_p region that extends north-south from Centre Hills; this is thought to be structurally controlled (*Miller et al.*, 2010). Seismicity at Windy Hill is thought to have evolved from similar mechanisms to that of St George's Hill. *Miller et al.* (2010) proposed that a NNE trending intruding dyke would result in a contractive strain over St George's Hill and Windy Hill, which is also consistent with focal mechanisms recorded under St George's Hill and Windy Hill. This is consistent with orientations proposed by *Roman et al.* (2008), but differs from other geophysical studies. This also does not fit with results from this study, which propose a NNW trending dyke.

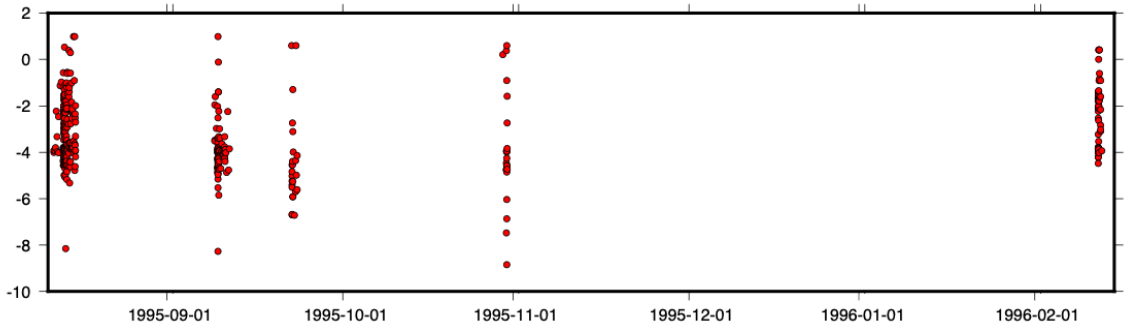

Figure 5.43: Depth of seismicity for mega-cluster 1 through time; events with errors greater than 3 km have been removed.

The reactivation of seismicity in this area suggests that similar processes were occurring each time. The hypothesis that seismicity at distal clusters occurs during magmatic intrusion at a different site would fit for the different clusters seen. This suggests that as magma rose throughout the time period, different faults were triggered, and as the eruption continued and stabilised, there was then a reduction in distal clusters. However, dome building had begun by February 1996, with a change to hybrid seismicity recorded by this point, indicating that the system had equilibrated with the surrounding country rock (*Aspinall et al.*, 1998; *Roman et al.*, 2008).

The presence of a distal cluster after a reduction of VT seismicity would be less likely, and therefore other processes may have been occurring during this time. It could be possible that increased magma flux increased pressures in the magmatic system, resulting in the triggering of distal clusters (*White and McCausland*, 2016). Or, extra magma flux could have reactivated dyke propagation originally seen on the 11^{th}–14^{th} August 1995; however, this is dependent on the original mechanism for this sequence. More research looking at microseismicity in this region, and modelling of increased magma flux on local fault systems would be needed to confidently interpret seismicity during this time period.

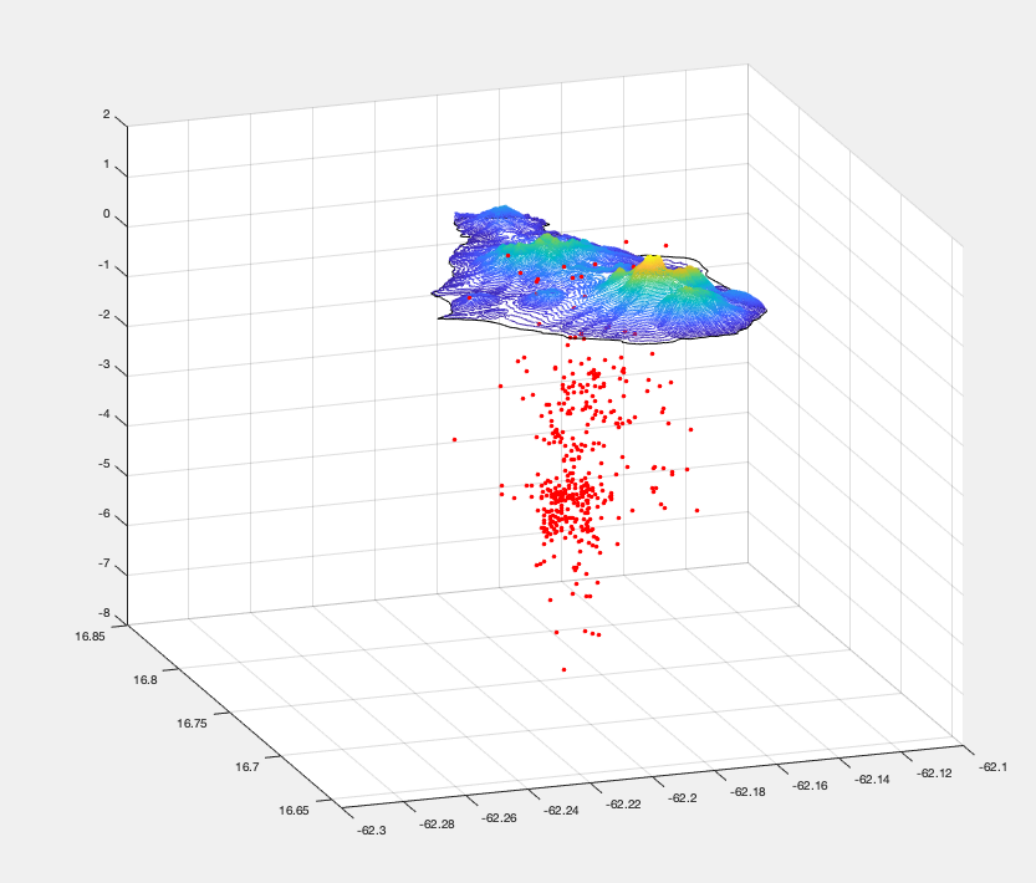

Figure 5.44: Depth of seismicity for mega-cluster 1 in 3D beneath Montserrat; events with errors greater than 3 km have been removed.

Mega-Cluster 2

Mega-cluster 2 is more complex, as fewer clusters link together. Cluster 11 is the main NE cluster recorded on the 5th–6th August 1995; this shows similarities with Cluster 12, which was thought to show a similar trend to the main NE cluster. However, Cluster 12 also shows similar locations to Cluster 6 and Cluster 10. Both Clusters 6 and 10 were originally thought to be in similar location to the original WH cluster, but both of these show a statistical difference to Cluster 2 (Windy Hill). Clusters 6, 7, and 10 all show similarities with each other, suggesting an overlap in mechanisms. These locations are plotted in Figure 5.45. Due to mega-cluster 2 not having at least two links between each cluster, it was decided not to investigate this mega-cluster further.

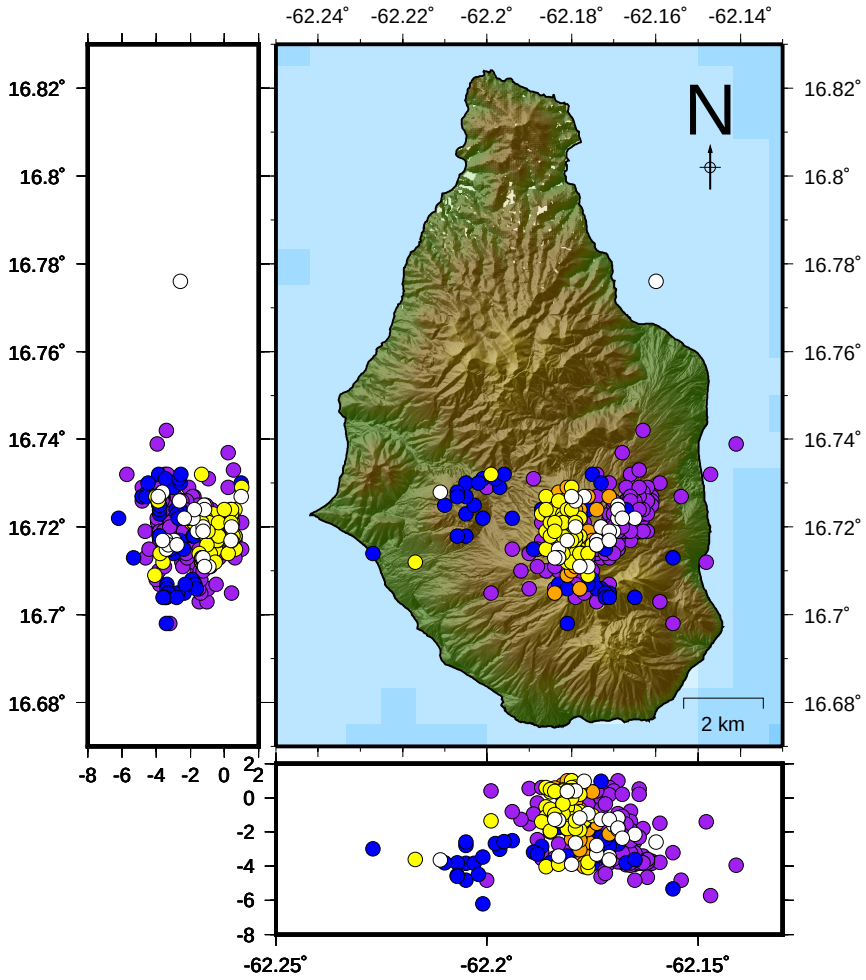

Figure 5.45: Location of seismicity for mega-cluster 2. Purple = Cluster 11 (5th–6th August 1995), Blue = Cluster 7 (15th–19th August 1995), Orange = Cluster 10 (23rd–25th July), Yellow = Cluster 6 (20th–21st July 1996), White = cluster 12 (11th October 1995). Earthquakes with errors greater than 3 km have been removed.

Mega-Cluster 3

Clusters 8 and 9 represent the 13^{th}–14^{th} November 1995 and 18^{th}–22^{nd} November 1995 respectively, their locations are shown in Figure 5.46. Both of these clusters occurred within a few days of each other suggesting that there is likely the same mechanism responsible for both of these clusters. Locations show a WNW trend in seismicity; this runs parallel to the St George's Hill seismicity but is located more to the south (Figure 5.47). Locations are mostly at a depth of 0.5-2 km bsl.

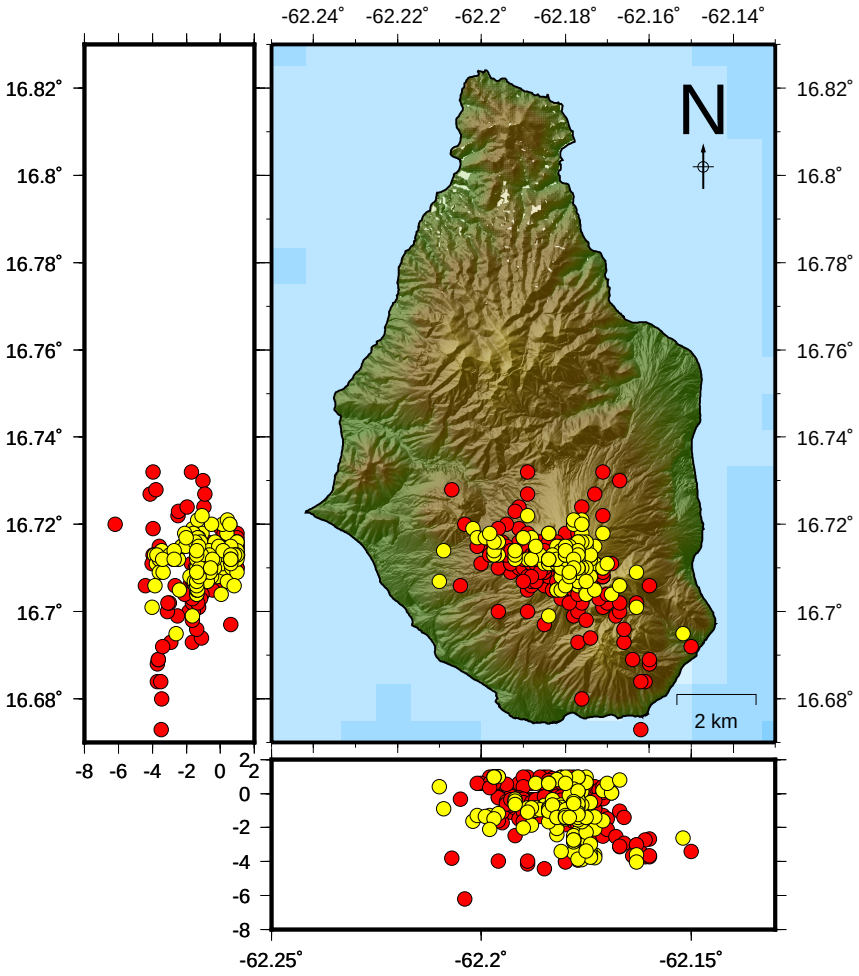

Figure 5.46: Location of seismicity for the third mega-cluster. Red represents seismicity from cluster 9 (18^{th}–22^{nd} November 1995), and yellow represents cluster 8 (13^{th}–14^{th} November 1995). Earthquakes with errors greater than 3 km have been removed.

No trend in hypocenters is seen with time (Figure 5.48). A projection was taken along the length of the WNW seismicity cluster at about 4 km long (shown by the black line in Figure 5.48). Earthquakes along the distance of this projection are then plotted through time to see if there is a progression in earthquakes to the WNW. Seismicity during the beginning

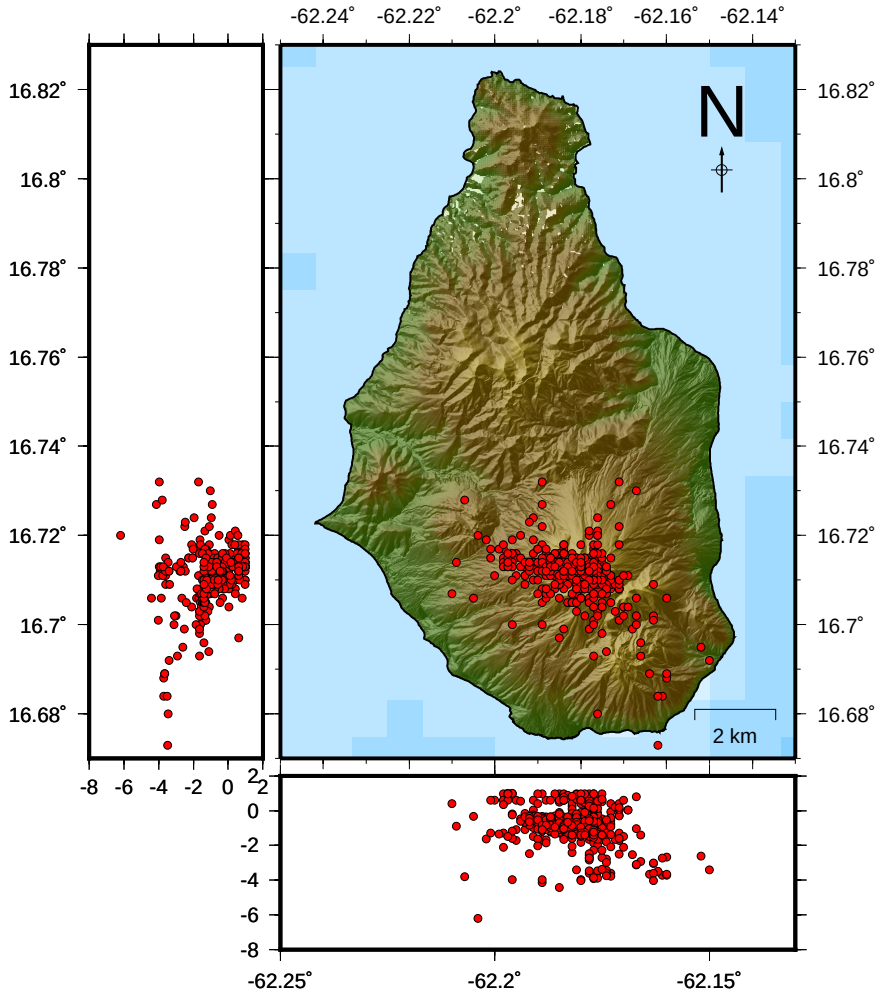

Figure 5.47: Location of seismicity for the third mega-cluster; earthquakes with errors greater than 3 km have been removed

of the mega-cluster is mainly beneath Soufrière Hills Volcano with just a few events to the NW. As time progresses more events are recorded along the NW trend. Six distinct periods of increased seismicity along this path are seen over the 10 days, with the fifth period showing increased seismicity; this period also had the most focussed depth locations at 0–1.8 km bsl.

Seismicity is mostly constrained in depth during this mega-cluster reaching depths up to 4 km, with only a small number of events being located above sea level. Increase in seismicity in this region coincided with dome growth initiation. Additionally no propagation of seismicity with time was recorded, suggesting seismicity in this region could be a result of external pressures reactivating faults (*Miller et al.*, 2010; *White and McCausland*, 2016).

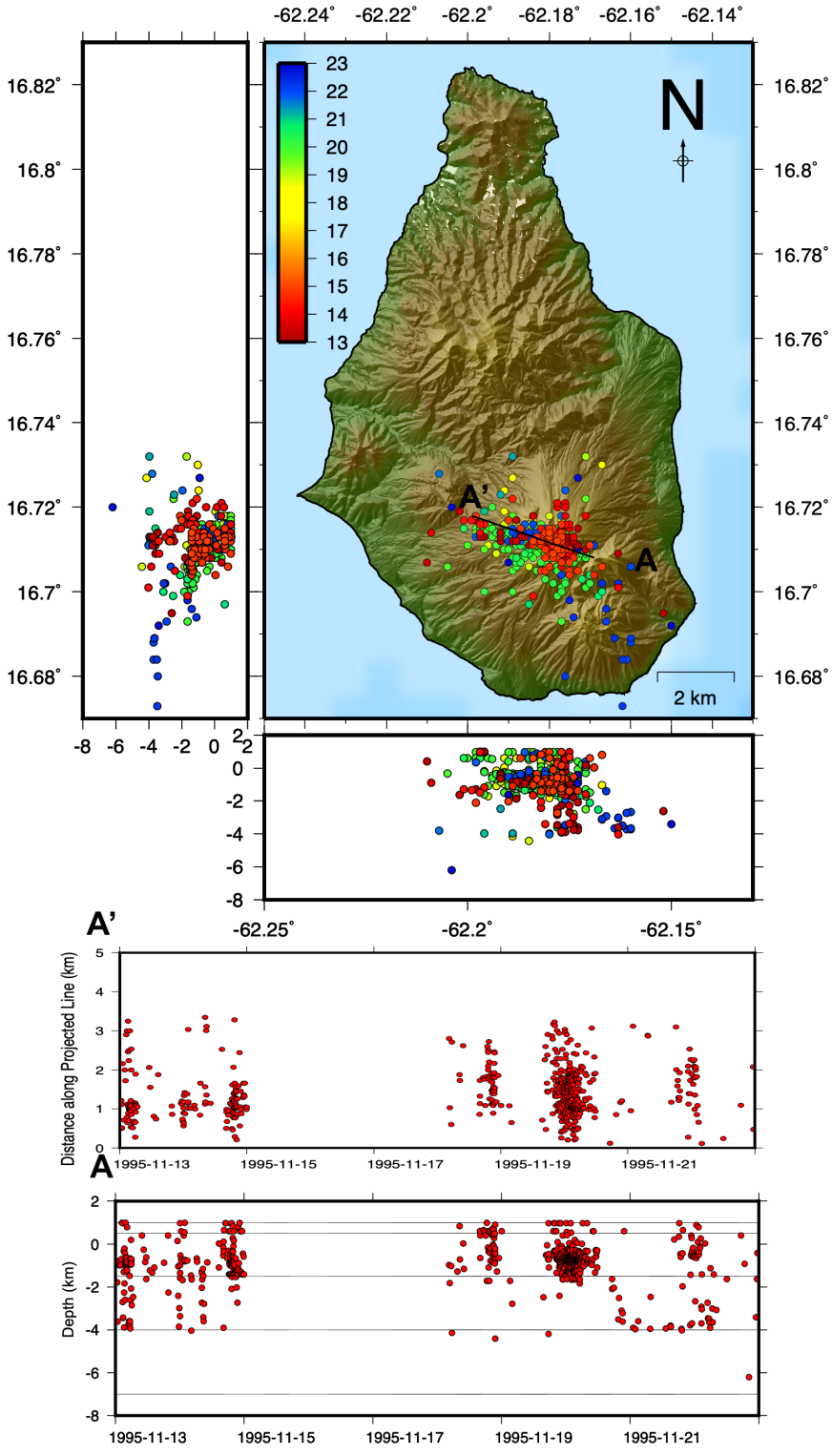

Figure 5.48: Top Panel: Location of seismicity during mega-cluster 3 coloured by date. Black line represents the projection taken to see if there is a trend with time. Middle Panel: Location of seismicity along projection with time for megacluster 3; bottom panel: Depth of earthquakes through time. Grey lines represent velocity boundaries of Rowe model.

5.3.7 Under Soufrière Hills Volcano

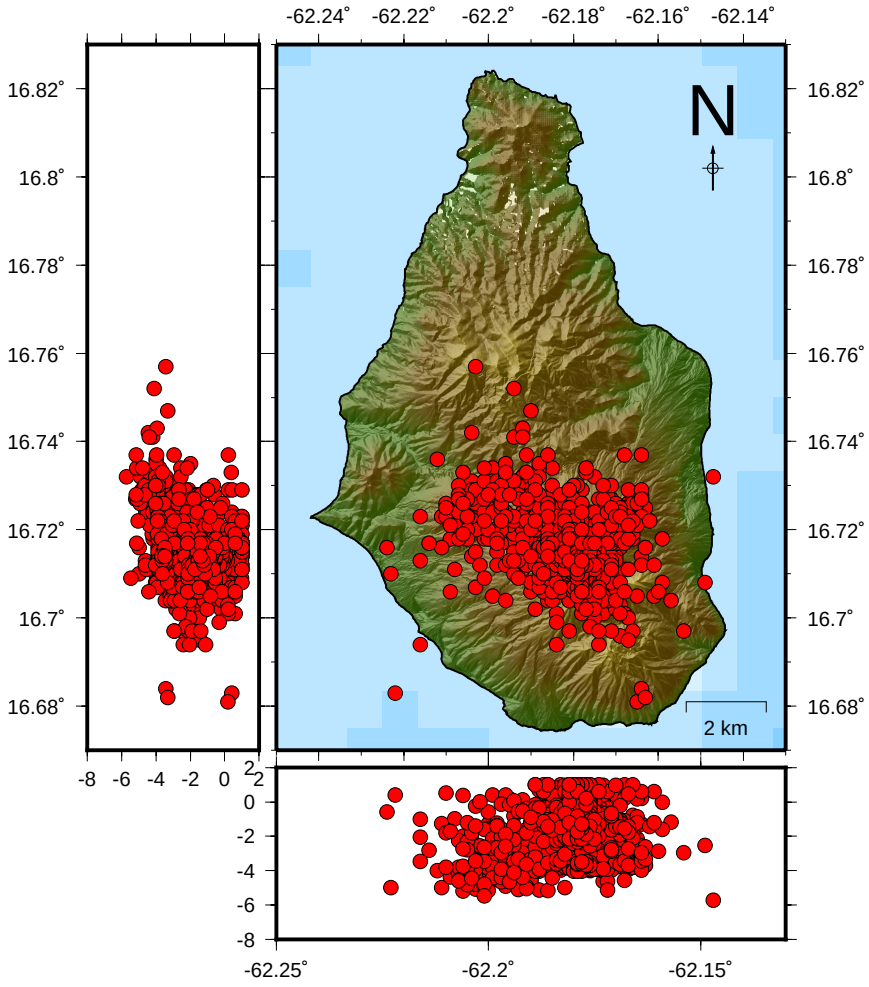

Figure 5.49: Earthquake locations during Phase 1: earthquakes with errors greater than 1.5 km have been removed.

Seismicity during Phase 1 covered the majority of southern Montserrat, with most earthquakes having errors less than 3 km. To reduce the number of events, and see more detail beneath the summit, Figure 5.49 shows earthquakes with errors less than 1.5 km. Earthquakes are mostly beneath Soufrière Hills Volcano, but earthquakes have been recorded at other regions in southern Montserrat that have been referred to as distal clusters. Seismicity beneath the summit extends to a depth of 4.5 km. This suggest that the top of the magmatic chamber is at depths greater than 4.5 km due to the lack of seismicity in this region, similar to results provided by *Aspinall et al.* (1998); this is also similar to petrological results from *Barclay et al.* (1998) which showed that magma was stored in

a water-saturated magma chamber at depths 5-6 km bsl. Pulses in discharge rate were preceded by an increase in earthquake swarms in January, July and October 1996 (*Voight et al.*, 1998).

Over 30% of VT earthquakes recorded until 2008 occurred during the first 6 months of the eruption (*Roman et al.*, 2008; *Young et al.*, 1998). As the eruption progressed, VT seismicity decreased, and hybrid seismicity became more dominant (*Miller et al.*, 1998). Hybrid earthquakes were first recorded in September 1995 prior to dome growth at Castle Peak (*Young et al.*, 1998), with hybrid seismicity becoming regular by July 1996. VT earthquakes are caused by changes in the magmatic system such as increased gas and magma flow, resulting in changes to the local stress field (*Miller et al.*, 1998). Decreased VT seismicity after the first 6 months could represent an increase in conduit openness and stabilisation of the magmatic system, reducing internal pressures in the surrounding country rock (*Roman et al.*, 2008).

A change to hybrid seismicity is suggested to correlate with magma transport, suggesting an increased magma flux (*Miller et al.*, 1998, 2010). Hybrid seismicity is generally shallow at depths of 1.5 km; it has been recorded to be directly above VT seismicity (*Rowe et al.*, 2004). This suggests that hybrid earthquakes could be a VT earthquake that has triggered an LP signal in a nearby resonator, or follows a different ray path, changing the frequency of the signal. For example: a VT earthquake occurring in a fluid filled crack or reservoir would result in a convolved signal comprising of both VT and LP components (*Benoit and McNutt*, 1997; *Chouet*, 1996). Other models suggest that there may be a continuum between LP and hybrid earthquakes, where they are considered end members of the same process (*Neuberg*, 2000); different interpretations of seismic signals are discussed in Section 2.1.

Several examples of hybrid earthquakes being preceded by VT earthquakes are shown in *Miller et al.* (1998) and have been discussed by *McNutt* (1996) as part of an eruption model, where a decrease in VT events, and an increase in low frequency events (such as hybrid and LP) indicates a shallowing of magma. Once an eruption starts, pressure around the conduit will start to equilibrate as pathways are formed, which can result in reduced VT seismicity (*Aspinall et al.*, 1998; *Roman et al.*, 2008). LP earthquakes have been shown to occur in swarms with similar waveforms; this indicates a stationary source location, which is being

repetitively triggered by the same process. These are normally found at very shallow depths of 500 m bsl (*Neuberg et al.*, 2006).

Very high b values (greater than 3) are recorded beneath English Crater and Chances Peak at depths of 0–1.5 km, during the first nine months of the eruption (*Power et al.*, 1998). This means there is a greater proportion of smaller earthquakes; this is thought to be related to high silica content at this depth, or an increase in heterogenity, temperature and stress conditions resulting from increased heat flow in this region (*Aspinall et al.*, 1998; *Power et al.*, 1998). Comparatively low b values of around 1 are recorded at 2–4 km depth beneath Soufrière Hills and south of English Crater; this is likely a result of magma intrusion beneath English Crater. The region is less fractured, and hence would result in larger magnitude earthquakes during magma movement (*Power et al.*, 1998)

Extrusion stopped on 10^{th} March 1998, but VT earthquakes, SO_2 and small explosions continued until November 1999 (*Miller et al.*, 1998). It is thought that magma influx continued at this time at 6 km bsl to the upper chamber (*Norton et al.*, 2002). Focal mechanisms during Phase 1 are suggestive of conduit deflation and relaxation of the host rock; this is supported by deformation data recorded during the time period (*Mattioli and Herd*, 2004). This is likely the reason for the high levels of VT seismicity recorded in the first 6 months of Phase 1 (*Roman et al.*, 2006).

5.4 Phase 2: 27th November 1999 to 1st August 2003

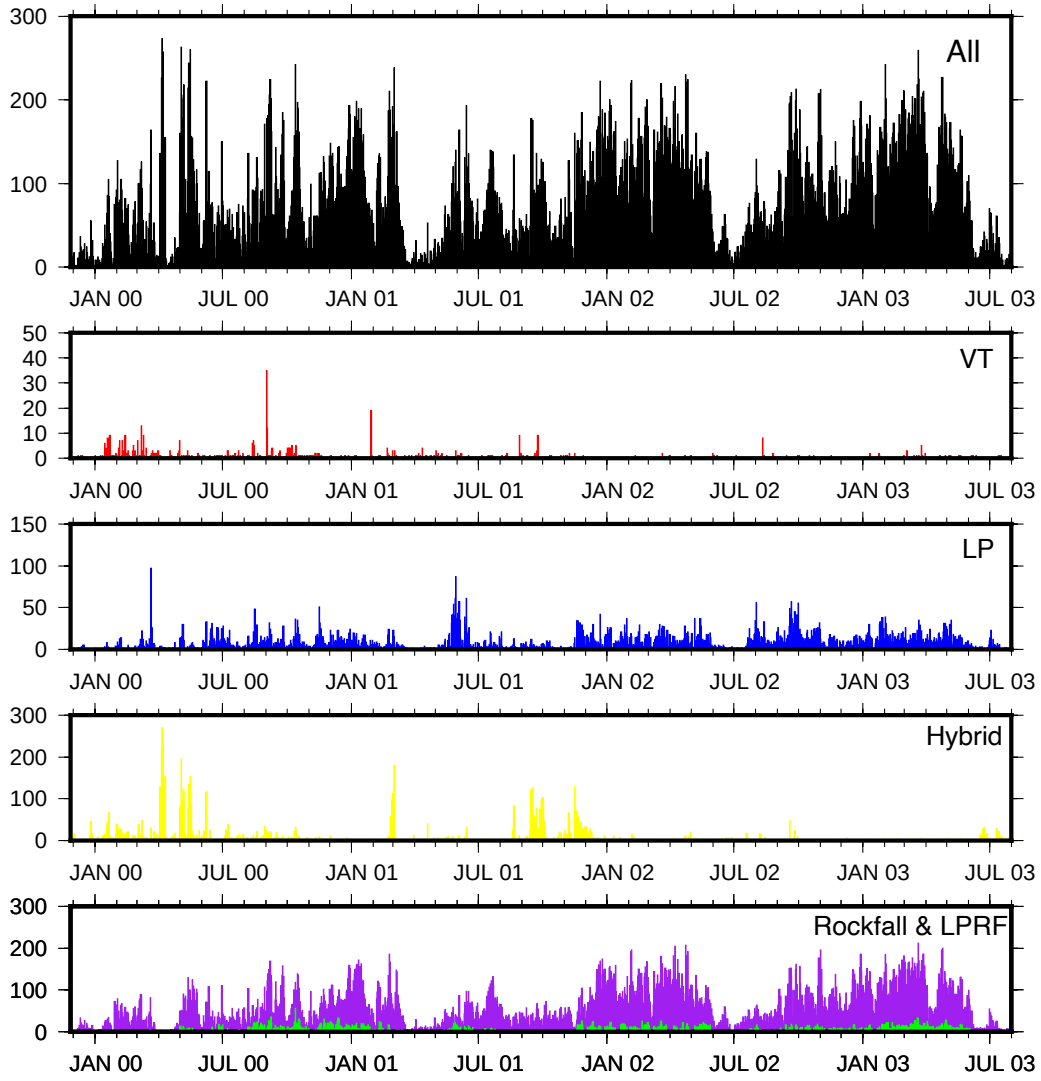

Figure 5.50: Histogram showing the number of earthquakes recorded by MVO per day in Phase 2. Red = VT, blue = LP, yellow = hybrid, green = LPRF, purple = rockfall.

Phase 2 began on the 27th November 1999 after a 19 month pause in surface lava extrusion (*Carn et al.*, 2004). An increase in LP earthquakes were recorded a few weeks before the eruption (*Miller et al.*, 1998). Phase 2 has been the longest period of lava extrusion so far, lasting 3.5 years and ending with a large dome collapse on the 12th July 2003 (*Wadge et al.*, 2014). A change in dominant P axis orientation with time was seen during May 1999 to November 1999, where P axes were orientated NW-SE (90 degrees from tectonic stress) (*Roman et al.*, 2006). This occurred in the six months leading up to the start of Phase 2, and indicated that the conduit was undergoing increasing pressurisation (*Roman et al.*,

2006).

Seismicity was mainly constant throughout, with an increase in seismicity recorded prior to the dome collapse in July 2003 (Figure 5.50). This increase in seismicity was mostly hybrid earthquakes; hybrid seismicity can suggest rapid ascent rates, or magma pressurisation in the conduit (*Chouet*, 1996; *Miller et al.*, 1998; *Neuberg et al.*, 2006). This suggests that there may have been shallow magma moving in the conduit in the lead up to the dome collapse in July (*Miller et al.*, 1998). Hypocenters were mostly focused around Soufrière Hills Volcano at depths of 1–5 km, as shown in Figure 5.51. A small cluster of earthquakes were recorded north of Soufrière Hills on the 20^{th}–30^{th} June 2004, but this did not extend to Windy Hill as seen in Phase 1.

Displacement data from six cGPS stations suggested a best fit source at 5 km depth for the shallow magmatic reservoir, with a deeper reservoir at 17 km (*Foroozan et al.*, 2010). This deeper reservoir is supported by crystal phases suggesting a reservoir at depths greater than 10 km (*Devine et al.*, 2003), and other geodetic data supporting a source as deep as 12 km (*Mattioli and Herd*, 2004). During phase 2, the lower chamber deflated whilst the upper chamber inflated slightly; this fits with interpretations that only the lower reservoir is depleted during eruptive episodes, with the upper reservoir inflating when inflow is greater than outflow (*Elsworth et al.*, 2008).

Dome growth was more stable throughout Phase 2, with fewer pyroclastic flows than in Phase 1; this resulted in larger volumes of material during dome collapses (*Carn et al.*, 2004). Sub daily cyclic trends of 10 hours were recorded in seismicity and gas from December 1999 to January 2000, allowing a rough hazard assessment to be attained of when PDC's were more likely (*Young et al.*, 2003).

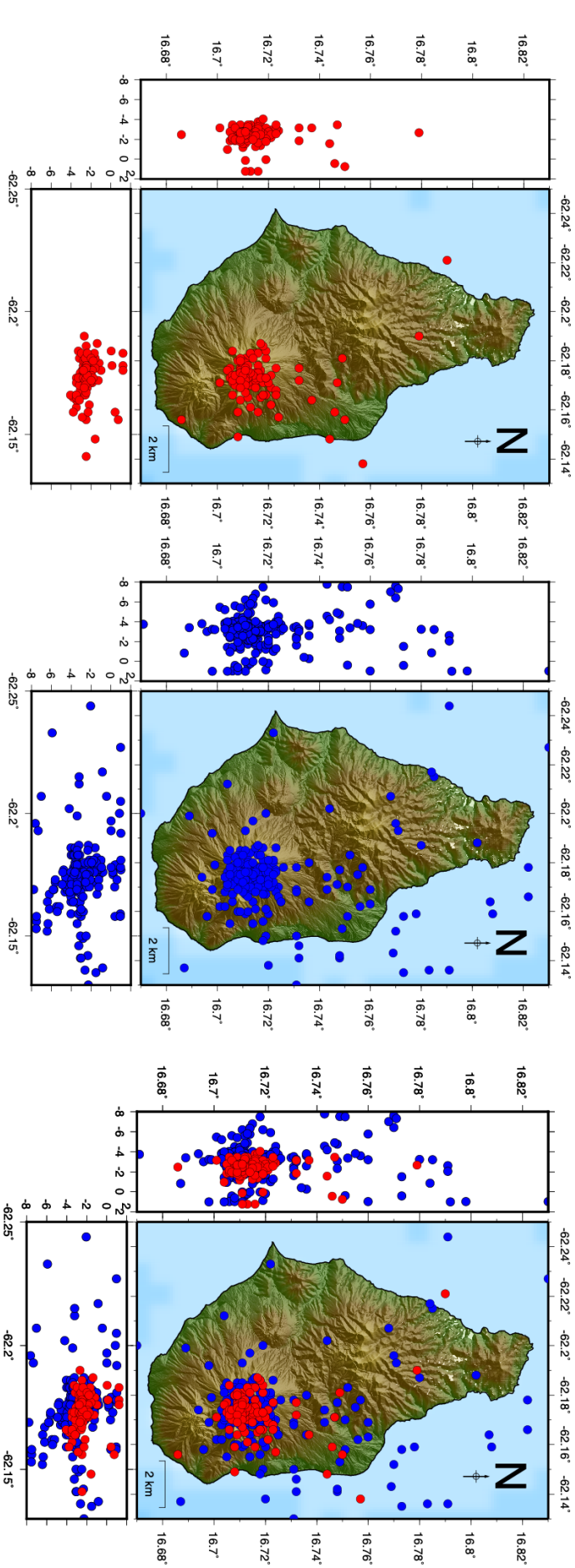

Figure 5.51: *Hypocenter* (red) and *NonLinLoc* (blue) earthquake locations for Phase 2: 27^{th} November 1999 to 1^{st} August 2003. Earthquakes with errors greater than 5 km have been removed.

5.4.1 Seismicity during Dome Collapses

There were three main dome collapses during this phase: 20th March 2000 (*Carn et al.*, 2004), 29th July 2001 (*Matthews et al.*, 2002) and 12th–13th July 2003 (*Herd et al.*, 2005). The 20th March 2000 collapse removed 95% of the new lava dome over five hours of activity, which included several pyroclastic flows and one explosion (*Carn et al.*, 2004). This was preceded by a period of heavy rainfall, with no change in seismicity leading up to the dome collapse (*Carn et al.*, 2004). Lava extrusion occurred immediately after the dome collapse and continued until the 29th July 2001 when the dome collapsed again (*Matthews et al.*, 2002). The collapse in 2001 was also preceded by extreme rainfall, with no change in seismicity recorded in the days prior (*Matthews et al.*, 2002). It is still uncertain if rainfall is a mechanism for dome collapse, however it is thought that rainfall is able to percolate into cracks of the dome, resulting in pressurised steam that would be enough to destabilise the dome (*Carn et al.*, 2004; *Matthews et al.*, 2002). Research by *Barclay et al.* (2006) showed a 6.3–9.2% increase in the probability of there being a dome collapse when more than 20 mm of rain was recorded; an increase in rain was also linked to an increase in the probability of a recorded PDC or explosion occurring on the same day. *Carn et al.* (2004) also suggested that rapid cooling of hot lava could lead to small phreatic explosions.

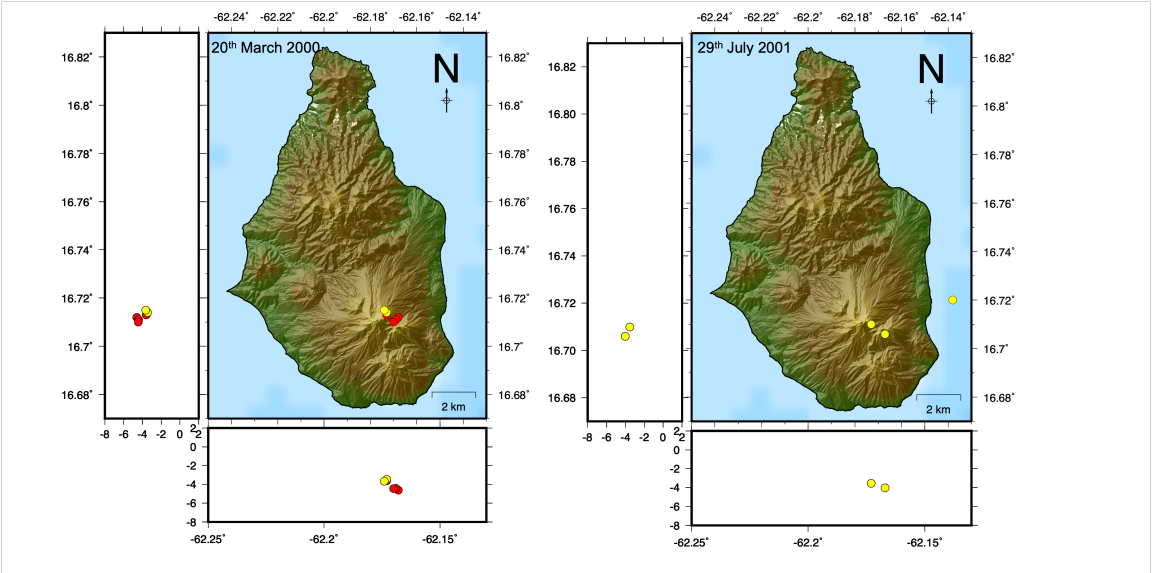

Figure 5.52: Relocations of earthquakes in the month prior to the dome collapses on the 20th March 2000, and 29th July 2001. Earthquakes with errors greater than 3 km have been removed. Red dots represent VT seismicity, blue represent LP seismicity and yellow represent hybrid earthquakes

Figure 5.52 shows the seismicity in the month prior to the two dome collapses on the 20^{th} March 2000 and 29^{th} July 2001. There is very little seismicity in the month leading up to the two dome collapses, with only 9 and 4 earthquakes being recorded in the 30 days prior (figure only shows location of earthquakes with errors less than 3 km). This ties in with results from *Carn et al.* (2004); *Matthews et al.* (2002) that suggest rainfall was a likely mechanism for these collapses.

The 12^{th}–13^{th} July dome collapse was the largest recorded, removing over 210 million m^3 of material over an 18 hour period (*Herd et al.*, 2005). The tephra fallout was estimated to be 10–20 million m^3 with PDC's occurring along the Tar River Valley reaching the sea and resulting in a small tsunami that impacted Guadeloupe on the 13^{th} July (*Edmonds et al.*, 2006). The dome collapse was followed by five Vulcanian explosions ending on the 15^{th} July (*Edmonds et al.*, 2006). Borehole strainmeters recorded a rapid change in pressurisation of the magma chamber after the dome collapse, estimating an overpressure of 1 MPa with a 1 km radius (*Voight et al.*, 2006). It is thought that dome collapse reduced pressures resulting in a volumetric expansion of the chamber and hence an increase in strain; pressurisation was thought to be due to growth of 1–3% gas bubbles (*Voight et al.*, 2006).

Seismicity in the month leading up to the 12^{th} July 2003 dome collapse was mostly hybrid earthquakes, and was spread out around the volcano at 3–4 km depth (Figure 5.53). There was no trend in hypocenters with the majority of earthquakes occurring from the 15^{th}–28^{th} June. Hybrid seismicity is indicative of the build up of pressure along conduit walls, with faulting on the surface between country rock and the fluid filled conduit (*Chouet*, 1996; *Lahr et al.*, 1994; *Voight et al.*, 1998, 1999). Therefore, this increase in hybrid seismicity could have been indicative of magma extrusion, and has been recorded during periods of other dome growth (*Miller et al.*, 1998; *White et al.*, 1998).

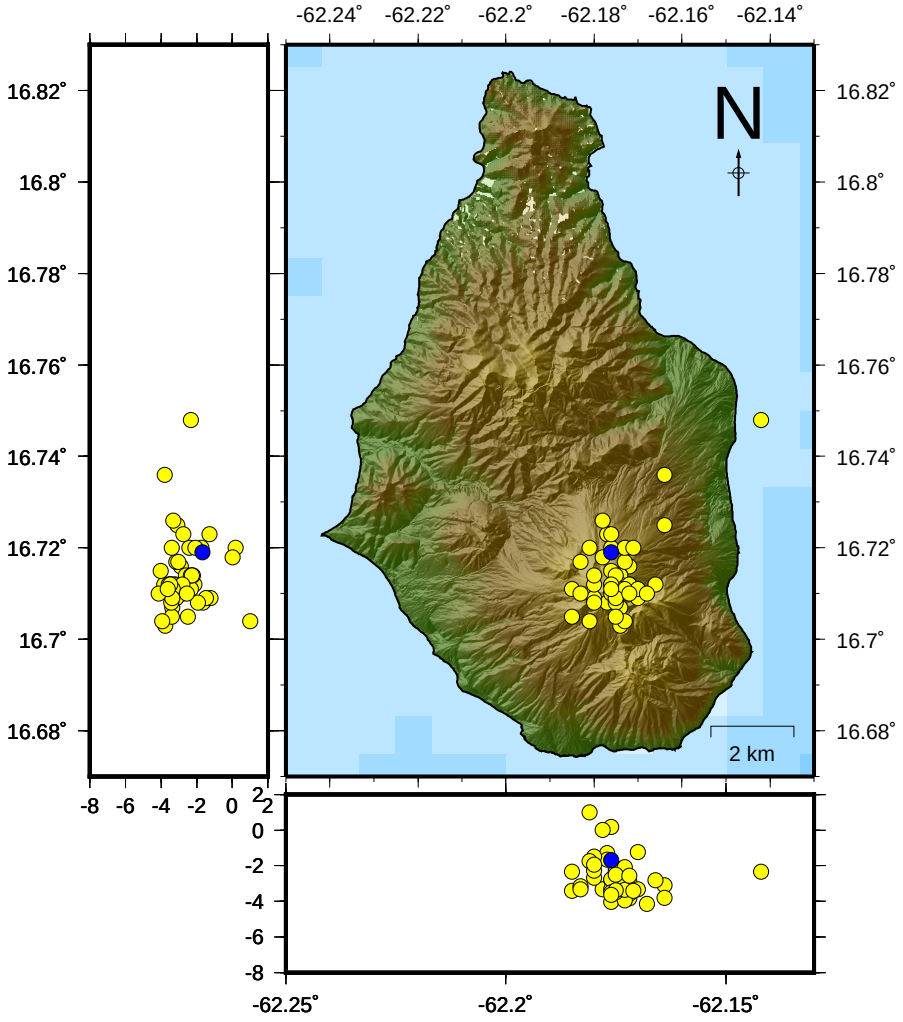

Figure 5.53: Relocations of earthquakes in the month prior to the 12th July 2003 dome collapse. Earthquakes with errors greater than 3 km have been removed. Blue represent LP seismicity and yellow represent hybrid earthquakes.

5.5 Phase 3: 15^{th} April 2005 to 20^{th} April 2007

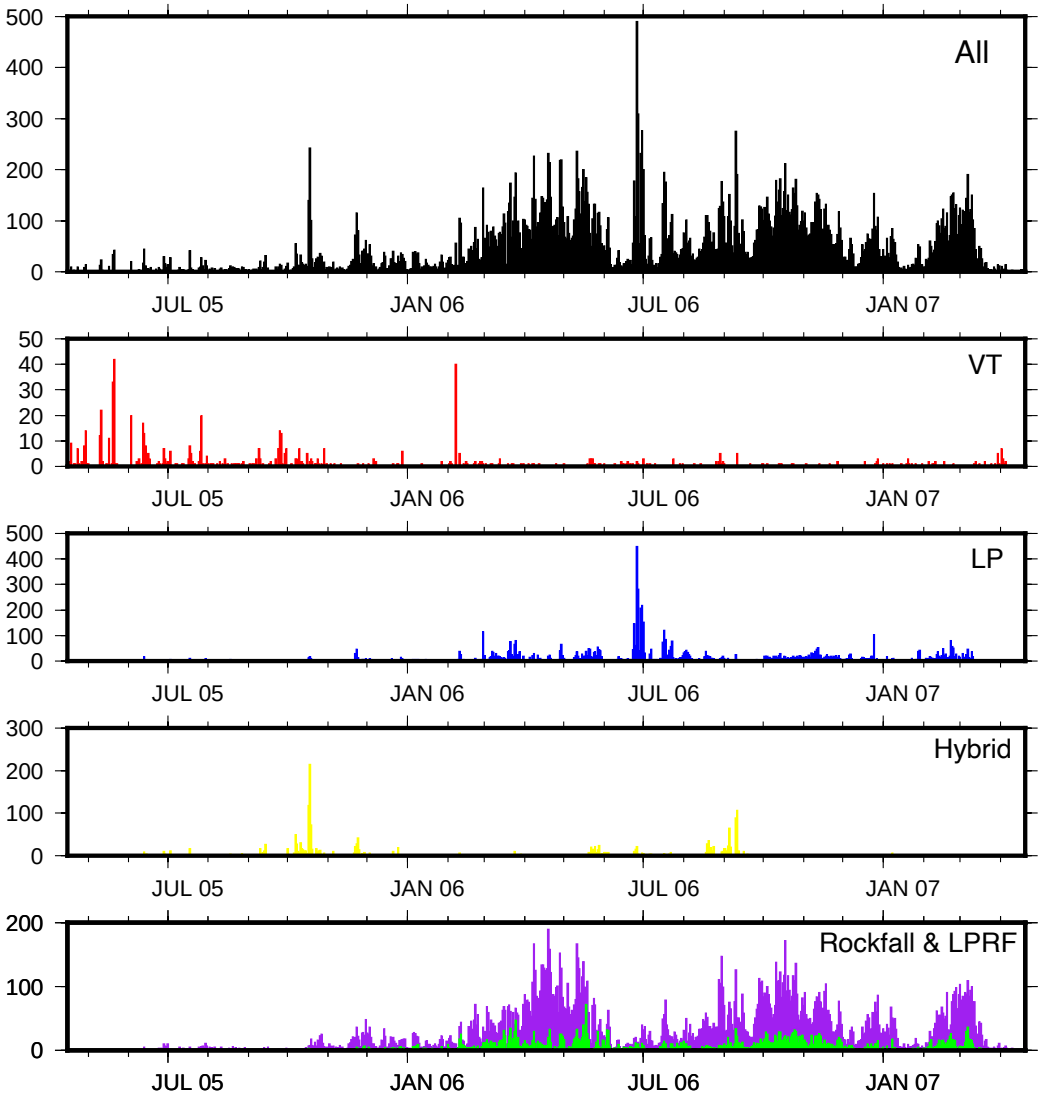

Figure 5.54: Histogram showing the number of earthquakes recorded by MVO per day in Phase 3. Red = VT, blue = LP, yellow = hybrid, green = LPRF, purple = rockfall.

VT seismicity accompanied by ash venting and minor explosive activity was recorded prior to the start of Phase 3 (*Smith*, 2013). A 90 degree rotation in p axes was recorded four months before the onset of Phase 3; this occurred during increased seismicity, coincident with a change in tilt from deflation to inflation (*Roman et al.*, 2006). A swarm of 31 low amplitude VT earthquakes were recorded on the 6^{th}–7^{th} March 2005; this was followed by a 400% increase in SO_2 emissions three days prior to ash venting on the 12^{th} March 2005 (*Cole et al.*, 2014a). The start of Phases 3,4 and 5 were very different to the first two

phases, with a decrease in precursory activity.

Phase 3 was characterised by higher discharge rate, a 2–6 week discharge cycle and fewer dome collapses (mainly due to the dome being removed at the end of Phase 2) (*Loughlin et al.*, 2010). The onset of each major pulse in discharge was characterised by a change in extrusion growth direction (*Loughlin et al.*, 2010). Activity was recorded from a NNE-SSW line of new vents in the dome crater during the beginning of the phase; an increase in hybrid and LP earthquakes was then recorded from the 13^{th} March (*Cole et al.*, 2014a). The volume of magma during this phase was similar to that in Phase 1, but with a higher discharge rate. This implied that there were faster ascent rates of magma, limiting degassing and inducing crystallisation (*Loughlin et al.*, 2010; *Ryan et al.*, 2010).

Higher seismicity levels were recorded during Phase 3 compared to Phase 2, with an increase in seismicity recorded during August 2006 (Figure 5.54). VT seismicity is dominant at the beginning of the phase, and is then replaced by mostly hybrid seismicity later on; this same pattern is seen throughout all phases in the eruption. Seismicity is located in a slight NW-SE trending cluster at depths from 1 km height to 4 km bsl (Figure 5.55); this trend is slightly more north than the Belham Valley Fault. There is also a large number of earthquakes that are located across southern Montserrat. These are most likely to be the result of poor arrival time picks, as they do not follow any faults or expected areas of seismicity.

A large dome collapse was recorded on the 20^{th} May 2006; this had no precursory seismicity but was during intense rainfall (*Loughlin et al.*, 2010; *Smith*, 2013). A small explosive event in January 2007 removed part of the dome (*De Angelis et al.*, 2007); dome growth then ended on the 20^{th} April 2007 with the dome volume of 203 Mm^3 (*Ryan et al.*, 2010; *Wadge et al.*, 2014). Seismicity changed throughout 2005 from earthquakes locating with an aligned trend and at 0 km depth on the 21^{st} May, to earthquakes with increasing depth to 3.5–4 km and movement towards the south after.

Elsworth et al. (2008) showed that the lower reservoir deflated more in Phase 3 than in Phase 2, but that this time the upper reservoir was also depleted. *Voight et al.* (2010) also proposed that magma transferred in and out of the upper reservoir could be accommodated by the compression/depression of a lower chamber. Models for Montserrat suggest an upper chamber at 10 km depth, but that the top of this chamber may be shallower to fit results

from petrology and seismology (*Aspinall et al.*, 1998; *Barclay et al.*, 1998; *Voight et al.*, 2010). There were more mafic inclusions during Phase 3; this suggests that magma mixing was taking place during the eruption, and that magma was continuously supplied from depth (*Barclay et al.*, 2010).

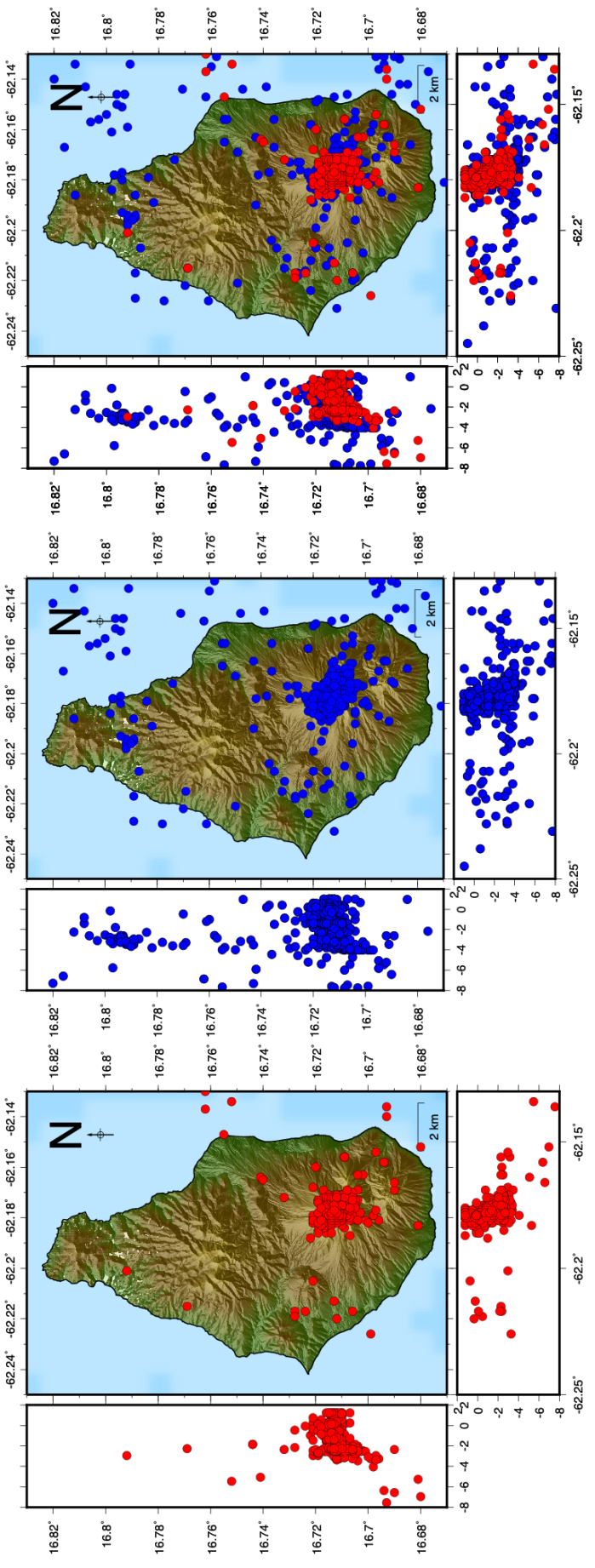

Figure 5.55: *Hypocenter* (red) and *NonLinLoc* (blue) earthquake locations for Phase 3: 15^{th} April 2005 to 20^{th} April 2007. Earthquakes with errors greater than 5 km have been removed.

5.6 Phase 4: 29^{th} July 2008 to 3^{rd} January 2009

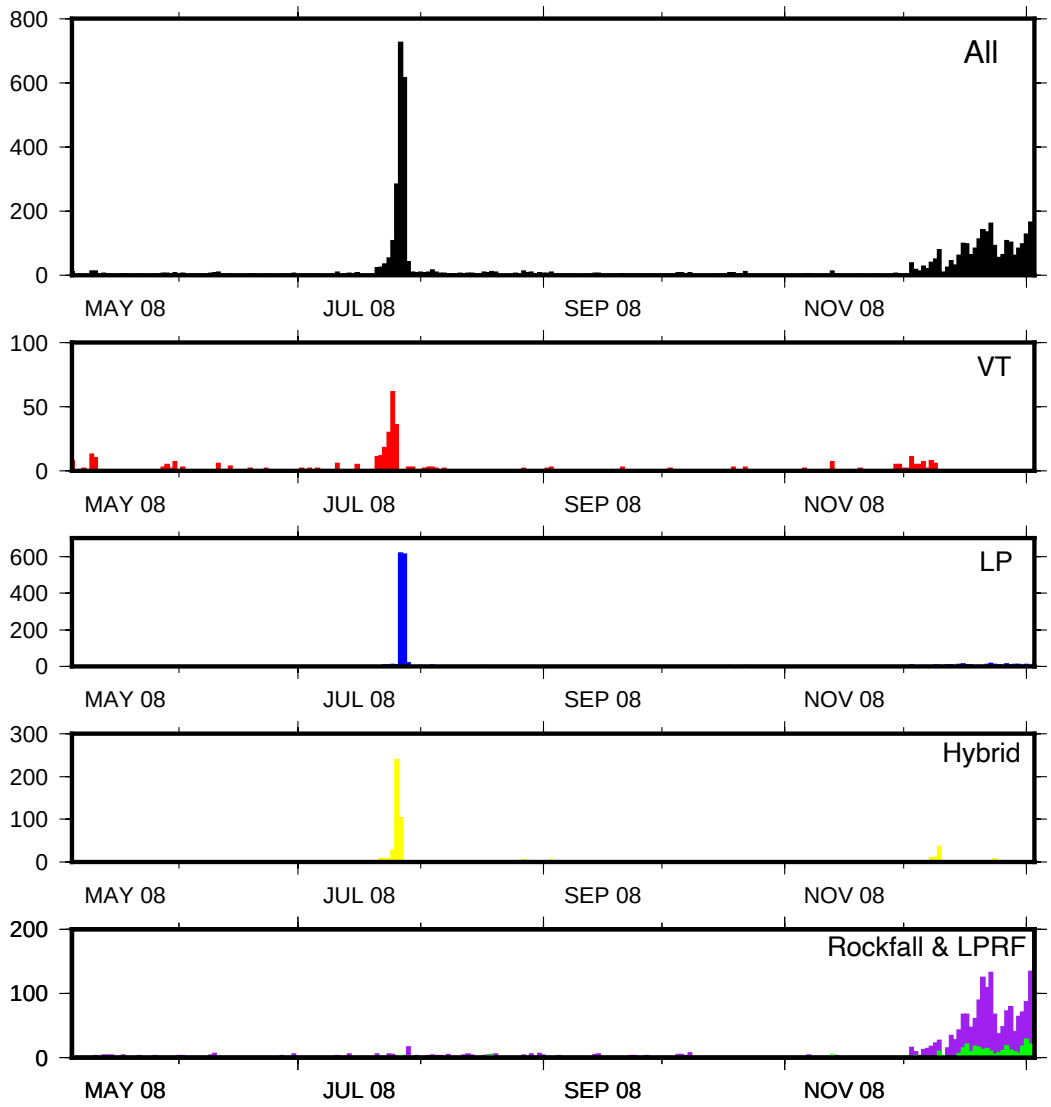

Figure 5.56: Histogram showing the number of earthquakes recorded by MVO per day during and in the lead up to Phase 4. Red = VT, blue = LP, yellow = hybrid, green = LPRF, purple = rockfall.

Phase 4 comprised of two short episodes of extrusion and explosions, known as Phase 4a and 4b (*Wadge et al.*, 2014). Episodes of VT seismicity with ash venting and explosive activity were recorded before the start of magma extrusion (*Smith*, 2013); this is known as the transition period, which occurred from the 5^{th} May to the beginning of Phase 4a on the 29^{th} July. An explosion on the 3^{rd} December 2008 marked an increase in seismicity for a month; this was followed by dome growth (*Komorowski et al.*, 2010). There was a slow rate of extrusion during Phase 4a in comparison with Phase 4b where rapid lava extrusion

was recorded (*Cole et al.*, 2014a). VT seismicity changed after Phase 3, with fewer intense swarms recorded and replaced with VT strings (short bursts of VT events) (*Smith*, 2013). VT strings were short in time with a mean of 10 events occurring within a 30 minute period (*Smith*, 2013).

Seismicity was low during Phase 4 with the exception of two time periods: July 2008 and the beginning of November 2008 (Figure 5.56). Increased seismicity in July 2008 occurred several days before a Vulcanian explosion on the 28^{th} July. Relocated hypocenters during Phase 4 were mostly beneath Soufrière Hills Volcano, with some earthquakes located towards the south-east, following the same trend as the Montserrat-Havers Fault System (Figure 5.57). There is a large increase in the number of earthquakes located with *NonLinLoc*; this is because *NonLinLoc* is able to relocate earthquakes using four arrival picks but on three seismic stations, whereas *Hypocenter* needs a minimum of four seismic stations.

These locations to the SE are from the increased seismicity on the lead up to the 28^{th} July explosion. This trend in seismicity to the SE was not seen with original MVO locations. An increase in seismicity towards Windy Hill was recorded on the 22^{nd} January, but with very limited events. Seismicity near St George's Hill was also recorded during the 21^{st}–29^{th} July 2008.

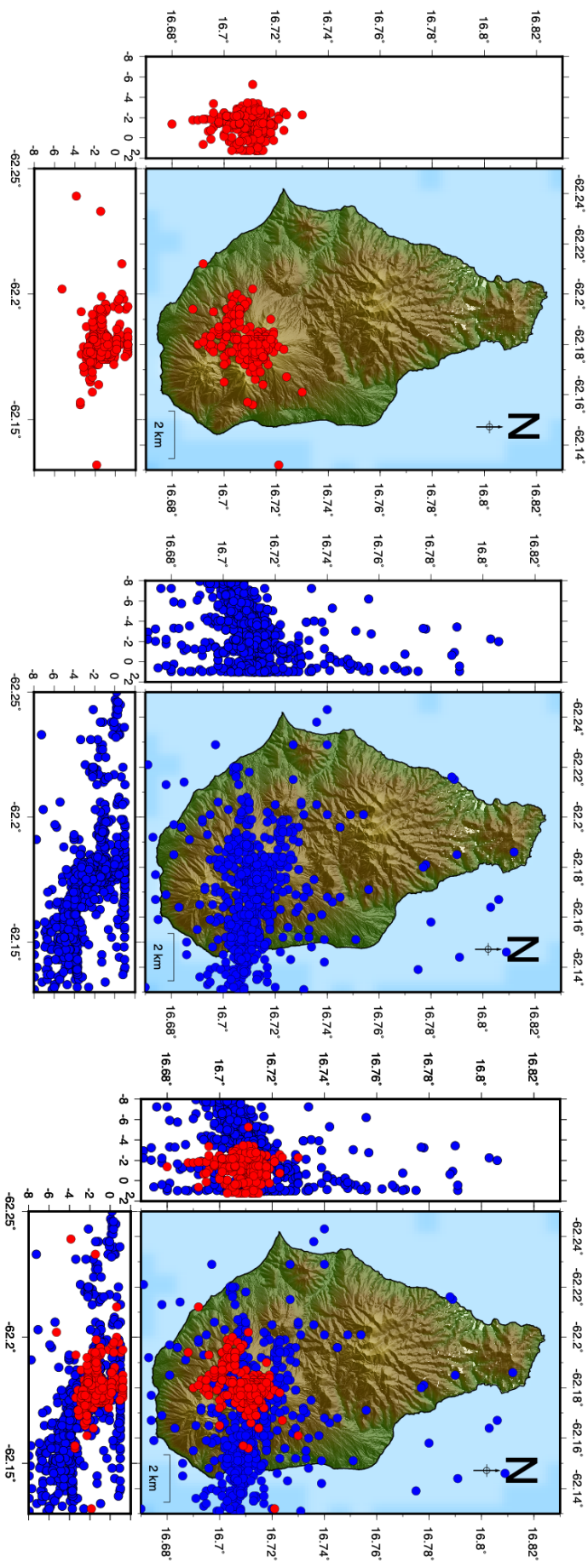

Figure 5.57: *Hypocenter* (red) and *NonLinLoc* (blue) earthquake locations for and in the lead up to Phase 4: 5^{th} May 2008 to 3^{rd} January 2009 inclusive. Earthquakes with errors greater than 5 km have been removed.

5.6.1 21^{st} to 31^{st} July 2008

July 2008 marked the onset of the extrusion for Phase 4a with increased seismicity and dome growth (*Rodgers et al.*, 2016). Irregular VT swarms were recorded from the 21^{st}–26^{th} July 2008, before hybrid followed by LP earthquakes replaced VT's for a two day period (*De Angelis*, 2009; *Rodgers et al.*, 2016). A total of 1818 earthquakes were recorded from the 21^{st}–29^{th} July, with earthquake rates peaking on the 28^{th} July (Figure 5.58). A series of small ash venting events occurred on the 21^{st} July, each preceded by a swarm of 7 VTs per hour (*Cole et al.*, 2014a). A 31 hour period of decreased seismicity was recorded prior to the Vulcanian explosion on the 29^{th} July at 03:32 UTC; this released a large amount of ash and tephra, with a plume reaching 12 km asl (*De Angelis*, 2009; *Rodgers et al.*, 2016). VT earthquakes during this time period were recorded at 1.6–3.9 km beneath the summit near Gages vent on the 21^{st}, and then at 2 km directly beneath the summit from the 24–26^{th} (*Rodgers et al.*, 2016).

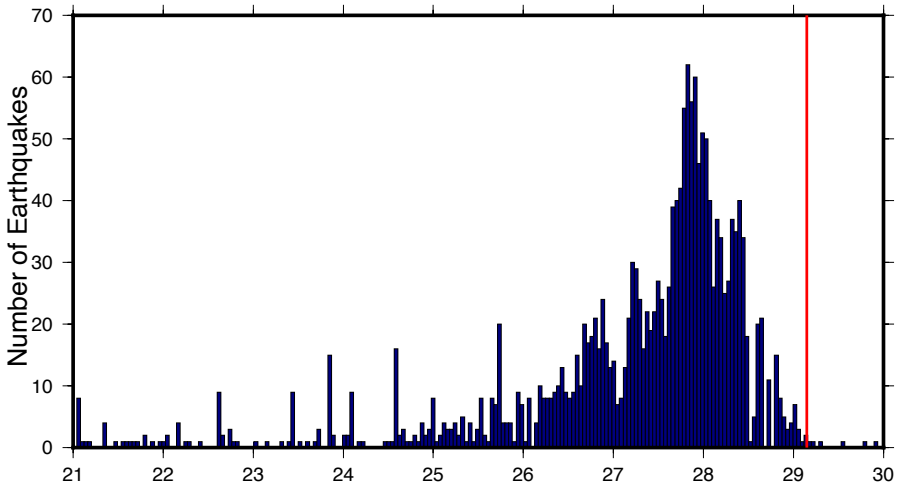

Figure 5.58: Time plot of number of earthquakes recorded by MVO per hour from the 21^{st} to 30^{th} July 2008. Red line represents time of Vulcanian explosion.

Relocations during this time period are shown in Figure 5.59; 223 additional earthquakes were relocated using *NonLinLoc* compared to the original MVO catalogue due to *NonLinLoc's* ability to locate earthquake with four arrival phases. Original *Hypocenter* locations are mostly clustered beneath SHV summit at depths of 0–3 km, with some events located near the east coast. Relocations with *NonLinLoc* show a clear trend of increasing depth to the ESE. There is a greater concentration of seismicity beneath the crater at depths of

2–6 km bsl; this is slightly deeper than original locations.

There is a clear trend in hypocenters located to the SSE during this time period; Figure 5.60a shows that the majority of the earthquakes in this trend occurred on the 28^{th} July — the day before the Vulcanian explosion. The majority of seismicity on this day was Long Period (LP) earthquakes with some hybrid events (Figure 5.60b). However, the majority of earthquakes during this time period have large errors greater than 3 km, which means they cannot be used for interpretation, as the errors are larger than any trends in location. When looking at earthquakes with errors less than 3 km, it can be seen that the majority of hypocenters to the SSE are removed, with just earthquakes beneath the summit at a depth of 0–4 km. Further investigation of this seismicity would be needed to see if this trend is real, or an artefact from low station coverage at the time; this is looked at further in Chapter 6.

LP earthquakes are indicative of fluid processes such as radiating energy from a fluid filled conduit (*McNutt*, 2005), underlying pressurisation of magmatic fluids (*Chouet*, 1996), and resonance produced by interference waves between magma-rock boundaries (*Neuberg*, 2000). The onset of LP seismicity is interpreted as a short term indicator for an eruption, and has often been associated with magma ascent and lava extrusion (*Iverson et al.*, 2006; *McNutt*, 1996; *Sparks*, 2003). LP seismicity observed in 1996 at SHV is thought to be a result of rapid bubble formation, and the formation and destruction of fluid filled cavities in the magma column (*Rowe et al.*, 2004). This could be suggestive that magma was migrating or being pressurised on the 28^{th} July, a day before the final eruption.

VT swarms are not usually recorded with LP seismicity (*Smith*, 2013), however, *Rodgers et al.* (2016) suggest that the ascent of decoupled magmatic fluid and gas triggered VT events in a overpressurised zone at 2.5 km depth. The reduction in seismicity prior to the explosion could have been a result of magma stalling due to an increase in viscosity from depressurisation and crystallisation; this would account for the SO_2 released during the eruption, which was equivalent to 8 days of pre-eruptive degassing (*Rodgers et al.*, 2016). Juvenile material in the erupted deposits also supports a theory of pressurisation of the system after an injection of fresh magma into the shallow reservoir (*De Angelis*, 2009; *Rodgers et al.*, 2016).

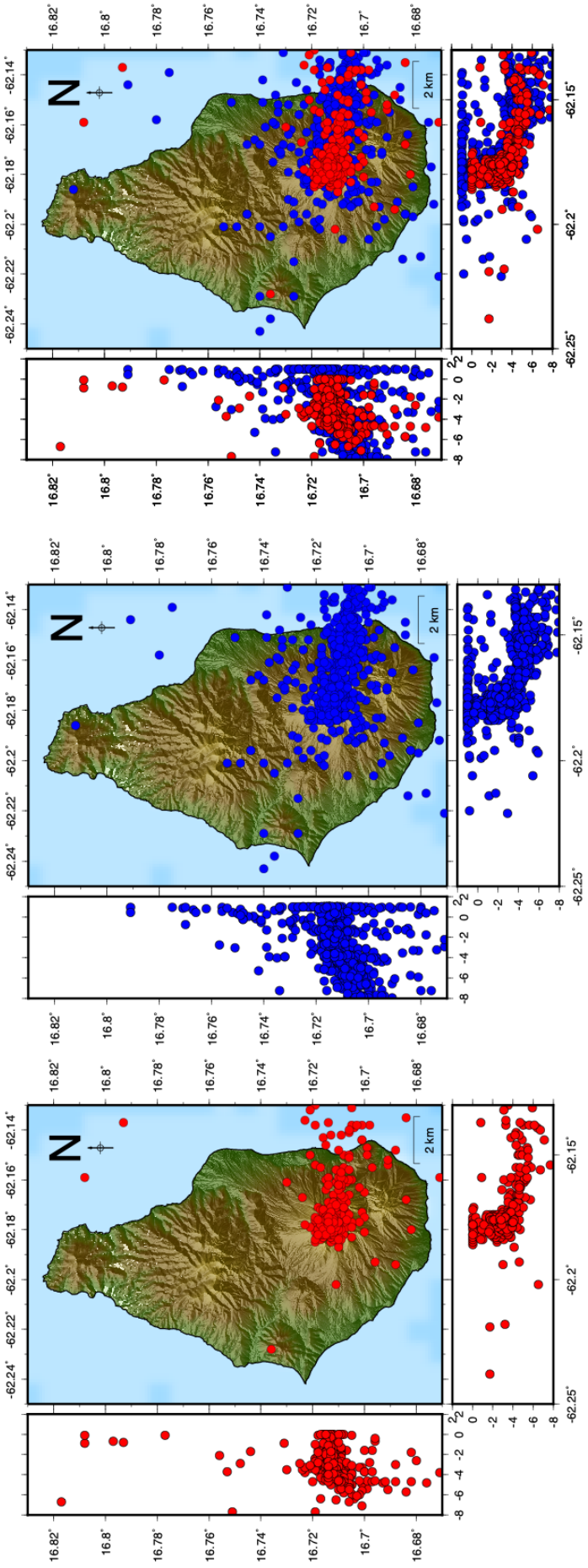

Figure 5.59: *Hypocenter* (red) and *NonLinLoc* (blue) earthquake locations from the 21^{st} to 31^{st} July 2008 inclusive.

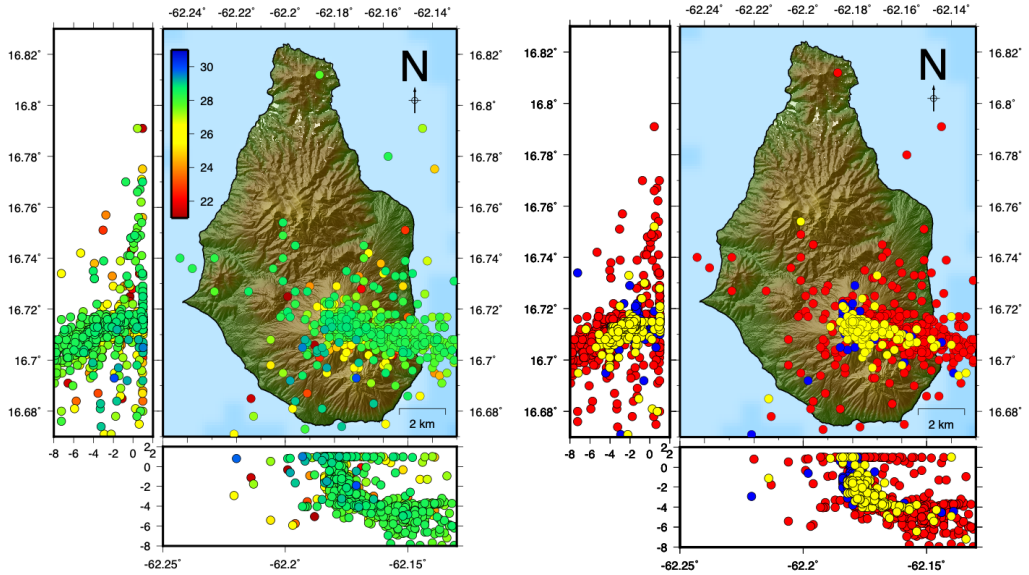

Figure 5.60: A)Earthquakes located in *NonLinLoc* from 21^{st} to 31^{st} July 2008 inclusive; earthquakes coloured by date of earthquake. Earthquakes with errors greater than 5 km have been removed. B) Earthquakes located in *NonLinLoc* from 21^{st} to 31^{st} July 2008 inclusive; earthquakes coloured by type of earthquake. Red = Long Period, Blue = Volcano-Tectonic, Yellow = Hybrid, Orange = Rockfall event, Green = Long Period Rockfall. Earthquakes with errors greater than 5 km have been removed

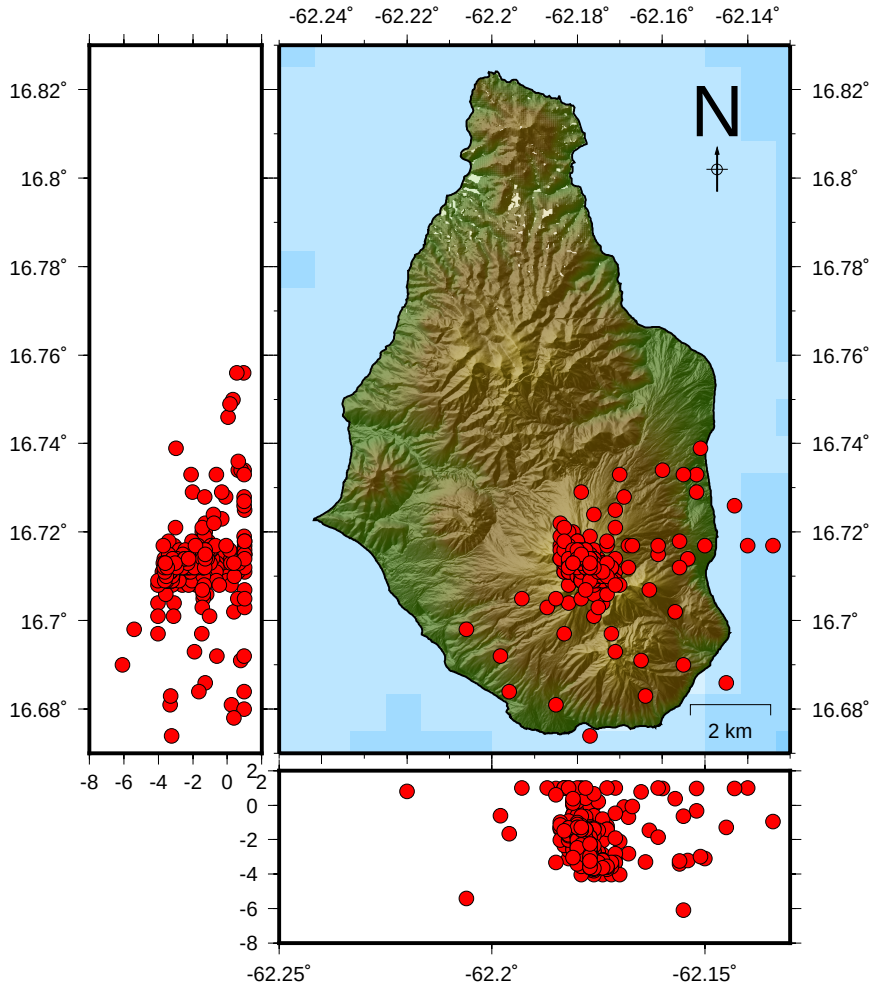

Figure 5.61: Earthquakes located in *NonLinLoc* from 21^{st} to 31^{st} July 2008 inclusive with errors less than 3 km

5.7 Phase 5: 5^{th} October 2009 to 11^{th} February 2010

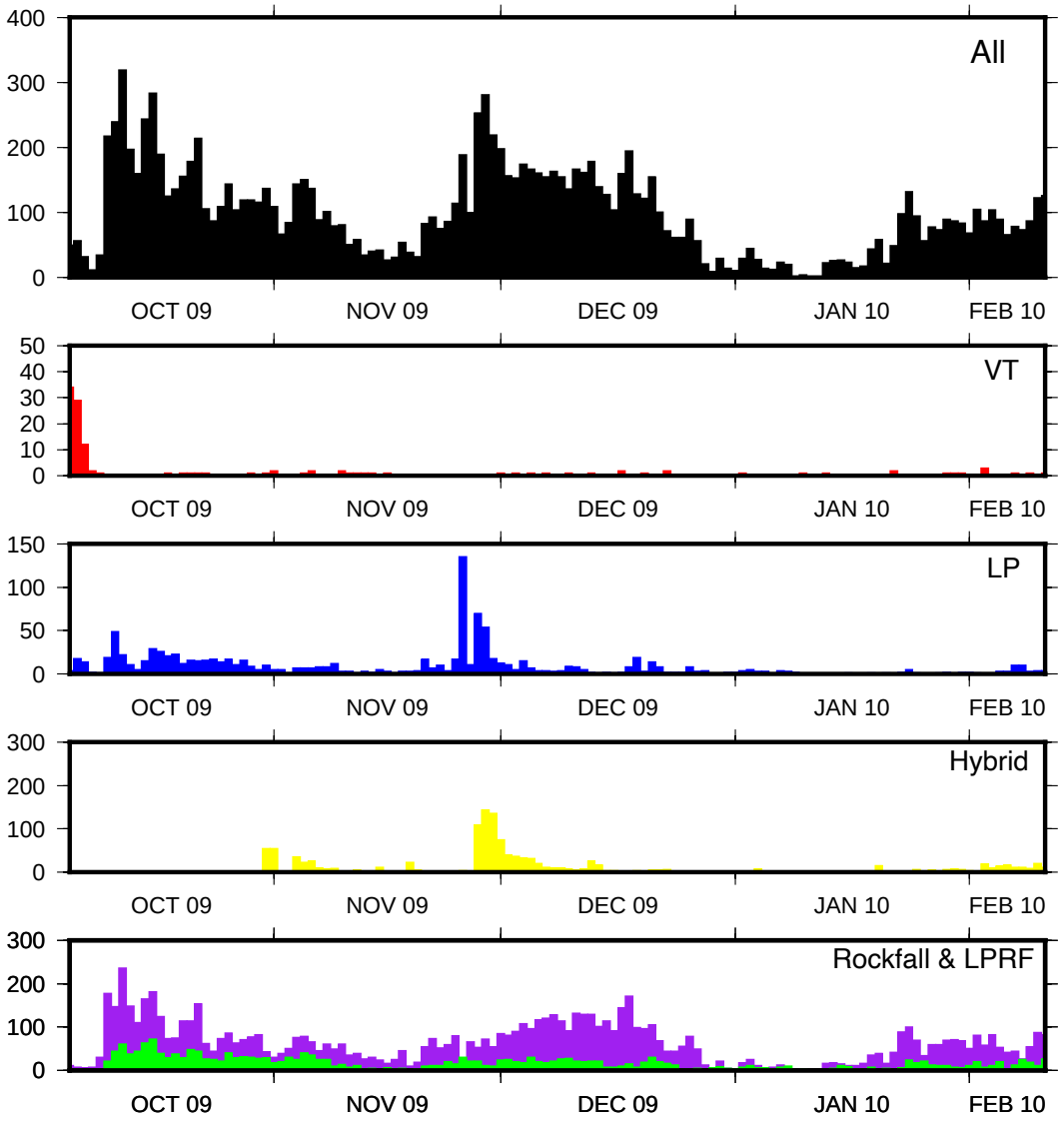

Figure 5.62: Histogram showing the number of earthquakes recorded by MVO per day in Phase 5. Red = VT, blue = LP, yellow = hybrid, green = LPRF, purple = rockfall

Phase 5 began on the 5^{th} October 2009 after an increase in hybrid and VT seismicity. A swarm of 24 VT earthquakes occurred on the 5^{th} October 2009 as a VT string marking the start of Phase 5 (*Smith*, 2013). This swarm preceded ash venting by 45 minutes (*Cole et al.*, 2014a). Cycles of seismicity and surface activity were present throughout, with ash venting and PDC's occurring during the peak of the cycles (*Wadge et al.*, 2014). There were several Vulcanian explosions with Phase 5 ending with a large north-directed collapse on the 11^{th} February 2010 (*Stinton et al.*, 2014).

Seismicity levels decreased in Phase 5 compared to previous phases, with only short bursts in seismic activity seen at the beginning of the Phase, the end of November, and the final few weeks in February 2010 (Figure 5.62). VT seismicity was dominant at the start of the phase, which has been seen with all five phases. Hypocenters are focussed at the North flank of Soufrière Hills Volcano, constrained to a depth of 1–4 km bsl (Figure 5.63).

5.7.1 VT Strings

VT strings were recorded throughout and after Phase 5; two VT strings comprising of 50 earthquakes each occurred on the 22^{nd} and 23^{rd} March 2012 (*Smith*, 2013). VT strings are VT earthquakes with similar coda occurring over a short period of time (*Smith*, 2013). The VT strings were followed by a strong output of gas, a large strain signal and accompanied by ash venting (*Smith*, 2013). Analysis shows that different VT strings have similarities suggesting a common driving process. It has been proposed that gas movement could be responsible, however an increase in gas is not recorded with all VT strings (*Smith*, 2013).

Locations from the VT string on the 5^{th}–6^{th} October 2009 marked the start of Phase 5 (Figure 5.64); there were 46 VT earthquakes over the 2-day period. These are mostly concentrated around the Soufrière Hills summit, at a 2 km depth. Locations found by MVO were slightly further north and are not as tightly clustered as the relocations with *NonLinLoc*. Precursory activity suggested that juvenile magma was responsible for the start of Phase 5 (*Smith*, 2013). VT earthquakes from this time period were larger and occurred less than an hour before the onset of ash venting (*Cole et al.*, 2014a). This suggests that the VT strings may be linked to magma/gas movement. However, more research is needed to compare all VT strings at Soufrière Hills Volcano to see if there is a correlation between these.

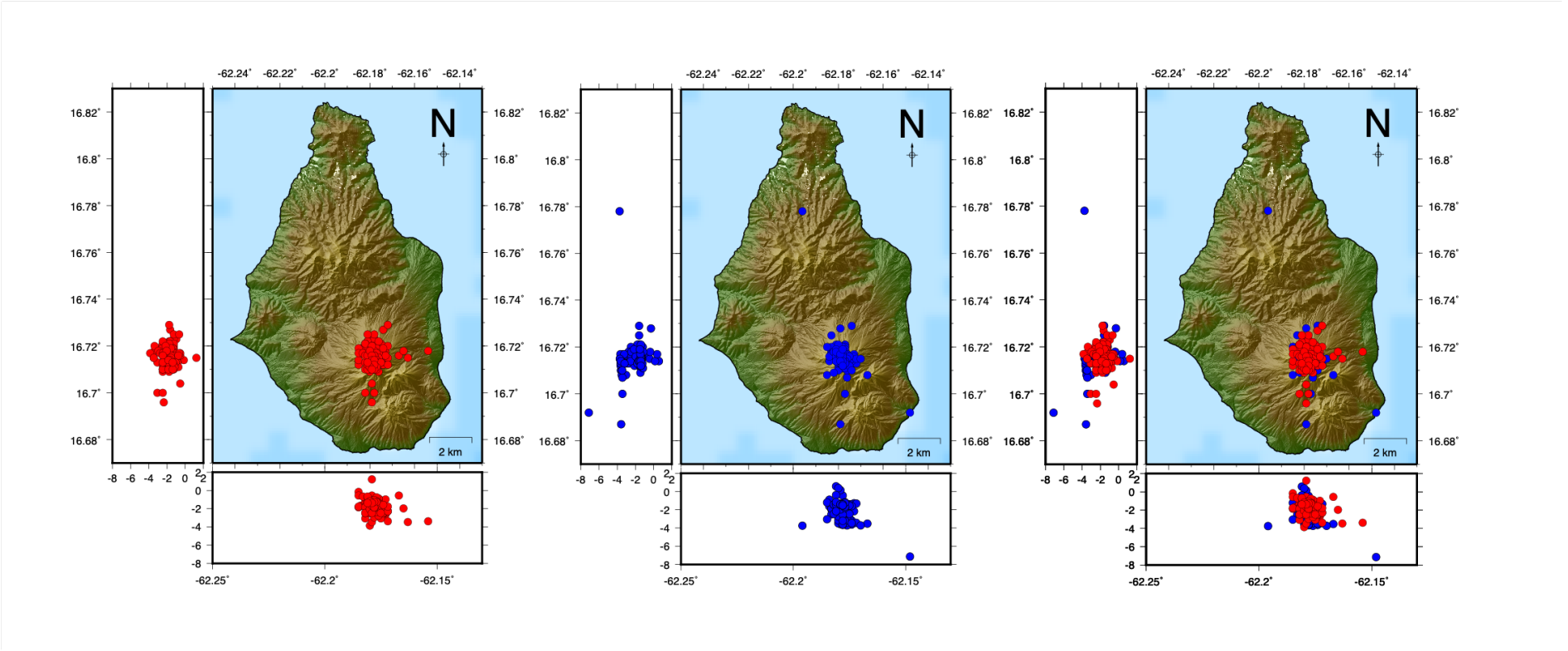

Figure 5.63: *Hypocenter* (red) and *NonLinLoc* (blue) earthquake locations for Phase 5: 5^{th} October 2009 to the 11^{th} February 2010 inclusive. Earthquakes with errors greater than 5 km have been removed.

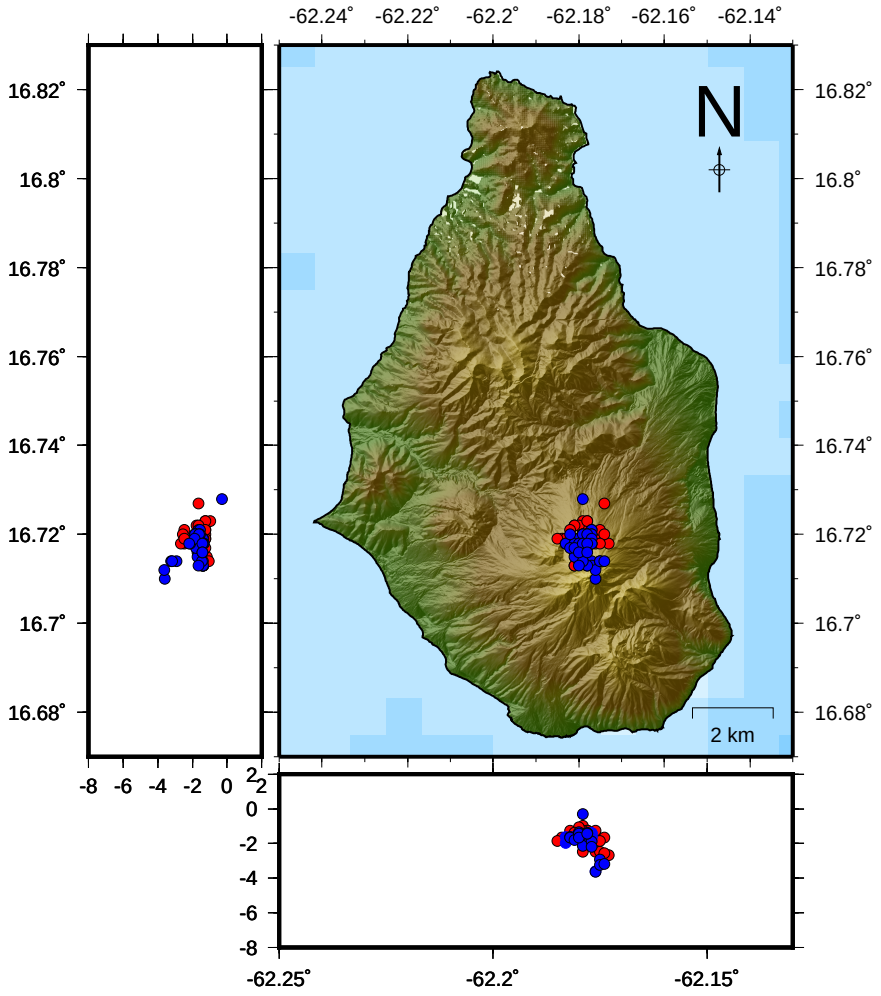

Figure 5.64: Location of earthquakes from a VT string on the 5^{th}–6^{th} October 2009. Earthquakes with errors greater than 3 km have been removed. Red are locations from *Hypocenter*, and blue are relocations from *NonLinLoc*.

5.7.2 Post Phase 5

An increase in Volcano-Tectonic earthquake depths from 2012 onwards was first highlighted in a MVO annual report (*MVO*, 2018). Only VT earthquakes are looked at in this section due to there being few Hybrid and LP earthquakes during this time frame, with only 32 hybrid earthquakes and zero LP earthquakes located during this time. Note, this does not mean there was no LP earthquakes over this 8 year period; but that MVO did not pick any arrival times for LP earthquakes during this timeframe. Figure 5.65 shows relocations post Phase 5 (February 2010 until February 2018) where VT earthquakes are coloured by year. A slight increase in depth is seen for the 2016 and 2017 period with few earthquakes shallower than 1 km bsl. Earlier time periods had a wider range in depths, with VT earthquakes in 2010–2013 being located up to 1 km asl.

To visualise this more clearly, we can look at the depth location throughout time, which is shown in Figure 5.66. A clear difference in depth location is seen post 2014 where there is a general lack in seismicity above 1.5 km depth; this coincides with the addition of Spider Stations to the network, which were added in 2014 (more information on the Spider stations is shown in section 1.5). The addition of the spider stations in 2014 has removed earthquakes clustering at the 1.5 km velocity layer. The reduction of earthquakes clustering at this velocity boundary is likely a result of an increase of seismic stations used for the location. The addition of the spider stations not only increases the number of seismic stations used for earthquake location, but also provides a wider range of station coverage, which also improves outputted hypocenters.

VT earthquakes from 2010 to 2018 were then relocated removing arrival times for the spider stations; this was to see if the spider stations were causing earthquakes to be located at a greater depth. Results still show a slight deepening even without the spider station arrival times, suggesting that this trend is real (Figure 5.67). However, the removal of the spider stations shows an increase in seismicity along the 1.5 km velocity boundary. 11 additional earthquakes were located with the Spider stations. This is likely due to increased station coverage improving overall locations, and hence removing the effect of earthquakes becoming stuck on velocity boundaries. A mean decrease in X, Y and Z errors was seen of around 100 m when including the spider stations, suggesting that the addition of these

extra stations improves the accuracy of locations.

Depth locations were compared to the number of phases that were used for each earthquake to see if there is a trend between earthquakes with smaller number of arrival times being located at the velocity boundaries (Figure 5.68). There is no trend between the number of arrival times and VT earthquakes that are located on the boundary, so instead this could be a result of the station location itself. With the spider stations resulting in a better configuration that 1) reduced errors of the earthquakes and 2) resulted in earthquakes not being located on velocity boundaries. However, this is an area that would need further research, especially if MVO wanted to use this for improving their station configuration. Overall, there is a clear deepening of hypocenters with time supporting results found by *MVO* (2018); this would benefit from further investigation to understand what mechanisms may be responsible for the deepening of VT hypocenters.

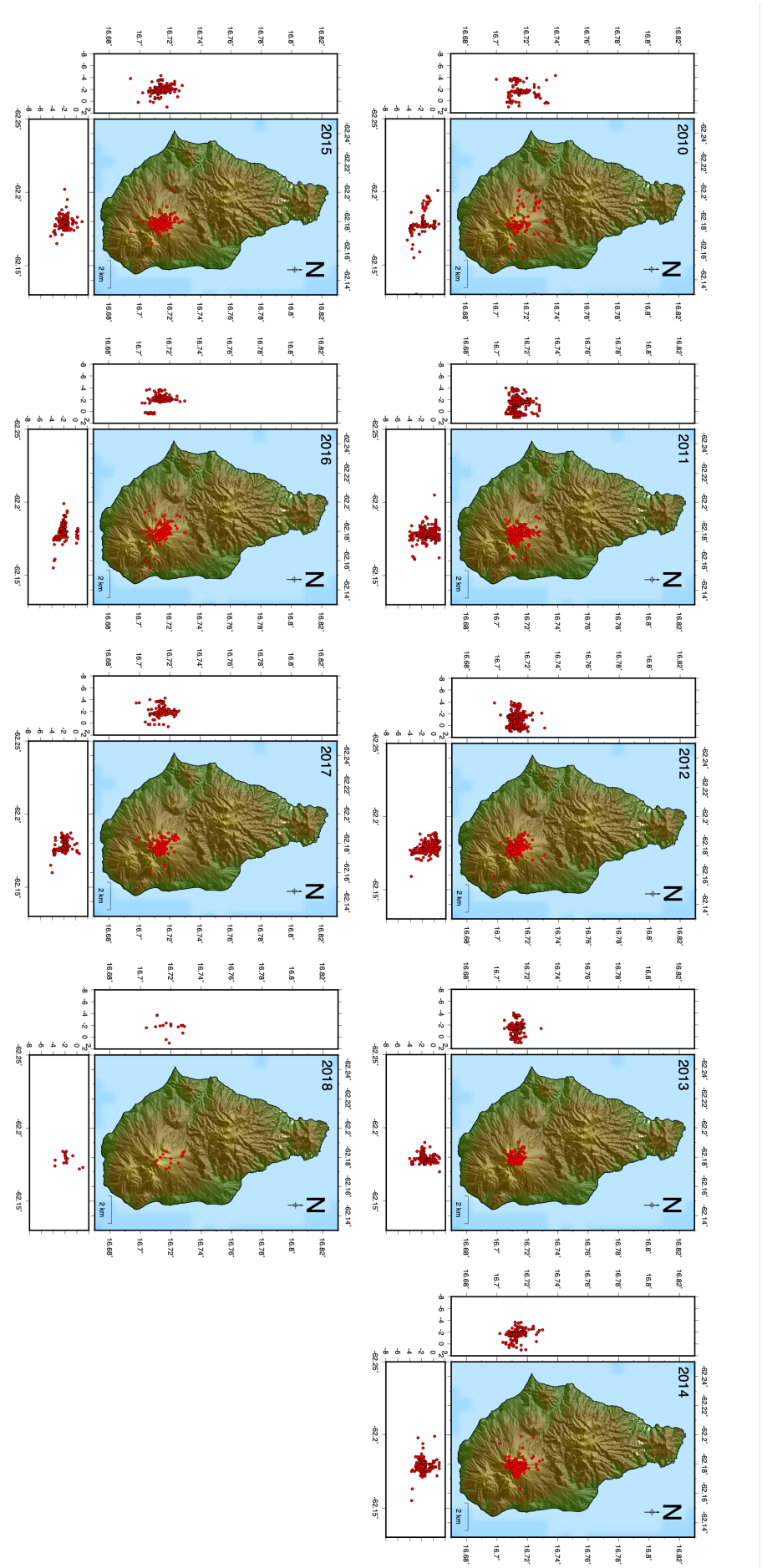

Figure 5.65: Relocation of VT earthquakes with errors less than 3 km from February 2010 to February 2018.

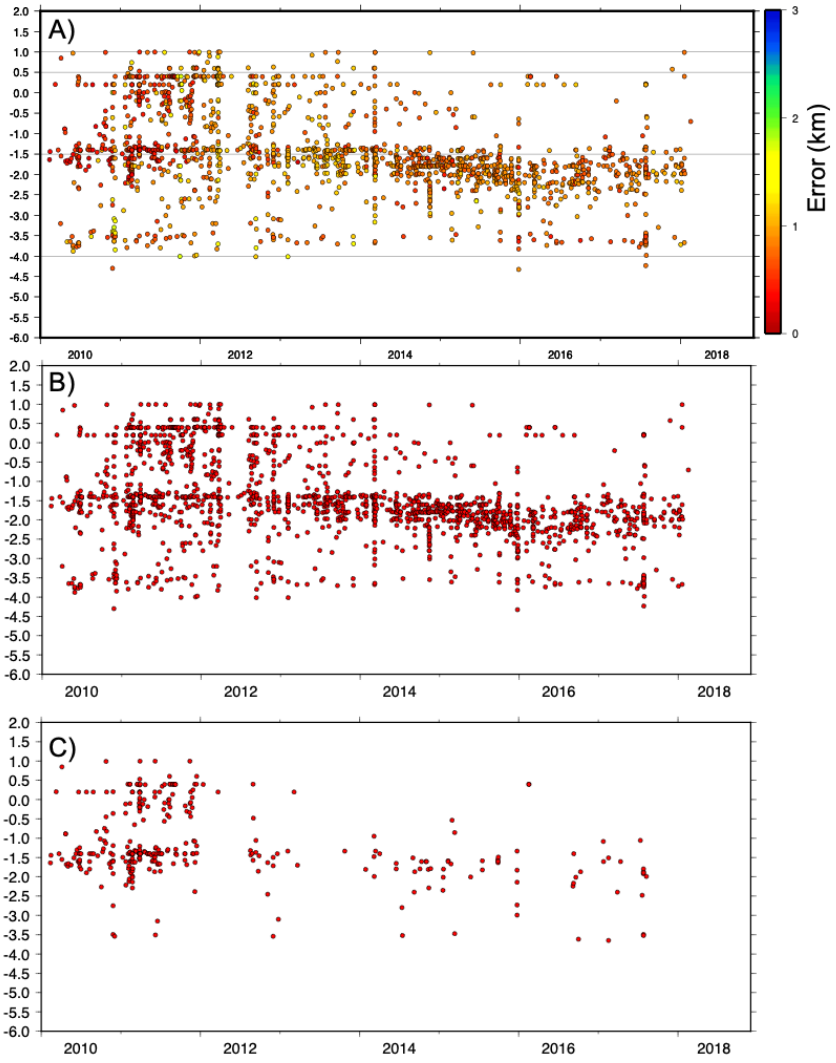

Figure 5.66: Change in depth location from February 2010 to 2018. A) VT earthquakes with errors less than 5 km and are coloured by the depth error. Grey lines represent velocity boundaries B) VT earthquakes with errors less than 3km C) VT earthquakes with errors less than 1 km.

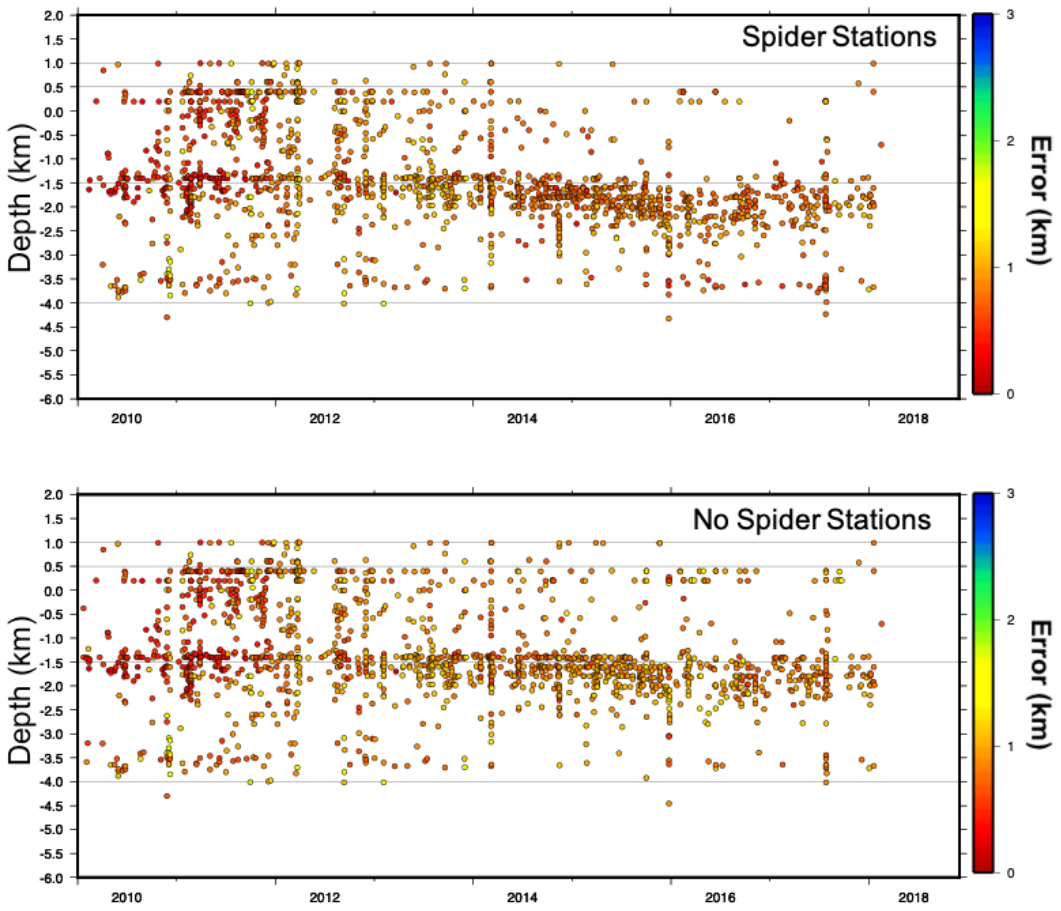

Figure 5.67: Change in depth location from February 2010 to 2018 all with errors less than 3km. VT earthquakes are coloured by error. Grey lines show velocity boundary layers. Top image shows locations with all seismic stations, and bottom image shows locations without spider stations included.

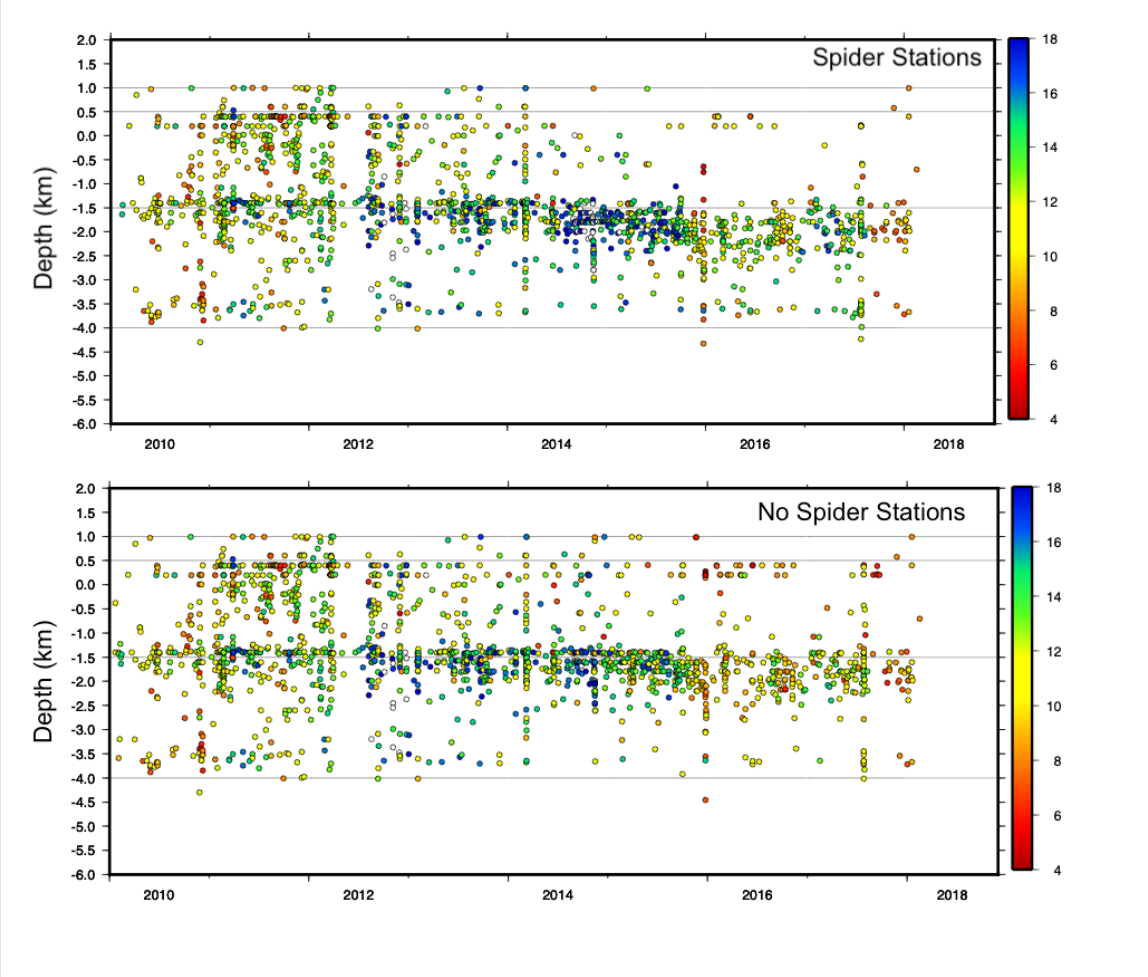

Figure 5.68: Change in depth location from February 2010 to 2018 all with errors less than 3km. VT earthquakes are coloured by number of picks. Grey lines show velocity boundary layers. Top image shows locations with all seismic stations, and bottom image shows locations without spider stations included.

5.8 Discussion

Seismicity at Soufrière Hills Volcano varied throughout the eruption, from being mostly VT dominant, to an increase in hybrid and LP earthquakes after Phase 1. Through all five phases of the eruption, an increase in VT seismicity was recorded during initial activity, before being replaced by hybrid earthquakes. VT strings were first recorded during Phase 4, and are still present today, although their mechanism remains unclear (*Smith*, 2013). An overall summary of main changes in seismic rates, locations and geological features is summarised in Figure 5.69.

Relocations using *NonLinLoc* with the *Rowe et al.* (2004) seismic velocity model have improved results, with a noticeable reduction in errors, especially for the time period 1999–2009 (Table 5.13). Overall locations are relatively similar from Phase 2 until present, with interpretations not altering much for this time period. The exception for this is relocated hypocenters in the lead up to the Vulcanian explosion on the 29^{th} July 2008, which now show a pattern in hypocenters to the SE. Phase 1 shows the main changes in hypocenters, especially for distal clusters that were recorded from 1995 to 1996.

New relocations have shown a clear migration in seismicity from the 12^{th} to the 14^{th} August 1995 from Soufrière Hills towards St George's Hill; this trend was not seen in previous studies by *Aspinall et al.* (1998); *Miller et al.* (2010). The migration of seismicity along with computed focal mechanisms by *Miller et al.* (2010) suggest dyke propagation and inflation, suggestive of a NW orientated dyke. This agrees with previous research by *Hautmann et al.* (2009) but disagrees with proposed NE orientated dykes by *Roman et al.* (2008). This is spoken about in more detail in Section 5.8.3. Seismicity to the NE of Soufrière Hills from the 5^{th}–6^{th} August 1995 also show a movement of located hypocenters towards Soufrière Hills from Long Ground. This agrees with previous interpretations by *Aspinall et al.* (1998) which suggested a migration in earthquakes over the two–day period. This was discounted by *Roman et al.* (2008) due to the large hypocenter errors. However, relocations in this study have reduced location errors, confirming the migration in earthquakes with time.

There were large changes in locations recorded during Phase 4 in the lead up to a Vulcanian explosion on the 29^{th} July 2008 when an additional 223 earthquakes were relocated. However, large location errors on earthquakes relocated to the SE resulted in these additional

events not being able to be included for interpretation. This highlighted the importance of having low location errors so that more events could be included for analysis, and is investigated further in Chapter 6.

Earthquakes after Phase 5 had been shown to have an increase in located depth from 2012 to 2018; this was first highlighted in a MVO annual report (*MVO*, 2018). Relocations confirm an increase in earthquake depth from 2012 to 2018. Portable seismic stations (referred to as Spider stations) were installed in 2014, and there was debate to whether this had caused an increase in recorded earthquake depth. Relocations of earthquakes from 2012 to 2018 using only permanent seismic stations, and not including the portable spider stations, also showed an increase in depth over time, supporting that this trend is real.

Relocations at Windy Hill on the 8^{th}–10^{th} September 1995, and to the WNW on the 18^{th}–22^{nd} November 1995 show similar results to locations by *Miller et al.* (2010) and *Aspinall et al.* (1998). Relocations are shifted slightly, but overall give the same interpretations. Cluster analysis suggests that the Windy Hill cluster on the 8^{th}–10^{th} September 1995 show similarities to seismicity recorded at St George's Hill, highlighting that there may be similar processes occurring in both regions. Changes to previous interpretations of seismicity recorded throughout the eruption are highlighted in Figure 5.69; this shows previous and updated interpretations of the volcanic system from 1995 to 2018.

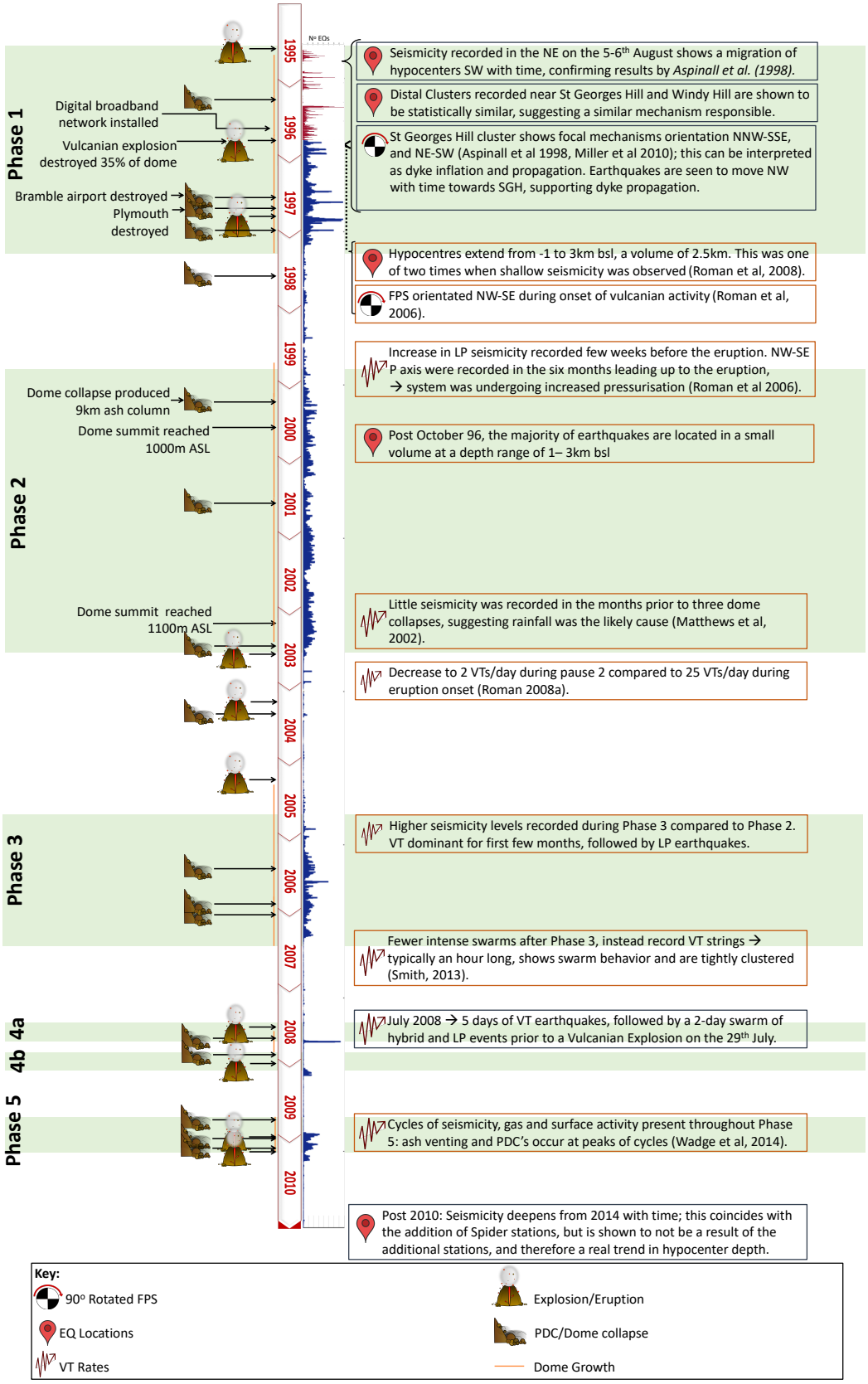

Figure 5.69: Summary of the main seismic events during the eruption from 1995–2018. This has been updated to include new interpretations found from the relocated catalogue in this chapter; these have been boxed in blue to distinguish between original interpretations.

5.8.1 Temporal Trends

Relocated earthquakes from Phase 1 show several distal clusters that are located to the NNW and NE of Soufrière Hills from August 1995 to February 1996. Twelve distal clusters were recorded during this time period, with the majority of clusters having hypocenters beneath St George's Hill and Windy Hill. Cluster analysis reveals that while these 12 clusters are temporally distinct, they can be combined into three distinct mega-clusters spanning Phase 1: 1) Underneath St George's Hill and Windy Hill, 2) to the NE near Long Ground, and 3) a WNW trend in hypocenters that occurred over a 10 day period. Analysis of the third cluster trending WNW suggests that the likely mechanism is intruding magma, which increased pressure in the surrounding conduits, resulting in the reactivation of faults in the local vicinity (*Miller et al.*, 2010; *White and McCausland*, 2016).

Earthquakes recorded on the 12^{th}–14^{th} August 1995 are located beneath St George's Hill. Previous analysis suggested that this was either a response to stress changes from a magmatic intrusion, disturbance of the local hydrothermal system or the triggering of pre-existing fault structures (*Aspinall et al.*, 1998; *Miller et al.*, 2010; *White and McCausland*, 2016). However, relocated hypocenters show a connection between the southern flanks of Soufrière Hills Volcano and St George's Hill with earthquakes located at depths of 1–5 km bsl. A migration in earthquakes towards St George's Hills is recorded over a day period. Focal mechanisms during this time are interpreted as an inflating and propagating dyke that suggest this seismicity could be a result of dyke migration. This dyke was stalled, likely reaching a stress barrier, or finding a new path of weakness, such as Soufrière Hills Volcano.

Over the next couple of months, earthquakes were recorded beneath St George's Hill and Windy Hill; these were shown to be statistically similar to the St George's Hill cluster in early August 1995. A possible solution for earthquakes being located in these distal clusters is that events are triggered by an increase in stress as the magmatic system was evolving beneath Soufrière Hills. There are a number of faults in this region that follow similar orientations to the trend in hypocenters for these distal clusters, which could have been reactivated due to an increase in stress (*White and McCausland*, 2016).

Aspinall et al. (1998) proposed a SW migration in seismicity on the 5^{th}–6^{th} August 1995.

However, *Roman et al.* (2008) did not find this migration, and suggested that this trend was recorded due to using lower quality events with errors greater than 1.5 km. Relocations show that a migration in hypocenters is recorded using events with errors less than 1.5 km concluding that this trend is real. It is uncertain why there was a migration of seismicity in this region, with earthquakes getting shallower as they migrate towards Soufrière Hills.

5.8.2 Insights into the Magmatic System

Aspinall et al. (1998) proposed a minimum depth of 5 km to the magma chamber due to hypocenters not reaching a depth greater than 7 km; this was also supported by *Elsworth et al.* (2008) who suggested an upper chamber at 6 km. Experimental work constrained the minimum depth to the magma chamber at 5 km when looking at the partial pressure of water in erupted magma from January 1996 (*Barclay et al.*, 1998). Relocations in this study show earthquakes up to 5 km depth (with errors less than 3 km), and up to 4.5 km (errors less than 1.5 km). This supports previous work that a magma chamber is likely to be greater than 5 km depth, as little seismicity is recorded beneath this point.

The presence of small amounts of basalt mixed into the erupted andesite implies there is also a deeper source of mafic magma (*Annen et al.*, 2006; *Murphy et al.*, 2000). Phase equilibria also suggested magma was reheated prior to ascent (*Barclay et al.*, 1998). Geodectic data from 1997 supports a deeper source up to 12 km (*Mattioli et al.*, 2004). *Elsworth et al.* (2008) also proposed a second magmatic chamber at depths of 12 km, connected to the upper chamber by vertical columns. This was interpreted from surface flux measurements of magma, which have been shown to respond to volume and pressure changes from a deeper level rather than deflation of the shallower reservoir (*Elsworth et al.*, 2008; *Sparks et al.*, 1998).

Deformation data suggest that the upper reservoir is largely open, with estimates that the source is 4 km^3 (*Elsworth et al.*, 2008; *Voight et al.*, 2006). Tilt measurements from December 1996 to August 1997 show a source depth to the magma conduit to be 740–970 m, with a radius of 200–340 m (*Widiwijayanti et al.*, 2005). This is similar to results by *Voight et al.* (1998) that modelled the source epicentre of the plug using a mogi model to be 700–800 m below the dome. This ties in with LP seismicity that is located in the shallow subsurface. This region would be larger than what would be estimated from magma flux.

Therefore it is suggested that the upper reservoir is largely open, with a magma mush that is transmitting overpressures from the conduit (*Elsworth et al.*, 2008; *Voight et al.*, 2006; *Widiwijayanti et al.*, 2005).

5.8.3 Dyke Projection

Regional stress and the orientation of mapped dykes on Montserrat is characterised by a NE-SW arc-normal compression (*Bonneton and Scheidegger*, 1981; *Wadge*, 1986). Using seismicity from Phase 1, *Roman et al.* (2008) proposed a 90 degree P axis change in orientation during October 1996 to June 1997, from NE-SW to NW-SE. Changes in focal mechanism orientations have been shown to relate to changes in eruption, with this change coinciding with a period of increased magma extrusion prior to a series of Vulcanian Explosions in June 1997 (*Roman et al.*, 2006). Pressures higher than regional stresses are needed to promote rotated VT's (*Vargas-Bracamontes and Neuberg*, 2012), and hence *Roman et al.* (2006) suggested that rotated P axis could be a result of an inflating magmatic system.

However, there are conflicting results to this, with different dyke projections suggested. Deformation data suggests a NW and NNW trend (*Hautmann et al.*, 2009; *Mattioli et al.*, 1998). This supports ground displacement in the area, NNW trending faults across the Soufrière Hills complex, and fits with other larger faults in the region such as the Belham Valley Fault, Richmond Hills Fault, and the Montserrat-Havers Fault Zone (which extends offshore from southern Montserrat towards Guadeloupe (*Feuillet et al.*, 2010)). Domes from the Soufrière Hills complex are similar to the strike of faults in the region, suggesting that these formed as a result of a NNE-SSW crustal extension, such as a NNW trending dyke (*Baird et al.*, 2015). Previous dyke orientations, volcanic complexes and faults are shown in Figure 5.70.

Hautmann et al. (2009) used 3D finite element modelling with data from 1997 to estimate a NNW-SSE dyke conduit with a width of 390–1100 m at a depth of 880–1230 m bsl. This agrees with results by *Mattioli et al.* (1998), which used GPS data from 1995–1996 to infer a dyke orientated at 320 degrees. Shear Wave Splitting measurements using data from 1996 to 2007 shows stations around Soufrière Hills to have a WNW strike, suggesting anisotropy is structurally controlled and fits with a NNW dyke orientation (*Baird et al.*, 2015). However, two stations (MBGH and MBGB) showed rotations in strike in the months prior to Phase

2; this was interpreted as changes in localised stresses due to dyke intrusion (*Baird et al.*, 2015). *Roman et al.* (2006, 2008) proposed a NE trending dyke based on trends in p axis from VT seismicity. A NE orientated dyke was also proposed by *Miller et al.* (2010) using 1995 seismic data, and by *Chardot et al.* (2010) using strain measurements in 2008; however, both suggested these were short lived trends.

There is still strong disagreement between these two interpretations for dyke orientation. Trends in hypocenters of relocated earthquakes from this study show a WNW trend for a distal cluster in November 1995, and a NW trend for the St George's Hill Cluster in August 1995. Earthquakes in August 1995 were shown to migrate from the flanks of Soufrière Hills Volcano NW to St George's Hill over a day period; this alongside focal mechanisms for the period suggests a propagating dyke with a NW trend, shown in Figure 5.70. Further, P axis parallel to the regional compressive stress (in this case NE-SW) have been shown to occur for VT seismicity at the tips of propagating dykes (*Ukawa and Tsukahara*, 1996), and for VT earthquakes occurring on shear planes extending obliquely from the edge on an inflating dyke (*Hill*, 1977). Time periods where NE-SW orientations were proposed were seen underneath St George's Hill, Windy Hill and Soufrière Hills (*Miller et al.*, 2010). These fit with time frames where we see the possibility for migration of seismicity in this region. Hence, a reason for the rotated p axis is more likely to be interpreted as propagation of an intruding dyke, instead of a newly proposed dyke orientation.

A NNW trend fits with geological evidence, mapped dykes and fault complexes across the island (*Feuillet et al.*, 2010), overall suggesting this orientation is the most likely. There was seismicity recorded earlier in August that showed a migration in seismicity to the SW from Long ground, showing an overall NE orientation. However, as proposed by *Miller et al.* (2010) it is likely that these are short lived trends, and could even be the activation of faults in the region due to magmatic intrusion, triggering distal clusters as proposed by *White and McCausland* (2016). This could also explain seismicity recorded beneath Windy Hill during the early stages of the eruption.

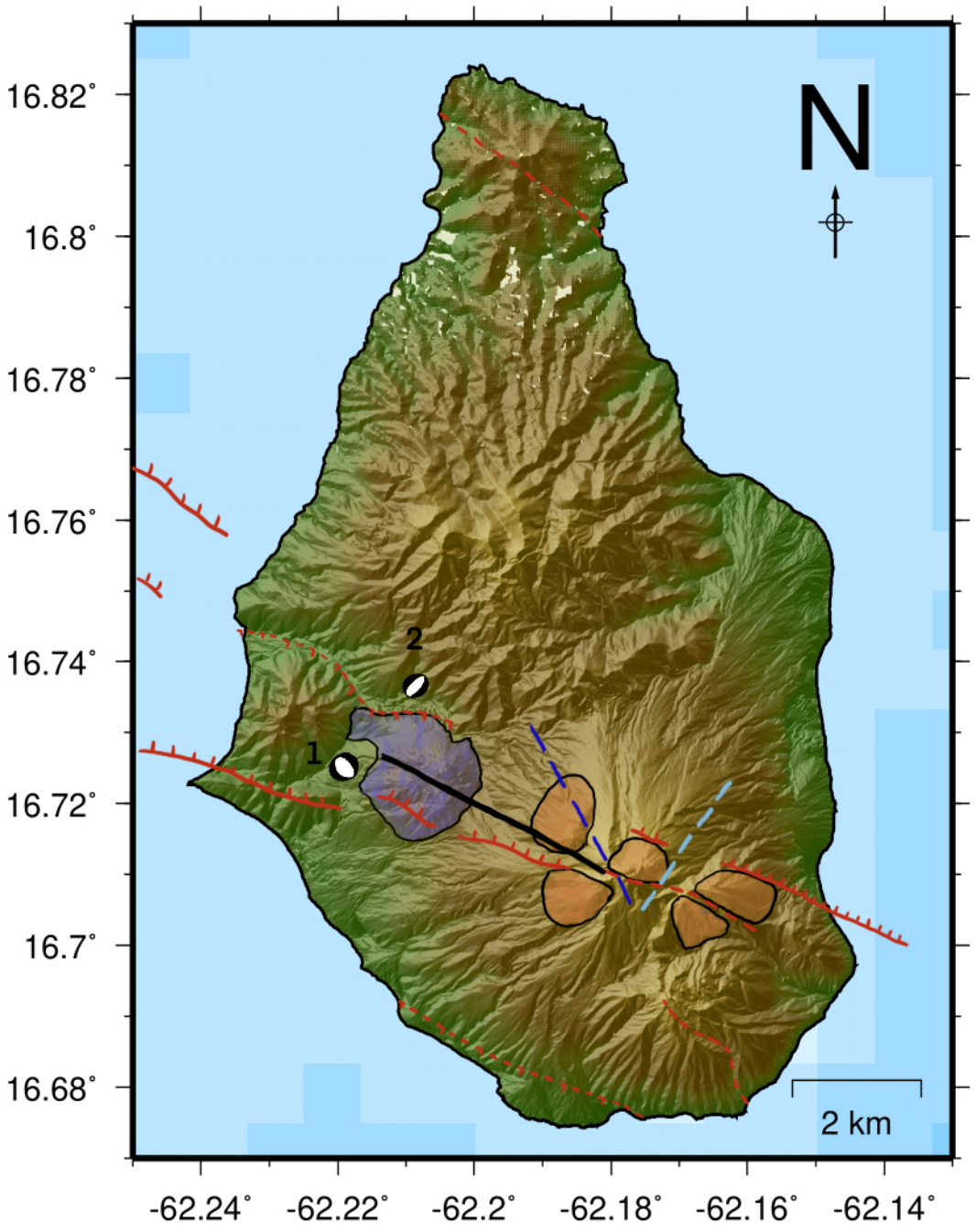

Figure 5.70: Summary of proposed dyke orientations from different research and the new proposed orientation from this study (black line). Dark blue dashed line represents proposed dyke orientations by *Mattioli et al.* (1998) and *Hautmann et al.* (2009); light blue dashed line represents proposed dyke orientations by *Miller et al.* (2010) - these were axknowledged to be short-lived trends. Shaded blue regions represents St George's Hill complex; orange regions represent volcanic complexes related to Soufrière Hills. Red lines represent main faults in the region. Focal mechanisms 1 and 2 are from *Miller et al.* (2010). Focal mechanism 1 shows normal faulting with NE extension; representation of dyke propagation; focal mechanism 2 shows WNW extension which can be interpreted as dyke inflation.

5.9 Conclusion

Relocating the seismic catalogue on Montserrat with the new methodology determined in Chapter 4 has been shown to reduce location errors compared to MVO's current methodology, ultimately improving the accuracy of the earthquake locations. The majority of relocated hypocenters have errors less than 5 km, with 75% having errors less than 2.5 km, greatly improving the number of earthquakes that can be used for interpretation. Relocations show new patterns in seismicity during Phase 1 where four distal clusters have been previously identified by *Aspinall et al.* (1998); *Miller et al.* (2010). Relocations show a total of 12 distal clusters during 1995–1996, with statistical similarities in locations shown between several clusters.

A distal cluster under St George's Hill had previously been thought to be a result of stress changes from a magmatic intrusion under Soufrière Hills Volcano triggering pre-existing fault structures or disturbing the local hydrothermal system (*Aspinall et al.*, 1998; *Miller et al.*, 2010; *White and McCausland*, 2016). However, relocations show a temporal trend in seismicity with hypocenters migrating from the flanks of Soufrière Hills Volcano towards St George's Hill over a 2 day period. Comparing this with focal mechanisms suggest that this distal cluster could be interpreted as an inflating and propagating dyke towards St George's Hill. This could suggest that St George's Hill could have been an eruption site, but the magma was stalled and later erupted beneath Soufrière Hills Volcano.

Previous research looking at St George's Hill and other distal clusters had to exclude several earthquakes due to large associated location errors (*Roman et al.*, 2008). Improving the methodology resulted in lower location errors, increasing the number of earthquakes used for interpretation. Relocations also refined results, allowing more detail in location trends to be shown. This has altered our interpretations for several time periods throughout the eruption, and in future may be used to improve early hazard assessment. An example of this was the recorded seismicity towards NE on the 5^{th}–6^{th} August 1995; *Aspinall et al.* (1998) proposed that there was a migration of seismicity to the SW towards Soufrière Hills, but *Roman et al.* (2008) discounted this due to large hypocenter errors. Relocations confirm this trend to be real when using hypocenters with errors less than 1.5 km, as a larger proportion of earthquakes during this time period now have smaller errors.

Differing interpretations shows the importance of testing the method used for locating earthquakes and should be applied at systems elsewhere. It is important to understand how the location method and models that are currently being used operate, and how well they perform at locating earthquakes in that region. Do the calculated errors represent the actual accuracy of outputted locations, and is there an alternate location method that may be more suited for this environment? Ultimately, this should be tested and improved at each location so that seismic catalogues are updated. It is likely that several observatories are using outdated methodologies, and improvements to the location methods and catalogues would result in additional understanding of the volcanic systems in the region.

Chapter 6

Case Study: Impact of Arrival Times on Earthquake Locations

6.1 Introduction

Relocation of the seismic catalogue from 1995 to 2018 in Chapter 5 highlighted differences in hypocentres between original and relocated locations. Relocations used the *Rowe et al.* (2004) velocity model with the *NonLinLoc* location method; this setup has been shown to reduce errors and improve the accuracy of locations (Chapter 4). A cluster of earthquakes extending to the SE was found in Section 5.6 in the days leading up to the Vulcanian explosion on the 29^{th} July 2008. This was not shown as clearly with MVO locations; however, an MVO report suggested an alignment of hypocenters to the SE (*MVO*, 2008). Other analyses have not interpreted this alignment of hypocenters due to large location errors (*Rodgers et al.*, 2016)

The majority of relocated earthquakes show large longitude errors, with most events having only four P wave arrival times (using four seismic stations). As a result, most of the earthquakes that extended to the SE were removed before the results could be interpreted. Arrival times were repicked for all earthquakes from the 21^{st} to the 31^{st} July 2008 inclusive. Due to the low number of arrival time picks, the aim was to investigate whether additional arrival times reduced location errors. The hypothesis is that the repicked dataset (with additional arrival times) would result in either reduced errors or a change in location, suggesting the previous pattern to the SE was false. Reducing the calculated errors of located earthquakes allows for better confidence in interpretations, and could add to the

understanding of volcanic processes during this time period.

Hence, this chapter aims to improve the accuracy of located earthquakes during the time period of 21^{st} to 31^{st} July 2008. First synthetic earthquakes are used to understand how using only four seismic stations for arrival times impacts locations, and how this affects calculated errors. The time period is then repicked for additional arrival times, and relocated using the method calculated in Chapter 5 to compare locations and associated errors. Finally, these locations are used to to understand the volcanic system in the lead up to the Vulcanian explosion, and to see if the seismicity recorded in the SE is still present, and if not, how this may change our interpretations. All times and dates of events are in UTC.

6.1.1 Seismicity prior to the 29^{th} July Vulcanian Explosion

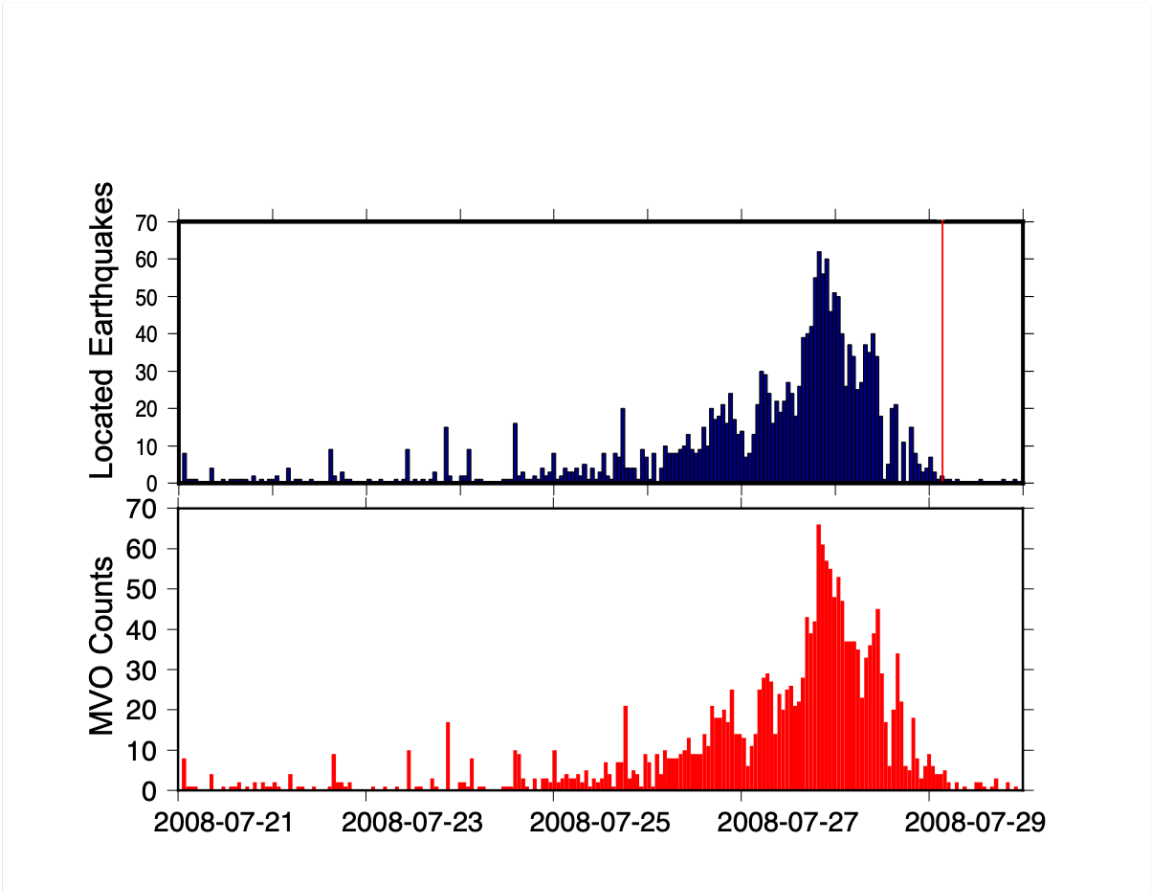

Figure 6.1: Top figure: Time plot of the number of located earthquakes per hour from the 21^{st} to 30^{th} July 2008. Red line represents time of Vulcanian explosion(UTC). Bottom figure: Number of recorded earthquakes detected by MVO, bins are separated per hour. Both plots show all types of seismicity.

An increase in VT seismicity, including several VT swarms, was recorded from the 27^{th}

April to the 2^{nd} May, prior to a Vulcanian explosion on the 29^{th} July 2008 at 03:32 UTC (Figure 5.56). This marked the restart of dome growth and the beginning of extrusion for Phase 4a (*MVO*, 2008; *Rodgers et al.*, 2016). More information of the eruptive phases is described in Section 1.4. A total of 1919 earthquakes were recorded by MVO from the 21^{st} to the 31^{st} July inclusive, with seismicity levels peaking on the 28^{th} July (Figure 6.1). The Vulcanian explosion was one of the largest explosions recorded by volume of ejected material, with a plume reaching 12 km height (*Cole et al.*, 2014b; *MVO*, 2008). Several VT swarms and ash venting episodes were recorded from April to July 2008 (*Cole et al.*, 2014a,b; *MVO*, 2008); this coincided with a strong decrease in recorded gas flux (*Nicholson et al.*, 2013). Lava extrusion at the surface was not observed until later in August 2008 (*Rodgers et al.*, 2016).

From the 13^{th} May to the 26^{th} July there was a series of small explosions from Gages wall vent alongside ash venting (*MVO*, 2008). VT seismicity was predominantly recorded in the first few days from the 21^{st}–26^{th} July, before being replaced by mostly hybrid events, and finally LP events that were dominant for a two-day period (*De Angelis*, 2009; *Rodgers et al.*, 2016). VT seismicity was located by MVO at 1.6–3.9 km beneath the summit near Gages vent on the 21^{st}, before migrating 2 km directly below the summit on the 24^{th}–26^{th}. MVO hypocenters from April–August show a cluster beneath the summit to depth of 3.5 km with a NW-SE alignment (Figure 5.59).

6.1.2 The effect of arrival times on error

An increase in the number of arrival time picks is thought to improve constraints on earthquake locations and help to reduce calculated errors (alongside other factors such as station distribution) (*Zhang et al.*, 2020). Figure 6.2 shows the number of arrival time picks against error for all earthquakes from 1996–2018. Errors are calculated in *NonLinLoc*; more information on how these errors are calculated is shown in Section 4.2.4. A slight negative correlation between the number of arrival picks and error is recorded, with correlation coefficients for X, Y and Z error of: -0.4653, -0.3291, and -0.3035 respectively. The Pearson correlation coefficient was used, which is a measure of the linear dependence between the calculated error and number of phases used. These all show a weak negative correlation, suggesting a decrease in error with more arrival time picks. Median values for the X, Y,

and Z error for each number of arrival time picks is shown in Table 6.1; a steady decrease in error is shown up to 12 arrival time picks, with errors then starting to increase slightly with the addition of more arrival times.

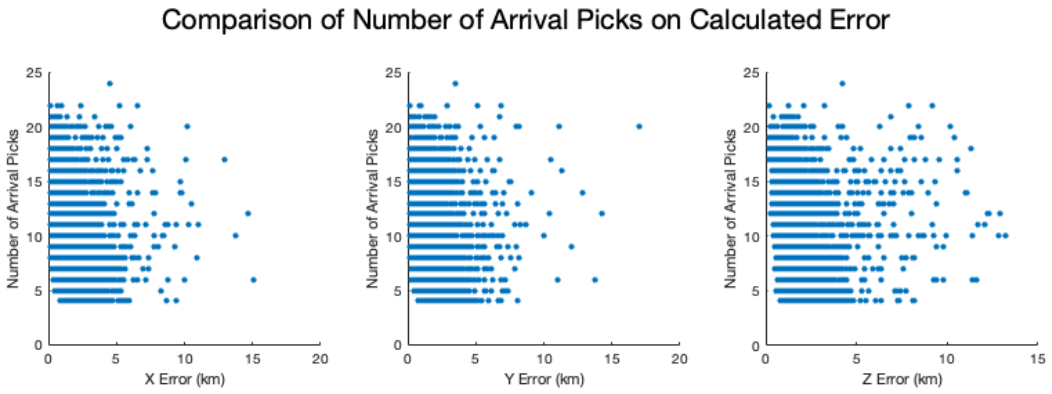

Figure 6.2: Number of arrival times (P and S waves) against the calculated error for X, Y and Z. These are current errors calculated by *NonLinLoc* for earthquake hypocenters calculated from 1996–2018.

Errors also vary with different types of seismicity. Several types of earthquakes are recorded on Montserrat, including Volcano-Tectonic, Long Period and Hybrid earthquakes; classifications for different types of seismicity are shown in Section 2.1. The range in errors for each type of seismicity is shown in Figure 6.3; these are the range in errors for each seismicity type during the July 2008 period when using the original MVO locations. VT earthquakes have relatively small errors under 2 km, whereas in general LP earthquakes have larger errors of 2–4 km. Hybrid seismicity is more varied, with errors mostly less than 2 km but with some peaks at 4 km error, similar to that seen with LP. One reason that the errors are larger with LP earthquakes is that these are harder to pick due to their emergent onsets. There is a bimodal error distribution which is particularly seen for LP and Hybrid events; this is due to the low number of arrival times used for some events, that result in large calculated errors, causing the second peak in large error.

Arrival Picks	X Error (km)	Y Error (km)	Z Error (km)
4	3.89	2.16	3.49
5	2.23	2.12	1.81
6	2.22	2.05	1.79
7	1.95	1.76	1.76
8	1.65	1.56	1.61
9	1.60	1.48	1.59
10	1.21	1.22	1.40
11	1.12	1.12	1.34
12	0.82	0.85	1.19
13	0.81	0.89	1.27
14	0.95	1.03	1.35
15	0.86	0.90	1.30
16	0.88	0.97	1.32
17	0.93	0.98	1.34
18	0.93	0.95	1.31
19	0.83	0.98	1.22
20	1.12	1.14	1.38

Table 6.1: Table showing median values for the X, Y and Z error with different number of arrival picks.

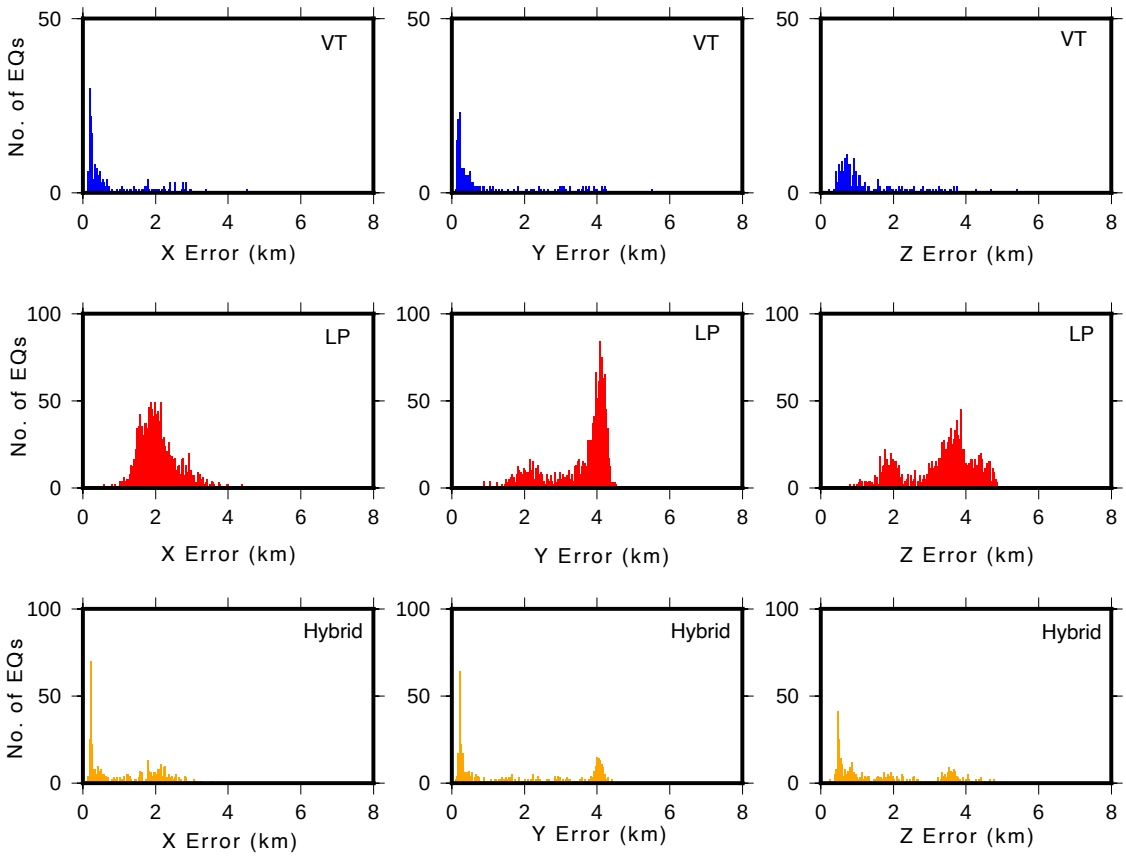

Figure 6.3: Histogram showing the X, Y and Z error distribution for each type of seismicity with original locations computed by MVO. Blue = VT, red = LP, Yellow = hybrid.

6.2 Methodology

6.2.1 Picking Arrival Times

Earthquakes were picked for P and S arrival times using the *plot* function in Seisan. For each earthquake window (predefined by the trigger in *Earthworm*), this plots all three components for each station allowing the P and S wave to be picked together. Arrival times were noted as emergent or impulsive P/S waves with a weighting of 0–4 being assigned to each pick, where 0 is best and 4 is poor. Both *NonLinLoc* and *Hypocenter* use pick weightings in the location algorithm. A low frequency filter was not applied to the waveforms due to the majority of LP seismicity being between 0.2-3Hz, which would impact picking arrival times. Figure 6.4 shows an example of an event on the 27^{th} July 2008 at 08:36 at station MBGB. The P wave was picked by MVO, but no S wave was picked at this event. The example of the S wave pick is displayed in blue. Some events had no arrival picks for the P wave at certain stations, and so these were picked where possible to do so.

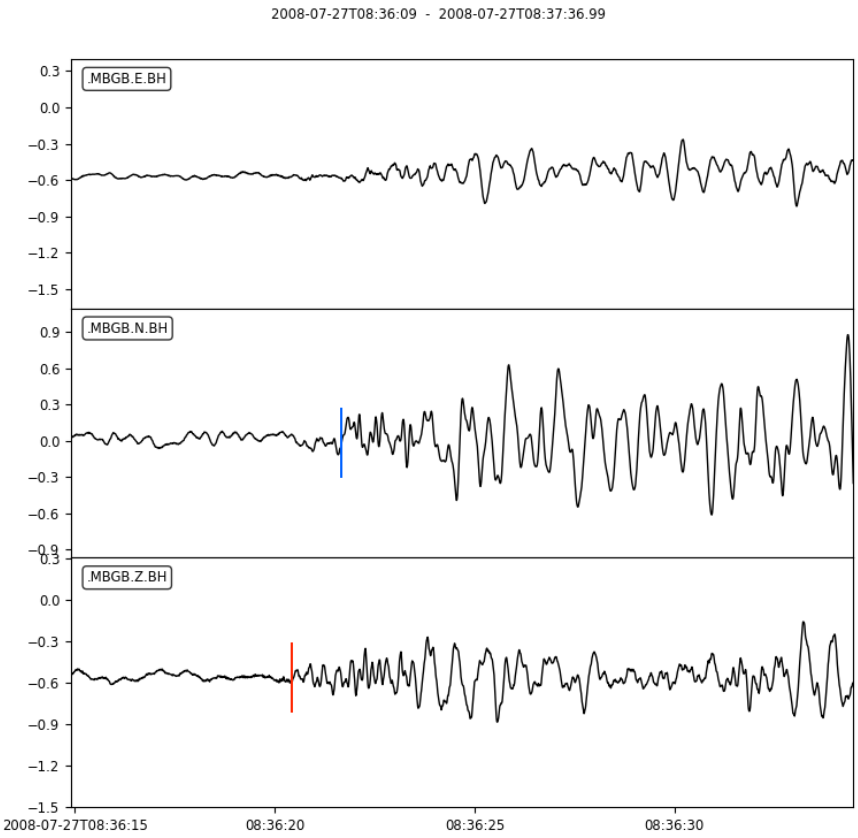

Figure 6.4: Example of waveform for an event on the 27^{th} July. Emergent P wave is shown in red, with additional S wave picked in this study.

During the peak in seismicity on the 27–28th July a lot of events only had four arrival time picks; this was likely a result of MVO having a limited amount of time during this time period. Another factor that may have influenced the number of arrival times picked in these 2 days was the emergent onset of LP earthquakes, which make the S wave less clear to pick. A lot of earthquakes had P wave arrival times picked at four stations: MBFR, MBBY, MBWH and MBGH. The network in July 2008 had nine stations that were active throughout, and therefore earthquakes during this time period had the potential for P and S wave arrivals to be picked at other stations. The impact of using only four P wave arrivals is looked at in detail in Section 6.3.

6.2.2 Comparison of S wave arrival

There were difficulties in picking the S wave for some earthquakes. The short distance between seismometers and predicted source (volcano) would suggest a P–S delay of 1–2 seconds. However, there was a clear increase in amplitude similar to the S wave at 5–6 seconds. In some cases this was the only clear increase in amplitude recorded on the E/W components, and at other events an additional peak in amplitude was recorded around 1–2 seconds. This led to some issues of whether this was an S wave or a S–P conversion (this could be triggered when the seismic wave passes through an area of melt); examples are seen in Figure 6.6. Additionally, sometimes the S wave was hard to pinpoint exactly due to the emergent nature of the LP earthquakes; as a result it was difficult to be sure whether to include these picks at low quality or to not include them at all.

To compare the importance of including the poor quality S waves, a subset of 10 LP earthquakes were used to compare how errors and locations varied when including these for locations. For example, does including lower quality S wave picks result in lower accuracy locations? Three different variations in earthquake picks were tested: 1) all visible S waves picked, 2) only very clear S waves picked, and 3) no S waves picked. This subset was located in *NonLinLoc* to compare how locations and errors differed.

This showed that excluding S wave arrival picks resulted in errors over 5 km for most earthquakes. Locations and calculated errors are shown in Figure 6.5. Picking only very clear S waves reduced the error, but still resulted in high errors of 4–5 km that would not be included in the threshold for interpretation. Picking all the S waves (including low

precision picks) resulted in the majority of hypocenters with low errors; however, this also produced a handful of hypocenters with large hypocenter errors. It was decided that having the majority of located earthquakes with small errors was more beneficial, and therefore it was decided to pick all visible S waves at each event.

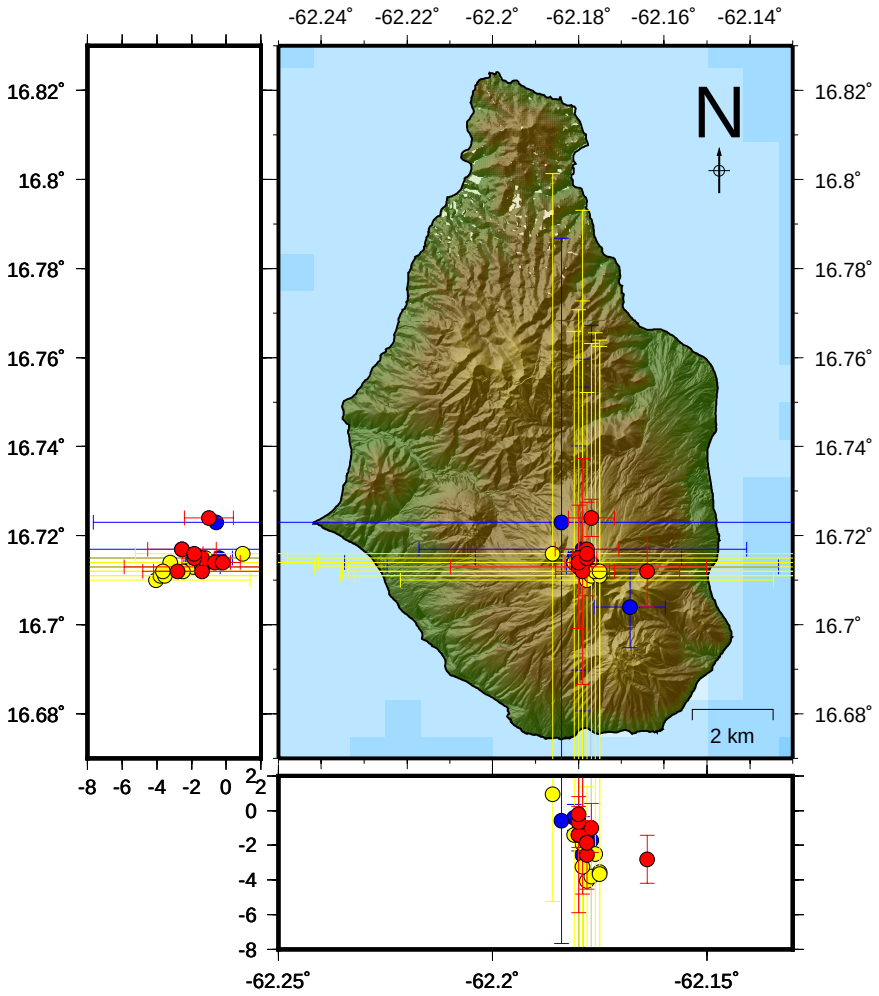

Figure 6.5: Comparison of relocations from three variations of S phase picks which have been included in determining the location, further explained in section 6.2.2. Error bars represent calculated hypocenter errors. Yellow = no S waves, Blue = only some S waves, Red = all S waves picked; see text for further explanation.

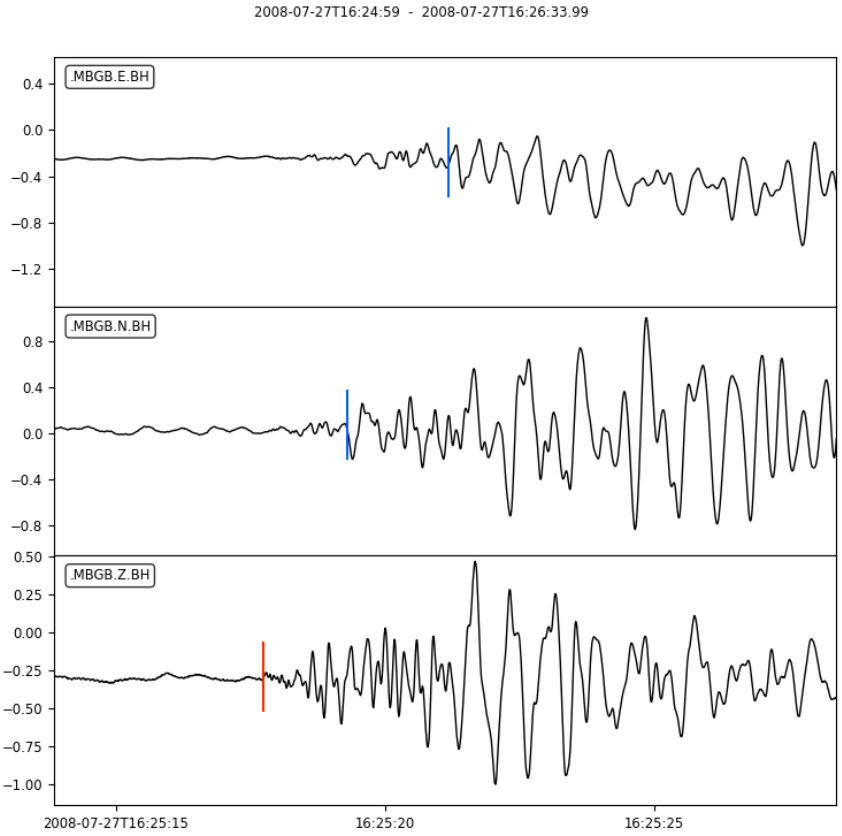

Figure 6.6: Example of waveform for an event on the 27^{th} July at 13:47. Emergent P wave is shown in red, with two different S wave picks shown in blue - comparison between where to pick the S wave.

6.3 Synthetic Results

During the time period 21^{st} to 28^{th} July, four main stations were used when seismicity was heightened due to time restrictions and to facilitate earthquake location in real-time, these were: MBFR, MBBY, MBWH and MBGH (Figure 2.5). A synthetic grid was used to relocate the earthquakes using arrival times from the four stations; the synthetic grid and setup of arrival times can be found in Section 4.2.1. Relocating the synthetic grid using only four arrival times gives an indication of how locations are affected by comparing original synthetic locations with relocations, and looking at the calculated hypocenter errors.

The aim is to understand how well we can trust earthquakes that were originally located using four P phases (accounting for over 1100 earthquakes during this time period), and if locations can be improved by the addition of an S phase at the four seismic stations used. A synthetic earthquake is 'trusted' if the change in location between original and relocated location is within the calculated hypocenter error (Section 4.2.3); this suggests that we have high confidence in the accuracy of the earthquake's location. Relocations of synthetic earthquakes first compared using only P phases, before looking at the impact of adding S phases for location. Relocations all use *NonLinLoc* with the *Rowe et al.* (2004) velocity model.

6.3.1 Change in Location

Change in location is defined as the difference in X, Y or Z location from the original synthetic location to the relocated location, more information on this is shown in Figure 4.4. Overall there are relatively small changes in location, with the majority of synthetic earthquakes showing less than 0.3 km change in location when using P and S phases (Figure 6.7 and 6.8). When using P phases only, there are some areas of Montserrat that show changes in location greater than 3 km, with this being higher for the X location. Figure 6.9 shows the direction and magnitude of change in location for the relocated earthquakes at all depths. When using P waves only, there is a strong change in location to the SW at depths 0-3 km. When including S phases this becomes more varied at each depth, with more events being located more NE and SW at each depth, with more variation in direction. Southern Montserrat has smaller changes in location, compared to north Montserrat, especially at

depths shallower than 5 km bsl.

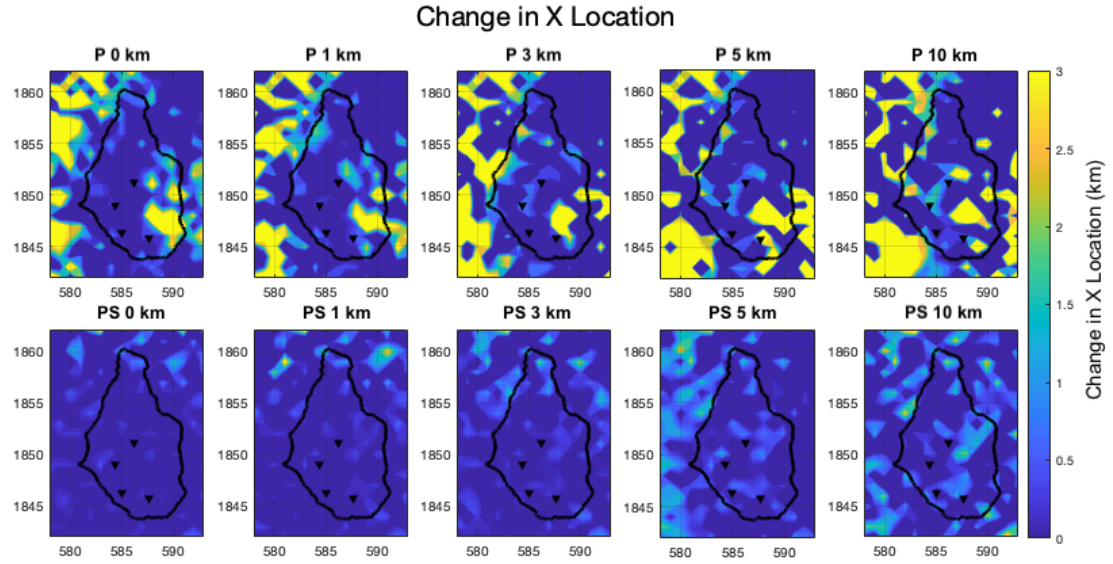

Figure 6.7: Change in X location (km) for each depth when using P waves only, and when using P and S waves for earthquake location.

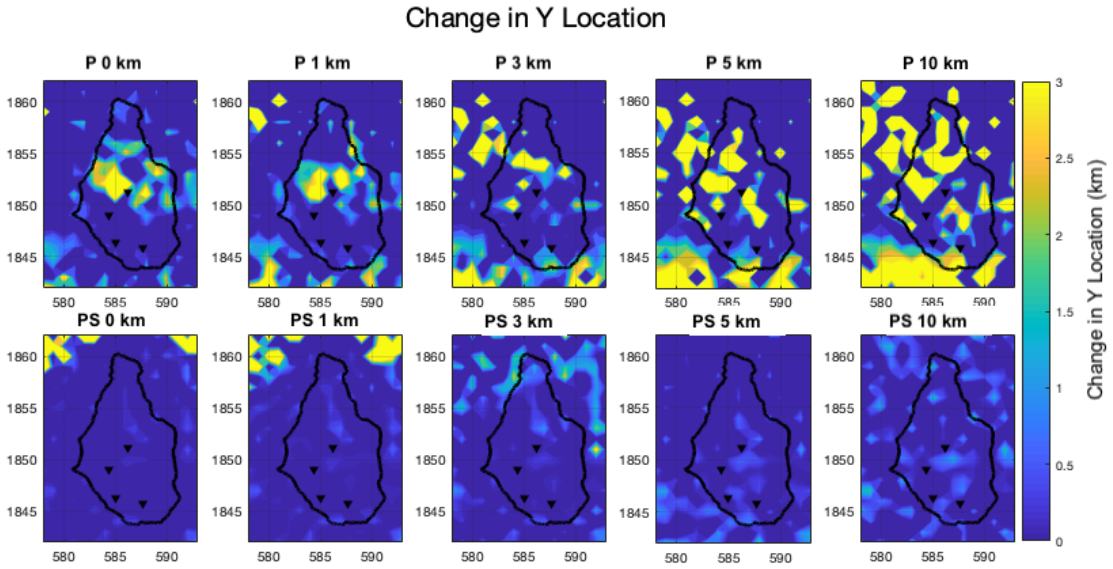

Figure 6.8: Change in Y location (km) for each depth when using P waves only, and when using P and S waves for earthquake location.

The change in depth is relatively small across the majority of Montserrat when depths are less than 3 km. At depths greater than 5 km the relocated earthquakes tend to have a greater change in depth across the majority of the island for both P and PS wave relocations (Figure 6.10). The addition of the S phase in relocation reduces the change in depth location, especially at greater depths.

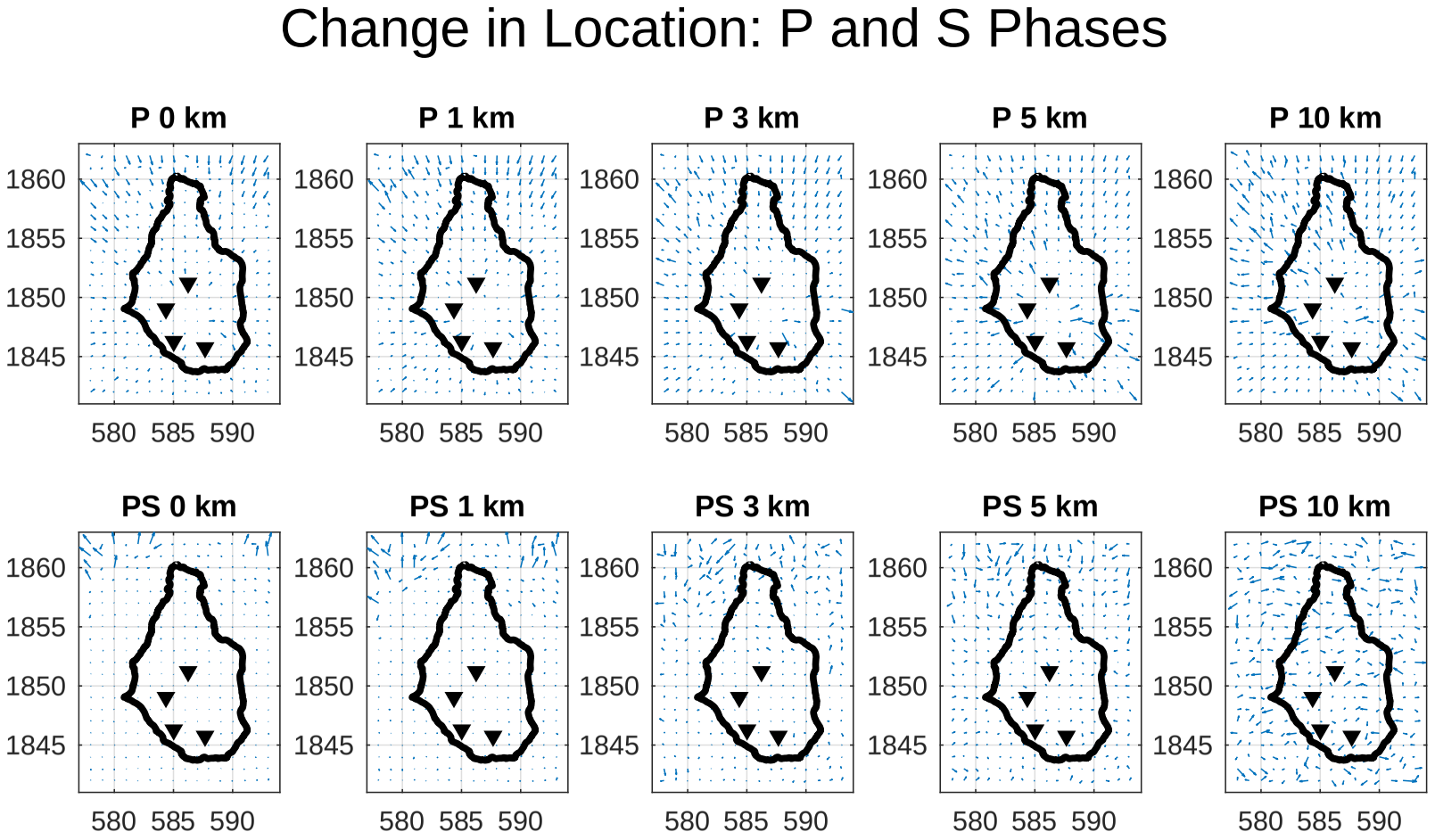

Figure 6.9: Vector plot showing the direction and magnitude of change in location at each depth when using P waves only, and when using P and S waves for synthetic location. P correspond to P wave arrivals only at all four stations, and PS corresponds to P and S wave arrivals at all four stations. There is no scale for the magnitude (length of the vector) due to each subplot being made independent of each other, and hence the length is used for relative comparison. Magnitudes for changes in location are shown in Figures 6.7 and 6.8.

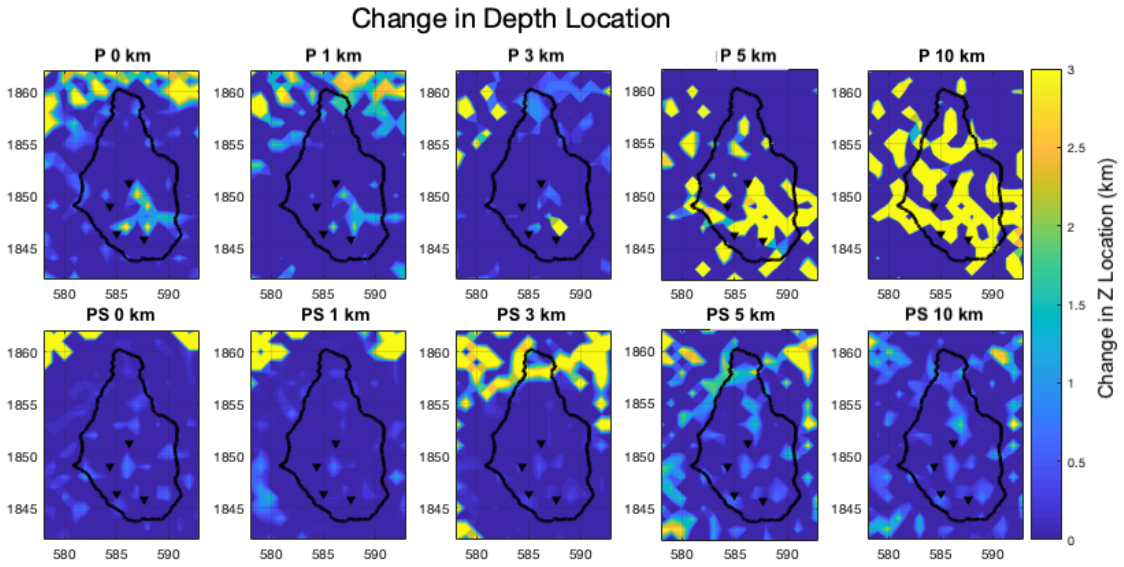

Figure 6.10: Change in Z location for each depth when using P waves only, and when using P and S waves.

6.3.2 Hypocenter Error

Calculated hypocenter errors for the synthetic earthquakes are greatly reduced when including four S phases (Figure 6.11, 6.12, 6.13).

Computed hypocenter errors are large when using only four P phases for location (Figure 6.11, 6.12, 6.13). The X error has the highest values, with an average error of 8 km; this is across all depths, with a slight increase in average X error at 10 km depth. The Y error is also large at shallow depths, but reduces with increasing depth to errors of 6 km across the island. This is likely a result of station coverage, as there is a greater spatial coverage in the Y location compared to the X location. Z (depth) errors are also large across all depths, with only a slight reduction in error at depths greater than 3 km. Hypocenter errors for the synthetic earthquakes is greatly reduced when including four S phases in the relocation.

Using four P phases has a significant impact on the accuracy of location, and results in locations with errors too large to use for interpretation across the majority of the island. As seen in the example of July 2008 this results in locations that would not pass data quality, and can provide a misleading interpretation if used. The importance of including S phases at each station can have a drastic effect on overall location and errors, however this is not always possible, especially for LP seismicity.

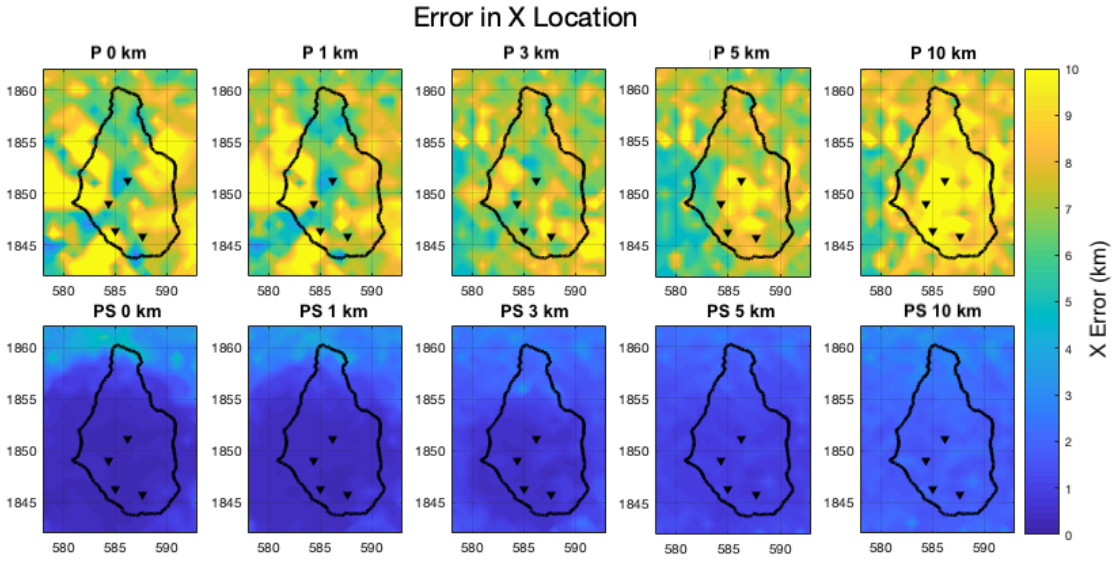

Figure 6.11: Error in X Location at each depth tested. P correspond to P wave arrivals only at all four stations, and PS corresponds to P and S wave arrivals at all four stations.

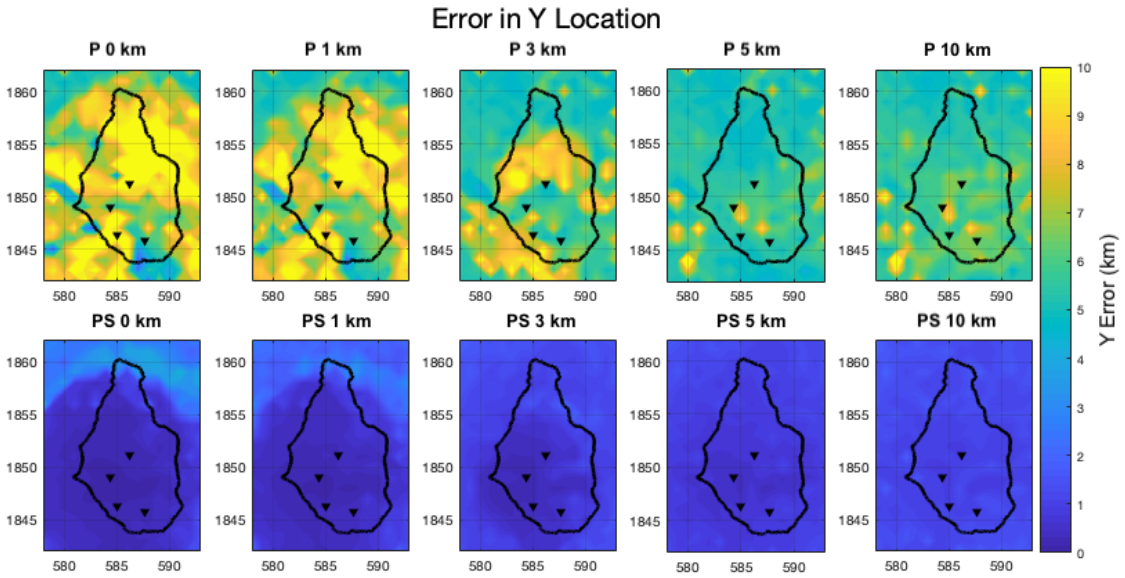

Figure 6.12: Error in Y Location at each depth tested. P correspond to P wave arrivals only at all four stations, and PS corresponds to P and S wave arrivals at all four stations.

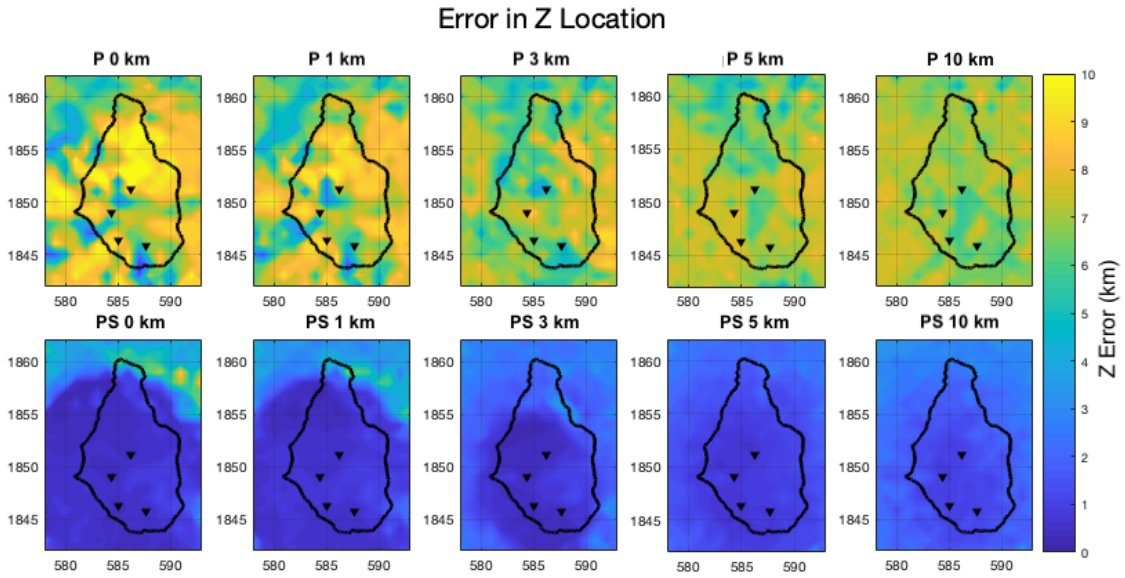

Figure 6.13: Error in Z Location at each depth tested. P correspond to P wave arrivals only at all four stations, and PS corresponds to P and S wave arrivals at all four stations.

6.3.3 Error Testing

Error testing is defined in Section 4.2.3, and is used to determine which synthetic earthquakes relocate back to their original location within the calculated error for that event. Results show a high percentage of trusted locations (Figure 6.14, 6.15, and 6.16). This shows that the program is calculating errors that are representing the location of the earthquake, improving our confidence in locations. However, having a good percentage of trusted earthquakes does not mean an accurate location, and this needs to be looked at alongside the calculated errors. The majority of locations have errors greater than 7 km when using P phases only, so although the results are trustworthy, we still have low accuracy in locations.

Trusted Z locations at 5 km shows a high percentage of untrusted events compared to other depths (Figure 6.16). This could be a result of located earthquakes being stuck on velocity model layers at this depth during the location algorithm; earthquakes are relocated to depths mostly around 1–2 km for this period, which corresponds to a velocity boundary in the Rowe velocity model. Calculated errors are small, and hence results are not being trusted as well. Locations in the SE are mostly trusted, suggesting that we would have a high confidence in the pattern of earthquake locations recorded in July 2008. However, once we include the calculated errors for earthquakes in that time period, it can be seen that these are quite large, and hence cannot confirm the presence of a SE trend.

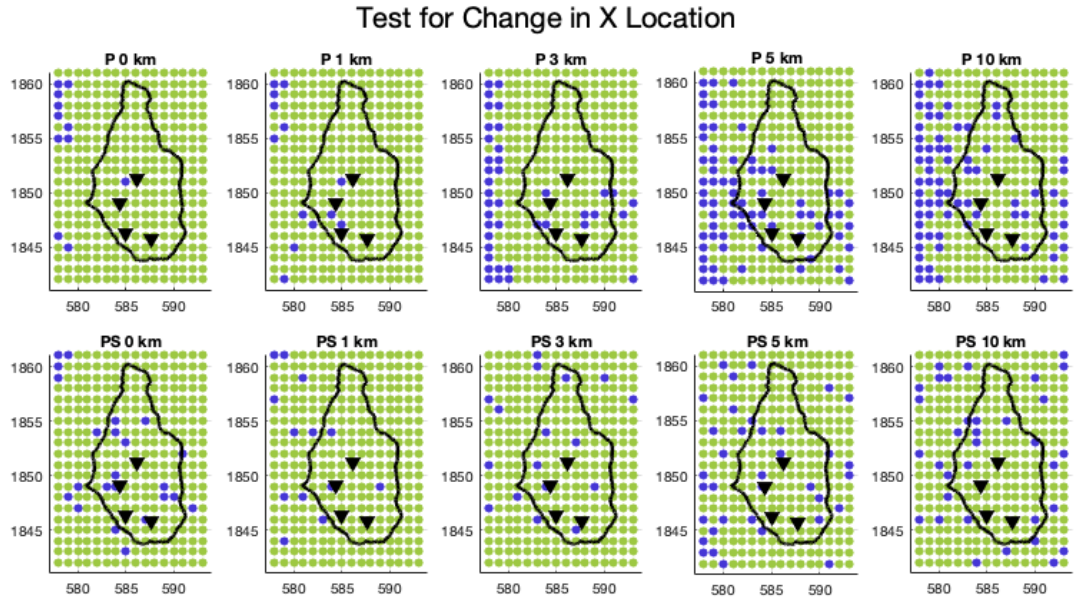

Figure 6.14: Errorcheck for the change in X location at each tested depth. P correspond to P wave arrivals only at all four stations, and PS corresponds to P and S wave arrivals at all four stations. Green represents a trusted location, blue represents an untrusted location.

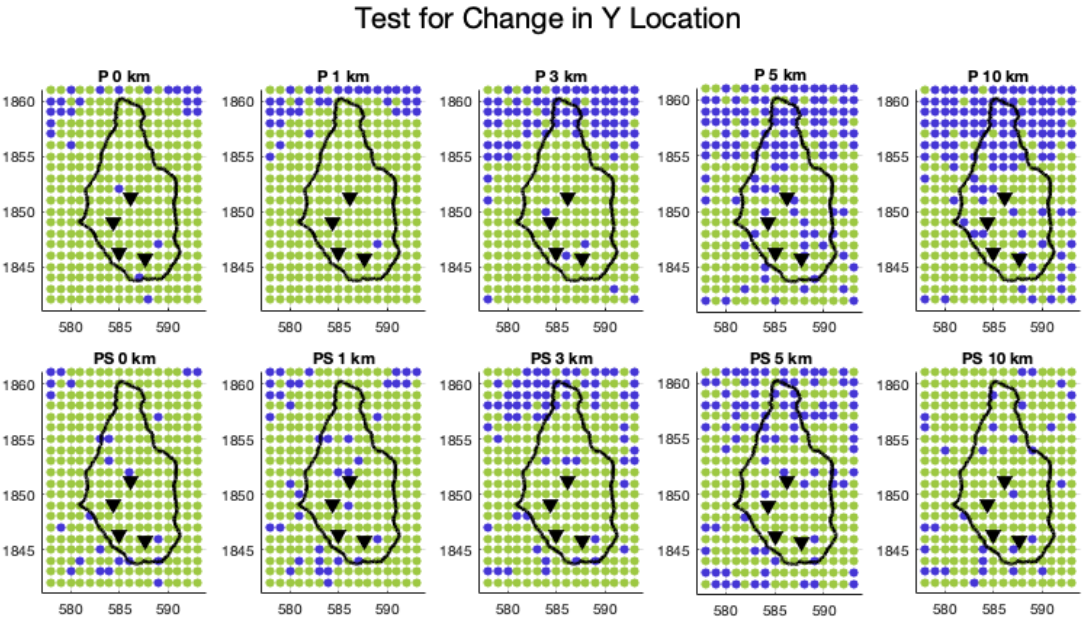

Figure 6.15: Errorcheck for the change in Y location at each tested depth. P correspond to P wave arrivals only at all four stations, and PS corresponds to P and S wave arrivals at all four stations. Green represents a trusted location, blue represents an untrusted location.

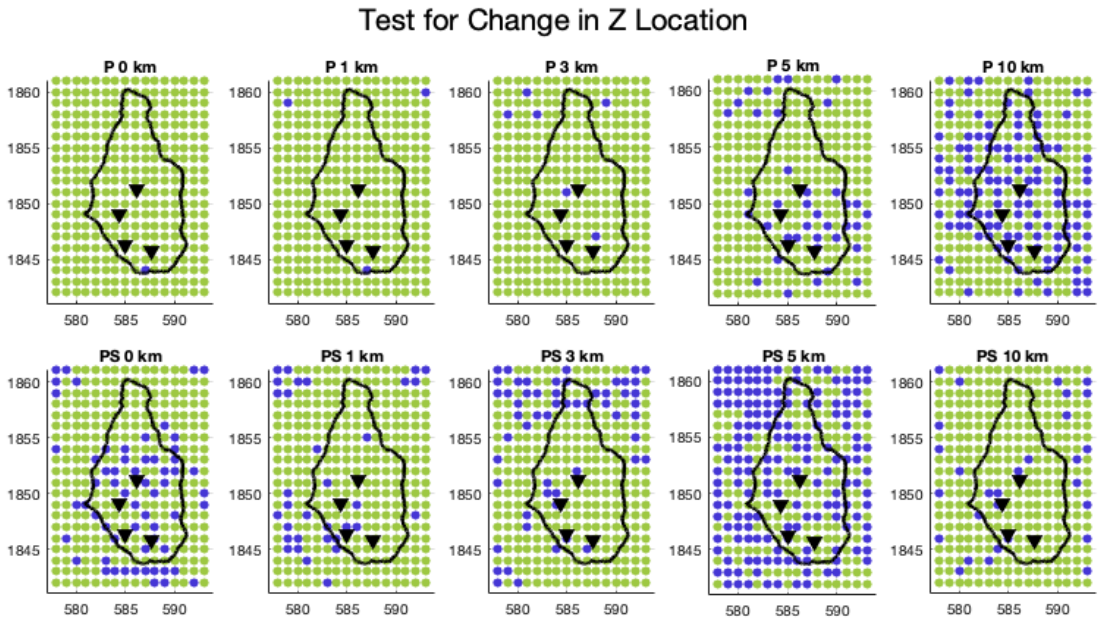

Figure 6.16: Errorcheck for the change in Z location at each tested depth. P correspond to P wave arrivals only at all four stations, and PS corresponds to P and S wave arrivals at all four stations. Green represents a trusted location, blue represents an untrusted location.

6.3.4 Station Weighting

The station weighting is calculated by *NonLinLoc* when locating each earthquake. For the Equal-Differential Time (EDT) method (Section 3.3.4), the station weighting is calculated for each earthquake, and is based on the contribution of the arrival times to the maximum likelihood solution (point of highest PDF). This means that the EDT location method is capable of removing outliers in arrival times; this was shown during the testing of the S phase, where it would weight an S wave arrival time with a 5–6 seconds P–S delay at 0. Comparing the station weighting for each relocated earthquake can give an indcation if certain stations are constantly being weighted higher or lower.

Table 6.2 shows that stations MBWH and MBFR are on average weighted higher than MBBY and MBGH, although standard deviations are lower for these stations suggesting less range in weighting. There is not much difference in station weighting at each location, with values mostly being around 1 across the island (Figure 6.17). Stations MBFR and MBBY are weighted lower for the earthquakes in the NW and NE of the island respectively, whereas MBWH and MBGH are weighted lower in the NW and SW. This is a result of the seismic stations location, with a lower weighting being applied for earthquakes further away from the seismic station.

	MBFR	MBBY	MBWH	MBGH
0 km	1.0031 ± 0.0486	0.9835 ± 0.0658	1.0147 ± 0.0542	0.9987 ± 0.0650
1 km	1.0021 ± 0.0355	0.9858 ± 0.0452	1.0110 ± 0.0601	1.0012 ± 0.0354
3 km	1.0029 ± 0.0301	0.9858 ± 0.0335	1.0131 ± 0.0261	0.9982 ± 0.0275
5 km	1.0044 ± 0.0245	0.9871 ± 0.0330	1.0120 ± 0.0251	0.9965 ± 0.0285
10km	1.0075 ± 0.0230	0.9856 ± 0.0343	1.0128 ± 0.0285	0.9942 ± 0.0302

Table 6.2: Means and standard deviations of each station weighting when using P waves only for each depth. Station weighting is calculated for each earthquake.

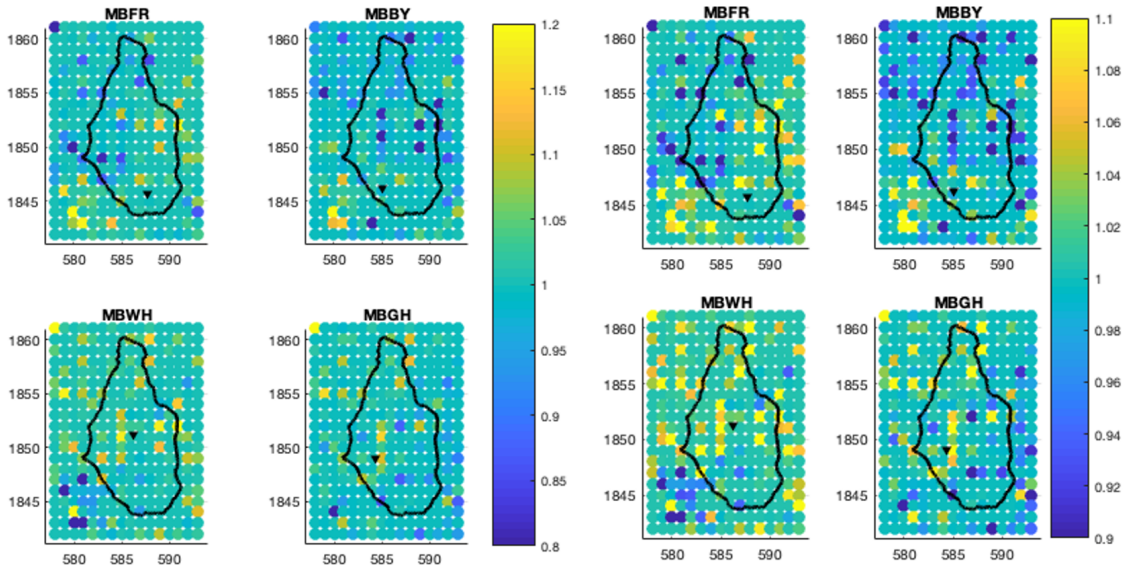

Figure 6.17: Figure showing the station weighting for each location at each station when using P waves only for 0 km depth. These weightings are calculated by *NonLinLoc* for each station for each earthquake. Image on right shows a tighter scale to show any variation across the island

6.3.5 One S Phase

The synthetics in the prior section looked at the addition of an S phase at all four stations, where in reality this would be unlikely. This section compares using P phases with the addition of one S phase (tested at each station iteratively) to see how this improves location and errors. This is later compared with the addition of two S phases in Section 6.3.6.

Change in location for X and Y locations is similar for all four variations of one S phase, with small regions having changes greater than 2 km (Figure 6.20 and 6.21). Changes in location are seen to generally increase in depth, especially for the X location, whereas the Y location shows an overall increase in location change, but a reduction in areas based on the station used. Figures 6.18 and 6.19 shows the direction in change in location for each configuration and at each depth. At depths greater than 1 km the direction in change in location is very similar across all configurations, with only events at 0 km depth showing a variation between stations. S phases picked at stations MBFR and MBWH show similar orientations with a peak to the SW at greater depths, whilst stations MBBY and MBGH have a more general scatter.

However, the calculated errors are still large, and show similar results to using four P phases. The X, Y and Z errors all show a similar pattern with an increase in error with depth, with the X errors most affected (Figures 6.23, 6.24 and 6.25). At depths greater than 5 km the majority of southern Montserrat has calculated errors greater than 7 km. At 0 and 1 km depth there is some variation between different stations. When using MBFR and MBBY stations for an S phase pick, there is more error to the west of the island compared to the other configurations. Both of these stations are the most southerly, and hence could increase errors further north.

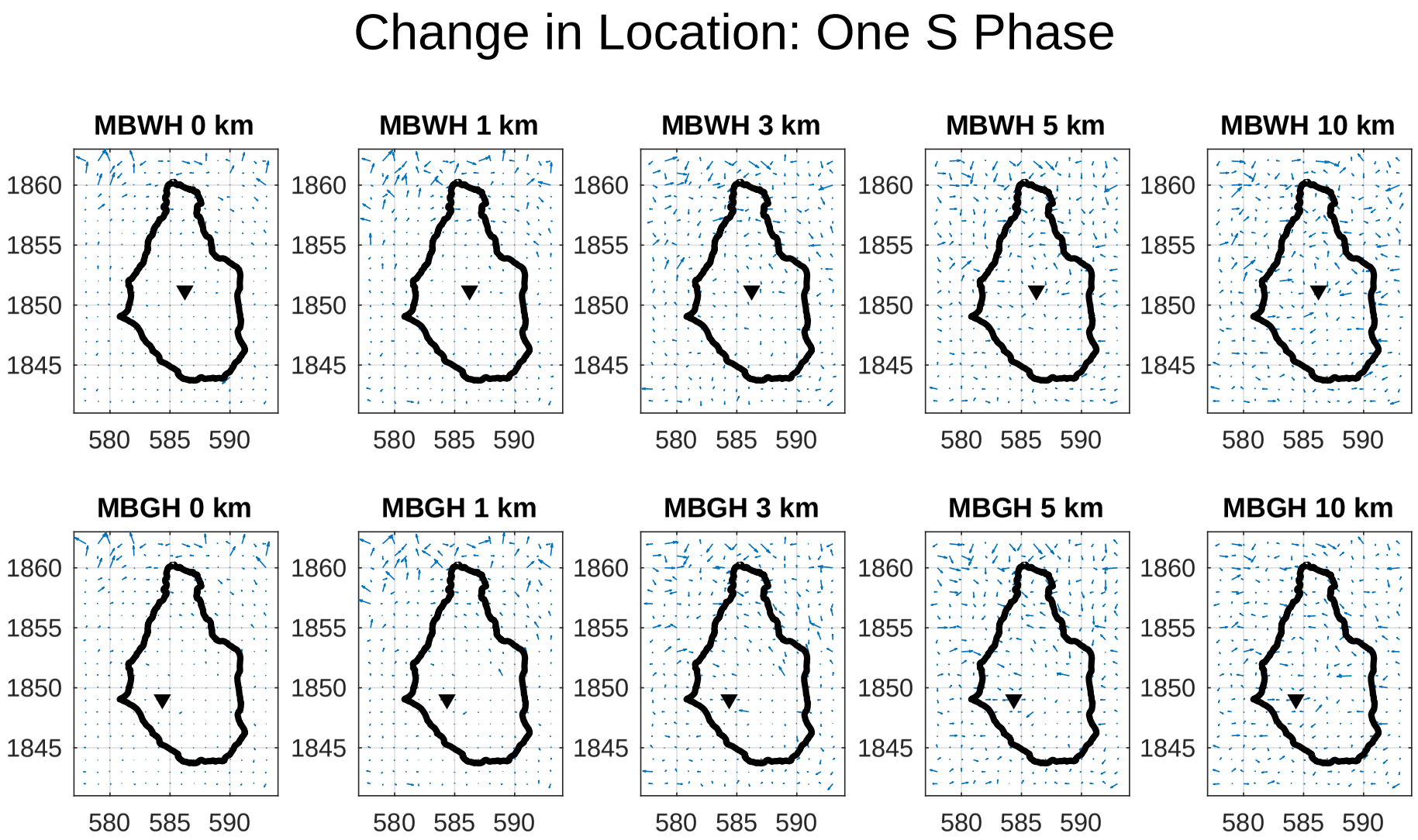

Figure 6.18: Figure 1 of 2. Vector plot showing the direction and magnitude of change in location at each depth when using one S Phase for synthetic location. There is no scale for the magnitude (length of the vector) due to each subplot being made independent of each other, and hence the length is used for relative comparison. Magnitudes for changes in location are shown in Figures 6.20 and 6.21.

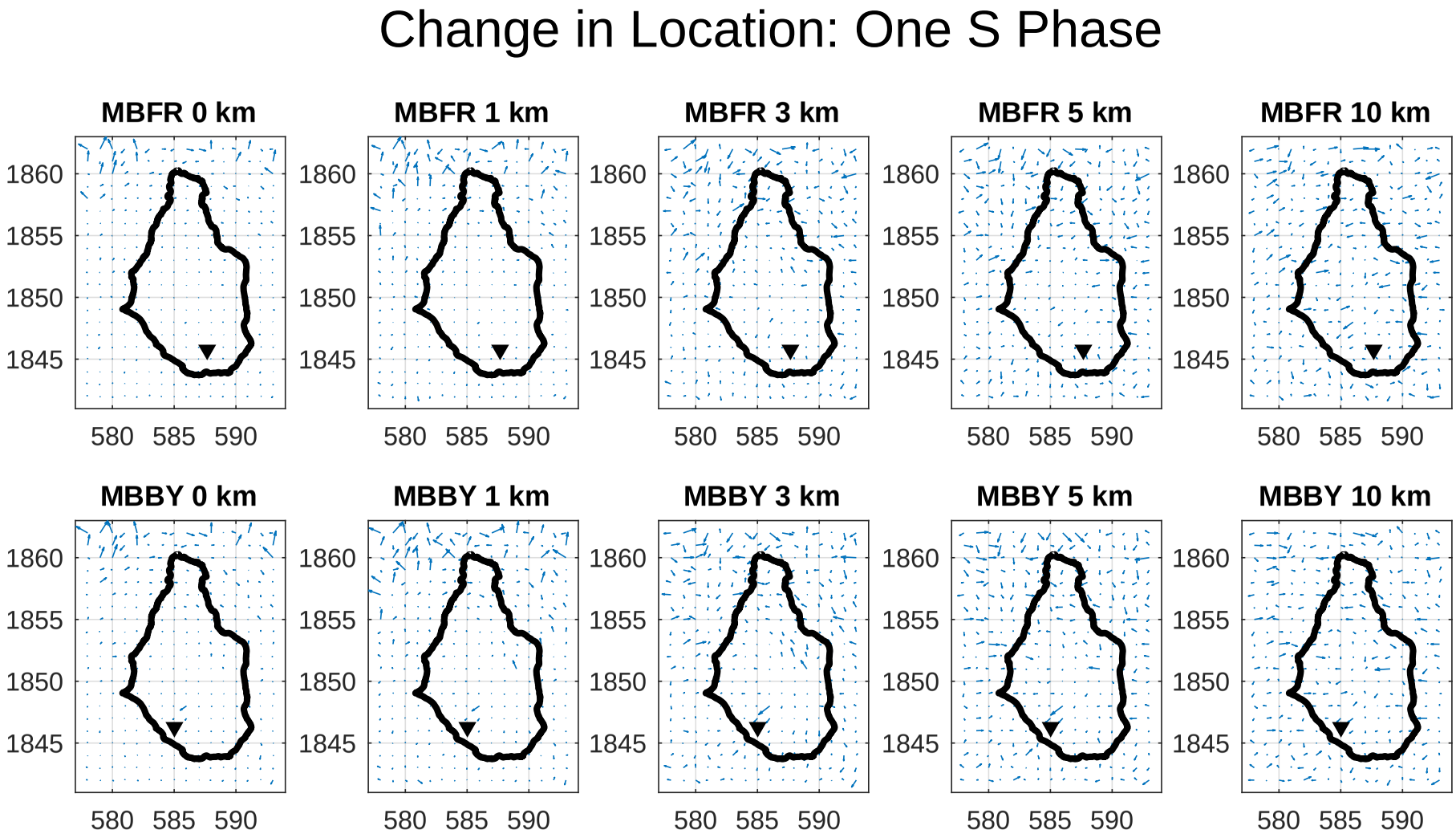

Figure 6.19: Figure 2 of 2. Vector plot showing the direction and magnitude of change in location at each depth when using one S Phase for synthetic location . There is no scale for the magnitude (length of the vector) due to each subplot being made independent of each other, and hence the length is used for relative comparison. Magnitudes for changes in location are shown in Figures 6.20 and 6.21.

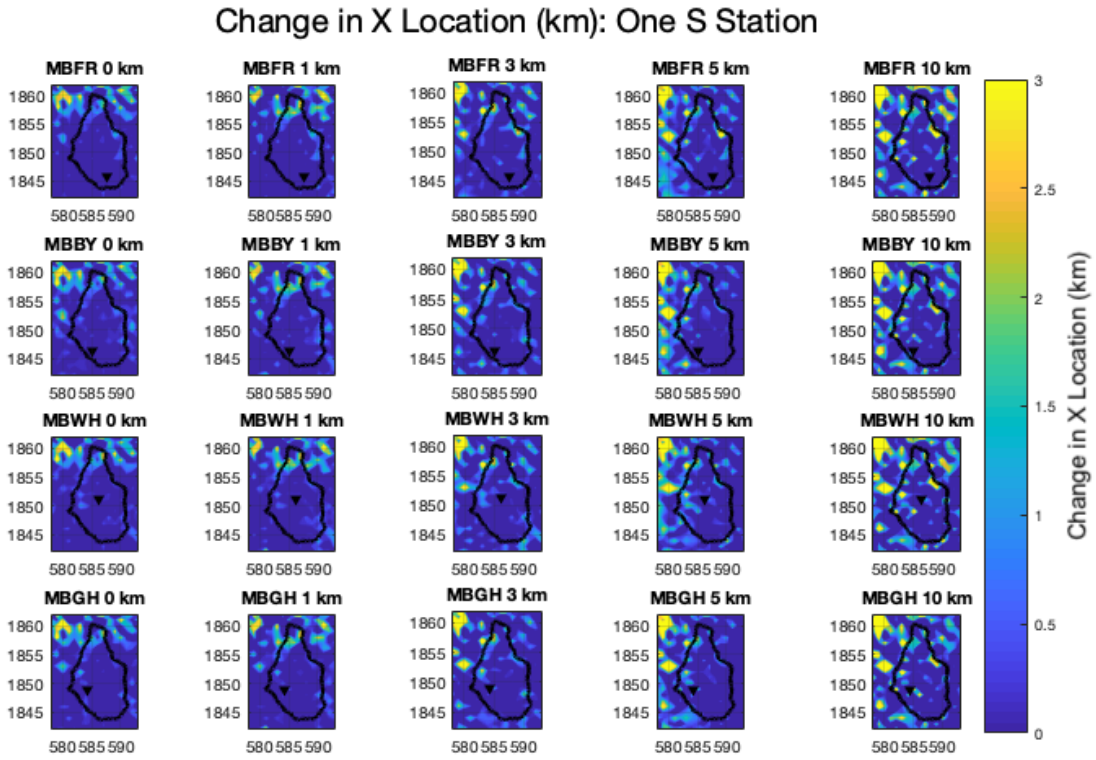

Figure 6.20: Change in X Location at each depth tested, when using one S wave from each of the four Seismic Stations.

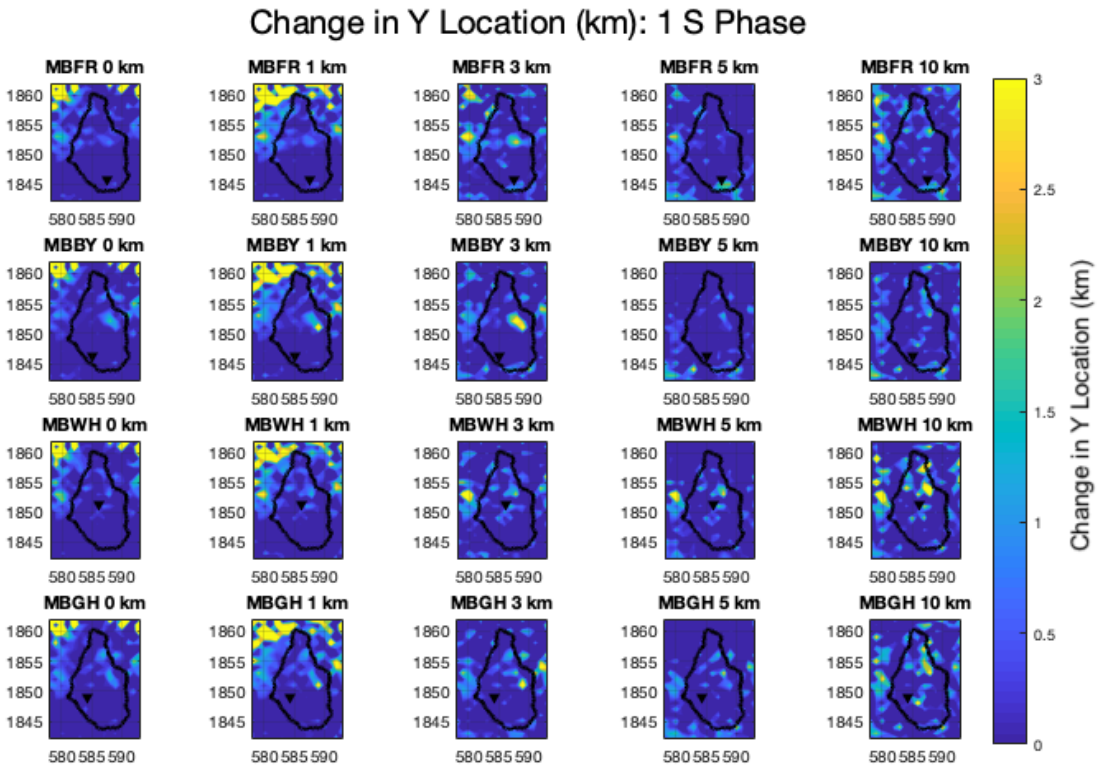

Figure 6.21: Change in Y Location at each depth tested, when using one S wave from each of the four Seismic Stations.

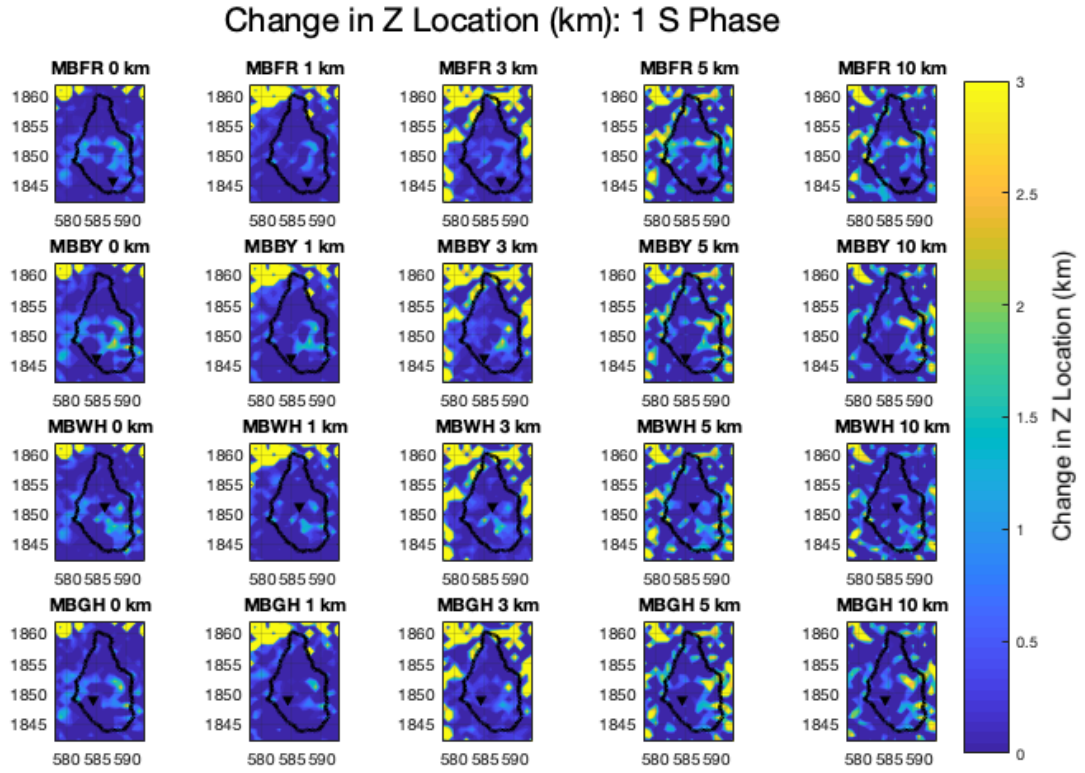

Figure 6.22: Change in Z Location at each depth tested, when using one S wave from each of the four Seismic Stations.

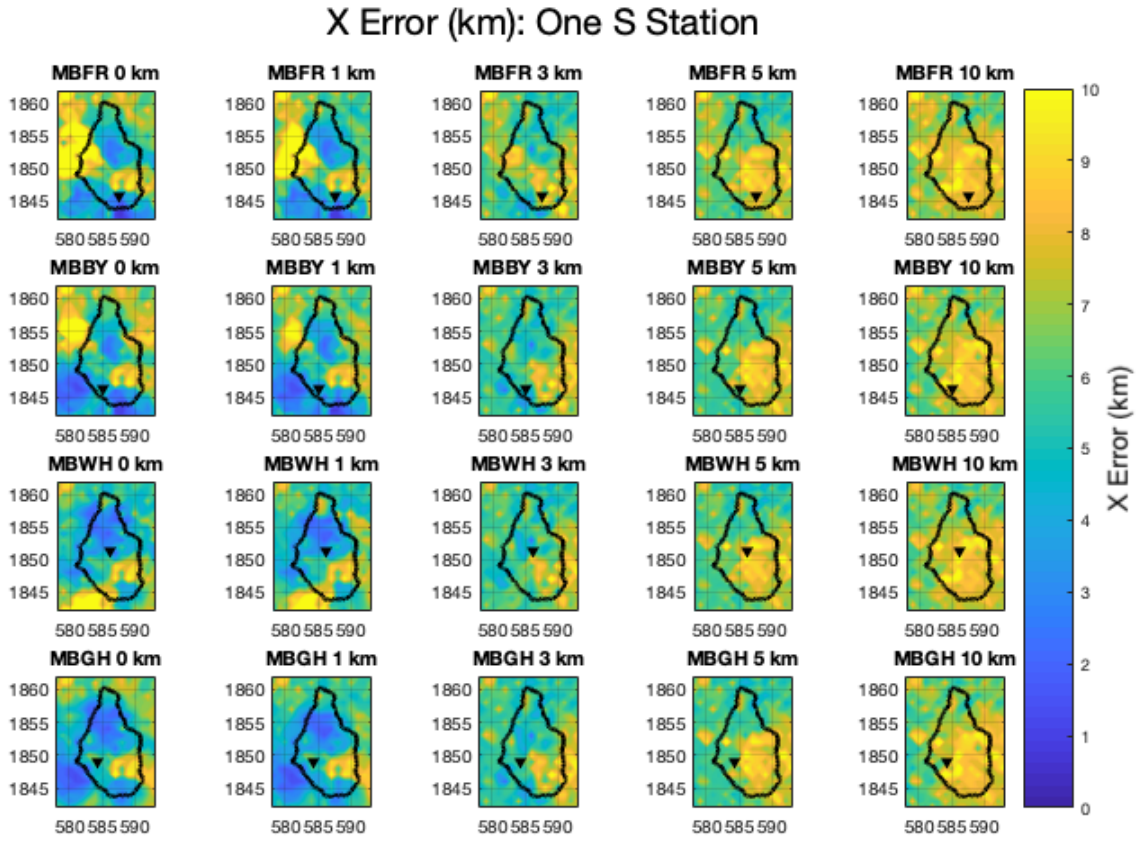

Figure 6.23: Error in X Location at each depth tested, when using one S wave from each of the four Seismic Stations.

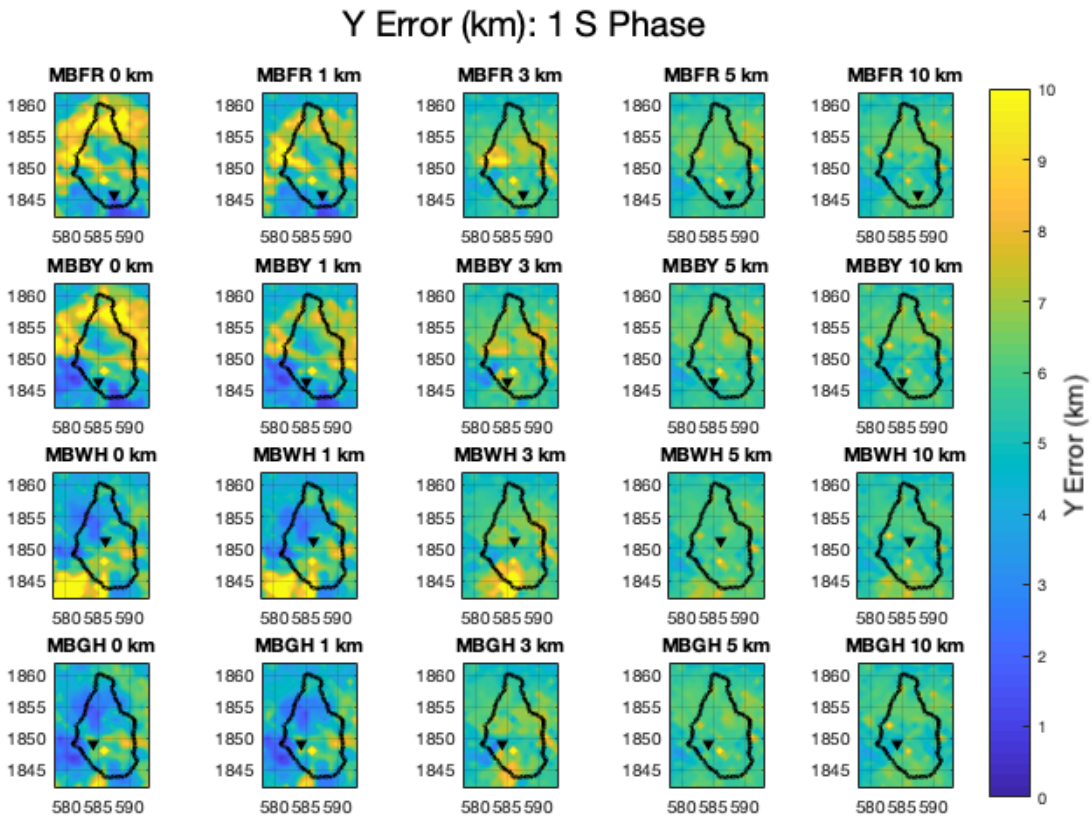

Figure 6.24: Error in Y Location at each depth tested, when using one S wave from each of the four Seismic Stations.

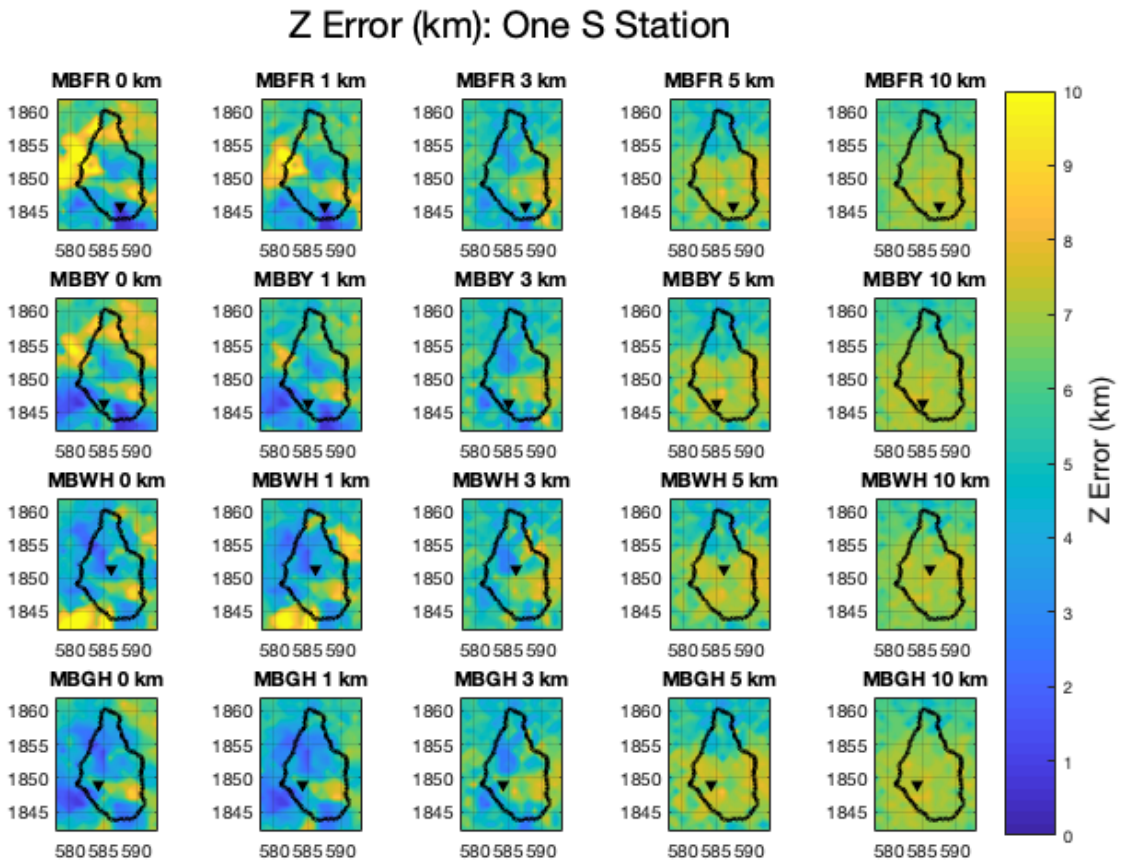

Figure 6.25: Error in Z Location at each depth tested, when using one S wave from each of the four Seismic Stations.

6.3.6 Two S Phases

The synthetic earthquakes were then relocated using P phases with two additional S phases to test if this improved locations compared to using one S phase. This was tested in pairs so that each combination in stations could be compared, the following annotation was used:

- 2S-1: MBFR + MBBY
- 2S-2: MBWH + MBGH
- 2S-3: MBFR + MBGH
- 2S-4: MBBY + MBWH
- 2S-5: MBFR + MBWH
- 2S-6: MBBY + MBGH

Change in location is small for all depths and station configurations, shown in Figure 6.28, 6.29 and 6.30. However, this has been reduced slightly compared to when including one S phase. The direction of changes in location varies a lot between different configurations and at each depth, suggesting that there is not a dominant change in location that is occurring from using a particular set of stations (Figures 6.26 and 6.27). In general, there is an increase in magnitude of changes in location in southern Montserrat with an increase in depth.

Very large errors were computed when including one S phase, reaching 10 km in some regions of Montserrat. Including two S phases reduced hypocenter errors, with the majority of earthquakes having errors less than 6 km (Figure 6.31 and 6.32). This improves at greater depths, with errors lower than 3 km. The X, Y and Z error show similar results at greater depths, but the Z error is more affected by the station configuration at depths of 0 km (Figure 6.33). For the X and Z error, an addition of an S phase at station MBFR greatly increases errors around Soufrière Hills at 0 km depth. This is shown in all three of its pairings. When not using this station, there is very little anomaly in this region. Station MBFR is located in southern Montserrat, and is one of the few stations in this region. We would expect the additional network coverage to aid locations in this region, but this is not the case.

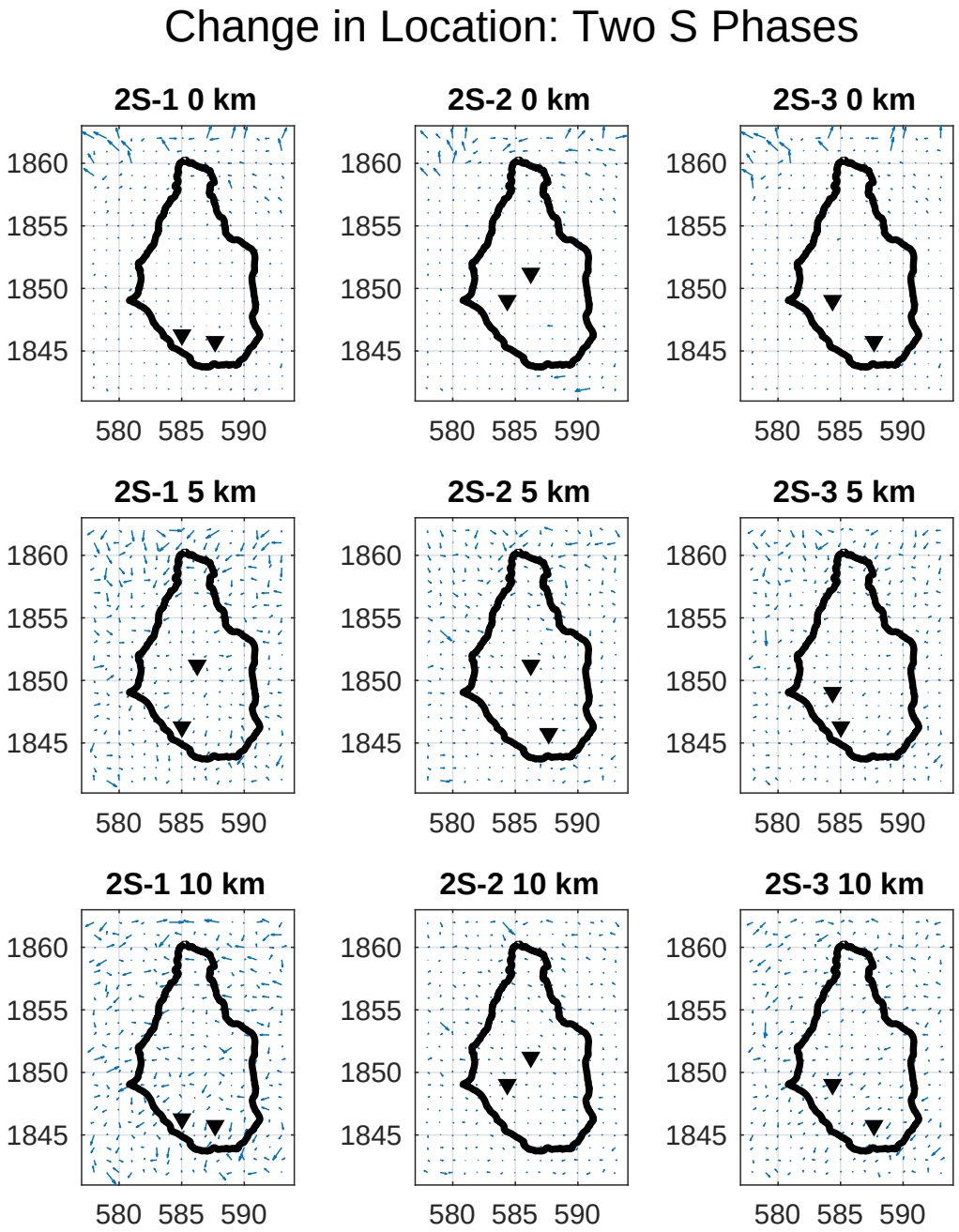

Figure 6.26: Figure 1 of 2. Vector plot showing the direction and magnitude of change in location at each depth when using two S Phases for synthetic location. There is no scale for the magnitude (length of the vector) due to each subplot being made independent of each other, and hence the length is used for relative comparison. Magnitudes for changes in location are shown in Figures 6.20 and 6.21. 2S-1: MBFR + MBBY; 2S-2: MBWH + MBGH; 2S-3: MBFR + MBGH; 2S-4: MBBY + MBWH; 2S-5: MBFR-MBWH; 2S-6: MBBY + MBGH.

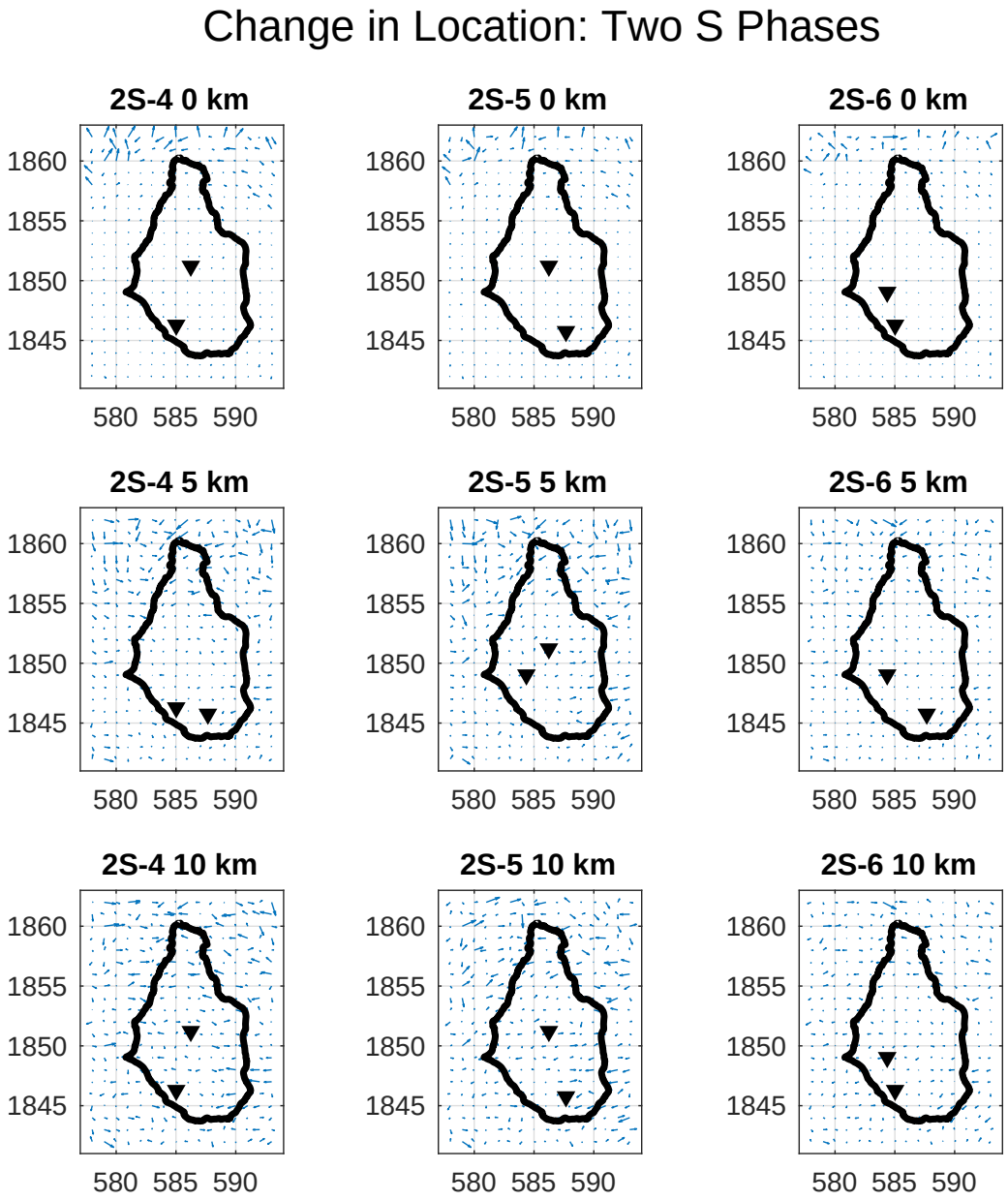

Figure 6.27: Figure 2 of 2. Vector plot showing the direction and magnitude of change in location at each depth when using two S Phases for synthetic location. There is no scale for the magnitude (length of the vector) due to each subplot being made independent of each other, and hence the length is used for relative comparison. Magnitudes for changes in location are shown in Figures 6.20 and 6.21. 2S-1: MBFR + MBBY; 2S-2: MBWH + MBGH; 2S-3: MBFR + MBGH; 2S-4: MBBY + MBWH; 2S-5: MBFR-MBWH; 2S-6: MBBY + MBGH.

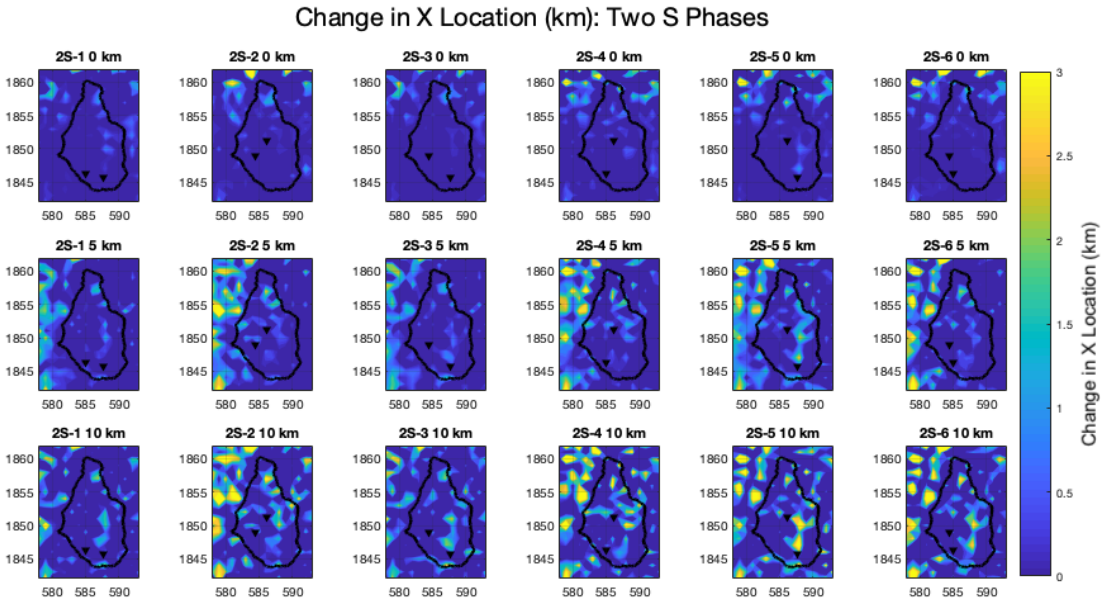

Figure 6.28: Change in X Location at each depth tested, when using one S wave from each of the four Seismic Stations.2S-1: MBFR + MBBY; 2S-2: MBWH + MBGH; 2S-3: MBFR + MBGH; 2S-4: MBBY + MBWH; 2S-5: MBFR-MBWH; 2S-6: MBBY + MBGH.

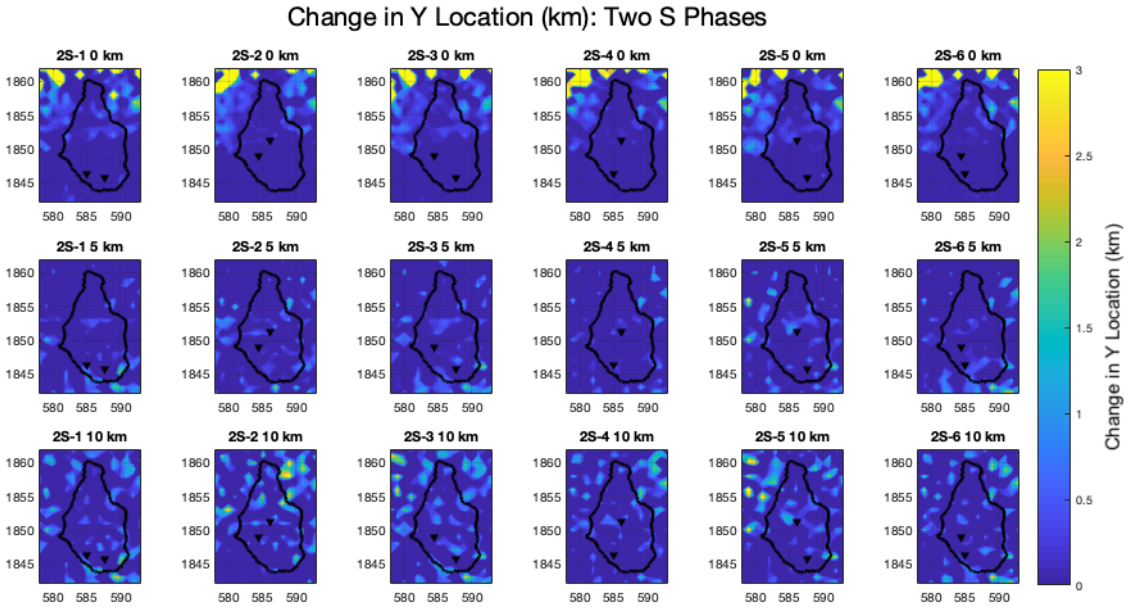

Figure 6.29: Change in Y Location at each depth tested, when using one S wave from each of the four Seismic Stations.2S-1: MBFR + MBBY; 2S-2: MBWH + MBGH; 2S-3: MBFR + MBGH; 2S-4: MBBY + MBWH; 2S-5: MBFR-MBWH; 2S-6: MBBY + MBGH.

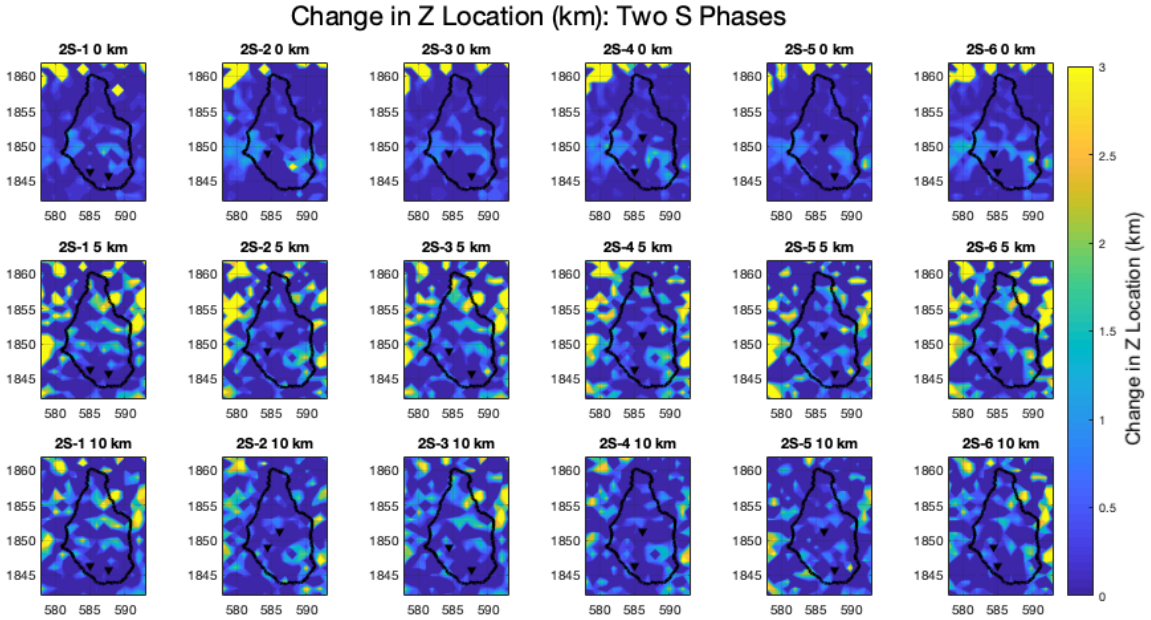

Figure 6.30: Change in Z Location at each depth tested, when using one S wave from each of the four Seismic Stations.2S-1: MBFR + MBBY; 2S-2: MBWH + MBGH; 2S-3: MBFR + MBGH; 2S-4: MBBY + MBWH; 2S-5: MBFR-MBWH; 2S-6: MBBY + MBGH.

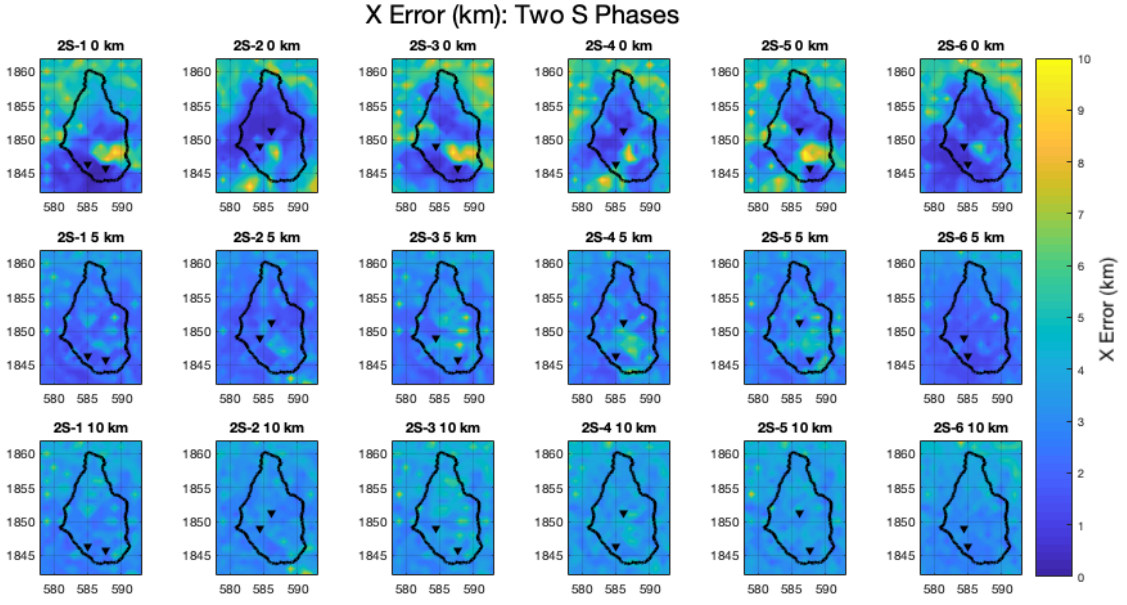

Figure 6.31: Error in X Location at each depth tested, when using two S phases from different seismic stations. 2S-1: MBFR + MBBY; 2S-2: MBWH + MBGH; 2S-3: MBFR + MBGH; 2S-4: MBBY + MBWH; 2S-5: MBFR-MBWH; 2S-6: MBBY + MBGH.

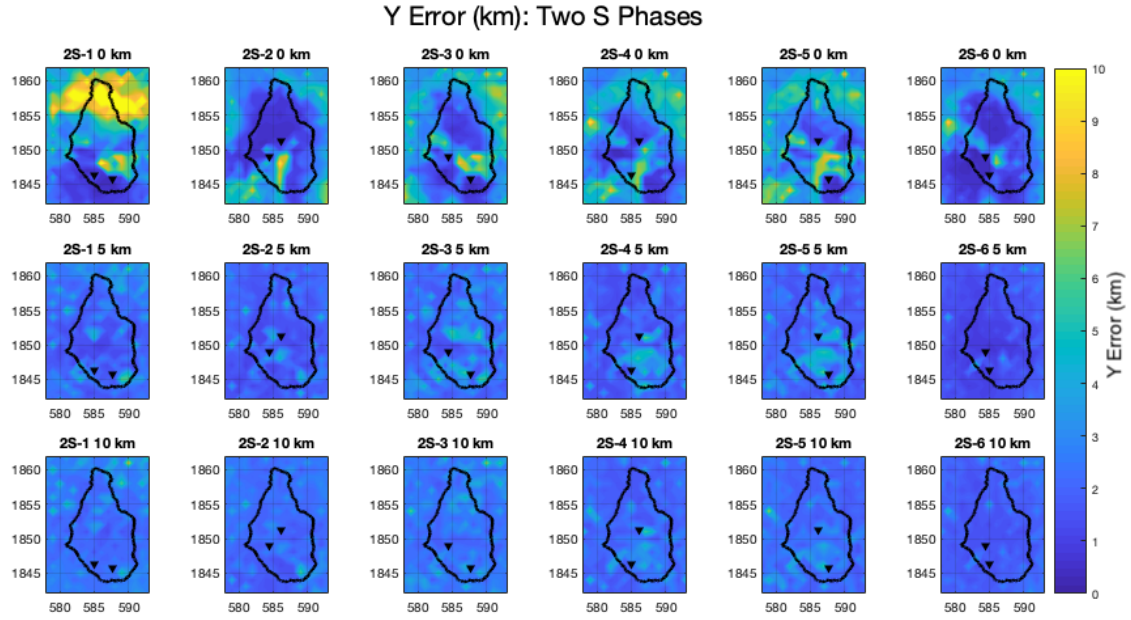

Figure 6.32: Error in Y Location at each depth tested, when using two S phases from different seismic stations. 2S-1: MBFR + MBBY; 2S-2: MBWH + MBGH; 2S-3: MBFR + MBGH; 2S-4: MBBY + MBWH; 2S-5: MBFR-MBWH; 2S-6: MBBY + MBGH.

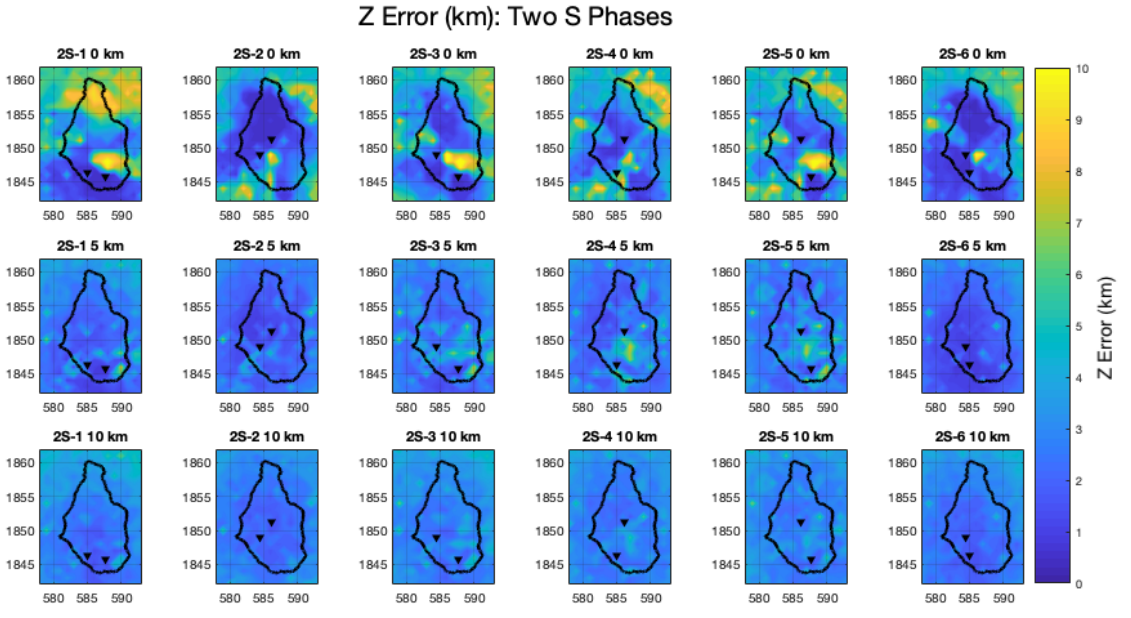

Figure 6.33: Error in Z Location at each depth tested, when using two S phases from different seismic stations. 2S-1: MBFR + MBBY; 2S-2: MBWH + MBGH; 2S-3: MBFR + MBGH; 2S-4: MBBY + MBWH; 2S-5: MBFR-MBWH; 2S-6: MBBY + MBGH.

6.3.7 Discussion of Synthetic Data

Using only four P wave arrivals resulted in large errors across Montserrat; this leads to low accuracy locations that can not be used for interpretation and further analysis. However, there are very small changes in locations recorded with the synthetic data, which suggests that the accuracy could be better than the errors suggest. When using an S phase arrival in the synthetic relocations, errors more closely matched changes in location, removing the overestimation in calculated error that was seen when using P phases only. Although it is better for the program to overestimate the error than underestimate it, it can be problematic for interpretation as this can result in some earthquakes being removed during data quality that may have accurate locations.

The addition of S wave arrival times reduces X, Y and Z errors (Table 6.3); this also reduced the standard deviation and the average errors, meaning that a greater proportion of events have small errors. Including two S phases has the greatest impact on reducing errors, and brings the average errors below 3 km, which means they can be included for interpretation. An error cut-off of 3 km was chosen for interpretations due to this allowing a good proportion of events to be used, without severely impacting the number of earthquakes used for analysis. Where possible, any trends that are shown with 3 km are checked at a tighter confidence of errors less than 1.5 km to confirm that the trend is real. This demonstrates the value of spending more time during picking to make sure S phases are included where possible.

An increase in error near Soufrière Hills Volcano is recorded when using station MBFR; this has a negative impact on locations when using only four seismic stations. However, it is important to note that MVO had the resource to use more than four seismic stations, and so this anomaly with MBFR would need to be tested with a full configuration to see if this still shows the same impact on locations. *Roman et al.* (2008) and *Shearer* (2009) suggests that events located outside of the seismic network have large horizontal errors; this is shown with the synthetic data but also with the July 2008 data which had large horizontal errors for most events located in the SE.

	X Error (km)			
	All P	1S	2S	4S
Median	7.49	6.28	3.19	1.29
25^{th} Percentile	6.29	5.21	2.27	0.64
75^{th} Percentile	9.01	7.52	4.23	2.07
Mean	7.70	6.38	3.38	1.46
Standard Deviation	1.96	1.99	1.56	0.96

	Y Error (km)			
	All P	1S	2S	4S
Median	5.93	5.72	2.28	0.99
25^{th} Percentile	5.20	4.74	1.72	0.53
75^{th} Percentile	7.82	6.43	3.24	1.29
Mean	6.65	5.69	2.69	1.04
Standard Deviation	1.96	1.70	1.51	0.67

	Z Error (km)			
	All P	1S	2S	4S
Median	7.17	6.01	2.85	1.37
25^{th} Percentile	6.29	4.71	2.08	0.72
75^{th} Percentile	7.84	6.93	3.94	2.27
Mean	7.03	5.77	3.18	1.65
Standard Deviation	1.44	1.65	1.65	1.19

Table 6.3: Mean, Median, standard deviation and 25^{th} and 75^{th} percentiles for different variation of S phases included in relocations. All statistics tests include all depths and each variations of 1 and 2 S phases.

6.4 Analysis of Repicked Earthquakes

All earthquakes from the 21^{st} July to the 31^{st} July were repicked for P and S wave arrivals at all available stations; these were then relocated in *NonLinLoc* using the EDT location method with the Rowe seismic velocity model. All available P and S repicked phases were used in relocation; more information on the number of phases used for the relocation is shown in Section 6.4.1. The following sections compare the differences in locations when using the original dataset and the repicked locations to understand how this alters interpretations during this time period.

6.4.1 Arrival Times

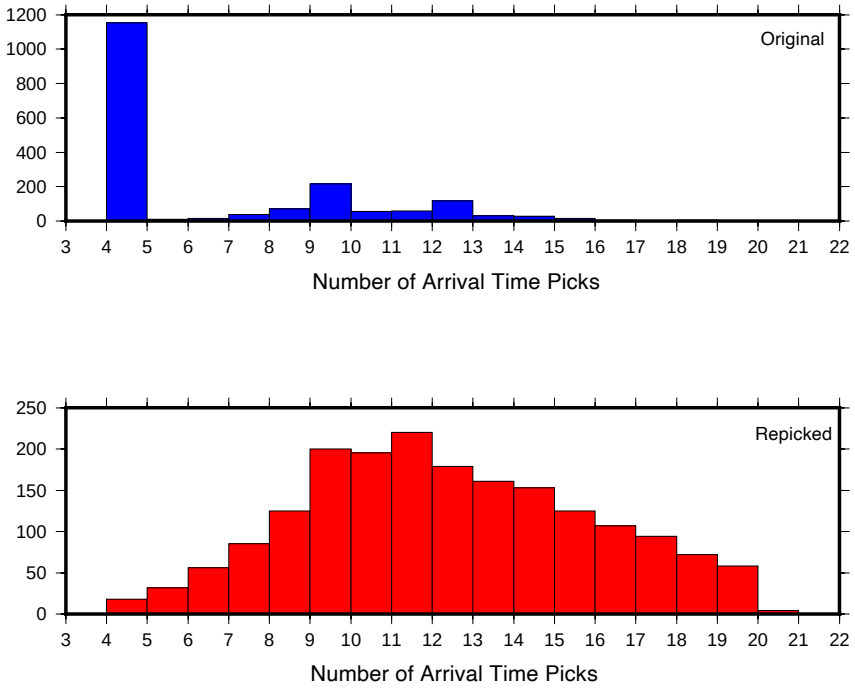

Figure 6.34: Number of arrival picks per earthquake with original MVO picks (blue) and the repicked dataset from this study (red). This is for all types of seismicity.

Figure 6.34 shows the number of arrival time picks (P and S) per earthquake for the original dataset (MVO) and the repicked dataset in this study. MVO picks show the majority of events to have only four arrival time picks, with these being P wave phases at the four stations tested in Section 6.3. Repicking the dataset for additional arrival times has given a gaussian distribution in arrival picks, with the majority of earthquakes having over 10

arrival time picks. This includes a mixture of P and S phases on several of the stations.

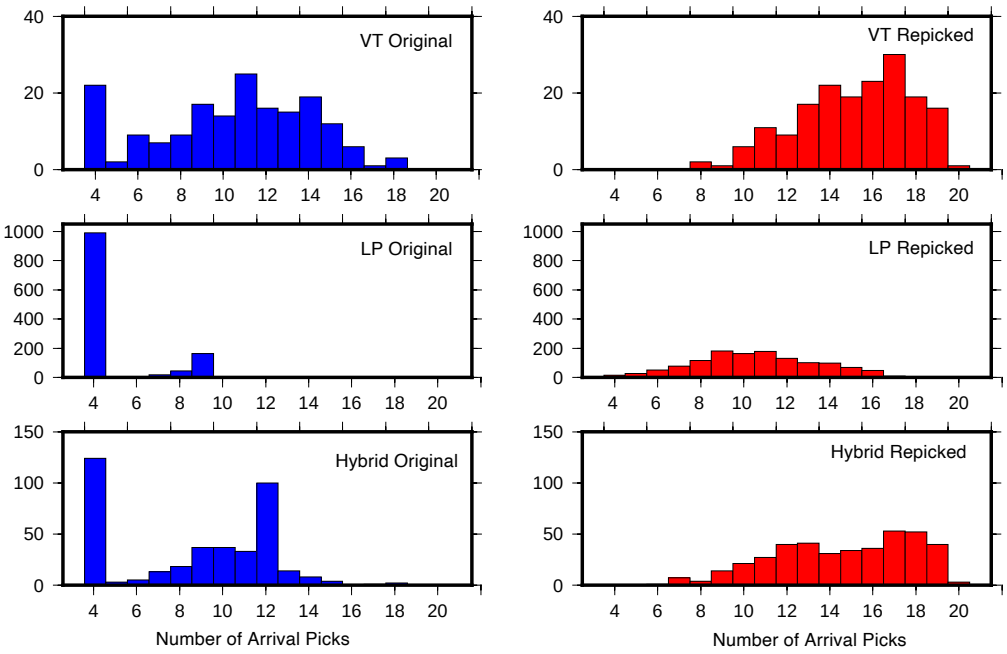

Figure 6.35: Number of arrival picks per earthquake with original MVO picks (blue) and repicked dataset from this study per type (red)

LP seismicity dominated this time period; these have emergent S wave arrivals which are more difficult to pick, and hence normally have a low number of arrival time picks associated per event. Figure 6.35 shows the number of arrival time picks for each type of seismicity. VT earthquakes show a shift in the number of phases used, with no VT earthquake having fewer than four arrival time picks, where around 25% of events had under 8 picks previously. LP and hybrid earthquakes both had a large proportion of earthquakes with four arrival times. Both now show a more distributed variation in the number of arrival time picks, with few events having four phases used for location. In general, LP earthquakes have a lower number of picks, but this is to be expected due to the difficulty in picking the S wave.

6.4.2 Comparison of Original and Repicked Locations

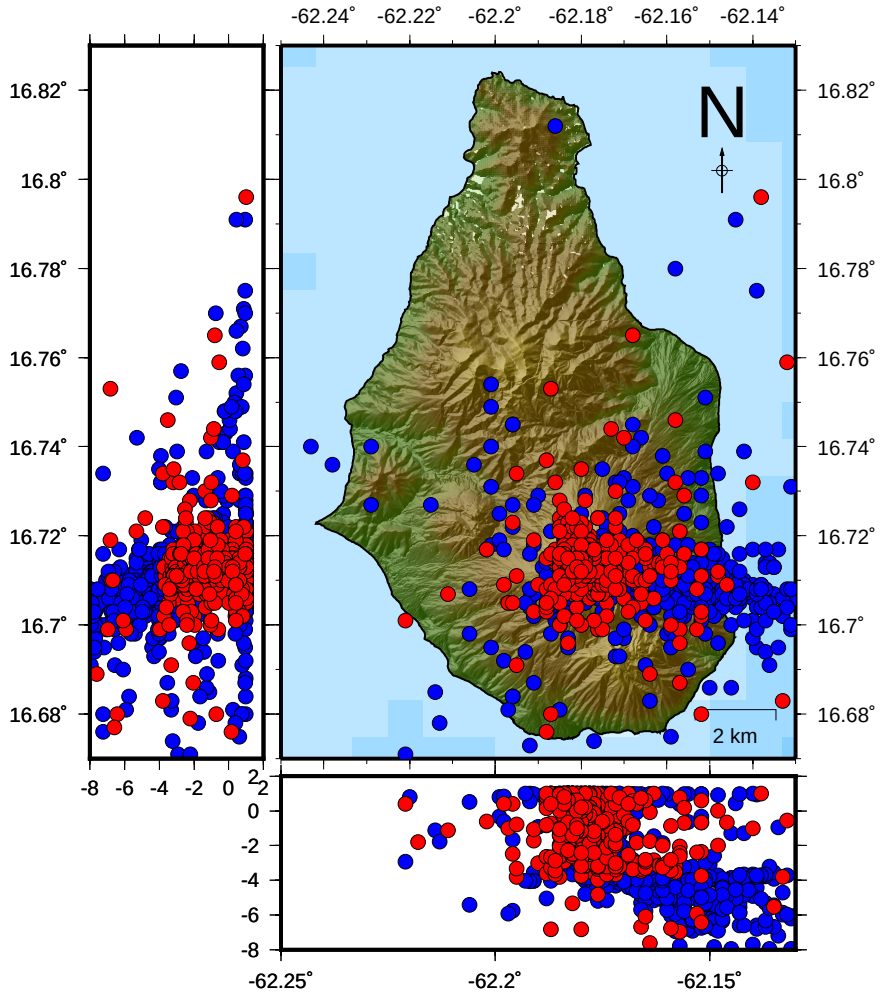

Figure 6.36: Relocation of earthquakes in *NonLinLoc* using the original data located in *NonLinLoc* (blue) and the repicked data located in *NonLinLoc* (red). Earthquakes plotted with errors less than 5 km

A total of 1818 earthquakes were originally located in *NonLinLoc* during the analysis in Chapter 5. After the earthquakes were repicked for P and S wave arrivals, a total of 1884 earthquakes were relocated; this increase is due to some earthquakes now having additional arrival times to be used for relocation. Figure 6.36 shows the original and repicked *NonLinLoc* locations (note the original locations are those calculated in Chapter 5, and not those computed by MVO). Original *NonLinLoc* locations show seismicity that extends out to the SE, following the orientation of faults in the region. The repicked locations are tightly clustered around Soufrière Hills Volcano, with only a few earthquakes located in the SE quadrant (Figure 6.36). Depth is further constrained at 1 km asl to 3 km

bsl, similar to seismicity during other phases in the eruption.

A comparison of type of seismicity for the original and repicked *NonLinLoc* locations is shown in Figure 6.37. LP earthquakes were responsible for the majority of earthquakes located in the SE in the original dataset; these have relocated to beneath the summit. LP earthquakes had the most drastic change in locations, and this is likely a result of the addition of arrival times to these earthquakes; the addition of S phases was shown to improve locations in Section 6.3. There is also less clustering of earthquakes at the top of the velocity model with the repicked dataset, compared to the original *NonLinLoc* locations.

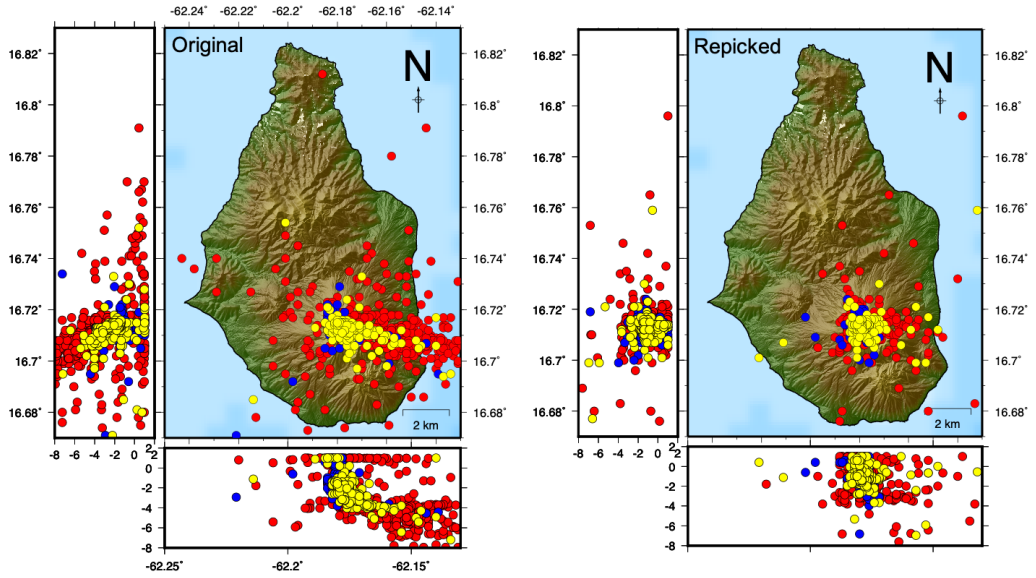

Figure 6.37: Location of earthquakes with errors less than 5 km located in *NonLinLoc* coloured by type of earthquake. Left figure is original arrival picks, and right figure is locations with repicked dataset. Red = LP, Blue = VT, Yellow = Hybrid

Calculated Error

The main issue with the original *NonLinLoc* locations were the large errors associated with the majority of locations. This was shown to be a result of a low number of arrival times, and a low number of S phases when using only four stations. The addition of P and S phases has reduced the calculated X, Y and Z errors for the majority of earthquakes, as shown in Figure 6.38. A clear reduction in error is seen with the repicked *NonLinLoc* locations, with the majority of X and Y errors being less than 1 km, and Z error under 1.5 km. The

original data showed an increase in the number of earthquakes with errors at 4 km for the X and Z location; these have been removed with the repicked dataset. There is a small increase in large errors above 5 km for the reanalysed data up to 10 km; this is likely a result of incorrect S wave arrival times being picked. This was expected from the trials in Section 6.2.2, but overall repicking arrival times has had a positive impact on locations.

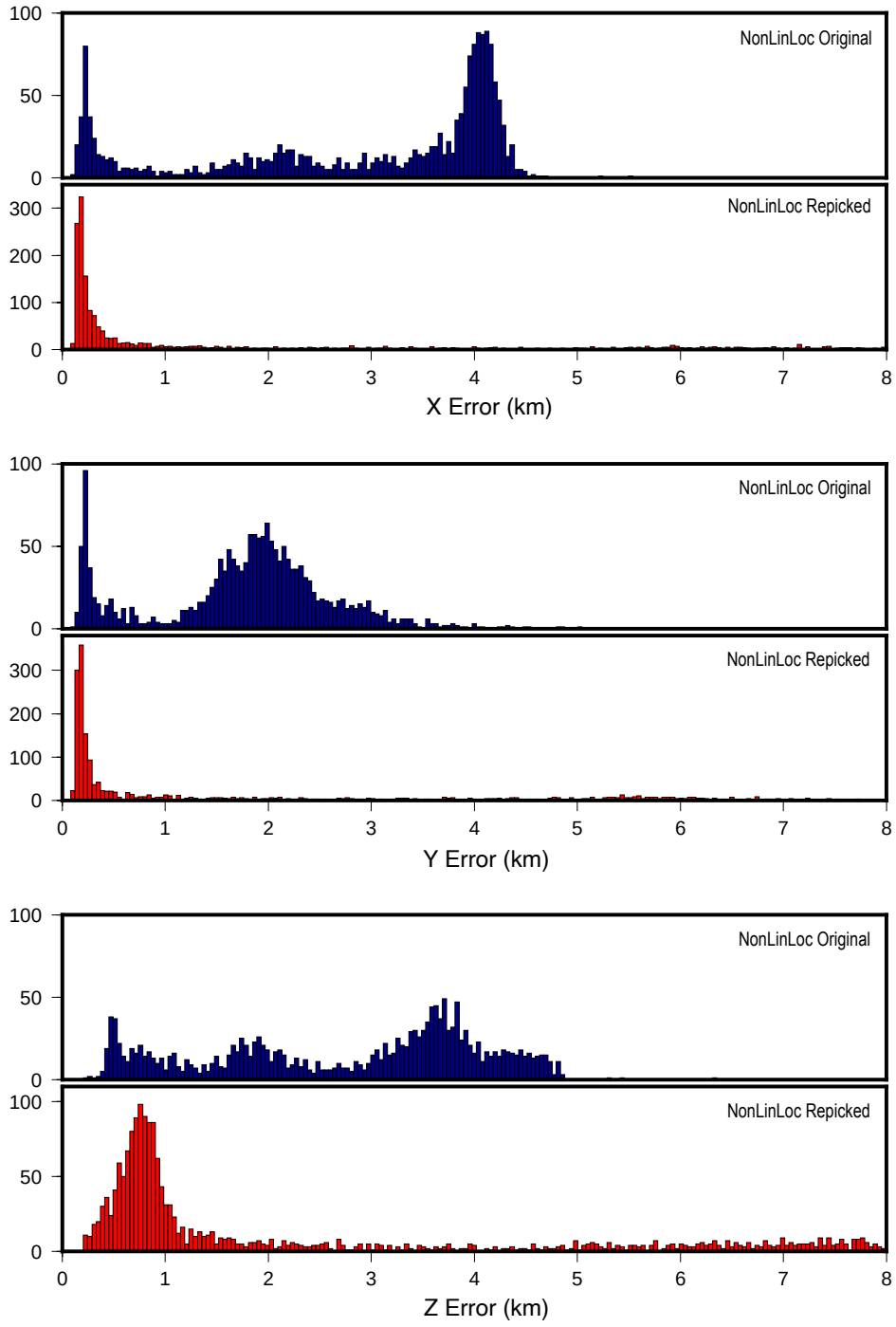

Figure 6.38: Histograms showing the range of errors throughout the research period for the original data and the repicked dataset. Navy — hypocenter errors from original *NonLinLoc* locations computed in Chapter 5; Red — hypocenter errors from repicked dataset in this chapter, relocated with *NonLinLoc*.

6.4.3 Comparison of *NonLinLoc* locations with *Hypocenter* Locations

MVO currently use *Hypocenter* with the MVO seismic velocity model to locate earthquakes. As a result, it was decided to compare how locations would change with the repicked dataset if using the location methods used by MVO, as this would display the changes MVO would have for interpretation if they had had more time for picking arrival times during this period. A higher impact in the number of located earthquakes was seen with *Hypocenter*, with 1880 earthquakes relocated compared to an original 1594 located earthquakes. This is due to *Hypocenter's* limitation that the program is unable to locate earthquakes using only three seismic stations.

Figure 6.39 shows the hypocenters for each relocation using the original and repicked dataset in both *Hypocenter* (with the MVO model), and *NonLinLoc* (with the Rowe model). Earthquakes in the SE were shown with *Hypocenter* locations, but with less events being located in this region compared to *NonLinLoc* original locations. This difference in the number of earthquakes in the SE region was due to events here having only four arrival times as most were LP events, and hence *Hypocenter* would be unable to locate these. The errors for these events were very high for both *Hypocenter* and *NonLinLoc*, and so would not be used in interpretation.

The repicked *Hypocenter* locations have a slight pattern to the NE (Figure 6.39), following a similar trend recorded in 1995 by *Miller et al.* (2010). Repicked *Hypocenter* locations show more earthquakes to the east than *NonLinLoc* relocations, but overall have the majority of events centred around Soufrière Hills Volcano. Figure 6.39 shows the locations for all earthquakes relocated, and hence may include earthquakes with very large errors that would normally be removed during data processing.

Figure 6.40, 6.41 and 6.42 show the latitude, longitude and depth locations for all four relocations. Original *NonLinLoc* locations show a spread in latitude and longitude locations from the 27^{th} July; this is mostly removed when using the repicked dataset. *Hypocenter* relocations with the repicked dataset are also more constrained, but show more variation than with the *NonLinLoc* locations. Average X, Y, and Z errors for repicked *Hypocenter* locations are 4.7, 4.7 and 2.6 km respectively, whereas repicked *NonLinLoc* X, Y and Z errors are 1.8, 2.0, 2.5 km respectively.

Original *NonLinLoc* relocations had depths varying from 1 km asl to 8 km bsl. Repicked data show the majority of seismicity to be shallower than 3 km and 4 km for *Hypocenter* and *NonLinLoc* relocations respectively. *Hypocenter* relocations show some earthquakes are being located to the top of the velocity model at 1.241 km; these can be assumed to be false locations. A similar issue is seen with the *NonLinLoc* relocations with earthquakes grouping at 1.8 km, corresponding to a velocity model boundary.

Comparing *NonLinLoc* locations, the repicked dataset is more constrained with a smaller range in latitude, longitude and depth than the original locations. This alongside reduced hypocenter errors suggests that the previous trend in seismicity to the SE was likely an artefact from using four seismic stations for location. A scatter in longitude and depth locations can be seen for the repicked *NonLinLoc* locations from the 27^{th} July; this corresponds to a change from hybrid to LP seismicity. The scatter in location at this time could be the result of the analyst as they adjust to the change in seismic signal, or could be a result of volcanic processes that may produce a poorer signal at this time.

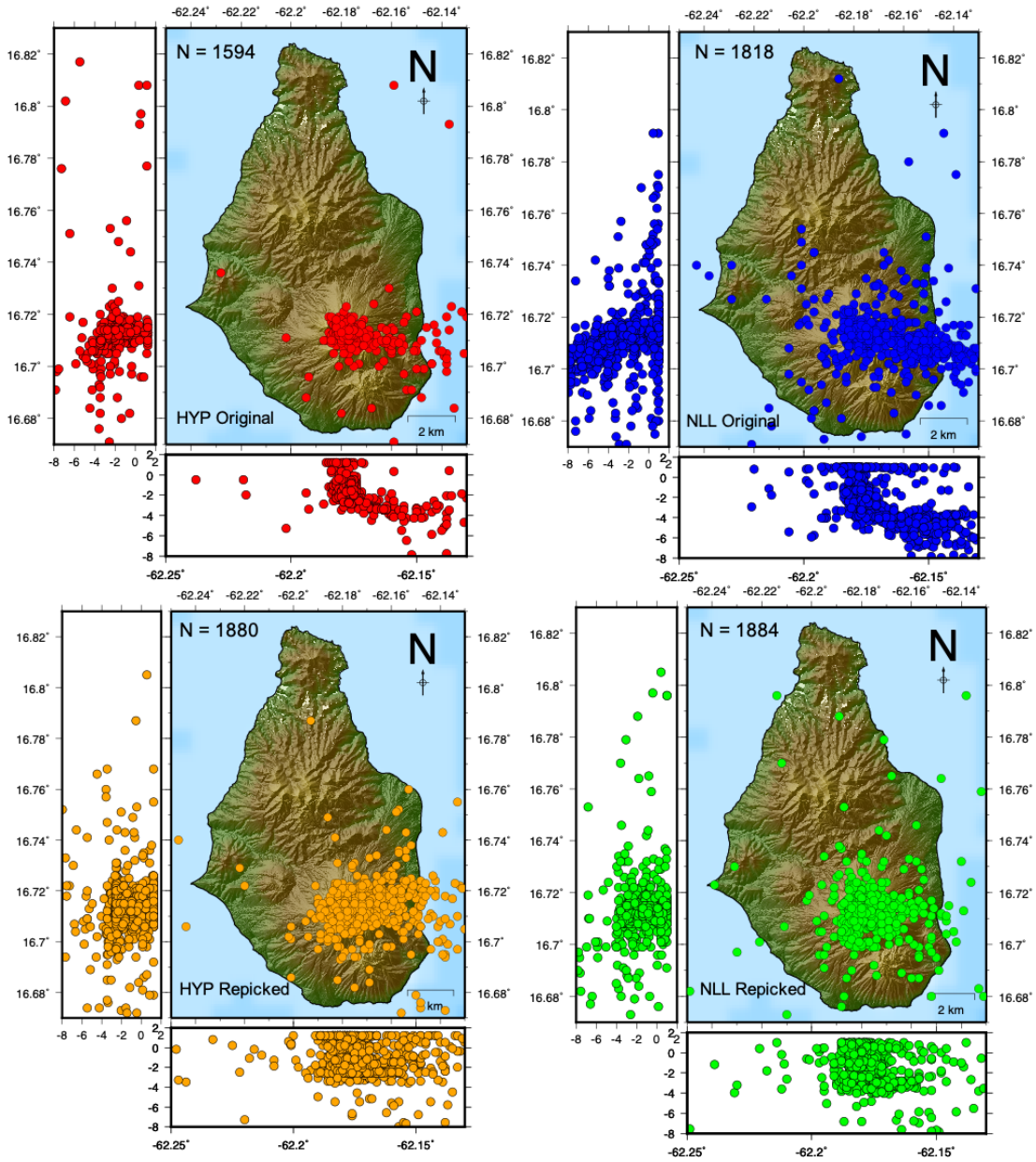

Figure 6.39: Locations of all earthquakes from July 2008 when located with *Hypocenter* and *NonLinLoc*, and when using the original arrival times, and the repicked arrival times. This is for all earthquakes irrespective of calculated error. HYP corresponds to *Hypocenter* relocations; NLL corresponds to *NonLinLoc* relocations.

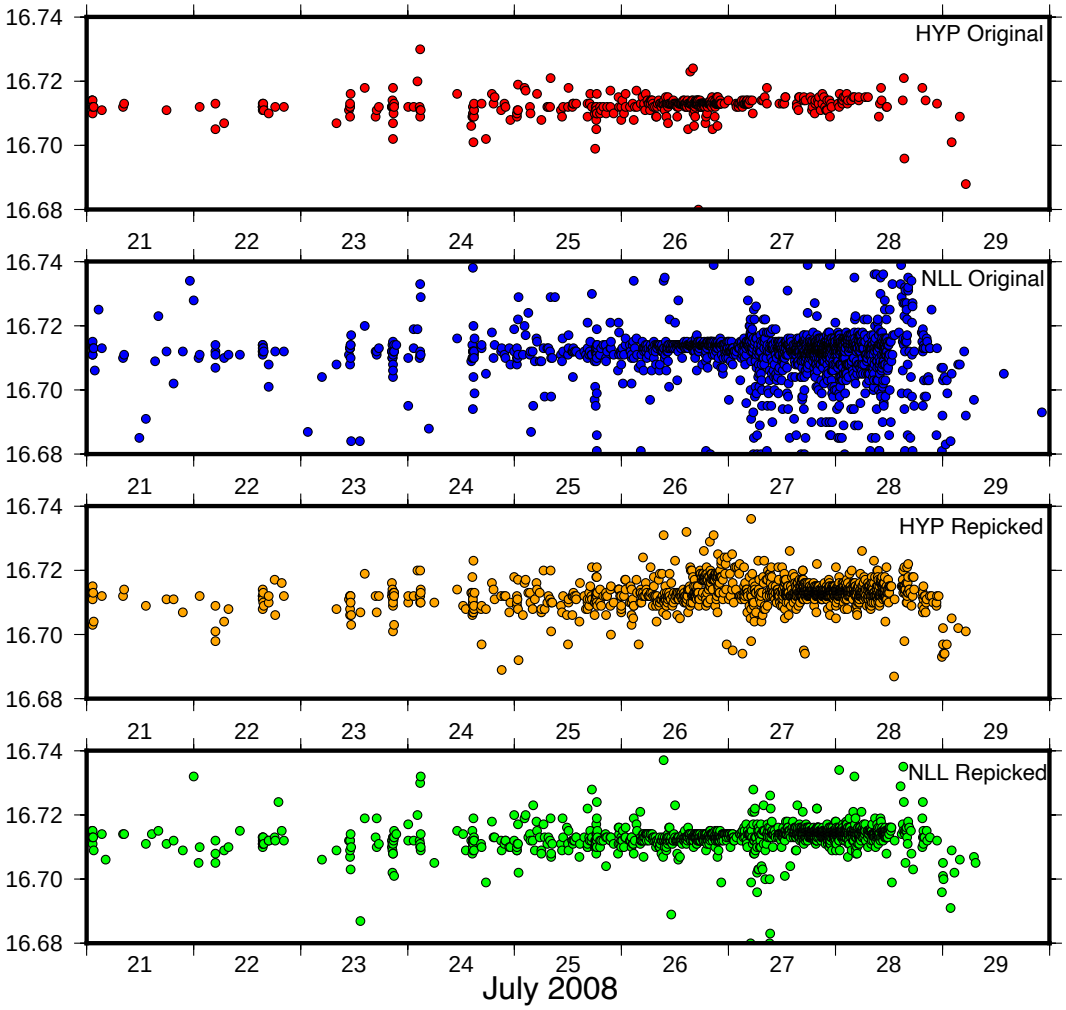

Figure 6.40: Latitude locations of earthquakes from July 2008 when located with *Hypocenter* and *NonLinLoc*, and when using the original arrival times, and the repicked arrival times. Earthquakes plotted have errors less than 5 km to remove any large anomalies. HYP corresponds to *Hypocenter* relocations; NLL corresponds to *NonLinLoc* relocations.

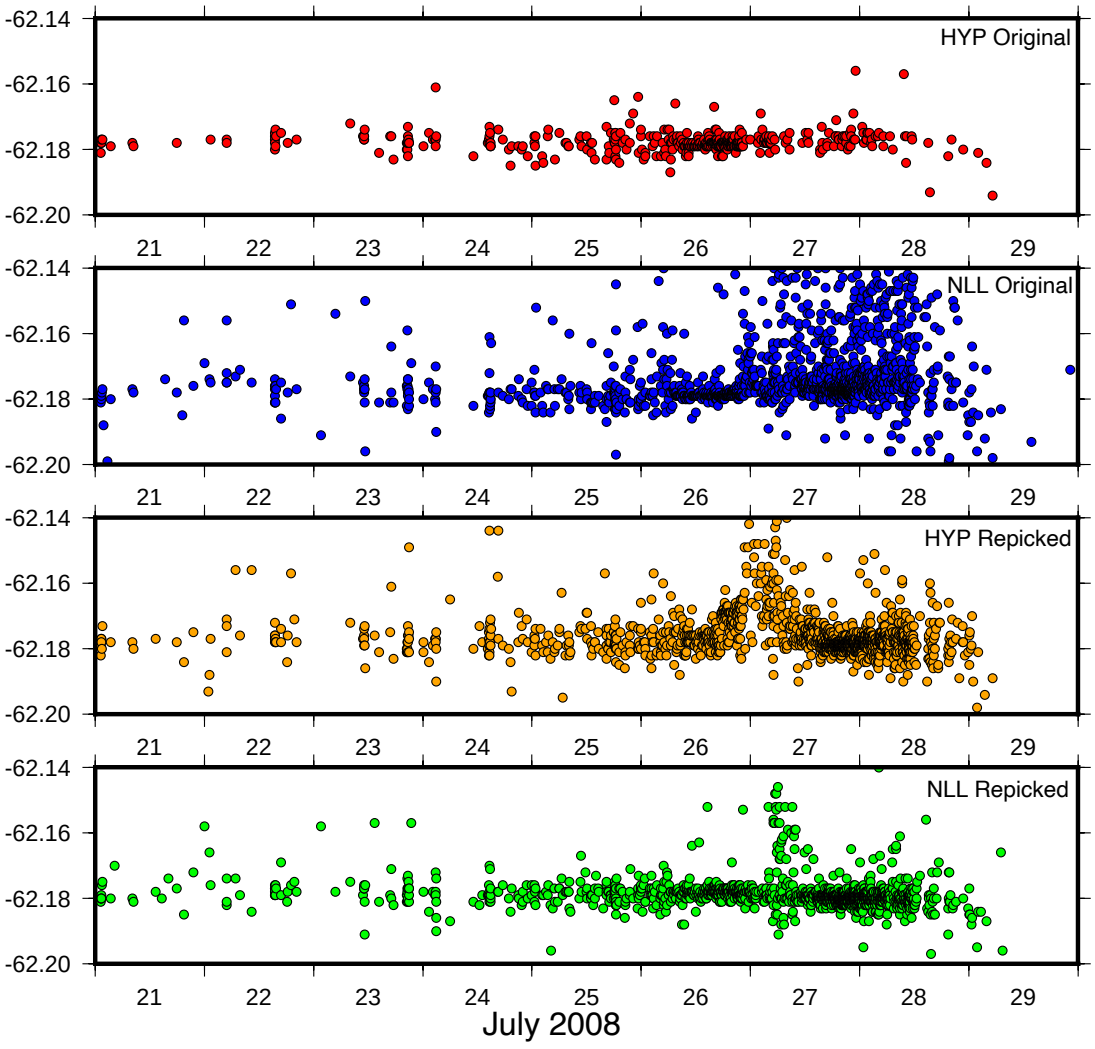

Figure 6.41: Longitude locations of earthquakes from July 2008 when located with *Hypocenter* and *NonLinLoc*, and when using the original arrival times, and the repicked arrival times. Earthquakes plotted have errors less than 5 km to remove any large anomalies. HYP corresponds to *Hypocenter* relocations; NLL corresponds to *NonLinLoc* relocations.

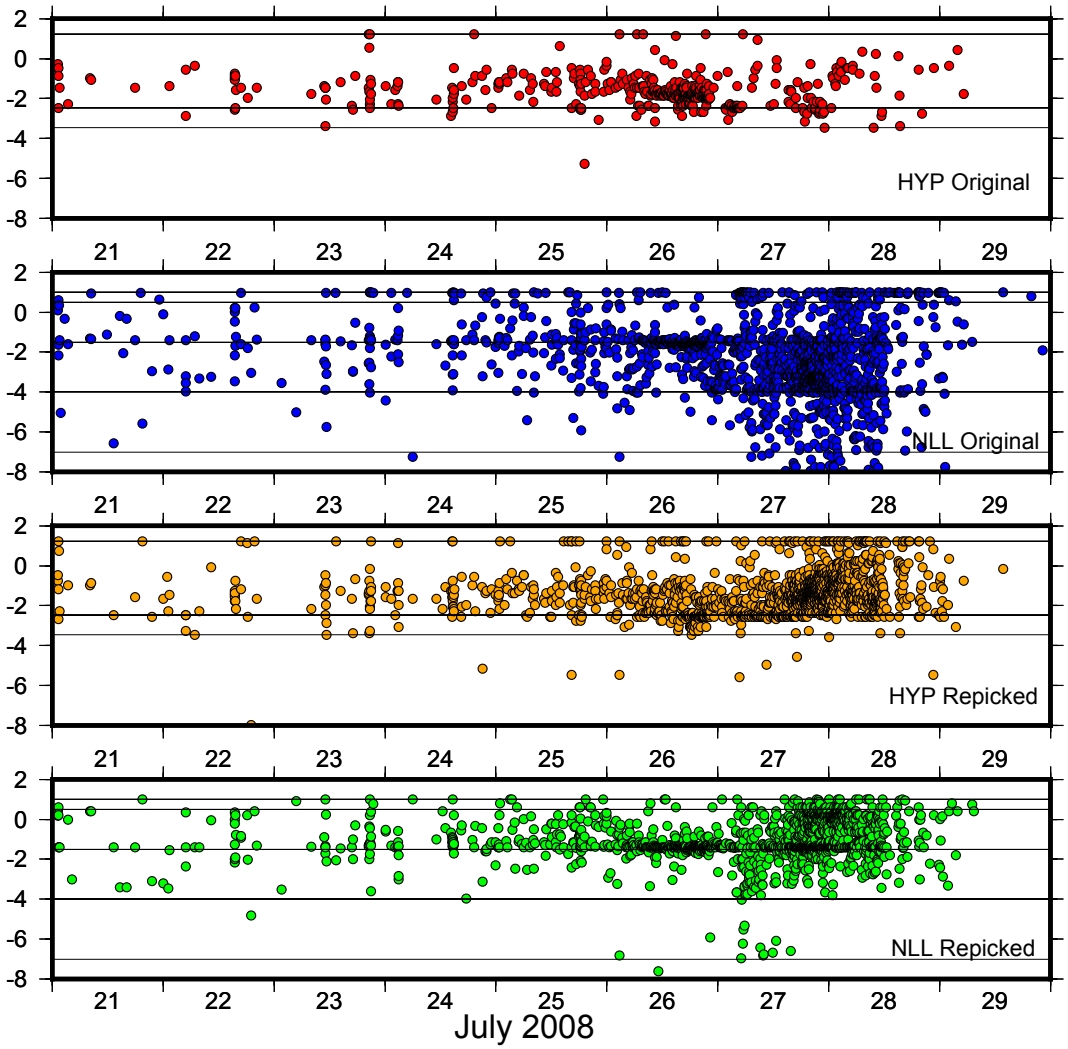

Figure 6.42: Depth locations of earthquakes from July 2008 when located with *Hypocenter* and *NonLinLoc*, and when using the original arrival times, and the repicked arrival times. Earthquakes plotted have errors less than 5 km to remove any large anomalies. HYP corresponds to *Hypocenter* relocations; NLL corresponds to *NonLinLoc* relocations.

6.4.4 Final locations

Final locations used to interpret the seismicity in the lead-up to the Vulcanian explosion on the 29^{th} July used the repicked dataset from *NonLinLoc*. A comparison of these locations with the original locations computed by MVO is shown in Figure 6.43; these are for all events with errors less than 3 km. MVO locations are tightly clustered around the summit compared to relocations which show a greater spread to the east. This is mostly due to the small number of earthquakes that can be used for analysis with the original MVO locations. 347 earthquakes had errors less than 3 km with MVO locations, where the repicked dataset has a total of 1319 earthquakes with errors less than 3 km. Relocated hypocenters in *NonLinLoc* show earthquakes clustered around the summit at depths of 1 km asl to 4 km bsl, with the trend to the SE no longer visible.

In Figure 6.44 the earthquakes have been coloured by the number of arrival time phases to understand if some locations are a result of a lower number of arrival times. Most earthquakes now have 8–12 arrival time picks, and this has been shown to reduce the errors significantly (Table 6.4.4). Although the errors are quite low, these are still higher on average than average errors for the relocation of the whole catalogue. This is likely due to the large number of LP earthquakes that are recorded in this time period, whereas the rest of the time period has a greater proportion of VT seismicity which has been shown to produce lower errors (Figure 6.3).

	X (km)	**Y (km)**	**Z (km)**
Minimum Value	0.1015	0.1048	0.2163
Maximum Value	14.3220	19.0560	10.6840
Mean	2.037	1.8250	2.4516
Standard Deviation	2.8265	2.5359	2.6365
25^{th} Percentile	1.848	1.786	0.7065
75^{th} Percentile	3.1490	3.0004	3.7925
99^{th} Percentile	10.4146	9.6851	9.2452

Table 6.4: Table showing mean, standard deviation, 25^{th}, 75^{th} and 99^{th} percentiles, and minimum and maxium values of relocated errors

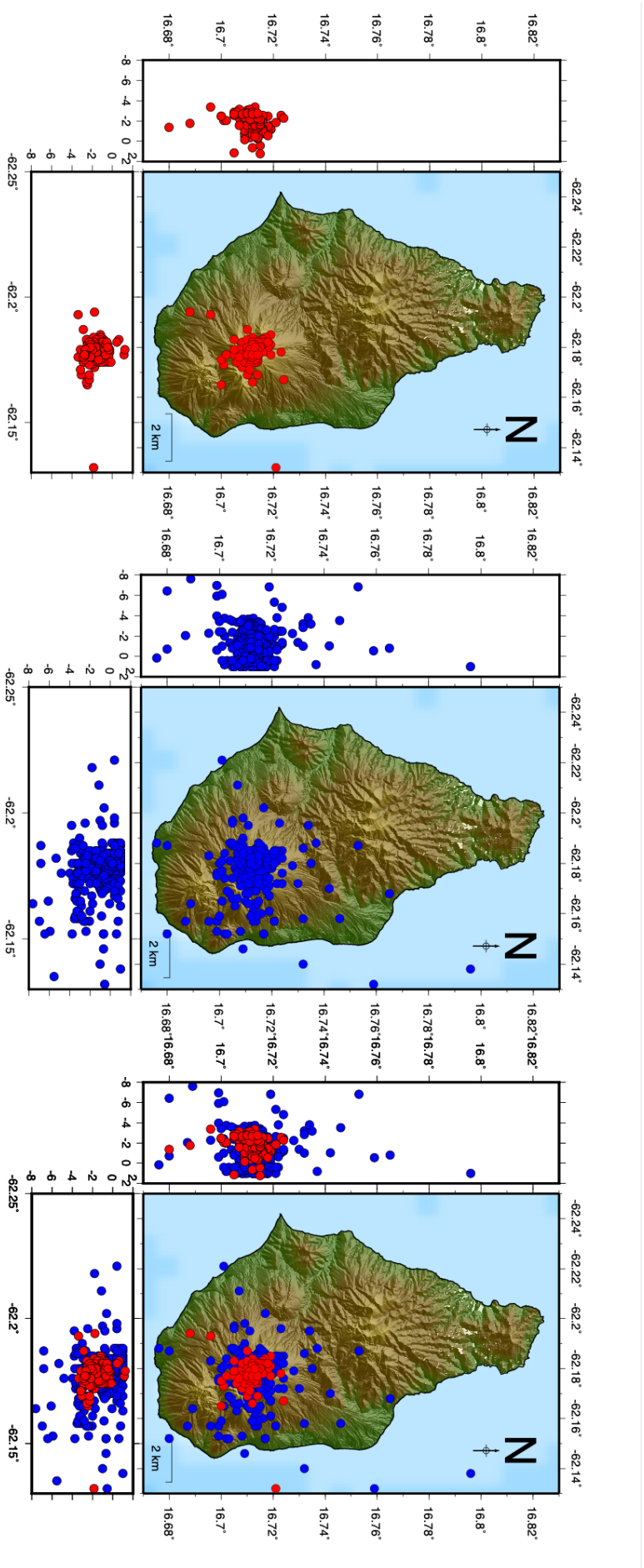

Figure 6.43: Original MVO locations from *Hypocenter (red)* and repicked *NonLinLoc* locations (blue) for earthquakes from the 21^{st} to 31^{st} July 2008 inclusive. Only earthquakes with errors less than 3 km have been plotted.

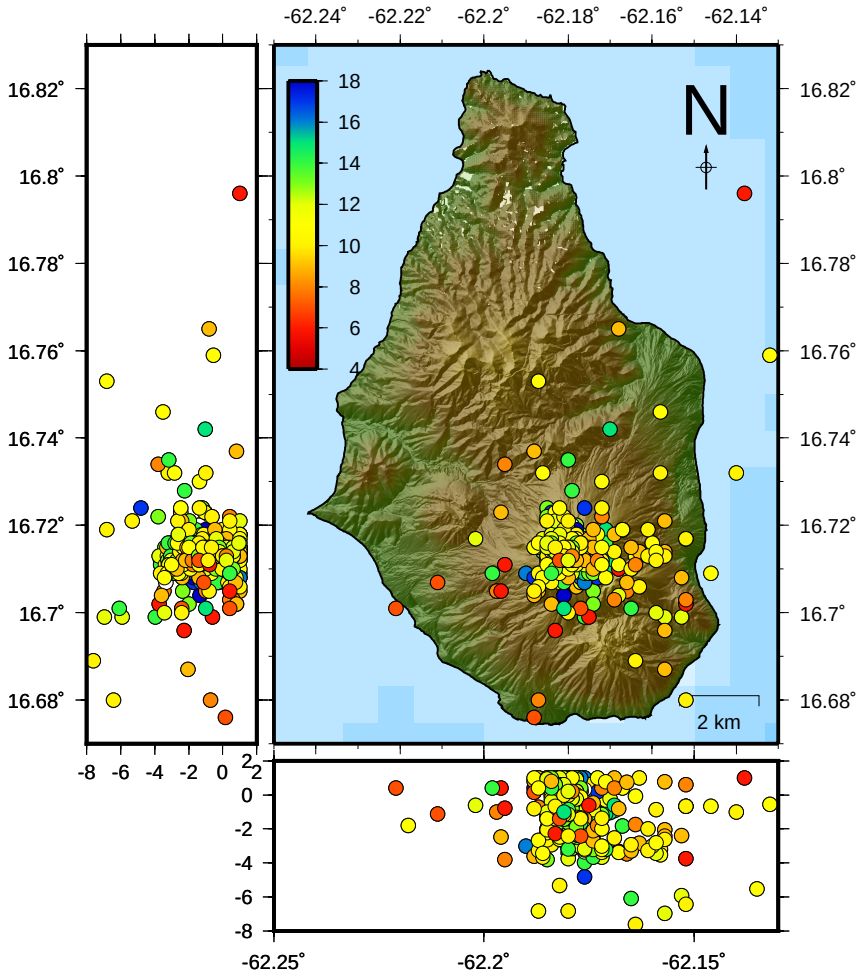

Figure 6.44: Repicked earthquakes located in *NonLinLoc* from 21st to 31st July 2008 inclusive; earthquakes coloured by number of phases used. Only earthquakes with errors less than 3 km have been plotted.

Earthquake Types

The locations of the relocated VT, LP and Hybrid earthquakes are shown in Figure 6.45. LP and hybrid earthquakes have the largest number of events with 871 and 361 earthquakes respectively with errors less than 3 km. LP seismicity is not as concentrated around Soufrière Hills Volcano, with some events locating further to the east. This is likely a result of LP earthquakes being less constrained than VT events, due to the difficulty in picking S wave arrival times from these signals. LP earthquakes are usually associated with magma movement; the reason for the earthquakes not appearing as concentrated is a result of the large hypocenter errors typical of LP earthquakes. This is because the S wave arrival is more emergent, and hence harder to pick; as a result LP earthquakes are not as well constrained compared to VT earthquakes. Events are located up to 3.5 km bsl. VT and hybrid seismicity is mostly beneath the summit at depths up to 2.5 km; this is relatively shallow for VT seismicity and is normally recorded at depths up to 6 km.

Rodgers et al. (2016) showed a deepening of hypocenters through time as seismicity changed from VT to LP. *Rodgers et al.* (2016) used MVO locations, but using events with a calculated error less than 1 km. VT hypocenters from *Rodgers et al.* (2016) are clustered around the summit at depths of 0.65–2.95 km bsl; during periods of higher VT rates on the 24^{th}–26^{th} July, these were shallower at an average depth of 1 km bsl. Hybrid hypocenters had a similar range in depth compared to VT, but with a slightly deeper average of 1.95 km bsl (*Rodgers et al.*, 2016). A model proposed by *Huppert and Sparks* (2016) suggests that VT earthquakes occur in a critical overpressure zone at two thirds the vertical distance between the origin of the fluid and the surface. The magmatic chamber is thought to be at a minimum depth of 5 km bsl (*Aspinall et al.*, 1998; *Barclay et al.*, 1998). Relocated VT hypocenters would fit in this depth range at approximately 2 km beneath the surface (the height of the dome summit was 0.951 km at this time).

LP earthquakes were located deeper, ranging from 1–3 km bsl. Continuous data suggests that there was no evidence for rapid changes in frequency, and hence the frequency changes recorded were the result of slow processes that occurred over hours to days (*Rodgers et al.*, 2016). Relocations in this study show VT seismicity to range from 1 km asl–2.5 km bsl; this is shallower than locations calculated by MVO. Hybrid hypocenters are also in a similar depth range. LP seismicity extends to greater depths up to 3.5 km bsl, suggesting slightly

deeper locations than computed by MVO. This could suggest that the different types of signals recorded are a result of the path effect, with an LP signal being recorded due to the increased depth of the signal (compared to a Hybrid event which is recorded at shallower depths). However, this is not always the case, with LP earthquakes recorded at a range of depths, and therefore it is more likely to be a result of a different process occurring in the magmatic system. Figure 6.46 shows the depth location through time; seismicity can be seen to extend to greater depths after the 27^{th} July when the majority of earthquakes were then LP. However, there are also a greater number of events with larger errors. The majority of LP earthquakes are still being located at depths of 0–2 km bsl, similar to that seen with VT and hybrid events, but with some LPs reaching to 4 km depth.

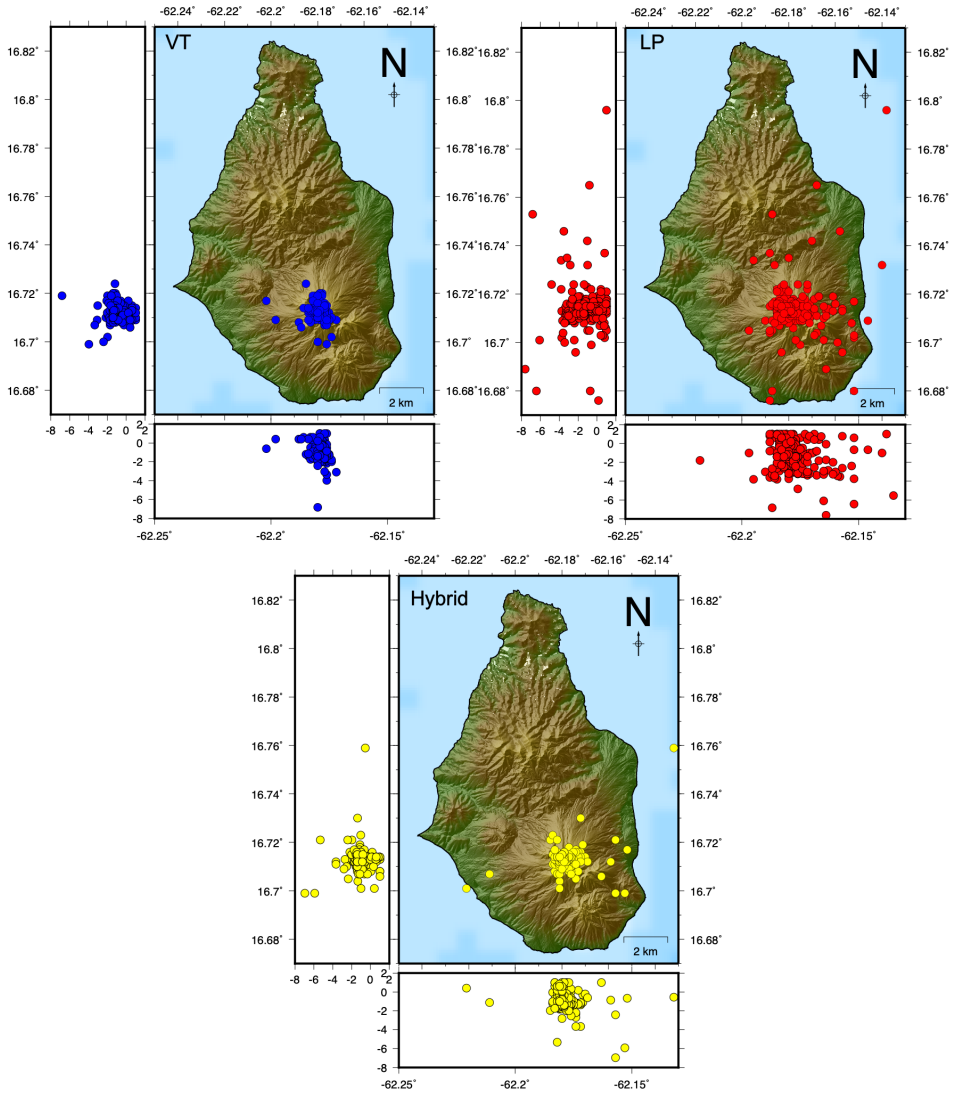

Figure 6.45: Repicked earthquakes located in NonLinLoc from 21st to 31st July 2008 inclusive by type. All earthquakes plotted have errors less than 3 km

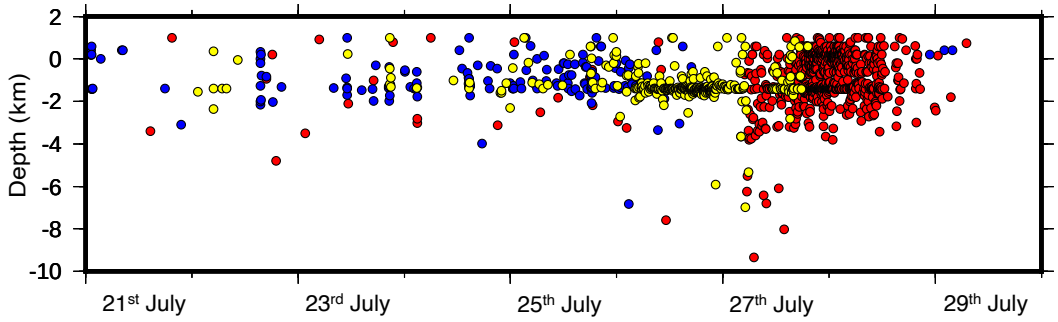

Figure 6.46: Depth of repicked earthquakes located in *NonLinLoc* from 21^{st} to 29^{th} July 2008 through time. All earthquakes plotted have errors less than 3 km. Blue = VT, yellow = hybrid, and red =LP.

6.5 Discussion

MVO locations from July 2008 show earthquakes beneath the summit up to a depth of 3.5 km with a NW-SE alignment, however the majority of earthquakes located in the SE have large calculated errors (*MVO*, 2008). Relocations with *NonLinLoc* in Chapter 5 also show a NW-SE alignment of LP seismicity from the 27^{th} July, with increasing depth over a two-day period. This trend of earthquakes to the SE follows other fault orientations in the region such as the Montserrat-Havers Fault System, and the Belham Valley Fault. The 21^{st} to 31^{st} July was repicked for additional P and S wave arrival times; relocations of the repicked earthquakes show the pattern to the SE is no longer present. Repicked relocations show seismicity centred around Soufrière Hills Volcano up to depths of 3.5 km. This suggests that the trend in seismicity to the SE was likely an artefact of poor accuracy locations; all earthquakes in the SE had a low number of arrival times with large errors, contributing to poor locations.

Associated location errors are greatly reduced, resulting in an increase of 972 hypocenters that can be used for analysis, compared to 347 original MVO locations (when using earthquakes with errors less than 3 km). Errors were reduced by the addition of other P and S wave arrival phases per earthquake that were not originally picked by MVO. The use of only four P wave phases was shown to produce large errors in Section 6.3, with the inclusion of S wave phases greatly reducing calculated hypocenter errors. This shows the importance of having additional arrival time phases, and hence improved locations as a) more earthquakes are able to be used in analysis, improving our understanding and interpretations, and b) this results in more trusted hypocenters, e.g. this has indicated that the SE trend was a result of poor locations.

VT seismicity during this period was tightly clustered beneath Soufrière Hills at a depth range of 0.6 asl to 2.4 km bsl, similar to locations found by *Rodgers et al.* (2016). Errors are very small for VT earthquakes, with the majority of events having errors less than 0.3, 0.5 and 0.7 km for X,Y and Z errors respectively. Location of VT seismicity has been previously shown to extend to depths up to 5 km, especially during the early stages in the eruption. The shallow nature of this VT seismicity could suggest that magma movement was occurring during this time frame.

LP seismicity at Montserrat has accompanied dome forming eruptions and Vulcanian explosions. This has been interpreted at Montserrat to be a result of pressurisation of fluid-filled cracks (*Chouet*, 1996; *Chouet et al.*, 1994), degassing processes in a pressurised magma conduit/dome (*Stix et al.*, 1997; *Varley et al.*, 2010), and the ascent of magma in a conduit (*Hammer and Neuberg*, 2009; *Neuberg et al.*, 2006). *Rowe et al.* (2004) suggested that Low Frequency (including hybrid and LP) seismicity during the 1996 dome growth was triggered by rapid bubble formation throughout an ascending magma column; this highlights the uncertainties in interpreting from seismicity type alone.

The Low Frequency swarm (including LP and Hybrid earthquakes) on the 25^{th} to 27^{th} July was interpreted as the final ascent of magma through the shallow conduit (*Hammer and Neuberg*, 2009; *Rodgers et al.*, 2016). *De Angelis* (2009) used waveform cross correlation on Low Frequency earthquakes to look at changes detected in the coda of earthquakes during this time period. There was a lack of systematic time shifts in the waveforms, which suggests that there was a movement of seismic source with time, instead of change in properties within the volcanic system; a source displacement of 235 m was calculated over the day (*De Angelis*, 2009). A continuous change in seismic waveforms also suggested an evolving process; Figure 6.46 shows the change over the nine-day period from VT earthquakes to LP earthquakes by the end of the sequence.

A change in source location supported by coda wave interferometry, is interpreted to represent an upward change in source location via magma ascent (*De Angelis*, 2009). Figure 6.47 shows the repicked relocations for hybrid and LP earthquakes during this period. There is a shallowing of seismicity from the 27^{th} July where LP events migrate from a constant depth of 1.5-2 km bsl up to 0.5 km asl; however a lot of these events are located around velocity boundary layers. Additionally there is also an increase of seismicity up to 4 km depth, although the majority of earthquakes are still concentrated within the first 1.5 km. An upward change in source location could be supported by the relocations in this study, but this is not able to be resolved fully due to the associated errors. Relative location methods such as *HypoDD* (*Waldhauser*, 2001b) or *Bayesloc* (*Myers et al.*, 2011) could be used to further constrain seismicity during this time, and to confirm upward trend in source location.

If we take the interpretation that LP seismicity indicated magma ascent or processes at-

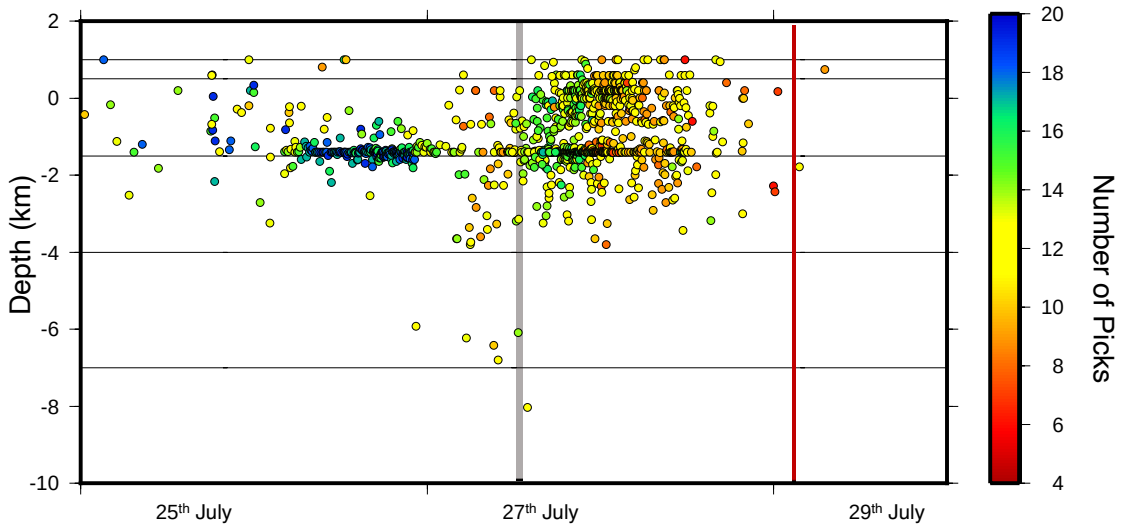

Figure 6.47: LP and hybrid earthquakes depth location through time. These are coloured by the number of picks used. Events with errors less than 3 km are shown. Red line denotes the time of the Vulcanian Explosion. Grey line represents time of Ash Venting.

tributed to magma movement, then the reduction in events seen in the 12 hours before the Vulcanian explosion could indicate the stalling of magma. Ash venting was recorded at 13:24 UTC on the 27^{th} July six hours before the peak seismicity rate; this could cause an increase in viscosity resulting in magma being stalled (*Rodgers et al.*, 2016). Microlite textures also support magmatic crystallisation, which supports an increase in viscosity and magma stalling (*Komorowski et al.*, 2010). The cessation of magma ascent would have led to an increase in pressure as gasses accumulated, resulting in the Vulcanian explosion on the 29^{th} July (*Rodgers et al.*, 2016).

Relocations from this study, support findings from *Rodgers et al.* (2016) with depth locations for different types of seismicity being similar; in turn this supports *Rodgers et al.* (2016) interpretations for the sequence of events in the build up to the Vulcanian explosion on the 29^{th} July. The main difference in hypocenter locations, is the removal of seismicity in the SE that was previously recorded by MVO and *Rodgers et al.* (2016) but was discounted in this thesis and *Rodgers et al.* (2016), due to large calculated hypocenter errors (greater than 3 km). Repicked relocations show this apparent trend to no longer be present even with the inclusion of earthquakes with large calculated errors. The majority of seismicity is beneath Soufrière Hills Volcano, suggesting original locations were an artefact of a low number of P and S arrival times, leading to poor accuracy locations. This absence of the

SE trend is shown when including large error events, showing the importance of having additional arrival phases for location.

A four fold increase in located earthquakes were able to be used for interpretation (when using a threshold of 3 km error) after the addition of extra arrival time phases, and relocation using *NonLinLoc*. Errors were significantly lower for repicked earthquakes, allowing a greater percentage of events to be used for analysis. This gives a strong indication that the SE trend was a result of poor earthquake location, and highlights the importance of using data from all active seismic stations.

This shows the impact low accuracy earthquake locations could have on interpretations made about the volcanic system, especially during real time monitoring. Not all volcanic sites have a high density of seismic stations; a low number of seismic stations could lead to poor earthquake locations in some areas of the region if prior testing is not completed to understand how well the seismic network performs. This could lead to the mis-interpretation of trends in seismicity that may affect hazard assessment and our understanding of the plumbing system.

Chapter 7

Synthesis

The aim of this thesis was to determine whether the current earthquake location method used at the Montserrat Volcano Observatory is suitable for locating earthquakes on Montserrat, which in turn is used to monitor and understand the volcanic system beneath Soufrière Hills Volcano. The current location setup at MVO was compared with alternate location methods and velocity models to see if earthquake locations could be improved when using a synthetic grid of earthquakes. The improved location method for Montserrat is then used to relocate the past seismic catalogue from 1995-2018 to compare differences in hypocenters, and understand how this may change previous interpretations of the volcanic activity at Soufrière Hills Volcano.

Earthquake hypocenters are particularly important at volcanic systems: rates, the type of seismicity and hypocenter location are all used to understand the state of the volcanic system prior to and during an eruption. Hypocenters at other volcanic systems have been shown to track the migration of magma beneath the surface (*Woods et al.*, 2018), and infer the location of the magma chamber (*Ohlendorf et al.*, 2014). For earthquakes located at Montserrat Volcano Observatory, hypocenters had large depth errors, with some time periods showing large latitude and longitude errors. The uncertainty from poor constraints on location of earthquakes contributes uncertainty to ongoing risk assessment.

This thesis compared several velocity models and location methods with the current earthquake location method at Montserrat Volcano Observatory using a grid of synthetic earthquakes, to see if an improvement in the accuracy of locations could be achieved. Comparison of different seismic velocity models and location methods produced an improved location setup, which was then used to relocate the seismic catalogue on Montserrat to compare

hypocenters between the original and relocated catalogue. Finally, a time period from the relocated catalogue is further investigated due to a new pattern in seismicity recorded in relocated hypocenters. Locations during this time period were restricted by a low number of arrival time phases; therefore the data was repicked for additional P and S phases to help understand the importance of the number of arrival time phases on earthquake location.

In Chapter 4, the original location method used by Montserrat Volcano Observatory (MVO) was tested to understand its accuracy at locating earthquakes on Montserrat. A grid of synthetic earthquakes spaced 1 km at several depths across Montserrat was relocated to help understand how accurately the location method relocated earthquakes. This was compared by looking at changes in location between original and relocated synthetic earthquakes, and the calculated hypocenter errors produced by each method. Results showed that the MVO seismic velocity model with *Hypocenter* (MVO's current operations) performed poorly with large changes in depth between original and relocated synthetic locations. Errors were higher for the depth location compared to the latitude and longitude error. The number of trusted earthquakes are relatively high at shallow depths, but performed poorly at intermediate depths.

The MVO location method was then compared with three additional velocity models and three alternative location methods to determine if there was a different methodology that could reduce calculated hypocenter errors and improve earthquake locations (smaller changes in synthetic relocation that correlate to a more accurate location). A total of 15 location setups (combination of different velocity models with location methods) was tested by relocating synthetic earthquakes. Results showed that using the location method *Hypocenter* increases recorded changes in location and reduces the number of trusted locations for all velocity models compared to using *NonLinLoc*. The Rowe velocity model performed the best at relocating synthetic earthquakes at shallow depths, whereas the 1D SEA-CALIPSO model performed better at depths greater than 3 km. However, the main issue with the 1D SEA-CALIPSO model is that it is limited to a depth of 6 km; seismicity on Montserrat has been recorded at depths greater than this, and hence this velocity model cannot be used solely on its own for earthquake location at MVO. For this reason, it was decided that the Rowe seismic velocity model would be the most suitable for Montserrat.

The *NonLinLoc* EDT location method produced slightly higher errors than the weighted

GAU *NonLinLoc* location method, but produced a high percentage of trusted locations at most depths. It was decided that having slightly higher uncertainty errors (of around 50 m) would be better if there was a greater confidence in the outputted hypocenters and associated errors. A Dunn statistical test was performed on each of the relocations to see if there was a significant change in location and error for using the EDT *NonLinLoc* method with the Rowe Velocity model compared to using the original method of *Hypocenter* with the MVO model. Results showed that the new method produced significantly less changes in location and lower errors than the majority of other seismic velocity models and location methods, and importantly showed a significant reduction from Montserrat's Volcano Observatory current operations.

Using the improved location method from Chapter 4, the seismic catalogue from 1995 to 2018 was relocated in Chapter 5 to 1) improve the accuracy of locations and, 2) compare with original locations to understand if new locations changed interpretations of the volcanic plumbing system. The majority of relocated hypocenters had errors less than 5 km, with over 75% having errors less than 2.5 km. Comparison between original locations and relocated locations show changes up to 50 km for the time period 1999–2008; this is thought to be linked to the number of seismic arrival times, as the average number of picks per earthquakes was lower during this time period. Mean errors for original hypocenters were up to 50 km; this has been reduced with *NonLinLoc* relocations with mean errors below 2.5 km. Greater errors alongside the large changes in location suggests that the current operations are not optimal at locating earthquakes during this time period, most likely due to a reduction in the number of arrival times — this could either be due to reduction in active seismic stations, or time constraints resulting in earthquakes not being picked fully for arrival times.

Relocations show similar hypocenters for Phases 2–5, but show significant changes in location for Phase 1. Four distal clusters were first recognised during 1995–1996 by *Aspinall et al.* (1998) and *Miller et al.* (2010). Relocations show there to be 12 distal clusters recorded over the same time period, with some clusters showing the same spatial properties. A Dunns statistical test was perfromed to see which groups showed statistically significant locations; this resulted in three mega-clusters throughout 1995–1996 where seismicity was located in a statistically similar location. This suggests that similar processes

may have been responsible for each cluster in activity, such as a dyke being reactivated during the early stages of the eruption.

Earthquakes on the 5^{th}–6^{th} August 1995 was previously located extending to Long Ground in the NE of the island from Soufrière Hills Volcano. Research by *Aspinall et al.* (1998) suggested that there was a migration of hypocenters with time towards Soufrière Hills, but this was discounted by *Roman et al.* (2008) due to large hypocenter errors. Relocations in this thesis show a similar migration of earthquakes with time from Long Ground to Soufrière Hills; these relocated earthquakes have smaller errors allowing for them to be included in interpretation, and show a clear correlation of movement to the SW, agreeing with previous work by *Aspinall et al.* (1998).

Earthquakes were recorded at St George's Hill on the 12–14^{th} August 1995 by *Aspinall et al.* (1998) and *Miller et al.* (2010). Relocations show earthquakes recorded beneath St George's Hill but with a clear migration from Soufrière Hills Volcano over the 2-day period. This migration of hypocenters alongside computed focal mechanisms from *Miller et al.* (2010) suggest that this seismicity can be explained as a propagating and inflating dyke orientated NW. This differs from interpretations by *Miller et al.* (2010) and *White and McCausland* (2016) which proposed that this was a distal cluster triggered along pre-existing faults due to an increase in stress beneath Soufrière Hills Volcanos, likely from an injection in magma. However, for this to be a distal cluster, no migration in seismicity should be recorded. Hence, the new relocations suggest an alternative hypothesis for the seismicity recorded over the two–day period.

This also highlights the likelihood of a NW orientated dyke, which has been debated by several studies. Deformation studies by *Mattioli et al.* (1998) and *Hautmann et al.* (2009) suggests a NW and NNW orientated dyke respectively. This follows a similar trend in faults and volcanic complexes in the region. However, research by *Miller et al.* (2010) and *Roman et al.* (2008) have suggested a NE trending dyke based on the trends of P axis during VT seismicity in the early stages of the eruption. However, both have suggested these were short lived trends. Relocated earthquakes in this thesis show two time periods where earthquakes extend to the NW running parallel to the Belham Valley Fault. This includes the St George's Hill sequence which shows a migration of earthquakes with time to the NW, suggestive of a propagating dyke. Therefore it is inferred that the most likely

orientation would be NW, supported by this study.

Since Phase 5, earthquakes have been thought to be located deeper from 2012 to 2018; this was first highlighted in an MVO report in 2018. This coincided with the installation of Spider stations in 2014, which are portable vertical seismometers that are easily deployed. Relocations show that there is an increasing trend in depth from 2014 to 2018. Relocating this same time period without including the spider station arrival times also showed the presence of an increase in depth location throughout the four year period. This confirms that there is a real trend of increasing depth, and not a false effect due to the additional spider stations, supporting work in *MVO* (2018).

Another period of interest highlighted in Chapter 5 was July 2008 where relocations showed an extension of hypocenters to the SE following the trend of local faults and suggested dyke orientations in the region. However, these events had large hypocenter errors and therefore could not be used for interpretation. In Chapter 6, the seismic catalogue from the 21^{st} to 31^{st} July 2008 was repicked for P and S wave arrivals, as most events only had four arrival time phases. The majority of these earthquakes were Long Period earthquakes which are known to be difficult in picking the S wave arrival time. Over 1900 earthquakes were repicked and relocated using the method defined in Chapter 4. Hypocenter errors were reduced drastically, with the majority of repicked earthquakes having errors less than 1.5 km.

The repicked earthquakes showed the majority of events to be beneath Soufrière Hills Volcano, with the trend of seismicity to the SE not present in the repicked dataset. A larger number of earthquakes were able to be included in the analysis for this time period due to reduced errors. The lack of relocated seismicity to the SE suggest that this previous trend was false and was a result of using a small number of arrival times, that resulted in poorly constrained locations.

The synthetic earthquake grid defined in Chapter 4 was used to understand how using only four P wave arrivals impacted locations (using four seismic stations), and how the addition of S wave phases can reduce errors and improve hypocenter locations. Relocations have poorly constrained hypocenters when using four P phases, but locations improved greatly with the addition of 2 S phases. Earthquakes during this time only had four P waves picked for location, even though there was the potential for additional arrival times to be picked.

This was most likely a result of time constraints by MVO staff due to the increase in number of earthquakes during this time period. This chapter highlights the importance of having a complete arrival time dataset, with additional arrival phases having a great impact on locations. This can also alter interpretations and analysis of seismicity, with relocations using additional phases giving a clearer indication of interpretations of the volcanic system during this time.

This thesis has shown the importance of testing the location methods that are used at volcanic observatories and making sure there are not more suitable or relevant methods and models available that could improve the accuracy and precision of located earthquakes. This shows the value of implementing the relocation of previous seismic catalogues using new location methods and model, for long term hazard assessment. This was shown to have an impact on interpretations of the volcanic system at Soufrière Hills Volcano, especially in the early stages of the eruption when there was more inherent variability in the sub-surface feeder system. Additionally, earthquake locations can be improved by making use of the data available and picking all available P and S wave arrivals. This has been shown to reduce errors by several km when using more than four seismic phases.

Results from this study will have implications at systems elsewhere, especially at other observatories worldwide that have not explored multiple location methods. Although previous methods are useful for comparing counts, changes in frequency and rough location, finer details are being missed in locations which could have an impact on overall interpretations, especially during the early stages of the eruption. A reduction in location errors, and an increase on the accuracy of hypocenters ultimately increases the confidence in locations, and can add understanding of the volcanic system, which may be missed when using poor accuracy locations. Improving and testing location methods should be trialed at all sites, and during temporary deployments so that the user has confidence in the outputted results and understands the limitations of the seismic network and the outputted results.

7.1 Future Work

Although this thesis tackles some of the main aspects of earthquake location, and tests ways to improve the accuracy of located earthquakes, there are some additional steps that

could be taken to further increase the knowledge at Montserrat Volcano Observatory and other systems worldwide. One important step that should be explored further is looking at the importance of each station in a seismic network. Are certain stations more useful for locating earthquakes, and do these have a greater impact on earthquake locations if the station is down? Having a good azimuthal coverage is important for refining locations, but in some systems earthquake locations may be more affected by some stations than others, especially for regions with a seismic velocity model that is not representative of the whole region. In this study it was found that the station in the north of the island did not always have a positive effect on locations when used. Understanding which stations affect results the most and ranking these in order of importance would result in an observatory being able to prioritise stations when certain stations fail — perhaps replacing that station with one from a lesser important site. This would maintain high standards thoughout operations maintaining high accuracy locations.

Microseismicity can be a useful tool to understand more about the volcanic system. At Montserrat Volcano Observatory, only earthquakes with a certain amplitude and higher are triggered resulting in a lot of smaller events being missed. The method QuakeMigrate automatically detects earthquakes by using the coherence of seismic phase arrivals to identify an earthquake; this can then give a rough estimate of arrival phases and location that can be further constrained later (*Winder et al.*, 2021). Using this on the raw waveform data would allow additional earthquakes to be picked and located, adding a wealth of information to the current seismic catalogue. This would have been particularly useful during the St George's Hill cluster in 1995, and during July 2008 where a large amount of events were recorded in a short period of time. Earthquake magnitudes were not known for all events in the seismic catalogue; having this additional data would have allowed the magnitude of completeness to be calculated throughout the catalogue to understand if this varies with a changing seismic network. This could have then been used in conjunction with seismic rates to understand if an increase in a number of earthquakes between different phases was due to smaller earthquakes being recorded, or a result of actual variations.

Finally, joint inversion programs such as Bayesloc (*Myers et al.*, 2011) and HypoDD (*Waldhauser*, 2001a) could be used to help refine locations further during periods of distal clusters. This could have been used on data from 1995–1996 where several distal clusters were

recorded. Refining earthquake locations using joint inversion programs can help show further trends and patterns in the seismicity, such as faults which may not be visible before. Using this method with the megaclusters from Chapter 5 could help constrain seismicity further, confirming if a migration in seismicity was recorded from the 12–14th August towards St George's Hill. This thesis provides a stepping stone towards improving locations; the steps highlighted in Chapter 4 should be applied before continuing with further seismic analysis that are known to improve locations and add to previous interpretations.

Bibliography

Aki, K., M. Fehler, and S. Das (1977), Source mechanism of volcanic tremor: Fluid-driven crack models and their application to the 1963 Kilauea eruption, *J. Volcanol. Geotherm. Res.*, *2*(3), 259–287.

Ambeh, W., and L. Lynch (1996), Seismicity preceding the current eruption of the Soufrière Hills volcano, Montserrat, West Indies, in *Science, Hazards, and Hazard Management—Volcanism in Montserrat, 2nd Caribbean Conference on Natural Hazards and Disasters*, p. 30.

Annen, C., J. D. Blundy, and R. S. J. Sparks (2006), The Genesis of Intermediate and Silicic Magmas in Deep Crustal Hot Zones, *Journal of Petrology*, *47*(3), 505–539, doi: 10.1093/petrology/egi084.

Aspinall, W., A. Miller, L. Lynch, J. Latchman, R. Stewart, R. White, and J. Power (1998), Soufrière Hills eruption, Montserrat, 1995–1997: Volcanic earthquake locations and fault plane solutions, *Geophysical Research Letters*, *25*(18), 3397–3400.

Aspinall, W. P., S. Loughlin, F. Michael, A. Miller, G. Norton, K. Rowley, R. Sparks, and S. Young (2002), The Montserrat Volcano Observatory: its evolution, organization, role and activities, *Geological Society, London, Memoirs*, *21*(1), 71–91.

Baird, A. F., J.-M. Kendall, R. S. J. Sparks, and B. Baptie (2015), Transtensional deformation of Montserrat revealed by shear wave splitting, *Earth and Planetary Science Letters*, *425*, 179–186.

Bakker, R. R., M. Fazio, P. M. Benson, K.-U. Hess, and D. B. Dingwell (2016), The propagation and seismicity of dyke injection, new experimental evidence, *Geophysical Research Letters*, *43*(5), 1876–1883.

Barclay, J., M. J. Rutherford, M. Carroll, M. Murphy, J. Devine, J. Gardner, and R. Sparks (1998), Experimental phase equilibria constraints on pre-eruptive storage conditions of the Soufrière Hills magma, *Geophysical Research Letters*, *25*(18), 3437–3440.

Barclay, J., J. E. Johnstone, and A. J. Matthews (2006), Meteorological monitoring of an active volcano: implications for eruption prediction, *Journal of volcanology and geothermal research*, *150*(4), 339–358.

Barclay, J., R. A. Herd, B. R. Edwards, T. Christopher, E. J. Kiddle, M. Plail, and A. Donovan (2010), Caught in the act: Implications for the increasing abundance of mafic enclaves during the recent eruptive episodes of the Soufrière Hills Volcano, Montserrat, *Geophysical Research Letters*, *37*(19).

Benoit, J. P., and S. R. McNutt (1997), New constraints on source processes of volcanic tremor at Arenal Volcano, Costa Rica, using broadband seismic data, *Geophysical Research Letters*, *24*(4), 449–452.

Bird, P. (2003), An updated digital model of plate boundaries, *Geochemistry, Geophysics, Geosystems*, *4*(3).

Bonneton, J.-R., and A. Scheidegger (1981), Relations between fracture patterns, seismicity and plate motions in the Lesser Antilles, *Journal of Structural Geology*, *3*(4), 359–369.

Boudon, G., B. Villemant, J.-C. Komorowski, P. Ildefonse, and M. P. Semet (1998), The hydrothermal system at Soufrière Hills Volcano, Montserrat (West Indies): Characterization and role in the on-going eruption, *Geophysical Research Letters*, *25*(19), 3693–3696.

Bouysse, P., and D. Westercamp (1990), Subduction of Atlantic aseismic ridges and Late Cenozoic evolution of the Lesser Antilles island arc, *Tectonophysics*, *175*(4), 349–380.

Buland, R. (1976), The mechanics of locating earthquakes, *Bulletin of the Seismological Society of America*, *66*(1), 173–187.

Burlini, L., S. Vinciguerra, G. Di Toro, G. De Natale, P. Meredith, and J.-P. Burg (2007), Seismicity preceding volcanic eruptions: New experimental insights, *Geology*, *35*(2), 183–186.

Calder, E., J. Cortes, J. Palma, and R. Luckett (2005), Probabilistic analysis of rockfall frequencies during an andesite lava dome eruption: The soufriere hills volcano, montserrat, *Geophysical research letters*, *32*(16).

Carlson, R. (2001), The effects of temperature, pressure, and alteration on seismic properties of diabase dike rocks from DSDP/ODP Hole 504B, *Geophysical research letters*, *28*(20), 3979–3982.

Carn, S., R. Watts, G. Thompson, and G. Norton (2004), Anatomy of a lava dome collapse: the 20 March 2000 event at Soufrière Hills Volcano, Montserrat, *Journal of Volcanology and Geothermal Research*, *131*(3-4), 241–264.

Chardot, L., B. Voight, R. Foroozan, S. Sacks, A. Linde, R. Stewart, D. Hidayat, A. Clarke, D. Elsworth, N. Fournier, et al. (2010), Explosion dynamics from strainmeter and microbarometer observations, Soufrière Hills Volcano, Montserrat: 2008–2009, *Geophysical Research Letters*, *37*(19).

Chicangana, G. (2005), The Romeral fault system: a shear and deformed extinct subduction zone between oceanic and continental lithospheres in northwestern South America, *Earth Sciences Research Journal*, *9*(1), 50–64.

Chiodini, G., R. Cioni, A. Frullani, M. Guidi, L. Marini, F. Prati, and B. Raco (1996), Fluid geochemistry of Montserrat Island, West Indies, *Bulletin of Volcanology*, *58*(5), 380–392.

Chouet, B. (1985), Excitation of a buried magmatic pipe: a seismic source model for volcanic tremor, *J. Geophys. Res.*, *90*(B2), 1881–1893.

Chouet, B. (1988), Resonance of a fluid-driven crack: Radiation properties and implications for the source of long-period events and harmonic tremor, *Journal of Geophysical Research: Solid Earth*, *93*(B5), 4375–4400.

Chouet, B. (2003), Volcano seismology, *Pure and Applied Geophysics*, *160*(3-4), 739–788.

Chouet, B., and P. Dawson (2011), Shallow conduit system at Kilauea Volcano, Hawaii, revealed by seismic signals associated with degassing bursts, *J. Geophys. Res.*, *116*(B12).

Chouet, B. A. (1996), Long-period volcano seismicity: its source and use in eruption forecasting, *Nature*, *380*(6572), 309–316.

Chouet, B. A., and R. S. Matoza (2013), A multi-decadal view of seismic methods for detecting precursors of magma movement and eruption, *J. Volcanol. Geotherm. Res.*, *252*, 108–175.

Chouet, B. A., R. A. Page, C. D. Stephens, J. C. Lahr, and J. A. Power (1994), Precursory swarms of long-period events at Redoubt Volcano (1989–1990), Alaska: their origin and use as a forecasting tool, *Journal of Volcanology and Geothermal Research*, *62*(1-4), 95–135.

Christopher, T., J. Blundy, K. Cashman, P. Cole, M. Edmonds, P. Smith, R. Sparks, and A. Stinton (2015), Crustal-scale degassing due to magma system destabilization and magma-gas decoupling at Soufrière Hills Volcano, Montserrat, *Geochemistry, Geophysics, Geosystems*, *16*(9), 2797–2811.

Cole, P., P. Smith, J.-C. Komorowski, F. Alfano, C. Bonadonna, A. Stinton, T. Christopher, H. Odbert, and S. Loughlin (2014a), Ash venting occurring both prior to and during lava extrusion at Soufrière Hills Volcano, Montserrat, from 2005 to 2010, *Geological Society, London, Memoirs*, *39*(1), 71–92.

Cole, P., P. Smith, A. Stinton, H. Odbert, M. Bernstein, J. Komorowski, and R. Stewart (2014b), Vulcanian explosions at Soufrière Hills Volcano, Montserrat between 2008 and 2010, *Geological Society, London, Memoirs*, *39*(1), 93–111.

Cooper, K., C. Donnelly, D. Sherrod, W. Scott, and P. Stauffer (2008), A Volcano Rekindled: The First Year of Renewed Eruption at Mount St. Helens, 2004–2006, *Tech. rep.*, U.S. Geological Survey.

Cruz, F. G., and B. A. Chouet (1997), Long-period events, the most characteristic seismicity accompanying the emplacement and extrusion of a lava dome in Galeras Volcano, Colombia, in 1991, *Journal of Volcanology and Geothermal Research*, *77*(1-4), 121–158.

De Angelis, S. (2009), Seismic source displacement by coda wave interferometry at Soufrière Hills Volcano, Montserrat, WI, *Natural Hazards and Earth System Sciences*, *9*(4), 1341.

De Angelis, S., V. Bass, V. Hards, and G. Ryan (2007), Seismic characterization of pyroclastic flow activity at Soufrière Hills Volcano, Montserrat, 8 January 2007, *Natural Hazards and Earth System Sciences*, *7*(4), 467–472.

Devine, J., M. Rutherford, G. Norton, and S. Young (2003), Magma storage region processes inferred from geochemistry of Fe–Ti oxides in andesitic magma, Soufrière Hills Volcano, Montserrat, WI, *Journal of Petrology*, *44*(8), 1375–1400.

Ebinger, C., D. Keir, A. Ayele, E. Calais, T. Wright, M. Belachew, J. O. Hammond, E. Campbell, and W. Buck (2008), Capturing magma intrusion and faulting processes during continental rupture: seismicity of the Dabbahu (Afar) rift, *Geophysical Journal International*, *174*(3), 1138–1152.

Edmonds, M., C. Oppenheimer, D. M. Pyle, R. A. Herd, and G. Thompson (2003), So2 emissions from soufrière hills volcano and their relationship to conduit permeability, hydrothermal interaction and degassing regime, *Journal of Volcanology and Geothermal Research*, *124*(1-2), 23–43.

Edmonds, M., R. A. Herd, and M. H. Strutt (2006), Tephra deposits associated with a large lava dome collapse, Soufrière Hills Volcano, Montserrat, 12–15 July 2003, *Journal of Volcanology and Geothermal Research*, *153*(3-4), 313–330.

Elsworth, D., G. Mattioli, J. Taron, B. Voight, and R. Herd (2008), Implications of magma transfer between multiple reservoirs on eruption cycling, *Science*, *322*(5899), 246–248.

Endo, E. T., S. D. Malone, L. L. Noson, and C. Weaver (1981), Locations, magnitudes, and statistics of the March 20–May 18 earthquake sequence, *US Geol. Surv. Prof. Pap*, *1250*, 93–107.

Eyles, J. H., F. Illsley-Kemp, D. Keir, J. Ruch, and S. Jónsson (2018), Seismicity associated with the formation of a new island in the Southern Red Sea, *Frontiers in Earth Science*, *6*, 141.

Faulds, J. E., N. H. Hinz, M. F. Coolbaugh, P. H. Cashman, C. Kratt, G. Dering, J. Edwards, B. Mayhew, and H. McLachlan (2011), Assessment of favorable structural settings of geothermal systems in the Great Basin, western USA, *Geothermal Resources Council Transactions*, *35*, 777–783.

Fehler, M., and B. Chouet (1982), Operation of a digital seismic network on Mount St. Helens volcano and observations of long period seismic events that originate under the volcano, *Geophysical Research Letters*, *9*(9), 1017–1020.

Feuillet, N., I. Manighetti, and P. Tapponnier (2001), Active arc-transverse normal faulting in Guadeloupe (French Lesser Antilles), *Comptes Rendus De L Academie Des Sciences Serie II Fascicule A-Sciences De La Terre Et Des Planetes*, *333*(9), 583–590.

Feuillet, N., I. Manighetti, P. Tapponnier, and E. Jacques (2002), Arc parallel extension and localization of volcanic complexes in Guadeloupe, Lesser Antilles, *Journal of Geophysical Research: Solid Earth*, *107*(B12), ETG–3.

Feuillet, N., F. Leclerc, P. Tapponnier, F. Beauducel, G. Boudon, A. Le Friant, C. Deplus, J.-F. Lebrun, A. Nercessian, J.-M. Saurel, et al. (2010), Active faulting induced by slip partitioning in Montserrat and link with volcanic activity: New insights from the 2009 GWADASEIS marine cruise data, *Geophysical Research Letters*, *37*(19).

Foroozan, R., D. Elsworth, B. Voight, and G. S. Mattioli (2010), Dual reservoir structure at Soufrière Hills Volcano inferred from continuous GPS observations and heterogeneous elastic modeling, *Geophysical Research Letters*, *37*(19).

Gardner, C., and R. White (2002), Seismicity, gas emission and deformation from 18 July to 25 September 1995 during the initial phreatic phase of the eruption of Soufrière Hills Volcano, Montserrat, *Geological Society, London, Memoirs*, *21*(1), 567–581.

Geiger, L. (1912), Probability method for the determination of earthquake epicenters from the arrival time only, *Bull. St. Louis Univ*, *8*(1), 56–71.

Goto, A. (1999), A new model for volcanic earthquake at Unzen Volcano: Melt rupture model, *Geophysical Research Letters*, *26*(16), 2541–2544.

Green, D., and J. Neuberg (2005), Seismic and infrasonic signals associated with an unusual collapse event at the Soufrière Hills volcano, Montserrat, *Geophysical Research Letters*, *32*(7).

Hammer, C., and J. Neuberg (2009), On the dynamical behaviour of low-frequency earthquake swarms prior to a dome collapse of Soufrière Hill volcano, Montserrat, *Geophysical Research Letters*, *36*(6).

Hammouya, G., P. Allard, P. Jean-Baptiste, F. Parello, M. Semet, and S. Young (1998), Pre-and syn-eruptive geochemistry of volcanic gases from Soufrière Hills of Montserrat, West Indies, *Geophysical Research Letters*, *25*(19), 3685–3688.

Harford, C., M. Pringle, R. Sparks, and S. Young (2002), The volcanic evolution of Montserrat using 40Ar/39Ar geochronology, *Geological Society, London, Memoirs*, *21*(1), 93–113.

Harford, C. L., and R. S. J. Sparks (2001), Recent remobilisation of shallow-level intrusions on Montserrat revealed by hydrogen isotope composition of amphiboles, *Earth and Planetary Science Letters*, *185*(3-4), 285–297.

Hautmann, S., J. Gottsmann, R. S. J. Sparks, A. Costa, O. Melnik, and B. Voight (2009), Modelling ground deformation caused by oscillating overpressure in a dyke conduit at Soufrière Hills Volcano, Montserrat, *Tectonophysics*, *471*(1-2), 87–95.

Hautmann, S., A. G. Camacho, J. Gottsmann, H. M. Odbert, and R. T. Syers (2013), The shallow structure beneath Montserrat (West Indies) from new Bouguer gravity data, *Geophysical Research Letters*, *40*(19), 5113–5118.

Herd, R. A., M. Edmonds, and V. A. Bass (2005), Catastrophic lava dome failure at Soufrière Hills volcano, Montserrat, 12–13 July 2003, *Journal of Volcanology and Geothermal Research*, *148*(3-4), 234–252.

Hill, D. P. (1977), A model for earthquake swarms, *J. Geophys. Res.*, *82*(8), 1347–1352.

Hobro, J. W., S. C. Singh, and T. A. Minshull (2003), Three-dimensional tomographic inversion of combined reflection and refraction seismic traveltime data, *Geophysical Journal International*, *152*(1), 79–93.

Huppert, H. E., and R. S. Sparks (2016), Compressible vapour flow in conduits and fractures, *Journal of Fluid Mechanics*, *802*, 750–759.

Iverson, R. M., D. Dzurisin, C. A. Gardner, T. M. Gerlach, R. G. LaHusen, M. Lisowski, J. J. Major, S. D. Malone, J. A. Messerich, S. C. Moran, et al. (2006), Dynamics of seismogenic volcanic extrusion at Mount St Helens in 2004–05, *Nature*, *444*(7118), 439–443.

Johnson, C. E., A. Bittenbinder, B. Bogaert, L. Dietz, and W. Kohler (1995), Earthworm: A flexible approach to seismic network processing, *Iris newsletter*, *14*(2), 1–4.

Jones, J. P., C. H. Thurber, and W. J. Lutter (2001), High-precision location of pre-eruption seismicity at Mount Pinatubo, Philippines, 30 May–3 June, 1991, *Physics of the Earth and Planetary Interiors*, *123*(2-4), 221–232.

Jordan, T. H., and K. A. Sverdrup (1981), Teleseismic location techniques and their application to earthquake clusters in the south-central Pacific, *Bulletin of the Seismological Society of America*, *71*(4), 1105–1130.

Kawakatsu, H., S. Kaneshima, H. Matsubayashi, T. Ohminato, Y. Sudo, T. Tsutsui, K. Uhira, H. Yamasato, H. Ito, and D. Legrand (2000), Aso94: Aso seismic observation with broadband instruments, *J. Volcanol. Geotherm. Res.*, *101*(1), 129–154.

Kenedi, C., and G. Ryan (2010), Evidence for a Fracture Dominated Hydrothermal System at St. George's Hill, Montserrat, in *AGU Fall Meeting Abstracts*, vol. 2010, pp. V21E–2360.

Komorowski, J.-C., Y. Legendre, T. Christopher, M. Bernstein, R. Stewart, E. Joseph, N. Fournier, L. Chardot, A. Finizola, G. Wadge, et al. (2010), Insights into processes and deposits of hazardous vulcanian explosions at Soufrière Hills Volcano during 2008 and 2009 (Montserrat, West Indies), *Geophysical Research Letters*, *37*(19).

Konstantinou, K. I., and V. Schlindwein (2003), Nature, wavefield properties and source mechanism of volcanic tremor: a review, *J. Volc. Geoth. Res.*, *119*(1), 161–187.

Koyanagi, R. Y., B. Chouet, and K. Aki (1987), Origin of volcanic tremor in Hawaii, *US Geological Survey Professional Paper*, *1350*(2), 1221–1257.

Kumagai, H., T. Ohminato, M. Nakano, M. Ooi, A. Kubo, H. Inoue, and J. Oikawa (2001), Very-long-period seismic signals and caldera formation at miyake island, japan, *Science*, *293*(5530), 687–690.

Kumagai, H., K. Miyakawa, H. Negishi, H. Inoue, K. Obara, and D. Suetsugu (2003), Magmatic dike resonances inferred from very-long-period seismic signals, *Science*, *299*(5615), 2058–2061.

Kumagai, H., B. A. Chouet, and P. B. Dawson (2005), Source process of a long-period event at Kilauea volcano, Hawaii, *Geophysical Journal International*, *161*(1), 243–254.

Lahr, J., B. Chouet, C. Stephens, J. Power, and R. Page (1994), Earthquake classification, location, and error analysis in a volcanic environment: Implications for the magmatic system of the 1989–1990 eruptions at Redoubt Volcano, Alaska, *Journal of Volcanology and Geothermal Research*, *62*(1-4), 137–151.

Lahr, J. C. (1999), *HYPOELLIPSE: A computer program for determining local earthquake hypocentral parameters, magnitude, and first motion pattern*, US Geological Survey Denver, Colorado.

Latter, J. (1981), Volcanic earthquakes, and their relationship to eruptions at Ruapehu and Ngauruhoe volcanoes, *Journal of volcanology and geothermal research*, *9*(4), 293–309.

Latter, J. H. (1979), Volcanological observations at Tongariro National Park. II: Types and classification of volcanic earthquakes, 1976-1978, *Report-Geophysics Division*.

Legrand, D., S. Barrientos, K. Bataille, J. Cembrano, and A. Pavez (2011), The fluid-driven tectonic swarm of Aysen Fjord, Chile (2007) associated with two earthquakes (Mw= 6.1 and Mw= 6.2) within the Liquiñe-Ofqui Fault Zone, *Continental Shelf Research*, *31*(3-4), 154–161.

Lensky, N., R. Sparks, O. Navon, and V. Lyakhovsky (2008), Cyclic activity at soufrière hills volcano, montserrat: degassing-induced pressurization and stick-slip extrusion, *Geological Society, London, Special Publications*, *307*(1), 169–188.

Lienert, B. R., and J. Havskov (1995), A computer program for locating earthquakes both locally and globally, *Seismological Research Letters*, *66*(5), 26–36.

Lienert, B. R., E. Berg, and L. N. Frazer (1986), HYPOCENTER: An earthquake location method using centered, scaled, and adaptively damped least squares, *Bulletin of the Seismological Society of America*, *76*(3), 771–783.

Lockwood, J., N. Banks, T. English, P. Greenland, D. Jackson, D. Johnson, B. Koyanagi, K. McGee, A. Okamura, and M. Rhodes (1985), The 1984 eruption of Mauna Loa Volcano, Hawaii, *Eos, Transactions American Geophysical Union*, *66*(16), 169–171.

Lomax, A. (2001), NonLinLoc Home Page.

Lomax, A. (2005), A reanalysis of the hypocentral location and related observations for the great 1906 California earthquake, *Bull. Seis. Soc. Am.*, *95*(3), 861–877.

Lomax, A., and A. Curtis (2001), Fast, probabilistic earthquake location in 3D models using oct-tree importance sampling, in *Geophys. Res. Abstr*, vol. 3, p. 955.

Lomax, A., A. Michelini, and A. Curtis (2009), Earthquake Location, Direct, Global-SearchGlobal-search Methods, in *Encyclopedia of complexity and systems science*, pp. 2449–2473, Springer.

López, A. M., S. Stein, T. Dixon, G. Sella, E. Calais, P. Jansma, J. Weber, and P. LaFemina (2006), "is there a northern lesser antilles forearc block?", *Geophysical research letters*, *33*(7).

Loughlin, S., E. Calder, A. Clarke, P. Cole, R. Luckett, M. Mangan, D. Pyle, R. Sparks, B. Voight, and R. Watts (2002), Pyroclastic flows and surges generated by the 25 June 1997 dome collapse, Soufrière Hills Volcano, Montserrat, *Geological Society, London, Memoirs*, *21*(1), 191–209.

Loughlin, S., R. Luckett, G. Ryan, T. Christopher, V. Hards, S. De Angelis, L. Jones, and M. Strutt (2010), An overview of lava dome evolution, dome collapse and cyclicity at soufrière hills volcano, montserrat, 2005–2007, *Geophysical Research Letters*, *37*(19).

Luckett, R. (2005), Seismic data from the Montserrat eruption at BGS, *Open Report OR/09/57*.

Luckett, R., B. Baptie, L. Ottemoller, and G. Thompson (2007), Seismic monitoring of the Soufrière Hills volcano, Montserrat, *Seismological Research Letters*, *78*(2), 192–200.

Macdonald, R., C. Hawkesworth, and E. Heath (2000), The Lesser Antilles volcanic chain: a study in arc magmatism, *Earth-Science Reviews*, *49*(1-4), 1–76.

Marchetti, E., R. Genco, and M. Ripepe (2009), Ground deformation and seismicity related to the propagation and drainage of the dyke feeding system during the 2007 effusive eruption at Stromboli volcano (Italy), *Journal of volcanology and geothermal research*, *182*(3-4), 155–161.

Matthews, A. J., J. Barclay, S. Carn, G. Thompson, J. Alexander, R. Herd, and C. Williams (2002), Rainfall-induced volcanic activity on Montserrat, *Geophysical Research Letters*, *29*(13).

Matthews, C. (2009), Fracture mechanics of volcanic eruptions, Ph.D. thesis, UCL (University College London).

Mattioli, G., and R. Herd (2004), Correlation of cyclic surface deformation recorded by GPS geodesy with surface magma flux at Soufrière Hills Volcano, Montserrat, *Seismological Research Letters*, *74*(2), 230.

Mattioli, G. S., T. H. Dixon, F. Farina, E. S. Howell, P. E. Jansma, and A. L. Smith (1998), GPS measurement of surface deformation around Soufrière Hills volcano, Montserrat from October 1995 to July 1996, *Geophysical Research Letters*, *25*(18), 3417–3420.

Mattioli, G. S., S. R. Young, B. Voight, R. Steven, J. Sparks, E. Shalev, S. Sacks, P. Malin, A. Linde, W. Johnston, et al. (2004), Prototype pbo instrumentation of calipso project captures world-record lava dome collapse on montserrat volcano, *Eos, Transactions American Geophysical Union*, *85*(34), 317–325.

McNutt, S. R. (1996), Seismic monitoring and eruption forecasting of volcanoes: a review of the state-of-the-art and case histories, in *Monitoring and mitigation of volcano hazards*, pp. 99–146, Springer.

McNutt, S. R. (2005), Volcanic seismology, *Annu. Rev. Earth Planet. Sci.*, *32*, 461–491.

McNutt, S. R., and D. C. Roman (2015), Volcanic seismicity, in *The Encyclopedia of Volcanoes*, pp. 1011–1034, Elsevier.

Menke, W. (2018), *Geophysical data analysis: Discrete inverse theory*, Academic press.

Michaut, C., Y. Ricard, D. Bercovici, and R. S. J. Sparks (2013), Eruption cyclicity at silicic volcanoes potentially caused by magmatic gas waves, *Nature Geoscience*, *6*(10), 856–860.

Miller, A., R. Stewart, R. White, R. Luckett, B. Baptie, W. Aspinall, J. Latchman, L. Lynch, and B. Voight (1998), Seismicity associated with dome growth and collapse at the Soufrière Hills Volcano, Montserrat, *Geophysical Research Letters*, *25*(18), 3401–3404.

Miller, V., B. Voight, C. J. Ammon, E. Shalev, and G. Thompson (2010), Seismic expression of magma-induced crustal strains and localized fluid pressures during initial eruptive stages, Soufrière Hills Volcano, Montserrat, *Geophysical Research Letters*, *37*(19).

Miller, V. L. (2011), Crustal Response to Changes in the Magmatic System at the Soufrière Hills Volcano, Montserrat, Ph.D. thesis, Pennslyvania State University.

Milne, J. (1886), *Earthquakes and other earth movements*, vol. 56, K. Paul, Trench.

Mostaccio, A., T. Tuve, L. Zuccarello, D. Patane, G. Saccorotti, and M. D'Agostino (2005), Three-dimensional Probabilistic Earthquake Location Applied to 2002-2003 Mt. Etna Eruption, in *AGU Fall Meeting Abstracts*.

Mostaccio, A., T. Tuvè, D. Patanè, G. Barberi, and L. Zuccarello (2013), Improving Seismic Surveillance at Mt. Etna Volcano by Probabilistic Earthquake Location in a 3D Model Improving Seismic Surveillance at Mt. Etna Volcano by Probabilistic Earthquake Location in a 3D Model, *Bulletin of the Seismological Society of America*, *103*(4), 2447–2459.

Murphy, M., R. Sparks, J. Barclay, M. Carroll, and T. Brewer (2000), Remobilization of andesite magma by intrusion of mafic magma at the Soufrière Hills Volcano, Montserrat, West Indies, *Journal of petrology*, *41*(1), 21–42.

Murray, T., J. Ewert, A. Lockhart, and R. LaHusen (1996), The integrated mobile volcano-monitoring system used by the Volcano Disaster Assistance Program (VDAP), in *Monitoring and Mitigation of Volcano Hazards*, pp. 315–362, Springer.

MVO (2008), MVO OFR 08/02, *MVO Open File Rep.*

MVO (2018), MVO OFR 08/02, *MVO Open File Rep.*

Myers, S., G. Johannesson, and R. J. Mellors (2011), BayesLoc: A robust location program for multiple seismic events given an imperfect earth model and error-corrupted seismic data, *Tech. rep.*, Lawrence Livermore National Lab.(LLNL), Livermore, CA (United States).

Nakada, S., H. Shimizu, and K. Ohta (1999), Overview of the 1990–1995 eruption at unzen volcano, *Journal of Volcanology and Geothermal Research*, *89*(1-4), 1–22.

Neuberg, J. (2000), Characteristics and causes of shallow seismicity in andesite volcanoes, *Philosophical Transactions of the Royal Society of London A: Mathematical, Physical and Engineering Sciences*, *358*(1770), 1533–1546.

Neuberg, J., and T. Pointer (2000), Effects of volcano topography on seismic broad-band waveforms, *Geophysical Journal International*, *143*(1), 239–248.

Neuberg, J., B. Baptie, R. Luckett, and R. Stewart (1998), Results from the broadband seismic network on Montserrat, *Geophysical Research Letters*, *25*(19), 3661–3664.

Neuberg, J., R. Luckett, B. Baptie, and K. Olsen (2000), Models of tremor and low-frequency earthquake swarms on Montserrat, *J. Volcanol. Geotherm. Res.*, *101*(1), 83–104.

Neuberg, J. W., H. Tuffen, L. Collier, D. Green, T. Powell, and D. Dingwell (2006), The trigger mechanism of low-frequency earthquakes on Montserrat, *J. Volcanol. Geotherm. Res.*, *153*(1), 37–50.

Newhall, C. G., and R. Punongbayan (1996), *Fire and mud: eruptions and lahars of Mount Pinatubo, Philippines*, Philippine Institute of Volcanology and Seismology Quezon City.

Nicholson, E., T. A. Mather, D. Pyle, H. M. Odbert, and T. Christopher (2013), Cyclical patterns in volcanic degassing revealed by SO_2 flux timeseries analysis: An application to Soufrière Hills Volcano, Montserrat, *Earth and Planetary Science Letters*, *375*, 209–221.

Norton, G., R. Watts, B. Voight, G. Mattioli, R. Herd, S. Young, J. Devine, W. Aspinnall, C. Bonadonna, B. Baptie, et al. (2002), Pyroclastic flow and explosive activity at Soufrière Hills Volcano, Montserrat, during a period of virtually no magma extrusion (March 1998 to November 1999), *Geological Society, London, Memoirs*, *21*(1), 467–481.

Odbert, H. M., R. C. Stewart, and G. Wadge (2014), Cyclic phenomena at the Soufrière Hills volcano, Montserrat, *Geological Society, London, Memoirs*, *39*(1), 41–60.

Ohlendorf, S. J., C. H. Thurber, J. D. Pesicek, and S. G. Prejean (2014), Seismicity and seismic structure at Okmok Volcano, Alaska, *Journal of volcanology and geothermal research*, *278*, 103–119.

Okubo, P. G., J. S. Nakata, R. Y. Koyanagi, M. Poland, T. Takahashi, and C. Landowski (2014), The evolution of seismic monitoring systems at the Hawaiian Volcano Observatory, *US Geol. Surv. Prof. Pap*, *1801*, 67–94.

Oppenheimer, C., P. Francis, and A. J. Maciejewski (1998), Spectroscopic observation of HCl degassing from Soufrière Hills volcano, Montserrat, *Geophysical Research Letters*, *25*(19), 3689–3692.

Paulatto, M., T. Minshull, B. Baptie, S. Dean, J. O. Hammond, T. Henstock, C. Kenedi, E. Kiddle, P. Malin, C. Peirce, et al. (2010a), Upper crustal structure of an active volcano

from refraction/reflection tomography, Montserrat, Lesser Antilles, *Geophysical Journal International*, *180*(2), 685–696.

Paulatto, M., T. Minshull, and T. Henstock (2010b), Constraints on an intrusive system beneath the Soufriére Hills Volcano, Montserrat, from finite difference modeling of a controlled source seismic experiment, *Geophysical Research Letters*, *37*(19).

Paulatto, M., C. Annen, T. J. Henstock, E. Kiddle, T. A. Minshull, R. Sparks, and B. Voight (2012), Magma chamber properties from integrated seismic tomography and thermal modeling at Montserrat, *Geochemistry, Geophysics, Geosystems*, *13*(1).

Podvin, P., and I. Lecomte (1991), Finite difference computation of traveltimes in very contrasted velocity models: a massively parallel approach and its associated tools, *Geophysical Journal International*, *105*(1), 271–284.

Powell, C. (1938), The Royal Society expedition to Montserrat, BWI final report, *Phil. Trans. R. Soc. Lond. A*, *237*(771), 1–34.

Power, J. A., A. D. Jolly, R. A. Page, and S. R. McNutt (1995), Seismicity and forecasting of the 1992 eruptions of Crater Peak vent, Mount Spurr Volcano, Alaska: an overview, *US Geol. Surv. Bull*, *2139*, 149.

Power, J. A., M. Wyss, and J. L. Latchman (1998), Spatial variations in the frequency-magnitude distribution of earthquakes at Soufrière Hills Volcano, Montserrat, West Indies, *Geophysical Research Letters*, *25*(19), 3653–3656.

Press, W. H., S. A. Teukolsky, W. T. Vetterling, and B. P. Flannery (1992), Numerical Recipes in C, chapter 10, *Cambridge University Press*, *2*, 444–455.

Presti, D., B. Orecchio, G. Falcone, and G. Neri (2008), Linear versus non-linear earthquake location and seismogenic fault detection in the southern Tyrrhenian Sea, Italy, *Geophysical Journal International*, *172*(2), 607–618.

Qamar, A., W. St. Lawrence, J. N. Moore, and G. Kendrick (1983), Seismic signals preceding the explosive eruption of Mount St. Helens, Washington, on 18 May 1980, *Bulletin of the Seismological Society of America*, *73*(6A), 1797–1813.

Rodgers, M., P. J. Smith, T. A. Mather, and D. M. Pyle (2016), Quiescent-explosive transitions during dome-forming volcanic eruptions: Using seismicity to probe the volcanic

processes leading to the 29 July 2008 Vulcanian explosion of Soufrière Hills Volcano, Montserrat, *Journal of Geophysical Research: Solid Earth*, *121*(12), 8453–8471.

Roman, D., J. Neuberg, and R. Luckett (2006), Assessing the likelihood of volcanic eruption through analysis of volcanotectonic earthquake fault–plane solutions, *Earth and Planetary Science Letters*, *248*(1-2), 244–252.

Roman, D., S. De Angelis, J. Latchman, and R. White (2008), Patterns of volcanotectonic seismicity and stress during the ongoing eruption of the Soufrière Hills Volcano, Montserrat (1995–2007), *Journal of Volcanology and Geothermal Research*, *173*(3-4), 230–244.

Roman, D. C., and K. V. Cashman (2006), The origin of volcano-tectonic earthquake swarms, *Geology*, *34*(6), 457–460.

Roobol, M., and A. Smith (1998), Pyroclastic stratigraphy of the Soufrière Hills Volcano, Montserrat-Implications for the present eruption, *Geophysical Research Letters*, *25*(18), 3393–3396.

Rowe, C., C. Thurber, and R. White (2004), Dome growth behavior at Soufrière Hills Volcano, Montserrat, revealed by relocation of volcanic event swarms, 1995–1996, *Journal of Volcanology and Geothermal Research*, *134*(3), 199–221.

Rutherford, M. J., and J. D. Devine (2003), Magmatic conditions and magma ascent as indicated by hornblende phase equilibria and reactions in the 1995–2002 Soufrière Hills magma, *Journal of Petrology*, *44*(8), 1433–1453.

Ryan, G., S. A. Onacha, E. Shalev, and P. E. Malin (2009), Imaging the Montserrat geothermal prospect using Magnetotelluric (MT) and Time Domain Electromagnetic induction (TDEM) measurements, *IESE Report*.

Ryan, G., S. Loughlin, M. James, L. Jones, E. Calder, T. Christopher, M. Strutt, and G. Wadge (2010), Growth of the lava dome and extrusion rates at Soufrière Hills Volcano, Montserrat, West Indies: 2005–2008, *Geophysical Research Letters*, *37*(19).

Ryan, G., J. Peacock, E. Shalev, and J. Rugis (2013), Montserrat geothermal system: A 3D conceptual model, *Geophysical Research Letters*, *40*(10), 2038–2043.

Shalev, E., and J. M. Lees (1998), Cubic B-splines tomography at Loma Prieta, *Bulletin of the Seismological Society of America*, *88*(1), 256–269.

Shalev, E., C. Kenedi, P. Malin, V. Voight, V. Miller, D. Hidayat, R. Sparks, T. Minshull, M. Paulatto, L. Brown, et al. (2010), Three-dimensional seismic velocity tomography of Montserrat from the SEA-CALIPSO offshore/onshore experiment, *Geophysical Research Letters*, *37*(19).

Shearer, P. (2009), *Introduction to seismology, second edition*, Cambridge University Press.

Shepherd, J., J. Tomblin, and D. Woo (1971), Volcano-seismic crisis in Montserrat, West Indies, 1966–67, *Bulletin volcanologique*, *35*(1), 143–162.

Shepherd, J., R. Robertson, J. Latchman, and L. Lynch (2002), Precursory activity to the 1995 eruption of the Soufrière Hills volcano, Montserrat, *Seismic Research Unit, The University of the West Indies, St. Augustine, Trinidad.*

Shepherd, J., R. Robertson, J. Latchman, and L. Lynch (2003), Precursory Activity to the 1995 Eruption of Soufrière Hills Volcano, Montserrat., *Seismic Research Unit, Technical Report, University of the West Indies, Jamaica.*

Šindija, D., J. Neuberg, and P. Smith (2021), The complex, static displacement of a very long period seismic signal observed at soufrière hills volcano, montserrat, wi, *Journal of Volcanology and Geothermal Research*, *413*, 107,209.

Smith, P. (2013), Volcano-Tectonic Seismicity of Soufrière Hills Volcano, Montserrat, in *Encyclopedia of Earthquake Engineering*, pp. 3907–3919, Springer.

Sparks, R., and S. Young (2002), The eruption of Soufrière Hills Volcano, Montserrat (1995-1999): overview of scientific results, *Geological Society, London, Memoirs*, *21*(1), 45–69.

Sparks, R. S. J. (1997), Causes and consequences of pressurisation in lava dome eruptions, *Earth and Planetary Science Letters*, *150*(3), 177–190.

Sparks, R. S. J. (2003), Forecasting volcanic eruptions, *Earth and Planetary Science Letters*, *210*(1-2), 1–15.

Sparks, R. S. J., S. R. Young, J. Barclay, E. S. Calder, P. Cole, B. Darroux, M. Davies, T. Druitt, C. Harford, R. Herd, et al. (1998), Magma production and growth of the lava dome of the Soufrière Hills Volcano, Montserrat, West Indies: November 1995 to December 1997, *Geophysical Research Letters*, *25*(18), 3421–3424.

Stephens, C. D., B. A. Chouet, R. A. Page, J. C. Lahr, and J. A. Power (1994), Seismological aspects of the 1989–1990 eruptions at Redoubt Volcano, Alaska: the SSAM perspective, *Journal of volcanology and geothermal research*, *62*(1-4), 153–182.

Stinton, A. J. (2015), A new Digital Elevation Model of the Soufrière Hills Volcano, Montserrat, *Open File Report OFR*, pp. 15–01.

Stinton, A. J., P. D. Cole, R. C. Stewart, H. M. Odbert, and P. Smith (2014), The 11 february 2010 partial dome collapse at soufriere hills volcano, montserrat, *Geological Society, London, Memoirs*, *39*(1), 133–152.

Stix, J., R. C. Torres, L. Narváez, J. A. Raigosa, D. Gómez, R. Castonguay, et al. (1997), A model of vulcanian eruptions at Galeras volcano, Colombia, *Journal of Volcanology and Geothermal Research*, *77*(1-4), 285–303.

Tarantola, A., and B. Valette (1982), Inverse problems= quest for information, *J. geophys*, *50*(3), 150–170.

Team, P. V. O. (1991), Lessons from a major eruption: Mt. Pinatubo, Philippines, *Eos, Transactions American Geophysical Union*, *72*(49), 545–555.

Thompson, G., M. Beer, I. Kougioumtzoglou, E. Patelli, and S. Au (2015), Seismic monitoring of volcanoes, *Encyclopedia of earthquake engineering*, *10*, 978–3.

Trofimovs, J., L. Amy, G. Boudon, C. Deplus, E. Doyle, N. Fournier, M. Hart, J. Komorowski, A. Le Friant, E. Lock, et al. (2006), Submarine pyroclastic deposits formed at the Soufrière Hills volcano, Montserrat (1995–2003): What happens when pyroclastic flows enter the ocean?, *Geology*, *34*(7), 549–552.

Trofimovs, J., C. Foster, R. Sparks, S. Loughlin, A. Le Friant, C. Deplus, L. Porritt, T. Christopher, R. Luckett, P. Talling, et al. (2012), Submarine pyroclastic deposits formed during the 20th May 2006 dome collapse of the Soufrière Hills Volcano, Montserrat, *Bulletin of Volcanology*, *74*(2), 391–405.

Tuffen, H., R. Smith, and P. R. Sammonds (2008), Evidence for seismogenic fracture of silicic magma, *Nature*, *453*(7194), 511–514.

Turino, C., D. Scafidi, E. Eva, and S. Solarino (2009), Inferences on active faults at the Southern Alps–Liguria basin junction from accurate analysis of low energy seismicity, *Tectonophysics*, *475*(3), 470–479.

Ukawa, M., and H. Tsukahara (1996), Earthquake swarms and dike intrusions off the east coast of Izu Peninsula, central Japan, *Tectonophysics*, *253*(3), 285–303.

Utheim, T., and J. Havskov (1997), The SEISLOG data acquisition system version 7.0 user manual, *Institute of Solid Earth Physics, University of Bergen*.

Vargas-Bracamontes, D., and J. Neuberg (2012), Interaction between regional and magma-induced stresses and their impact on volcano-tectonic seismicity, *Journal of volcanology and geothermal research*, *243*, 91–96.

Varley, N. R., R. Arámbula-Mendoza, G. Reyes-Dávila, J. Stevenson, and R. Harwood (2010), Long-period seismicity during magma movement at Volcán de Colima, *Bulletin of volcanology*, *72*(9), 1093–1107.

Voight, B., R. Hoblitt, A. Clarke, A. Lockhart, A. Miller, L. Lynch, and J. McMahon (1998), Remarkable cyclic ground deformation monitored in real-time on Montserrat, and its use in eruption forecasting, *Geophysical Research Letters*, *25*(18), 3405–3408.

Voight, B., R. Sparks, A. Miller, R. Stewart, R. Hoblitt, A. Clarke, J. Ewart, W. Aspinall, B. Baptie, E. Calder, et al. (1999), Magma flow instability and cyclic activity at Soufrière Hills volcano, Montserrat, British West Indies, *Science*, *283*(5405), 1138–1142.

Voight, B., A. Linde, I. Sacks, G. Mattioli, R. Sparks, D. Elsworth, D. Hidayat, P. Malin, E. Shalev, C. Widiwijayanti, et al. (2006), Unprecedented pressure increase in deep magma reservoir triggered by lava-dome collapse, *Geophysical Research Letters*, *33*(3).

Voight, B., C. Widiwijayanti, G. Mattioli, D. Elsworth, D. Hidayat, and M. Strutt (2010), Magma-sponge hypothesis and stratovolcanoes: Case for a compressible reservoir and quasi-steady deep influx at Soufrière Hills Volcano, Montserrat, *Geophysical Research Letters*, *37*(19).

Voight, B., R. Sparks, E. Shalev, T. Minshull, M. Paulatto, C. Annen, C. Kenedi, J. Hammond, T. Henstock, L. Brown, et al. (2014), The sea-calipso volcano imaging experiment

at montserrat: plans, campaigns at sea and on land, scientific results, and lessons learned, *Geological Society, London, Memoirs*, *39*(1), 253–289.

Wadge, G. (1986), The dykes and structural setting of the volcanic front in the Lesser Antilles island arc, *Bulletin of Volcanology*, *48*(6), 349–372.

Wadge, G., and M. Isaacs (1988), Mapping the volcanic hazards from Soufrière Hills Volcano, Montserrat, West Indies using an image processor, *Journal of the Geological Society*, *145*(4), 541–551.

Wadge, G., B. Voight, R. Sparks, P. Cole, S. Loughlin, and R. Robertson (2014), An overview of the eruption of Soufrière Hills Volcano, Montserrat from 2000 to 2010, *Geological Society, London, Memoirs*, *39*(1), 1–40.

Waldhauser, F. (2001a), hypoDD–A program to compute double-difference hypocenter locations, *Tech. rep.*, Earthquake Science Center.

Waldhauser, F. (2001b), HypoDD-A program to compute double-difference hypocenter locations, *Tech. rep.*, Earthquake Science Center.

Watson, I., C. Oppenheimer, B. Voight, P. Francis, A. Clarke, J. Stix, A. Miller, D. Pyle, M. Burton, S. Young, et al. (2000), The relationship between degassing and ground deformation at Soufrière Hills Volcano, Montserrat, *Journal of Volcanology and Geothermal Research*, *98*(1-4), 117–126.

Wesson, R., W. Lee, and J. Gibbs (1971), Aftershocks of the earthquake, *The San Fernando, California, Earthquake of February 9, 1971, US Geol. Surv. Profess. Pap*, *733*, 24–29.

White, R., and W. McCausland (2016), Volcano-tectonic earthquakes: A new tool for estimating intrusive volumes and forecasting eruptions, *Journal of Volcanology and Geothermal Research*, *309*, 139–155.

White, R. A., A. D. Miller, L. Lynch, and J. Power (1998), Observations of hybrid seismic events at Soufrière Hills volcano, Montserrat: July 1995 to September 1996, *Geophysical Research Letters*, *25*(19), 3657–3660.

Widiwijayanti, C., A. Clarke, D. Elsworth, and B. Voight (2005), Geodetic constraints on the shallow magma system at Soufrière Hills Volcano, Montserrat, *Geophysical Research Letters*, *32*(11).

Winder, T., C. Bacon, J. Smith, T. Hudson, T. Greenfield, and R. White (2021), QuakeMigrate: a Modular, Open-Source Python Package for Automatic Earthquake Detection and Location, *Earth and Space Science Open Archive ESSOAr*.

Woods, J., C. Donaldson, R. S. White, C. Caudron, B. Brandsdóttir, T. S. Hudson, and T. Ágústsdóttir (2018), Long-period seismicity reveals magma pathways above a laterally propagating dyke during the 2014–15 Bardharbunga rifting event, Iceland, *Earth and Planetary Science Letters*, *490*, 216–229.

Woods, J., T. Winder, R. S. White, and B. Brandsdóttir (2019), Evolution of a lateral dike intrusion revealed by relatively-relocated dike-induced earthquakes: The 2014–15 bárdharbunga–holuhraun rifting event, iceland, *Earth and Planetary Science Letters*, *506*, 53–63.

Yokoo, A., M. Iguchi, T. Tameguri, and K. Yamamoto (2013), Processes Prior to Outbursts of Vulcanian Eruption at Showa Crater of Sakurajima Volcano (Special Section Sakurajima Special Issue), *Bulletin of the Volcanological Society of Japan*, *58*(1), 163–181.

Young, S., R. Hoblitt, A. Smith, J. Devine, G. Wadge, and J. Shepherd (1996), Dating of explosive volcanic eruptions associated with dome growth at the Soufrière Hills volcano, Montserrat, West Indies, in *Second Caribbean Conference on Natural Hazards and Hazard Management, MVO Open File Report*, vol. 96, p. 22.

Young, S., B. Voight, and H. Duffell (2003), Magma extrusion dynamics revealed by high-frequency gas monitoring at Soufrière Hills Volcano, Montserrat, *Geological Society, London, Special Publications*, *213*(1), 219–230.

Young, S. R., P. W. Francis, J. Barclay, T. Casadevall, C. Gardner, B. Darroux, M. Davies, P. Delmelle, G. Norton, A. Maciejewski, et al. (1998), Monitoring SO_2 emission at the Soufrière Hills Volcano: Implications for changes in eruptive conditions, *Geophysical Research Letters*, *25*(19), 3681–3684.

Zellmer, G., R. Sparks, C. Hawkesworth, and M. Wiedenbeck (2003), Magma emplacement and remobilization timescales beneath Montserrat: insights from Sr and Ba zonation in plagioclase phenocrysts, *Journal of Petrology*, *44*(8), 1413–1431.

Zhang, X., J. Zhang, C. Yuan, S. Liu, Z. Chen, and W. Li (2020), Locating induced

earthquakes with a network of seismic stations in Oklahoma via a deep learning method, *Scientific reports*, *10*(1), 1–12.

Zimanowski, B. (1998), Phreatomagmatic explosions, *From magma to tephra. Elsevier, Amsterdam*, *4*, 25–53.

Appendix A

NonLinLoc Configuration

A.1 *NonLinLoc* Parameters

One of the main issues that arises when setting up the seismic velocity model used by *NonLinLoc* is which projection to use to convert between latitude and longitude to X,Y, Z format. *NonLinLoc* recommends using geographical co-ordinates for the input of all data types. This is then converted from a geographical to cartesian co-ordinate system within *NonLinLoc* to calculate the earthquake hypocenter and origin time, before being converted back to a geographical system; which is widely more used for interpretations. As the conversion is calculated within *NonLinloc*, the method uses a simplified equation to map between the two co-ordinate systems, and so small errors will arise in locations from this. *NonLinLoc* uses simplified equations to convert between the two co-ordinate systems instead of a true conversion (unlike other programs such as ArcGIS).

This appendix aims to understand the different reference frames available through *NonLinLoc* and how this affects the outputted location by using a small dataset of earthquakes. The Grid Origin of the pre-defined velocity model is chosen by the user in *NonLinLoc*, and it is thought that using a Grid Origin further from your region causes a slight increase in error due to the increase in latitude distance (which amplifies the error calculated when using the simplified equations for conversion). Hence, different origins and reference frames are tested to see if there is a way to reduce this additional error. The option of inputting everything in a cartesian format is also tested to understand how this ultimately reduces errors compared to using *NonLinLoc's* preferred approach of geographical co-ordinates for input. The results from this section help determine the

setup parameters used for Chapter 4.

A.2 Reference Frame

NonLinLoc creates a 3D seismic velocity grid based on given dimensions, velocity structure and grid origin. This is used to calculate travel times throughout the grid for each seismic station. Normally, this information is given in latitude and longitude, and therefore a basic conversion into the X,Y,Z grid is used when creating the 3D seismic velocity grid. The grid origin is defined by the user, and a slight change in grid location is seen during each calculation step for different grid origins, resulting in an unsystematic change in earthquake locations. Different users using the same input data but different grid origins will result in different earthquake locations from one another. There are several ways the projections can be defined with *NonLinLoc*, all of which alter the final location. This section aims to understand how different projections and grid origins alter earthquake locations, and how these can be chosen to reduce error in location.

A.2.1 Projections

NonLinLoc has the following projections that can be used during the initial setup:

- Lambert - standard projection used for mapping large areas in the mid latitudes. Projection is conformed in that shapes are well preserved for a considerable extent near to the standard parallels
- Global - sets spherical regional/teleseismic mode with no geographic transformation - most are input and used directly as latitude and longitude in degrees
- Simple - transformation into a cartesian/rectangular system - only correct for longitudinal distances
- None - no geographical correction - input in XYZ
- Short Distance Correction - projection intended for use on very small study regions
- TRANS-MERC - delivers high accuracy in zones less than a few degrees in east-west extent (transverse lines are around poles).

Due to Montserrat being a small research area, it was decided to test the Simple, Lambert and None Projections as these represent the most likely choices by other users.

A.2.2 Grid Origin

The user also defines the grid origin for a 1D or 2D velocity model. This can be the centre point of the research area, or the left hand corner. Three co-ordinates were tested for the Left Hand Corner grid origin, and three were tested for the Centre origin. The grid origin (alongside parameters for the velocity model dimensions), determines the size of the velocity model, which in turn determines the search region for *NonLinLoc* to use during earthquake location. This is chosen due to *NonLinLoc* using arrival time tables for each seismic station for its earthquake location, and hence needs a search region to look into. The larger the search region, the greater amount of memory needed to store the arrival time tables per station, and hence the greater computational power needed for earthquake location. Therefore, this search region is determined by the user so it can be tailored to suit the region of interest; this results in the user inputting the size of the velocity model (X,Y,Z), with a grid origin for the starting point of that model.

For the Left Hand Corner grid origin, three left hand bottom co-ordinates were used, each with increasing distance from the island (Figure A.1):

- L1: 16.67N, 62.24W
- L2: 16.5N, 62.4W
- L3 (midway between L1 and L2): 16.58N, 62.3W

For the Centre grid origin, the following co-ordinates were used:

- C1: 16.72N 62.2W
- C2: 16.71N 62.21W
- C3: 16.73N 62.19W

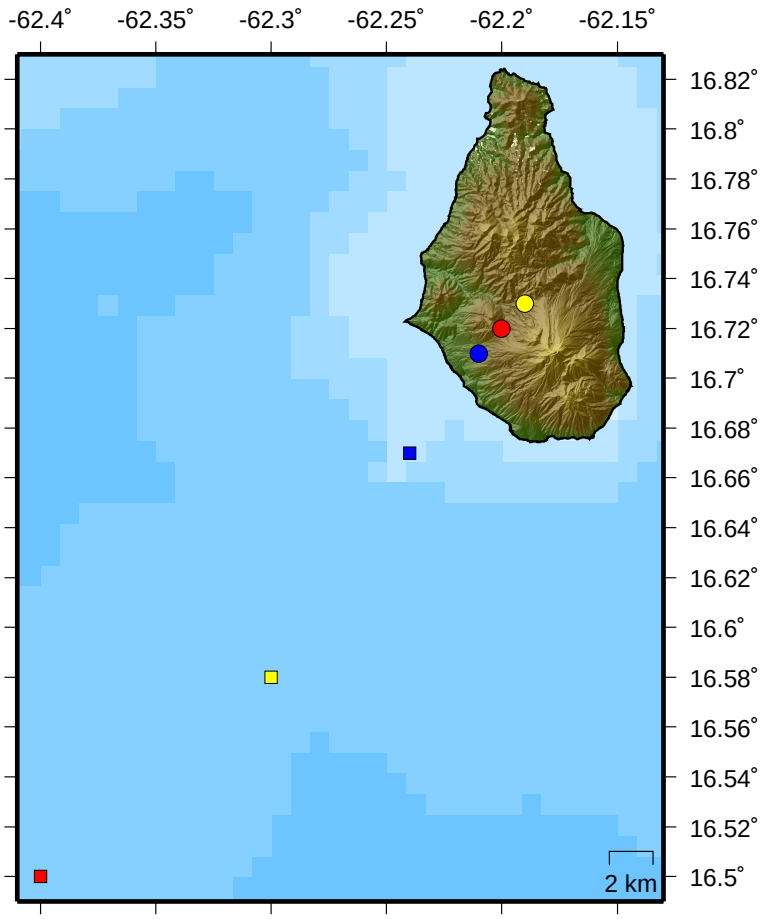

Figure A.1: Diagram shows the location of the co-ordinates for the Centre and Left Hand Corner Grid Origins used in testing. Square = LHC grid origins: blue - L1, red - L2, yellow - L3. Circles = centre grid origins: red - C1 blue - C2, yellow - C3.

A.2.3 Comparison of Left Hand Corner grid Origin

Users normally define the grid origin as the bottom left hand corner when creating the velocity model in *NonLinLoc*. To start, the three Left Hand co-ordinates were tested using the Simple projection. For simplicity, a group of 36 earthquakes from a VT string on the 27^{th} July 2017 were used for relocation; this provided a small dataset in the area of interest which would allow any small changes in location to be seen. In theory, all three relocations should relocate to the same location due to the same input data (velocity model, arrival times, method used). Having a grid origin further from Montserrat results in a larger (X,Y dimensions) velocity model, but importantly as using a 1D model, this model will still represent the same velocity changes with depth. Therefore any changes in location would be due to the effect of conversion to X,Y,Z using the grid origin only. Hypocenters for the three relocations are shown in Figure A.2.

The locations are very similar for each relocation, however there are slight variations. Earthquakes further from the grid origin, such as those located on the northern tip of Montserrat, show a greater variation in location than those down in the south.

The first step is to understand where the difference in location was occurring within *NonLinLoc*. The difference in X and Y between each station and an earthquake location should be equal for every grid origin (this was looked at before *NonLinLoc* converts back into Latitude and Longitude):

$$\Delta X_{L1} = \Delta X_{L2} = \Delta X_{L3} \tag{A.1}$$

However this equation does not hold true, with changes in X and Y (dX and dY) values of up to 500 m between each relocation. Before *NonLinLoc* relocates the earthquake, it creates a travel time grid per station comprising of travel times between every point in the search grid to the seismic station. *NonLinLoc* calculates the distance to each station from the grid origin in creating the travel time grids. It would be expected that the change in distance between any two stations would be the same for each grid origin, with a

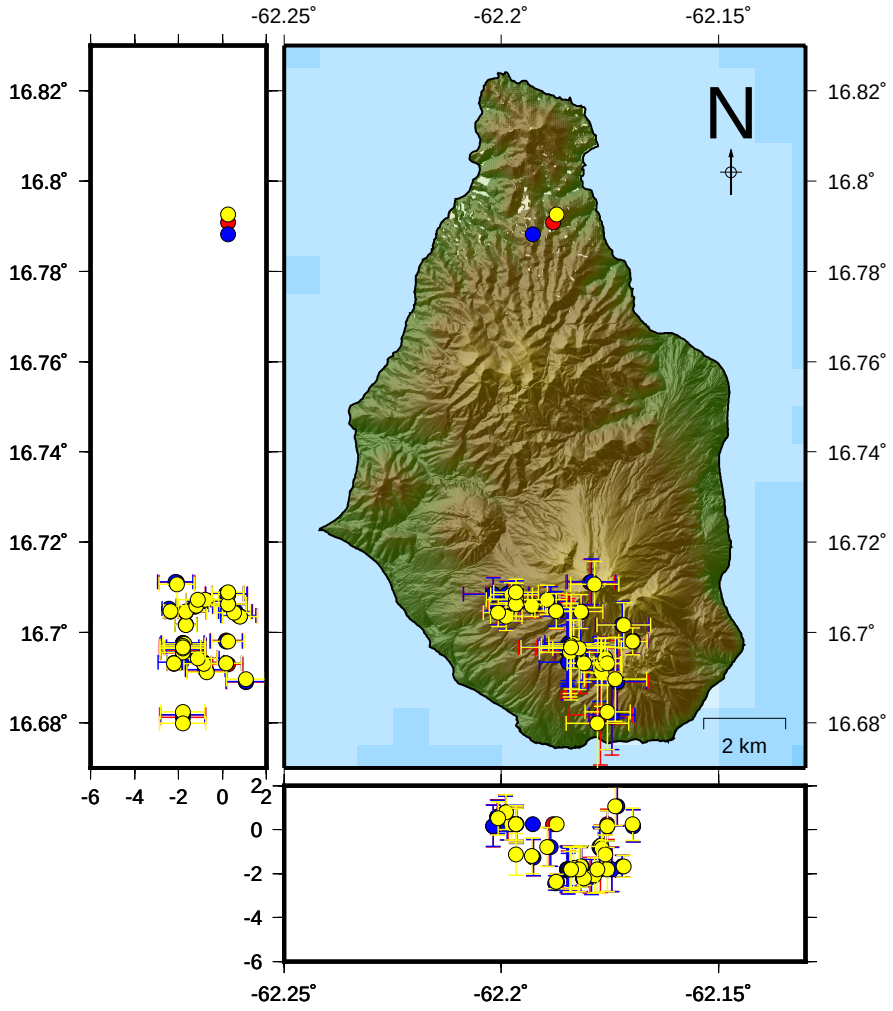

Figure A.2: Figure shows the relocation of earthquakes for different LHC grid origins, used with the Simple projection. blue - L1, red - L2, yellow - L3

schematic of this shown in Figure A.3.

The calculations show that the ΔY value stays the same for each grid origin, but the ΔX value varies on the scale of 1 m. This shows that the primary issue has originated in the conversion from longitude to X distance, which is caused by the following equation (*NonLinLoc* uses this equation to calculate distance for the SIMPLE projection):

$$X(km) = (Long - LongOrigin) * 111.111 * cos(latradians) \tag{A.2}$$

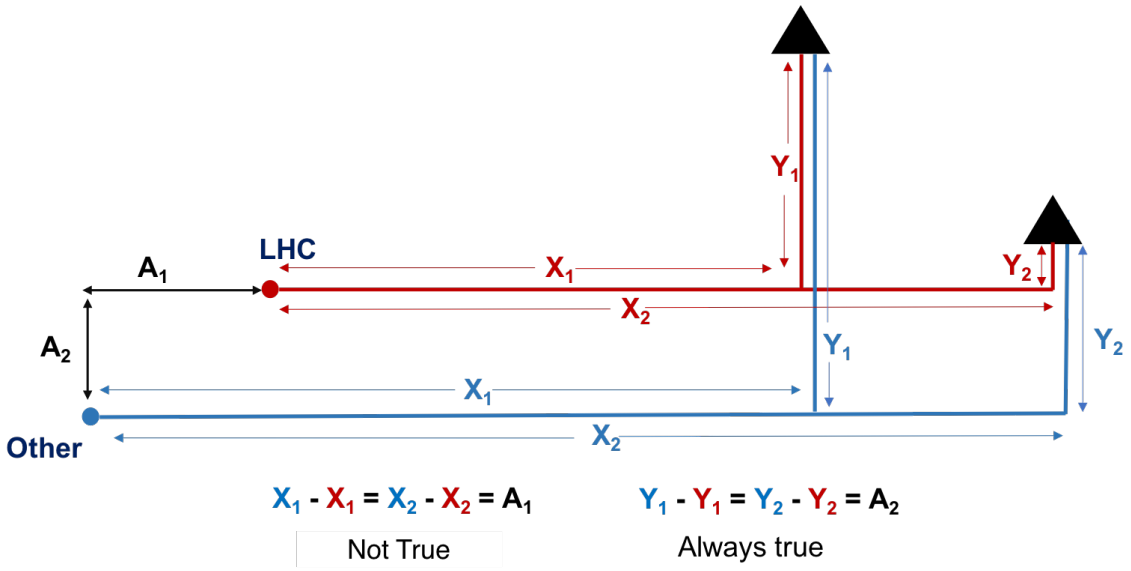

Figure A.3: Schematic showing the calculations used to compare the change in distance between two grid origins, and how this differs for the X and Y co-ordinates. Black triangles represent seismic stations. Red and Blue circles represent grid origins (defined by the user in velocity model setup), with red and blue lines representing distances between the grid origin and the seismic station. X_1, and X_2 represent the X distance between grid origin and seismic station 1 and 2 respectively. This is the same notation for the Y distance.

A.2.4 Comparison of Centre Grid Origins

It was decided to then compare the Left Hand Corner grid origin with the centre grid origin to see if this improved locations. The main issue in change in location was the difference in distance between the station and grid origin caused by calculation A.2 when converting to X,Y.Z. Events further away from the Left Hand Corner grid origin had greater changes in location, and therefore in theory, all events would be closer to the grid origin if using a central point. Results show some changes in location, but the changes in location are significantly lower than when using the Left Hand Corner as the grid origin. This suggests that using a central point as the grid origin when creating the velocity model will produce less change in location between different users.

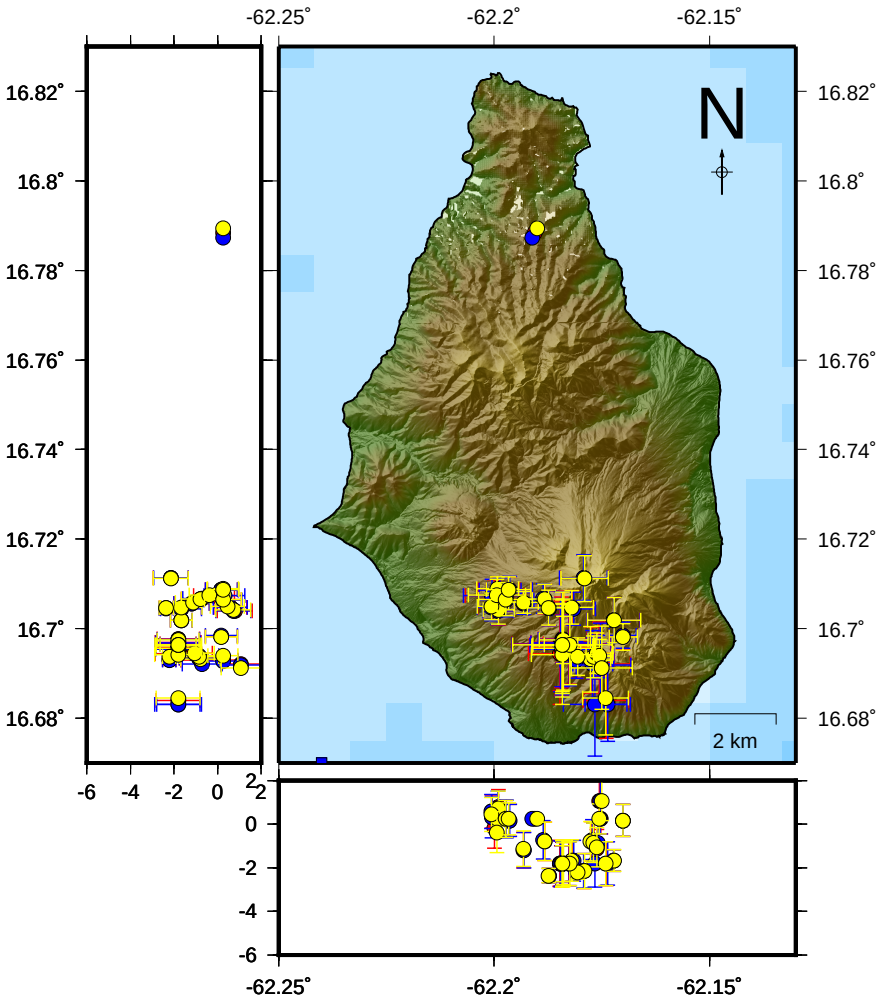

Figure A.4: Figure shows the relocation of earthquakes (circles) for different middle co-ordinates used with the simple projection. Red = C1, blue = C2, yellow = C3 - co-ordinates for these can be shown above.

A.2.5 Comparison of Projection Types

Using the central grid origin, the earthquakes were relocated using the Simple and Lambert projection to see how the relocations varied with different projection methods. For the Lambert projection, the reference ellipsoid used was WGS-84, with the 1st and 2nd parallels: 16.68 and 16.82. For each projection the change in earthquake location for X and Y between each pair of grid origins was calculated. I.e. this was done three times to make sure comparisons between each grid origin were looked at (C1 - C2, C3 - C1, C2 - C3). Average change in location, median and maximum and minimum values were calculated to compare each projection.

Simple Projection

The change in distance from C2 to C3 showed the largest variations with a change in location up to 1.24 km. On average, there was a change in latitude of 30-80 m and a change in longitude of 20-65 m.

Lambert Projection

On average the lambert projection showed a location change of 20-90 m for latitude and longitude, with a max change of 1.20 km. This showed similar results to that found with the simple projection. In comparison between the two methods, the simple projection performs slightly better with averages of 1 m less for change in location.

None Projection

To remove the problem of transformation between X,Y and latitude and longitude the None projection was looked at. This requires all information to be input into *NonLinLoc* in X,Y,Z format, removing issues in converting with different projections methods. Using a predefined grid for this initial transformation results in X,Y,Z co-ordinates being accurate within 1 m. The UTM Zone 20N was used for conversion which has an accuracy of 1 m. This would provide better constraints on relocation than using the Simple and Lambert projection in *NonLinLoc*.

For the None projection the grid origin is still chosen to create the velocity model, but this is given in X,Y, Z co-ordinates: 356993.64 E, 1823716.67 N. This was chosen to match the corner co-ordinates of the 3D model that would be used in comparisons later so that all velocity models are of the same size.

Relocations for the None projection showed very little change overall in comparison to the simple method (on scale of 1-2m). However, it was decided that it was best to use the None transformation to remove any effects of projection types and user-defined grid origins on earthquake relocations. This removes any user error produced when choosing the grid origin,

A.3 Final Setup for *NonLinLoc*

The final reference frame used in *NonLinLoc* was the UTM Zone 20N grid with the None projection. The grid origin was set at 356993.64 E, 1823716.67 N, with the 3D seismic velocity model grid being set to 50 km by 50 km, with a 35 km depth. All locations calculated are produced in the X,Y,Z format with no conversion between latitude and longitude.

Appendix B

NonLinLoc Parameters

Parameter	**Description**	**Typical Values**
CONTROL	Sets various general program control parameters	-
TRANS	Sets the transformation parameters used between geographic and XYZ	NONE
VGOUT	Specifies the directory path and file root name for the output velocity grid	[path to model directory]
VGTYPE	specifies the physical wave type for creation of velocity grid	P/S
VGGRID	Specifies the size and type of the velocity grid	[velocity model dimensions]
GTFILES	Specifies the the path for the inputted velocity grid, and the path name for the outputted time grids	[path to time directory]
GTMODE	Specifies several program run modes	GRID3D, ANGLES YES
GTSRCE	Specifies a source location; can be repeated for each station. A separate time and angles grid will be created for each source	-
GT PLFD	Selects Podvin and Lecomte finite difference, and method parameters. Must not be used otherwise	10^{03}
EQFILES	Specifies the file name for the input time grids and the file name for the output observations files	-
EQSTA	Specifies the station phase and timing error used to generate the synthetic phase reading	-
EQEVENT	Specifies the hypocentre location such as X,Y,Z and Origin Time	-
EQSRCE	Specifies a source location	-
EQMODE	Choice of calculation: Source to Station or Stations to Sources	Source to Station
EQUAL2ERR	Specifies the mapping of error to phase pick quality for output of observations for the HYPO71 file format	-
EQVPVS	Specifies ratio for P velocity to S velocity	1.80
LOCSIG	Used for identification written in all output files	[User name]
LOCFILES	Specifies the input filename for the observation files, the filenames for the time grids and the output filename for the location files	-
LOCSEARCH	Specifies the search type and parameters: GRID, MET or OCT	OCT
LOCMETH	Specifies the location method and method parameters	EDT OT WT
LOCGAU	Specifies the parameters for the Gaussian modelisation error covariances	0.1s, 1 km
LOC QUAL2ERR	Specifies the mapping of phase pick qualities to time uncertainities (Seconds)	-
LOCGRID	Specifies the size of an initial or nested search grid	[match VGGRID]

Table B.1: Table describing the main functions used in *NonLinLoc*.

Appendix C

Statistics Data

	DX		DY		DZ	
Compare	**AdjP**	**Z**	**AdjP**	**Z**	**AdjP**	**Z**
1 - 10	3.54E-47	14.744	5.60E-58	16.338	4.60E-124	23.885
1 - 11	8.99E-28	11.337	1.20E-51	15.423	3.73E-178	28.622
10 - 11	6.91E-02	-3.406	1.00E+00	-0.914	2.27E-04	4.737
1 - 12	1.39E-52	15.562	1.65E-63	17.097	6.45E-125	23.967
10 - 12	1.00E+00	0.818	1.00E+00	0.759	1.00E+00	0.082
11 - 12	2.52E-03	4.224	1.00E+00	1.673	3.40E-04	-4.655
1 - 13	9.26E-82	19.393	2.16E-95	20.946	3.62E-196	30.035
10 - 13	3.50E-04	4.649	4.27E-04	4.608	8.15E-08	6.150
11 - 13	8.29E-14	8.056	3.52E-06	5.522	1.00E+00	1.413
12 - 13	1.34E-02	3.831	1.25E-02	3.849	1.36E-07	6.068
1 - 14	7.87E-50	15.151	2.01E-60	16.677	1.59E-124	23.929
10 - 14	1.00E+00	0.407	1.00E+00	0.340	1.00E+00	0.044
11 - 14	1.44E-02	3.813	1.00E+00	1.254	2.83E-04	-4.693
12 - 14	1.00E+00	-0.411	1.00E+00	-0.419	1.00E+00	-0.038
13 - 14	2.32E-03	-4.242	2.07E-03	-4.268	1.08E-07	-6.105
1 - 15	8.52E-10	-6.837	4.50E-05	-5.056	5.28E-06	5.450
10 - 15	2.88E-101	-21.580	1.62E-99	-21.393	7.24E-74	-18.435
11 - 15	8.72E-72	-18.174	3.47E-91	-20.479	9.14E-117	-23.172
12 - 15	4.30E-109	-22.398	1.04E-106	-22.152	1.59E-74	-18.517
13 - 15	1.28E-149	-26.230	5.03E-147	-26.001	1.93E-131	-24.585
14 - 15	4.01E-105	-21.987	1.05E-102	-21.733	3.19E-74	-18.479
1 - 2	2.20E-275	-35.589	6.37E-249	-33.835	1.97E-16	-8.765
10 - 2	0.00E+00	-50.333	0.00E+00	-50.172	8.55E-232	-32.650
11 - 2	0.00E+00	-46.926	0.00E+00	-49.258	6.73E-304	-37.387
12 - 2	0.00E+00	-51.150	0.00E+00	-50.931	5.84E-233	-32.732
13 - 2	0.00E+00	-54.982	0.00E+00	-54.780	0.00E+00	-38.799
14 - 2	0.00E+00	-50.739	0.00E+00	-50.512	2.01E-232	-32.694
15 - 2	8.94E-180	-28.752	4.11E-180	-28.779	7.80E-44	-14.215
1 - 3	1.02E-71	-18.166	1.16E-50	-15.276	1.31E-13	-8.000
10 - 3	1.69E-235	-32.909	2.54E-217	-31.613	4.59E-221	-31.885
11 - 3	2.77E-189	-29.503	6.11E-205	-30.699	1.35E-291	-36.622
12 - 3	2.42E-247	-33.727	7.03E-228	-32.373	3.34E-222	-31.967
13 - 3	0.00E+00	-37.559	2.94E-285	-36.221	0.00E+00	-38.034
14 - 3	2.36E-241	-33.316	5.13E-222	-31.953	1.12E-221	-31.929
15 - 3	9.90E-28	-11.329	1.69E-22	-10.220	3.25E-39	-13.450
2 - 3	5.78E-66	17.423	7.24E-75	18.559	1.00E+00	0.765
1 - 4	1.47E-52	15.558	2.93E-63	17.063	5.92E-124	23.875
10 - 4	1.00E+00	0.814	1.00E+00	0.726	1.00E+00	-0.011
11 - 4	2.56E-03	4.221	1.00E+00	1.640	2.16E-04	-4.748
12 - 4	1.00E+00	-0.003	1.00E+00	-0.033	1.00E+00	-0.093
13 - 4	1.32E-02	-3.835	1.09E-02	-3.882	7.62E-08	-6.160
14 - 4	1.00E+00	0.408	1.00E+00	0.386	1.00E+00	-0.055
15 - 4	4.65E-109	22.395	2.18E-106	22.119	8.80E-74	18.424

Table C.1: Part 1 of 3: Adjusted P values and Z values from Dunn Test. If values in the Adjusted P column are less than 0.05 then the result is significant, if the Z value is positive then a is significantly more than b (aka has significantly larger changes in location). Model numbers stand for: 1 - MVO Hypocenter; 2 - Rowe Hypocenter; 3 - 1D Sea Calipso Hypocenter; 4 - MVO GAU NonLinLoc; 5 - Rowe GAU NonLinLoc; 6 - 1D Sea Calipso GAU NonLinLoc; 7 - 3D GAU NonLinLoc; 8 - MVO EDT NonLInLoc; 9 - Rowe EDT NonLinLoc; 10 - 1D Sea Calipso EDT NonLinLoc; 11 - 3D EDT NonLinLoc; 12 - MVO Weighted NonLinLoc; 13 - Rowe Weighted NonLinLoc; 14 - 1D Sea Calipso Weighted NonLinLoc; 15 - 3D Weighted NonLinLoc.

	DX		DY		DZ	
Compare	**AdjP**	**Z**	**AdjP**	**Z**	**AdjP**	**Z**
2 - 4	0.00E+00	51.147	0.00E+00	50.898	1.20E-231	32.639
3 - 4	2.72E-247	33.724	2.08E-227	32.339	6.42E-221	31.874
1 - 5	2.26E-82	19.466	4.43E-95	20.911	4.50E-196	30.028
10 - 5	2.46E-04	4.722	5.03E-04	4.574	8.53E-08	6.143
11 - 5	4.58E-14	8.128	4.27E-06	5.488	1.00E+00	1.405
12 - 5	9.94E-03	3.904	1.43E-02	3.815	1.42E-07	6.061
13 - 5	1.00E+00	0.072	1.00E+00	-0.034	1.00E+00	-0.007
14 - 5	1.68E-03	4.315	2.41E-03	4.234	1.13E-07	6.098
15 - 5	1.90E-150	26.302	1.23E-146	25.967	2.31E-131	24.577
2 - 5	0.00E+00	55.054	0.00E+00	54.746	0.00E+00	38.792
3 - 5	0.00E+00	37.631	1.02E-284	36.187	0.00E+00	38.027
4 - 5	9.80E-03	3.907	1.25E-02	3.848	7.98E-08	6.153
1 - 6	1.39E-49	15.113	4.01E-61	16.773	7.54E-125	23.960
10 - 6	1.00E+00	0.369	1.00E+00	0.436	1.00E+00	0.075
11 - 6	1.67E-02	3.776	1.00E+00	1.350	3.29E-04	-4.662
12 - 6	1.00E+00	-0.448	1.00E+00	-0.323	1.00E+00	-0.007
13 - 6	1.96E-03	-4.280	3.17E-03	-4.172	1.31E-07	-6.074
14 - 6	1.00E+00	-0.037	1.00E+00	0.096	1.00E+00	0.031
15 - 6	9.14E-105	21.950	1.29E-103	21.829	1.79E-74	18.510
2 - 6	0.00E+00	50.702	0.00E+00	50.608	7.23E-233	32.725
3 - 6	8.21E-241	33.279	2.36E-223	32.049	4.12E-222	31.960
4 - 6	1.00E+00	-0.445	1.00E+00	-0.290	1.00E+00	0.086
5 - 6	1.41E-03	-4.352	3.68E-03	-4.138	1.37E-07	-6.067
1 - 7	1.21E-09	-6.787	5.27E-05	-5.026	1.01E-05	5.334
10 - 7	8.49E-101	-21.530	3.09E-99	-21.363	8.33E-75	-18.552
11 - 7	2.17E-71	-18.124	6.44E-91	-20.449	6.05E-118	-23.289
12 - 7	1.32E-108	-22.348	2.03E-106	-22.122	1.80E-75	-18.634
13 - 7	4.76E-149	-26.180	1.10E-146	-25.971	1.09E-132	-24.701
14 - 7	1.20E-104	-21.937	2.02E-102	-21.703	3.65E-75	-18.596
15 - 7	1.00E+00	0.050	1.00E+00	0.030	1.00E+00	-0.117
2 - 7	2.11E-180	28.802	1.73E-180	28.809	4.10E-43	14.098
3 - 7	5.58E-28	11.379	1.24E-22	10.250	1.56E-38	13.333
4 - 7	1.43E-108	-22.345	4.25E-106	-22.089	1.01E-74	-18.541
5 - 7	7.10E-150	-26.252	2.68E-146	-25.937	1.30E-132	-24.694
6 - 7	2.74E-104	-21.900	2.49E-103	-21.799	2.04E-75	-18.627
1 - 8	6.60E-51	15.313	1.27E-59	16.567	2.84E-125	24.001
10 - 8	1.00E+00	0.569	1.00E+00	0.229	1.00E+00	0.116
11 - 8	7.38E-03	3.975	1.00E+00	1.143	4.01E-04	-4.621
12 - 8	1.00E+00	-0.249	1.00E+00	-0.530	1.00E+00	0.034
13 - 8	4.72E-03	-4.080	1.25E-03	-4.379	1.68E-07	-6.034

Table C.2: Part 2 of 3: Adjusted P values and Z values from Dunn Test. If values in the Adjusted P column are less than 0.05 then the result is significant, if the Z value is positive then a is significantly more than b (aka has significantly larger changes in location). Model numbers stand for: 1 - MVO Hypocenter; 2 - Rowe Hypocenter; 3 - 1D Sea Calipso Hypocenter; 4 - MVO GAU NonLinLoc; 5 - Rowe GAU NonLinLoc; 6 - 1D Sea Calipso GAU NonLinLoc; 7 - 3D GAU NonLinLoc; 8 - MVO EDT NonLInLoc; 9 - Rowe EDT NonLinLoc; 10 - 1D Sea Calipso EDT NonLinLoc; 11 - 3D EDT NonLinLoc; 12 - MVO Weighted NonLinLoc; 13 - Rowe Weighted NonLinLoc; 14 - 1D Sea Calipso Weighted NonLinLoc; 15 - 3D Weighted NonLinLoc.

	DX		DY		DZ	
Compare	**AdjP**	**Z**	**AdjP**	**Z**	**AdjP**	**Z**
14 - 8	1.00E+00	0.162	1.00E+00	-0.111	1.00E+00	0.072
15 - 8	1.11E-106	22.149	1.16E-101	21.622	8.40E-75	18.551
2 - 8	0.00E+00	50.901	0.00E+00	50.402	1.91E-233	32.766
3 - 8	1.05E-243	33.478	1.75E-220	31.843	1.12E-222	32.001
4 - 8	1.00E+00	-0.246	1.00E+00	-0.496	1.00E+00	0.127
5 - 8	3.45E-03	-4.153	1.47E-03	-4.345	1.76E-07	-6.026
6 - 8	1.00E+00	0.199	1.00E+00	-0.207	1.00E+00	0.041
7 - 8	3.38E-106	22.099	2.22E-101	21.592	9.53E-76	18.668
1 - 9	2.22E-78	18.989	3.75E-92	20.587	4.92E-196	30.025
10 - 9	2.30E-03	4.245	2.25E-03	4.250	8.69E-08	6.140
11 - 9	2.09E-12	7.651	2.54E-05	5.164	1.00E+00	1.402
12 - 9	6.41E-02	3.427	5.06E-02	3.491	1.45E-07	6.058
13 - 9	1.00E+00	-0.404	1.00E+00	-0.358	1.00E+00	-0.010
14 - 9	1.30E-02	3.838	9.69E-03	3.910	1.15E-07	6.095
15 - 9	4.85E-145	25.825	5.32E-143	25.643	2.49E-131	24.574
2 - 9	0.00E+00	54.577	0.00E+00	54.422	0.00E+00	38.789
3 - 9	3.93E-300	37.154	1.21E-279	35.863	0.00E+00	38.024
4 - 9	6.33E-02	3.430	4.46E-02	3.524	8.13E-08	6.150
5 - 9	1.00E+00	-0.477	1.00E+00	-0.324	1.00E+00	-0.003
6 - 9	1.12E-02	3.875	1.44E-02	3.814	1.39E-07	6.064
7 - 9	1.77E-144	25.775	1.15E-142	25.613	1.40E-132	24.691
8 - 9	2.49E-02	3.676	6.10E-03	4.020	1.79E-07	6.023

Table C.3: Part 3 of 3: Adjusted P values and Z values from Dunn Test. If values in the Adjusted P column are less than 0.05 then the result is significant, if the Z value is positive then a is significantly more than b (aka has significantly larger changes in location). Model numbers stand for: 1 - MVO Hypocenter; 2 - Rowe Hypocenter; 3 - 1D Sea Calipso Hypocenter; 4 - MVO GAU NonLinLoc; 5 - Rowe GAU NonLinLoc; 6 - 1D Sea Calipso GAU NonLinLoc; 7 - 3D GAU NonLinLoc; 8 - MVO EDT NonLInLoc; 9 - Rowe EDT NonLinLoc; 10 - 1D Sea Calipso EDT NonLinLoc; 11 - 3D EDT NonLinLoc; 12 - MVO Weighted NonLinLoc; 13 - Rowe Weighted NonLinLoc; 14 - 1D Sea Calipso Weighted NonLinLoc; 15 - 3D Weighted NonLinLoc.

	EX		EY		EZ	
Compare	**AdjP**	**Z**	**AdjP**	**Z**	**AdjP**	**Z**
1 - 10	7.52E-73	18.308	1.98E-136	25.047	4.09E-05	-5.074
1 - 11	5.70E-32	12.154	6.08E-106	22.073	1.00E+00	1.623
10 - 11	7.96E-08	-6.153	3.08E-01	-2.974	2.23E-09	6.697
1 - 12	4.48E-191	29.642	1.68E-262	34.746	2.23E-04	4.742
10 - 12	9.31E-28	11.334	3.20E-20	9.699	1.01E-20	9.815
11 - 12	1.86E-66	17.488	8.75E-35	12.673	1.91E-01	3.118
1 - 13	1.38E-277	35.731	0.00E+00	42.766	4.55E-60	16.629
10 - 13	5.80E-66	17.423	3.14E-68	17.719	2.04E-102	21.702
11 - 13	7.08E-121	23.576	4.18E-93	20.693	7.10E-49	15.005
12 - 13	1.20E-07	6.089	1.11E-13	8.020	1.45E-30	11.887
1 - 14	1.03E-164	27.521	2.64E-247	33.725	1.00E+00	2.229
10 - 14	3.32E-18	9.213	4.24E-16	8.678	2.95E-11	7.303
11 - 14	2.87E-51	15.367	2.35E-29	11.652	1.00E+00	0.606
12 - 14	1.00E+00	-2.121	1.00E+00	-1.021	1.00E+00	-2.512
13 - 14	2.33E-14	-8.210	1.63E-17	-9.041	5.51E-45	-14.399
1 - 15	1.96E-20	9.749	4.93E-79	19.068	1.39E-20	9.784
10 - 15	1.19E-15	-8.559	2.35E-07	-5.979	6.51E-48	14.858
11 - 15	1.00E+00	-2.406	2.79E-01	-3.005	3.50E-14	8.161
12 - 15	4.86E-86	-19.894	2.24E-53	-15.678	4.83E-05	5.042
13 - 15	8.27E-147	-25.982	3.94E-122	-23.698	8.05E-10	-6.845
14 - 15	1.21E-68	-17.773	1.27E-46	-14.657	4.42E-12	7.554
1 - 2	2.13E-129	-24.393	7.43E-77	-18.803	2.23E-230	32.550
10 - 2	0.00E+00	-42.701	0.00E+00	-43.850	0.00E+00	37.623
11 - 2	2.06E-290	-36.547	0.00E+00	-40.876	5.53E-208	30.926
12 - 2	0.00E+00	-54.035	0.00E+00	-53.549	3.64E-168	27.808
13 - 2	0.00E+00	-60.124	0.00E+00	-61.569	4.76E-55	15.921
14 - 2	0.00E+00	-51.914	0.00E+00	-52.528	6.55E-200	30.320
15 - 2	1.87E-253	-34.142	0.00E+00	-37.871	1.05E-112	22.766
1 - 3	1.00E+00	1.691	1.87E-03	-4.290	2.11E-66	-17.481
10 - 3	5.50E-60	-16.617	3.66E-187	-29.337	2.52E-33	-12.407
11 - 3	1.33E-23	-10.464	3.83E-151	-26.363	2.47E-79	-19.104
12 - 3	6.63E-170	-27.952	0.00E+00	-39.036	2.20E-107	-22.222
13 - 3	5.97E-252	-34.040	0.00E+00	-47.056	5.67E-253	-34.109
14 - 3	4.23E-145	-25.831	0.00E+00	-38.015	1.85E-84	-19.710
15 - 3	8.15E-14	-8.058	1.20E-118	-23.358	1.18E-161	-27.264
2 - 3	5.87E-148	26.084	1.05E-45	14.513	0.00E+00	-50.030
1 - 4	4.57E-180	28.775	3.72E-252	34.054	1.35E-03	4.362
10 - 4	1.28E-23	10.468	2.22E-17	9.007	4.06E-19	9.436
11 - 4	5.15E-60	16.621	4.67E-31	11.981	6.47E-01	2.739
12 - 4	1.00E+00	-0.867	1.00E+00	-0.692	1.00E+00	-0.379
13 - 4	3.69E-10	-6.955	3.14E-16	-8.712	1.44E-32	-12.266
14 - 4	1.00E+00	1.254	1.00E+00	0.329	1.00E+00	2.133

Table C.4: Part 1 of 3: Adjusted P values and Z values from Dunn Test. If values in the Adjusted P column are less than 0.05 then the result is significant, if the Z value is positive then a is significantly more than b (aka has significantly larger error). Model numbers stand for: 1 - MVO Hypocenter; 2 - Rowe Hypocenter; 3 - 1D Sea Calipso Hypocenter; 4 - MVO GAU NonLinLoc; 5 - Rowe GAU NonLinLoc; 6 - 1D Sea Calipso GAU NonLinLoc; 7 - 3D GAU NonLinLoc; 8 - MVO EDT NonLInLoc; 9 - Rowe EDT NonLinLoc; 10 - 1D Sea Calipso EDT NonLinLoc; 11 - 3D EDT NonLinLoc; 12 - MVO Weighted NonLinLoc; 13 - Rowe Weighted NonLinLoc; 14 - 1D Sea Calipso Weighted NonLinLoc; 15 - 3D Weighted NonLinLoc.

	EX		EY		EZ	
Compare	**AdjP**	**Z**	**AdjP**	**Z**	**AdjP**	**Z**
15 - 4	1.07E-78	19.027	9.46E-49	14.986	6.21E-06	-5.422
2 - 4	0.00E+00	53.168	0.00E+00	52.857	8.80E-173	-28.187
3 - 4	1.56E-159	27.085	0.00E+00	38.344	9.53E-104	21.843
1 - 5	1.83E-266	35.007	0.00E+00	42.146	1.20E-57	16.291
10 - 5	1.39E-60	16.699	1.58E-63	17.099	2.98E-99	21.365
11 - 5	1.44E-113	22.853	1.32E-87	20.074	1.09E-46	14.668
12 - 5	8.50E-06	5.365	1.42E-11	7.400	7.80E-29	11.549
13 - 5	1.00E+00	-0.724	1.00E+00	-0.620	1.00E+00	-0.338
14 - 5	7.46E-12	7.486	3.90E-15	8.422	6.88E-43	14.061
15 - 5	9.57E-139	25.259	7.96E-116	23.079	8.04E-09	6.507
2 - 5	0.00E+00	59.400	0.00E+00	60.950	2.04E-57	-16.259
3 - 5	2.33E-241	33.317	0.00E+00	46.437	5.42E-248	33.772
4 - 5	4.84E-08	6.232	6.15E-14	8.092	8.81E-31	11.929
1 - 6	1.47E-152	26.486	1.98E-234	32.835	1.00E+00	1.773
10 - 6	3.02E-14	8.178	7.16E-13	7.788	7.90E-10	6.847
11 - 6	1.46E-44	14.332	5.46E-25	10.762	1.00E+00	0.150
12 - 6	1.68E-01	-3.156	1.00E+00	-1.911	3.15E-01	-2.968
13 - 6	2.48E-18	-9.245	3.20E-21	-9.931	6.77E-48	-14.855
14 - 6	1.00E+00	-1.035	1.00E+00	-0.890	1.00E+00	-0.456
15 - 6	7.34E-61	16.737	4.22E-41	13.767	1.20E-13	-8.010
2 - 6	0.00E+00	50.879	0.00E+00	51.638	5.74E-206	-30.776
3 - 6	1.05E-133	24.795	1.17E-299	37.125	1.37E-80	19.254
4 - 6	1.00E+00	-2.289	1.00E+00	-1.219	1.00E+00	-2.589
5 - 6	1.66E-15	-8.521	1.32E-18	-9.312	9.85E-46	-14.518
1 - 7	2.25E-17	9.006	1.22E-73	18.406	7.36E-19	9.374
10 - 7	1.45E-18	-9.302	3.28E-09	-6.640	2.73E-45	14.447
11 - 7	1.72E-01	-3.149	2.59E-02	-3.666	9.61E-13	7.750
12 - 7	1.35E-92	-20.637	5.44E-58	-16.339	3.80E-04	4.632
13 - 7	2.53E-155	-26.725	4.84E-129	-24.359	4.22E-11	-7.255
14 - 7	1.63E-74	-18.516	6.07E-51	-15.318	9.51E-11	7.144
15 - 7	1.00E+00	-0.743	1.00E+00	-0.661	1.00E+00	-0.410
2 - 7	1.51E-242	33.399	4.96E-301	37.210	8.36E-117	-23.176
3 - 7	2.70E-11	7.315	5.07E-112	22.697	7.91E-157	26.854
4 - 7	5.70E-85	-19.770	3.63E-53	-15.648	5.68E-05	5.011
5 - 7	5.00E-147	-26.002	1.47E-122	-23.740	4.83E-10	-6.917
6 - 7	2.12E-66	-17.480	3.61E-45	-14.428	3.11E-12	7.600
1 - 8	1.09E-104	21.942	1.07E-168	27.852	1.00E+00	-0.818

Table C.5: Part 2 of 3: Adjusted P values and Z values from Dunn Test. If values in the Adjusted P column are less than 0.05 then the result is significant, if the Z value is positive then a is significantly more than b (aka has significantly larger error). Model numbers stand for: 1 - MVO Hypocenter; 2 - Rowe Hypocenter; 3 - 1D Sea Calipso Hypocenter; 4 - MVO GAU NonLinLoc; 5 - Rowe GAU NonLinLoc; 6 - 1D Sea Calipso GAU NonLinLoc; 7 - 3D GAU NonLinLoc; 8 - MVO EDT NonLInLoc; 9 - Rowe EDT NonLinLoc; 10 - 1D Sea Calipso EDT NonLinLoc; 11 - 3D EDT NonLinLoc; 12 - MVO Weighted NonLinLoc; 13 - Rowe Weighted NonLinLoc; 14 - 1D Sea Calipso Weighted NonLinLoc; 15 - 3D Weighted NonLinLoc.

	EX		EY		EZ	
Compare	**AdjP**	**Z**	**AdjP**	**Z**	**AdjP**	**Z**
10 - 8	2.93E-02	3.634	5.28E-01	2.805	2.18E-03	4.256
11 - 8	1.34E-20	9.787	7.88E-07	5.779	1.00E+00	-2.441
12 - 8	1.43E-12	-7.700	5.70E-10	-6.894	2.84E-06	-5.559
13 - 8	3.12E-41	-13.789	2.81E-48	-14.914	3.86E-66	-17.446
14 - 8	2.54E-06	-5.579	4.50E-07	-5.873	2.43E-01	-3.047
15 - 8	3.54E-32	12.193	1.65E-16	8.784	3.08E-24	-10.602
2 - 8	0.00E+00	46.335	0.00E+00	46.655	4.30E-242	-33.367
3 - 8	3.64E-89	20.251	1.19E-224	32.142	2.56E-60	16.663
4 - 8	8.70E-10	-6.834	5.85E-08	-6.202	2.33E-05	-5.180
5 - 8	5.46E-37	-13.065	2.49E-44	-14.294	1.34E-63	-17.109
6 - 8	5.79E-04	-4.544	6.58E-05	-4.983	1.00E+00	-2.591
7 - 8	2.95E-36	12.936	3.72E-19	9.445	2.28E-22	-10.191
1 - 9	1.43E-179	28.736	3.99E-282	36.022	6.31E-26	10.959
10 - 9	1.94E-23	10.428	5.30E-26	10.975	7.90E-56	16.033
11 - 9	9.98E-60	16.581	3.34E-42	13.949	1.05E-18	9.336
12 - 9	1.00E+00	-0.906	1.00E+00	1.276	5.30E-08	6.218
13 - 9	2.78E-10	-6.995	1.62E-09	-6.744	1.50E-06	-5.669
14 - 9	1.00E+00	1.215	1.00E+00	2.297	2.68E-16	8.730
15 - 9	2.29E-78	18.987	1.88E-62	16.954	1.00E+00	1.175
2 - 9	0.00E+00	53.129	0.00E+00	54.825	2.32E-101	-21.590
3 - 9	4.58E-159	27.045	0.00E+00	40.312	6.87E-176	28.440
4 - 9	1.00E+00	-0.040	1.00E+00	1.968	4.41E-09	6.597
5 - 9	3.76E-08	-6.271	9.56E-08	-6.124	1.02E-05	-5.332
6 - 9	1.00E+00	2.250	1.51E-01	3.187	4.30E-18	9.186
7 - 9	1.25E-84	19.730	1.97E-67	17.615	1.00E+00	1.585
8 - 9	1.15E-09	6.794	3.24E-14	8.170	5.40E-30	11.777

Table C.6: Part 3 of 3: Adjusted P values and Z values from Dunn Test. If values in the Adjusted P column are less than 0.05 then the result is significant, if the Z value is positive then a is significantly more than b (aka has significantly larger error). Model numbers stand for: 1 - MVO Hypocenter; 2 - Rowe Hypocenter; 3 - 1D Sea Calipso Hypocenter; 4 - MVO GAU NonLinLoc; 5 - Rowe GAU NonLinLoc; 6 - 1D Sea Calipso GAU NonLinLoc; 7 - 3D GAU NonLinLoc; 8 - MVO EDT NonLInLoc; 9 - Rowe EDT NonLinLoc; 10 - 1D Sea Calipso EDT NonLinLoc; 11 - 3D EDT NonLinLoc; 12 - MVO Weighted NonLinLoc; 13 - Rowe Weighted NonLinLoc; 14 - 1D Sea Calipso Weighted NonLinLoc; 15 - 3D Weighted NonLinLoc.

Appendix D

Mean Change in Location

	DX (km)	DY (km)	DZ (km)
1995	1.38	1.22	1.43
1996	1.85	2.65	1.39
1997	19.19	28.51	3.17
1998	11.81	10.49	2.33
1999	38.61	35.80	3.21
2000	20.49	15.26	5.12
2001	27.32	26.25	3.93
2002	45.35	48.08	6.45
2003	50.17	74.06	5.78
2004	51.95	71.20	7.85
2005	30.13	41.22	3.76
2006	46.01	64.24	2.32
2007	40.83	50.21	7.29
2008	69.91	50.33	5.68
2009	16.70	23.00	4.42
2010	14.12	16.79	1.73
2011	8.92	9.43	2.28
2012	5.01	4.06	1.19
2013	4.17	5.90	1.19
2014	3.42	3.60	0.88
2015	1.53	2.05	0.80
2016	6.21	4.59	1.77
2017	6.35	5.06	1.71
2018	0.74	0.51	0.85

Table D.1: Table showing the mean change in location for X, Y and Z earthquake hypocenters for each year between *Hypocenter* and *NonLinLoc* in km.